AYAZ MEHMOOD

Ayaz Thesis 090726

PHD Thesis, PG & UG Projects

Document Details

Submission ID
trn:oid:::27535:145268560

Submission Date
Jul 9, 2026, 10:51 PM GMT+5:30

Download Date
Jul 9, 2026, 11:01 PM GMT+5:30

File Name
Ayaz Thesis 090726.pdf

File Size
7.6 MB

192 Pages

49,242 Words

262,627 Characters

4% Overall Similarity

The combined total of all matches, including overlapping sources, for each database.

Filtered from the Report

- Bibliography
- Quoted Text
- Cited Text
- Small Matches (less than 14 words)

Exclusions

- 4 Excluded Sources
- 1 Excluded Match

Match Groups

23 Not Cited or Quoted 4%
Matches with neither in-text citation nor quotation marks

0 Missing Quotations 0%
Matches that are still very similar to source material

0 Missing Citation 0%
Matches that have quotation marks, but no in-text citation

0 Cited and Quoted 0%
Matches with in-text citation present, but no quotation marks

Top Sources

3% Internet sources
1% Publications
2% Submitted works (Student Papers)

Integrity Flags

0 Integrity Flags for Review

Our system's algorithms look deeply at a document for any inconsistencies that would set it apart from a normal submission. If we notice something strange, we flag it for you to review.

A Flag is not necessarily an indicator of a problem. However, we'd recommend you focus your attention there for further review.

Match Groups

- **23** Not Cited or Quoted 4%
  Matches with neither in-text citation nor quotation marks
- **0** Missing Quotations 0%
  Matches that are still very similar to source material
- **0** Missing Citation 0%
  Matches that have quotation marks, but no in-text citation
- **0** Cited and Quoted 0%
  Matches with in-text citation present, but no quotation marks

Top Sources

3% Internet sources
1% Publications
2% Submitted works (Student Papers)

Top Sources

The sources with the highest number of matches within the submission. Overlapping sources will not be displayed.

1	Student papers	Delhi Technological University on 2026-05-20 <1%
2	Internet	ebin.pub <1%
3	Student papers	Delhi Technological University on 2026-06-01 <1%
4	Student papers	Delhi Technological University on 2026-05-28 <1%
5	Publication	Florentina-Luiza Zavalan, Aldo Rona. "A workflow for designing contoured axisym... <1%
6	Student papers	Delhi Technological University on 2026-06-12 <1%
7	Publication	Jinhe Li, Jiarui Xu, Yi Zheng, Jiahao Hu et al. "Optimization of impeller-assisted dir... <1%
8	Publication	Li, Chenze. "Superior Mechanical Properties and Tunable Mechanical Anisotropy ... <1%
9	Internet	www.mdpi.com <1%
10	Internet	ualberta.scholaris.ca <1%

11 Publication

Gabor, Theodore T.. "Analysis of Powder-Gas Flow in Nozzles of Spray-Based Addit... <1%

12 Internet

thesis.sgu.ac.id <1%

13 Publication

Debbie Hwee Leng Seng, Rui Ken Sim, Xipeng Tan, Zhi-qian Zhang, Te Ba, Tzee Lu... <1%

14 Student papers

School of Business and Management ITB on 2026-07-02 <1%

15 Student papers

Swinburne University of Technology on 2021-05-20 <1%

16 Internet

pure.nwpu.edu.cn <1%

17 Internet

www.dtic.mil <1%

18 Internet

www.researchgate.net <1%

NUMERICAL ANALYSIS AND OPTIMIZATION OF COLD SPRAY PROCESS PARAMETERS AND NOZZLE DESIGN

1

A Thesis Submitted
In Partial Fulfillment of the Requirements
for the Degree of

DOCTOR OF PHILOSOPHY

by

AYAZ MEHMOOD
(Roll No. 2K21/PHD/ME/14)

Under the Supervision of

DR. MOHAMMAD ZUNAID **PROF. ASHOK KUMAR MADAN**
(Supervisor) **(Jt. Supervisor)**

3

Department of Mechanical Engineering
DELHI TECHNOLOGICAL UNIVERSITY
(Formerly Delhi College of Engineering)
Shahbad Daulatpur, Bawana Road, Delhi-110042, India.

July, 2026

ACKNOWLEDGMENT

This thesis was prepared while I was a doctoral candidate at Delhi Technological University, Delhi. First and foremost, I thank the Almighty for his grace, strength and patience during this research and learning process.

I would like to express my sincere appreciation to my Ph.D. supervisors, **Dr. Mohammad Zunaid** and **Prof. Ashok Kumar Madan**, for their guidance, encouragement and support during this research. Their deep academic knowledge, valuable feedback, and mentoring were instrumental in the development of this research. I am grateful to them for guiding me in the areas of research methodology, writing, numerical analysis, optimization and future research directions. I also express my appreciation to the anonymous reviewers of our published research papers, whose valuable feedback and suggestions contributed to the expansion and enhancement of the current study.

I would like to express my gratitude to the Head of the Department, my SRC and DRC members for agreeing to be on my doctoral examination committee and for their feedback and questions, which helped to improve this work. I would also like to thank the Department of Mechanical Engineering, Delhi Technological University for providing a conducive research environment, facilities and administrative support for the successful completion of this research.

Finally, I would like to thank my family for their love, faith and encouragement. I would like to thank my wife and children for their patience, understanding and support, which gave me the courage and encouragement to complete this work. I would like to thank all those who contributed to the successful completion of this work and helped me reach this delighted moment of my life.

AYAZ MEHMOOD

DELHI TECHNOLOGICAL UNIVERSITY

(Formerly Delhi College of Engineering)

Shahbad Daulatpur, Main Bawana Road, Delhi-42

CANDIDATE'S DECLARATION

I, Ayaz Mehmood, hereby certify that the work which is being presented in the thesis titled "**Numerical Analysis and Optimization of Cold Spray Process Parameters and Nozzle Design**" in partial fulfilment of the requirements for the award of the Degree of Doctor of Philosophy, submitted in the Department of Mechanical Engineering, Delhi Technological University is an authentic record of my work carried out during the period from 2021 to 2026 under the supervision of Dr. Mohammad Zunaid and Prof. Ashok Kumar Madan.

The matter presented in the thesis has not been submitted by me for the award of any other degree of this or any other institute.

AYAZ MEHMOOD
(2K21/PHDME/14)

This is to certify that the student has incorporated all the corrections suggested by the examiners in the thesis, and the statement made by the candidate is correct to the best of our knowledge.

Signature of Supervisor(s) **Signature of External Examiner**

DELHI TECHNOLOGICAL UNIVERSITY

(Formerly Delhi College of Engineering)

Shahbad Daulatpur, Main Bawana Road, Delhi-42

CERTIFICATE BY THE SUPERVISOR (s)

Certified that **Ayaz Mehmood (**2K21/PHDME/14) has carried out their research work presented in this thesis entitled **"Numerical Analysis and Optimization of Cold Spray Process Parameters and Nozzle Design"** for the award of **Doctor of Philosophy** from the Department of Mechanical Engineering, Delhi Technological University, Delhi, under our supervision. The thesis embodies the results of the original work, and the studies were carried out by the student himself. The contents of the thesis do not form the basis for the award of any other degree to the candidate or anyone else from this or any other University/Institution.

DR. MOHAMMAD ZUNAID
(Associate Professor)
Department of Mechanical Engineering
Delhi Technological University
Delhi-110042, INDIA

PROF. ASHOK KUMAR MADAN
(Professor)
Department of Mechanical Engineering
Delhi Technological University
Delhi-110042, INDIA

Date:

ABSTRACT

This study develops an integrated framework for high-pressure cold spray (HPCS) by combining bibliometric assessment, computational fluid dynamics (CFD)-based nozzle analysis, process-parameter optimization, grey-relational evaluation, and morphology-sensitive particle analysis to improve coating-oriented performance. The bibliometric assessment covered 387 Scopus-indexed documents published during 1999–2022. The mapped analysis showed that research grew rapidly after 2008 and reached about 34 publications in 2020. The overall trend confirmed that the field has moved from basic deposition feasibility toward numerical modeling, optimization, additive manufacturing, and coating-quality-driven process design.

The nozzle-design study showed that convergent length (L_c), divergent length (L_d), injector inner diameter (D_{id}), injector length (L_i), and exit diameter (D_e) act as a coupled geometric set governing particle velocity (PV), particle temperature (PT), heat flux (HF), and surface pressure (SP) near the substrate. Comparative model assessment showed that response surface methodology coupled with numerical simulation (RSM-DF) models were more accurate than the artificial neural network-genetic algorithm (ANN-GA) model, with $R^2 = 0.9893$ for RSM and $R^2 = 0.9848$ for ANN, whereas the ANN model captured nonlinear interactions with an overall correlation coefficient of R = 0.99191. Sensitivity analysis showed that increasing L_c raised PV to a stabilizing range while PT decreased slightly because of expansion-related cooling. Increasing L_d improved PV toward an optimum range but reduced PT. A smaller D_{id} increased PV but lowered PT, while increasing L_i raised PV to a limiting range and increased SP. Increasing D_e increased PV, reduced PT and HF, and lowered SP. On this basis, RSM-DF improved PV, PT, HF, and SP by 9.1%, 4.4%, 17.9%, and 27.6%, while ANN-GA yielded about 5% higher PV, 5.4% higher PT, 15.7% higher HF, and 20.9% lower SP than the baseline design.

The process-parameter study established that gas pressure (G_p), gas temperature (G_t), particle size (D_p), nozzle throat diameter (D_t), and stand-off distance (SoD) must be

optimized together because high PV, controlled PT, and low radial dispersion (RD) do not occur under the same conditions. The regression models showed strong predictive performance, with R^2 = 0.9898 for PV, 0.9919 for PT, and 0.9820 for RD, and residuals within ±3.6218**.** Sensitivity analysis identified D_p and G_t as dominant factors affecting PV and PT, whereas D_t significantly influenced RD. Relative to the reference condition of 623.4 m/s, 404.5 K, and 1.7367 mm**,** the TOPSIS solution produced 744.7 m/s, 418.2 K, and 0.7303 mm, whereas the VIKOR solution produced 857.1 m/s, 426.1 K, and 0.9466 mm. CFD validation confirmed solution errors of 4.05%, 3.41%, and 4.11% for TOPSIS and 1.24%, 0.28%, and 3.85% for VIKOR in PV, PT, and RD, respectively. Overall, the optimized condition increased PV by 9.16%, increased PT by 10%, and reduced RD by 52.57%**.**

Grey relational analysis (GRA) showed that PV and PT can be combined into a single thermal-kinetic performance index. The best case was obtained at expansion ratio (ER) = 10, carrier-gas temperature (T_c) = 300 K, pressure differential (ΔP) = 0.1 MPa, and D_p = 5 μm, producing PV = 844.47 m/s, PT = 421 K, and the highest GRG of 0.9474. The morphology-sensitive analysis showed that increasing G_p and decreasing D_p increased PV, whereas decreasing particle sphericity (ψ) from 1.0 to 0.6 increased both PV and RD and widened the substrate impact footprint. Therefore, spherical to near-spherical particles were identified as the preferred morphology for coating-oriented performance because they provide adequate impact velocity, a narrower footprint, and controlled lateral spreading.

Overall, this integrated bibliometric-numerical-optimization framework establishes a reliable basis for HPCS. The results show that improved coating-oriented performance depends on the combined optimization of nozzle geometry, operating conditions, and realistic particle characteristics, and that this framework provides a practical foundation for improving particle impact condition, coating uniformity, and overall process design.

17

LIST OF FIGURES

FIGURE 1.1 COMPARISON OF GAS INLET TEMPERATURE AND PARTICLE VELOCITY FOR COLD SPRAY WITH OTHER SPRAY PROCESSES 1
FIGURE 1.2 THERMAL SPRAY AND COLD SPRAY PROCESS COMPARISON 2
FIGURE 1.3 SCHEMATIC OF CS SYSTEM 4
FIGURE 1.4 HIGH-PRESSURE COLD SPRAY (HPCS) WORKING CYCLE 5
FIGURE 1.5 LOW-PRESSURE COLD SPRAY (LPCS) WORKING CYCLE 5
FIGURE 1.6 FLOW CHARACTERISTICS OF DE LAVAL NOZZLE 7
FIGURE 1.7 SCHEMATIC REPRESENTATION OF THE COMPUTATIONAL DOMAIN AND BOUNDARY CONDITIONS 8
FIGURE 3.1 STEPS INVOLVED IN DATA ASSESSMENT AND BIBLIOMETRIC ANALYSIS 36
FIGURE 3.2 SCHEMATIC OF 2D GEOMETRY OF NOZZLE AND SUBSTRATE USED IN THE CFD SIMULATIONS 39
FIGURE 3.3 DETAILED ILLUSTRATION OF KEY GEOMETRIC PARAMETERS IN AN AXISYMMETRIC 2D CD NOZZLE (NOT TO SCALE) 39
FIGURE 3.4 BOUNDARY CONDITIONS FOR COUPLED GAS AND PARTICLE FLOW IN THE 2D AXISYMMETRIC NOZZLE MODEL (NOT TO SCALE) 47
FIGURE 3.5 COMPUTATIONAL DOMAIN AND MESH DETAILS: (A) FULL 2D NOZZLE MESH, (B) PRECHAMBER, (C) UPSTREAM AND THROAT ZONES, AND (D) NOZZLE EXIT AND EXPANSION REGION 49
FIGURE 3.6 (A) MESH QUALITY METRICS AND (B) SHOCK RESOLUTION WITH REFINEMENT 51
FIGURE 3.7 MODEL VALIDATION AGAINST LITERATURE MEASUREMENTS: (A) COMPARISON OF SUPERSONIC JET/SHOCK FEATURES [88], (B) SUBSTRATE SURFACE TEMPERATURE AT DIFFERENT SOD VALUES [32], (C) PV AT VARIOUS G_p VALUES UNDER COMPARABLE CONDITIONS [29], [79], AND (D) PV AND PT ACROSS DIFFERENT D_p VALUES COMPARED WITH EXPERIMENTS [89] 52

FIGURE 3.8 FLOWCHART DETAILING THE OPTIMIZATION PROCESS FOR NOZZLE DESIGN 54
FIGURE 3.9 DETAILED ILLUSTRATION OF KEY GEOMETRIC PARAMETERS AND ASSOCIATED RESPONSES IN AN AXISYMMETRIC 2D CD NOZZLE 55
FIGURE 3.10 ANN ARCHITECTURE MAPPING STRUCTURE 57
FIGURE 3.11 GRAPHS REPRESENTING THE ANN MODEL (A) MSE AND OVERALL R^2 WITH THE NUMBER OF NEURONS IN THE HIDDEN LAYER, (B) ANN TOPOLOGY 58
FIGURE 3.12 MULTI-OBJECTIVE OPTIMIZATION FLOWCHART 62
FIGURE 3. 13 SCHEMATIC OF THE HPCS SYSTEM HIGHLIGHTING THE KEY OPERATING PARAMETERS AND DESIGN PARAMETERS 63
FIGURE 3. 14 2D AXISYMMETRIC NOZZLE'S BOUNDARY CONDITIONS FOR COUPLED GAS-PARTICLE FLOWS AND RESPONSES (NOT TO SCALE) 63
FIGURE 3.15 SCHEMATIC OF PARTICLE RD SHOWING TRAJECTORIES FROM INJECTION TO THE SUBSTRATE PLANE (NOT TO SCALE) 66
FIGURE 3.16 NSGA-II WORKFLOW USED IN THIS STUDY 67
FIGURE 3.17 AVERAGE DISTANCE CONVERGENCE OVER GENERATIONS 68
FIGURE 4.1 LEVEL OF DEVELOPMENT OF RESEARCH ON COLD SPRAY COATINGS 79
FIGURE 4.2 SUBJECT AREAS OF IN THE COLD SPRAY STUDY 80
FIGURE 4.3 OVERLAY VISUALIZATION OF CO-AUTHORSHIP ANALYSIS 82
FIGURE 4.4 THE NUMBER OF PUBLICATIONS BY SOURCE 83
FIGURE 4.5 THE NETWORK VISUALIZATION OF SOURCES 84
FIGURE 4.6 THE NETWORK VISUALIZATION OF DOCUMENTS BASED ON CITATIONS 87
FIGURE 4.7 DENSITY VISUALIZATION OF KEYWORD CO-OCCURRENCE: (A) IN THE TITLE, ABSTRACT, AND KEYWORD LIST, MINIMUM 3 OCCURRENCES, (B) IN AUTHOR-PROVIDED KEYWORDS, MINIMUM 5 OCCURRENCES 88
FIGURE 4.8 SENSITIVITY ANALYSIS OF KEY NOZZLE PARAMETERS (A) L_c, (B) L_d, (C) D_{id}, (D) L_i, AND (E) D_e 92
FIGURE 4.9 THE PREDICTED VS. ACTUAL PLOTS FOR ALL RESPONSES (A) PV, (B) PT, (C) HF, AND (D) SP 95

FIGURE 4.10 MULTIVARIATE RESPONSE SURFACE ANALYSIS 98
FIGURE 4.11 ANN MODEL TRAINING PERFORMANCE REPRESENTING MSE VS. TEST PERIODS 99
FIGURE 4.12 REGRESSION PLOTS REPRESENTING OVERALL CORRELATION COEFFICIENTS (R) 99
FIGURE 4.13 COMPARATIVE ANALYSIS OF CFD, RSM, AND ANN PREDICTIONS FOR KEY PERFORMANCE METRICS (A) PV, (B) PT, (C) HF, AND (D) SP 101
FIGURE 4.14 RAMP PLOTS DEMONSTRATING OPTIMAL GEOMETRIC AND PERFORMANCE PARAMETERS VIA RSM-DF 103
FIGURE 4.15 PARETO FRONTS IN THREE PAIRWISE COMPARISONS (A) OBJECTIVE 1 (PV) AND OBJECTIVE 2 (PT), (B) OBJECTIVE 2 (PT) AND OBJECTIVE 3 (HF), AND (C) OBJECTIVE 3 (HF) AND OBJECTIVE 4 (SP) 106
FIGURE 4.16 MODEL PERFORMANCE COMPARISON: RSM-DF VS. ANN-GA 109
FIGURE 4.17 IMPACT OF PARTICLE DIAMETER ON PV AND PT 109
FIGURE 4.18 THE BEHAVIOR WHEN THE PARTICLES OF DIFFERENT SIZES 5 TO 60 (MM) ARE INJECTED ALONG WITH GAS VELOCITY CONTOUR (A) BASELINE NOZZLE, (B) OPTIMIZED ANN-GA NOZZLE 110
FIGURE 4.19 GAS TEMPERATURE DISTRIBUTION COMPARISON (A) BASELINE NOZZLE, (B) OPTIMIZED ANN-GA NOZZLE 111
FIGURE 4.20 COMPARISON OF RESULTS BETWEEN THE BASELINE AND OPTIMIZED NOZZLE FOR DIFFERENT PARTICLE INJECTION PRESSURE CORRESPONDS TO 3 MPA AND 4 MPA GAS INLET PRESSURE FOR (A) PV, (B) PT, (C) HF, AND (D) SP 113
FIGURE 4.21 AXIAL COMPARISON OF BASELINE AND OPTIMIZED NOZZLE (A) GAS VELOCITY, (B) GAS TEMPERATURE, (C) PV, AND (D) PT 114
FIGURE 4.22 RADIAL COMPARISON OF BASELINE AND OPTIMIZED NOZZLE (A) HF AND (B) SP 115
FIGURE 4.23 GAS VELOCITY (A−C) AND PV (D−F) ALONG X_L AT DIFFERENT G_p: (A, D) 2 MPA, (B, E) 3 MPA, (C, F) 4 MPA FOR VARIOUS G_t 117

FIGURE 4.24 VARIATION OF PV ALONG THE RADIAL DIRECTION AT DIFFERENT G_p: (A) 2 MPA, (B) 3 MPA, (C) 4 MPA FOR VARIOUS G_t 118
FIGURE 4.25 COMPARISON OF PREDICTED AND ACTUAL VALUES: (A) PV, (B) PT, AND (C) RD 122
FIGURE 4.26 RESIDUAL DISTRIBUTION OF THE REGRESSION MODEL: (A) PV, (B) PT, AND (C) RD 122
FIGURE 4.27 PARAMETER SENSITIVITY HISTOGRAM 124
FIGURE 4.28 COMBINED EFFECTS OF INTERACTIONS BETWEEN PARAMETERS ON PV 126
FIGURE 4.29 COMBINED EFFECTS OF INTERACTIONS BETWEEN PARAMETERS ON PT 127
FIGURE 4.30 COMBINED EFFECTS OF INTERACTIONS BETWEEN PARAMETERS ON RD 128
FIGURE 4.31 PARETO-OPTIMAL SOLUTIONS OBTAINED FROM NSGA-II FOR THE TRI-OBJECTIVE: (A) 3D PARETO FRONT WITH MARKED SPECIAL POINTS AND (B–D) 2D PROJECTIONS ILLUSTRATING TRADE-OFFS AMONG OBJECTIVES AND THE OPTIMIZATION DIRECTION 129
FIGURE 4.32 COMPARISON BETWEEN REFERENCE AND OPTIMIZED CASES: (A) PV AND PT AT SUBSTRATE SURFACE AND (B) VARIATION OF RD ALONG NOZZLE AXIS 133
FIGURE 4.33 THE PREDICTED RELATIONSHIP BETWEEN THE PV AT IMPACT AND THE V_{cr} IN TERMS OF D_p: (A) REFERENCE CASE, (B) TOPSIS, AND (C) VIKOR 135
FIGURE 4.34 PARTICLE TRACKS COLORED BY PT FOR THE D_P RANGE USING A ROSIN-RAMMLER DISTRIBUTION: (A) REFERENCE CASE, (B) TOPSIS, AND (C) VIKOR 136
FIGURE 4.35 TEMPERATURE CONTOURS IN THE NOZZLE DIVERGENT SECTION FOR BEST, AVERAGE, AND WORST CASES 138
FIGURE 4.36 RADIAL PT DISTRIBUTION AT THE NOZZLE THROAT FOR GREY ORDERS 1, 16, AND 32, SHOWING THEIR INFLUENCE ON DISPERSION AND HEATING 139
FIGURE 4.37 GRG VARIATION WITH D_p AND ER FOR: (A) ΔP = 0.1 MPA, T_c = 300 K, (B) ΔP = 0.3 MPA, T_c = 300 K, (C) ΔP = 0.1 MPA, T_c = 600 K, AND (D) ΔP = 0.3 MPA, T_c = 600 K 142

FIGURE 4. 38 EFFECT OF D_p ON PV FOR DIFFERENT PARTICLE SPHERICITIES AT G_p OF (A) 2 MPA, (B) 3 MPA, AND (C) 4 MPA 143
FIGURE 4.39 PARTICLE TRACKS AT 3 MPA FOR DIFFERENT D_p AND ψ VALUES (A) 5 MM, (B) 25 MM, (C) 45 MM, AND (D) 75 MM 144
FIGURE 4.40 RADIAL DISTRIBUTION OF PV ON THE SUBSTRATE AT G_p VALUES OF $2-4$ MPA FOR D_p OF 5, 25, 45, AND 75 MM, COMPARING SPHERICITIES VALUES OF (A) $\psi = 1.0$, (B) $\psi = 0.8$, (C) $\psi = 0.7$, AND (D) $\psi = 0.6$ 145
FIGURE 4.41 RADIAL DISPERSION OF CU PARTICLES AT THE SUBSTRATE FOR DIFFERENT SPHERICITIES: (A) 5 MM AND (B) 75 MM 146

LIST OF TABLES

TABLE 1.1 MAJOR DIFFERENCE BETWEEN THE TWO METHODS 5

TABLE 3.1 DETAILED GEOMETRIC AND OPERATING PARAMETERS 40

TABLE 3.2 THERMOPHYSICAL PROPERTIES OF THE GAS AND MATERIALS USED IN THE SIMULATION 46

TABLE 3.3 GRID-INDEPENDENCE RESULTS CORRESPONDING TO $G_p = 3$ MPA, $G_t = 773$ K, $D_p = 25$ MM, $D_t = 2.5$ MM, AND SOD $= 25$ MM 50

TABLE 3.4 RSM FACTOR LEVELS FOR KEY NOZZLE DESIGN PARAMETERS AT THREE LEVELS 55

TABLE 3.5 DETAILED SPECIFICATION OF THE ANN STRUCTURE 58

TABLE 3.6 LEVELS OF INPUT PARAMETERS USED FOR THE FCCD DESIGN 64

TABLE 3.7 PARAMETERS AND THEIR LEVELS 72

TABLE 3.8 PARTICLE MORPHOLOGY CLASSIFICATION BASED ON SPHERICITY 76

TABLE 4.1 LEADING AUTHORS OF THE TOPIC COLD SPRAY 81

TABLE 4.2 LIST OF MAIN SOURCES OF COLD SPRAY RESEARCH IN THE PERIOD 1999–2022 83

TABLE 4.3 LIST OF THE TOP TEN INFLUENTIAL PAPERS ON THE TOPIC OF COLD SPRAY OBTAINED UP TO JULY 2022 85

TABLE 4.4 DETAILED ANOVA AND FIT STATISTICS ACROSS MULTIPLE RESPONSE VARIABLES 93

TABLE 4.5 DETAILED COMPARATIVE ANALYSIS OF RSM AND ANN MODEL METRICS ACROSS ALL RESPONSE VARIABLES 100

TABLE 4.6 COMPARISON OF BASELINE AND OPTIMIZED NOZZLE GEOMETRIC AND RESPONSE PARAMETERS 107

TABLE 4.7 DETAILED VALIDATION OF THE SELECTED PARETO-OPTIMAL FRONT FOR CD NOZZLE OPTIMIZATION 108

TABLE 4.8 MASS LOADING, VOLUME FRACTION, AND STOKES NUMBER FOR DIFFERENT COMBINATIONS 118

TABLE 4.9 COMPARISON OF PREDICTED PV (M/S), USING DIFFERENT TURBULENCE MODELS WITH EXPERIMENTAL RESULT [87] 119
TABLE 4.10 ANOVA RESULTS ACROSS MULTIPLE RESPONSE VARIABLES 120
TABLE 4.11 SAATY'S SCALE FOR AHP SCORES 130
TABLE 4.12 AHP PAIRWISE COMPARISON MATRIX AND WEIGHTS 130
TABLE 4.13 WEIGHT DISTRIBUTION OF INDEXES 130
TABLE 4.14 REPRESENTATIVE OBJECTIVE FUNCTIONS AND CORRESPONDING VARIABLE VALUES 131
TABLE 4.15 ANOVA TABLE 140

NOMENCLATURE

Roman letters

A_{sp}	surface area of the spherical particle (m^2)
C_D	drag coefficient
D_e	exit diameter (mm)
D_i	diameter of nozzle inlet (mm)
D_{id}	injector inner diameter (mm)
D_{od}	injector outer diameter (mm)
D_p	particle size (μm)
D_t	nozzle throat diameter (mm)
F_d	drag force (N)
F_x	additional acceleration term (m/s^2)
G_p	gas inlet pressure (MPa)
G_t	gas inlet temperature (K)
L	prechamber length (mm)
L_c	convergent length (mm)
L_d	divergent length (mm)
L_i	injector length (mm)
N	total number of tracked particles
R	correlation coefficient
R^2	coefficient of determination
Re	particle Reynolds number
St	Stokes number
T_c	carrier gas temperature (K)
U_e	mean exit velocity (m/s)
X_i, X_j	coded input factor levels
Y	predicted response

Greek letters

$\beta, \beta_o, \beta_{ii}, \beta_{ij}$	regression coefficients
ΔP	pressure differential (MPa)
$\Delta_i(k)$	absolute deviation in grey relational analysis
$\Delta_{min}, \Delta_{max}$	minimum and maximum deviation in grey relational analysis
ζ	distinguishing coefficient in grey relational analysis
λ	thermal conductivity (W/m K)
μ	molecular viscosity (kg/m s)
ρ	density (kg/m^3)
τ	viscous shear stress (N/m^2)
Φ_m	mass loading ratio
Φ_v	particle volume fraction
ψ	particle sphericity
ω_{Ai}	AHP weights
ω_{Ei}	EWM weights
ω_{Mi}	combined weights

Subscripts

g	gas phase
i, j	indices of input factors
p	particle phase

Acronyms

AHP	analytic hierarchy process
ANN	artificial neural network
ANOVA	analysis of variance
CD	convergent-divergent nozzle
CFD	computational fluid dynamics

CS	cold spray
DE	deposition efficiency
DF	desirability function
DOE	design of experiments
DPM	discrete phase model
DRW	discrete random walk
ER	expansion ratio
EWM	entropy weight method
FCCD	face-centered central composite design
GA	genetic algorithm
GRA	grey relational analysis
HF	heat flux on substrate surface (kW/m^2)
MCDM	multi-criteria decision-making
MOO	multi-objective optimization
MSE	mean square error
NSGA-II	non-dominated sorting genetic algorithm II
PT	particle temperature (K)
PV	particle velocity (m/s)
RD	radial dispersion (mm)
RSM	response surface methodology
SoD	standoff distance (mm)
SP	impact surface pressure on substrate surface in front of nozzle exit (MPa)
TOPSIS	technique for order preference by similarity to ideal solution
VIKOR	vlseKriterijumska optimizacija i kompromisno resenje

8

TABLE OF CONTENTS

ACKNOWLEDGMENT I
ABSTRACT IV
LIST OF FIGURES VI
LIST OF TABLES XI
NOMENCLATURE XIII
TABLE OF CONTENTS XVI
CHAPTER 1 INTRODUCTION 1

1.1 Background of Cold Spray Coating 1

1.2 Engineering Significance and Major Applications 2

1.2.1 Repair of Engineering Components 2

1.2.2 Aerospace and Defense Components 2

1.2.3 Automotive and Marine Surface Protection 3

1.2.4 Electrical and Energy-Related Applications 3

1.2.5 Cold Spray Additive Manufacturing 3

1.2.6 Protective and Functional Coatings 3

1.3 Fundamentals of the CS Process 3

1.3.1 Deposition Principle and CS System Classification 4

1.3.2 Main Components and Their Roles in the Deposition Process 6

1.4 Nozzle and Gas-Particle Flow Physics 6

1.4.1 Convergent-Divergent Nozzle and Gas Expansion 6

1.4.2 Gas-Particle Interaction and the Effect of Nozzle Geometry 7

1.5 Need for Numerical Investigation and Optimization 7

1.6 Key Parameters Influencing CS Performance 8
1.6.1 Gas Pressure and Gas Temperature 8
1.6.2 Effects of Particle Characteristics and SoD on Particle Impact Conditions 9
1.6.3 Injector Geometry and Nozzle Design Parameters 9
1.7 Performance Measures for CS Deposition 10
CHAPTER 2 LITERATURE REVIEW 11
2.1 Literature Review 11
2.2 Research Progression 11
2.2.1 Bibliometric Trends 13
2.2.2 Major Research Clusters and Publication Directions 14
2.3 Experimental Studies 16
2.3.1 Particle Impact and Bonding Conditions 16
2.3.2 Powder and Substrate Combinations in Coating Formation 18
2.4 Numerical Modeling of Gas and Particle Flow 19
2.5 Nozzle Design Studies 22
2.5.1 Effect of Convergent Length and Throat Diameter 22
2.5.2 Effect of Divergent Length and Exit Diameter 23
2.5.3 Effect of Powder Injector Geometry 24
2.6 Effects of Process Parameters 25
2.6.1 Effect of Gas Pressure and Temperature 25
2.6.2 Effect of Standoff Distance 26

2.7 Particle Characteristics and Deposition Quality 27

2.8 Coating Quality Indicators 28

2.9 Optimization Approaches 30

2.10 Research Gaps 34

2.11 Research Objectives 34

CHAPTER 3 RESEARCH METHODOLOGY AND MODELING 35

3.1 Research Methodology 35

3.2 Methodology for Bibliometric Analysis 36

3.2.1 Data Source and Search Strategy 36

3.2.2 Bibliometric Mapping and Analysis Procedure 37

3.3 Technical Screening and Selection of Study Variables 37

3.4 Development of the CFD Model 38

3.4.1 Nozzle Geometry and Computational Domain 38

3.4.2 Governing Assumptions and Gas Flow Equations 40

3.4.3 Particle Tracking and Heat Transfer Modeling 42

3.4.4 Material Properties and Numerical Setup 45

3.5 Methodology for Nozzle Design Optimization 53

3.5.1 Selection of Input Variables and Sensitivity Analysis 54

3.5.2 FCCD and CFD Data Generation 55

3.5.3 Optimization Framework 56

3.5.4 Selection of Optimum Nozzle Design 61

3.6 Methodology for Process Parameter Optimization 61
3.6.1 Selection of Input Variables and Design Matrix 62
3.6.2 CFD Data Generation and Response Surface Modeling 64
3.6.3 Optimization and Ranking Procedure 66
3.6.4 Selection of Optimum Process Condition 71
3.7 Grey Relational Analysis (GRA) Based Optimization 72
3.7.1 Selection of Parameter Levels and Response Generation 72
3.7.2 Data Normalization and GRA Formulation 73
3.7.3 Selection of Favorable Parameter Combination 75
3.8 Methodology for Particle Size and Morphology Analysis 75
3.8.1 Selection of Morphology Analysis Parameters 75
3.8.2 Design of Particle Simulation Cases 76
3.8.3 Evaluation of Velocity Footprint and Radial Dispersion 76
3.8.4 Particle Shape Classification and Preferred Condition Selection 77
CHAPTER 4 RESULTS AND DISCUSSION 78
4.1 Introduction 78
4.2 Bibliometric Structure 78
4.2.1 Publication Growth and Subject Evolution 78
4.2.2 Research Contributors and Citation Structure 80
4.2.3 Keyword Networks and Research Directions 87
4.3 Nozzle Design Responses and Optimization Results 89
4.3.1 Sensitivity and Design Space Selection 89

4.3.2 Response Modeling and Pareto Results 92
4.3.3 Optimum Configuration and Comparative Performance 99
4.4 Process Parameter Effects and Optimization 116
4.4.1 Numerical Justification and Model Adequacy 118
4.4.2 Parametric Effects on Particle Responses 124
4.4.3 Pareto Ranking and Optimum Process Window 128
4.5 GRA-Based Optimization Results 136
4.5.1 Grey Relational Grade and Response Integration 137
4.5.2 Favorable Parameter Combination 142
4.6 Particle Size and Morphology Effects 142
4.6.1 Axial Particle Acceleration and Substrate Velocity Footprint 142
4.6.2 Radial Dispersion and Preferred Condition 146
CHAPTER 5 CONCLUSIONS AND FUTURE SCOPE 148
5.1 Conclusions 148
5.2 Future Scope 152
REFRENCES 153
APPENDIX 166
LIST OF PUBLICATIONS 170
CURRICULUM VITAE 171

CHAPTER 1 INTRODUCTION

1.1 Background of Cold Spray Coating

Cold spray (CS) is a coating and additive manufacturing technique where particles are accelerated towards a substrate without melting by a supersonic jet. Oxidation and thermal degradation are prevented by CS, and the properties of the feedstock are preserved because the particles do not reach the melting point Schmidt et al. [1]. These features are appropriate for CS repair, remanufacturing and surface engineering. It allows nozzle design, gas-particle flow analysis and process optimization, compared to conventional thermal spray, which has a lower gas inlet temperature and higher particle velocity (PV), as shown in Figure 1.1.

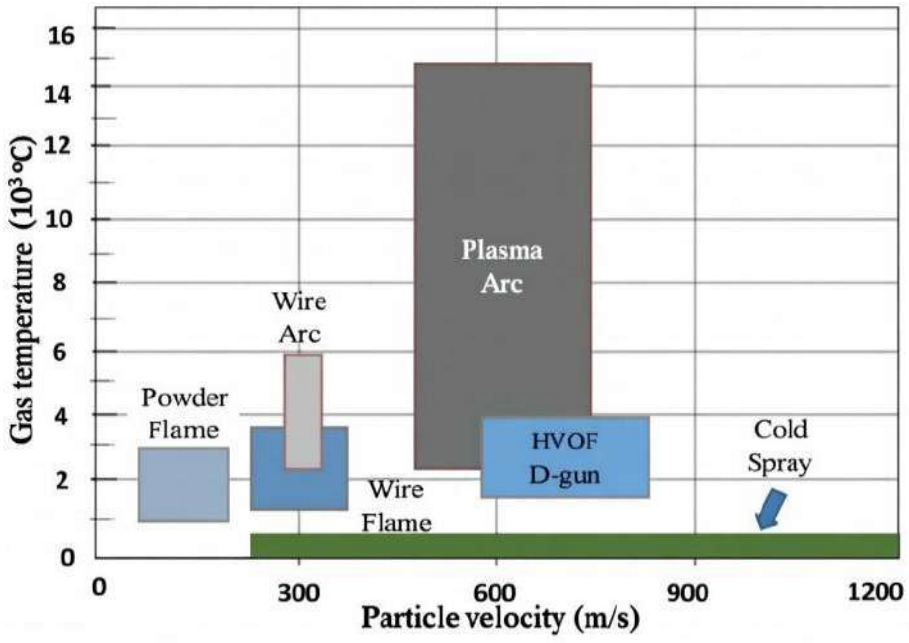

Figure 1.1 Comparison of gas inlet temperature and particle velocity for cold spray with other spray processes

High-velocity particle impact controls the formation of CS coatings. Pathak & Saha [2] compared the energy requirements of conventional thermal spray and cold gas dynamic

spray. In conventional thermal spray, the feedstock is molten or semi-molten before impact, and both thermal and kinetic energy are needed as illustrated in Figure 1.2. On the other hand, CS is based on the kinetic energy of the particles, and bonding is achieved by high velocity impact, plastic deformation, disruption of the oxide film, contact with the substrate, acceleration of the particles, impact velocity, and bonding conditions.

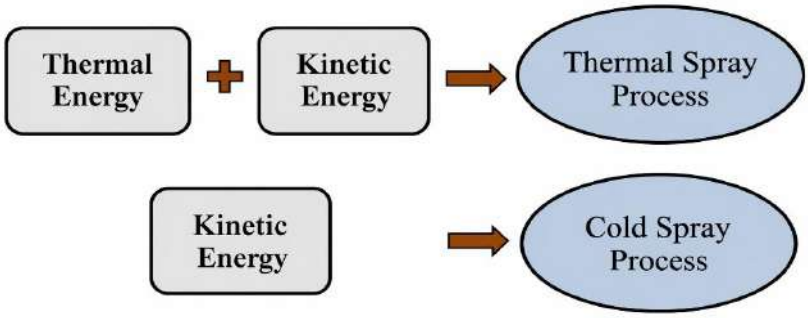

Figure 1.2 Thermal Spray and cold spray process comparison

1.2 Engineering Significance and Major Applications

CS improves surface condition, restores damaged surfaces, and provides functional deposits with minimal thermal effect, depending on impact conditions, nozzle design, and process control. The major applications are discussed below:

1.2.1 Repair of Engineering Components

CS is used to repair defects in engineering components by creating new material at the defect area and restoring their original geometry and service life [2].

1.2.2 Aerospace and Defense Components

CS can be employed to locally restore, protect against corrosion, and strengthen high-value aerospace and defense components with minimal heat input [3].

1.2.3 Automotive and Marine Surface Protection

Automotive and marine components face wear, corrosion, and loading; CS improves durability through dense deposition, adhesion, and uniform thickness [4].

1.2.4 Electrical and Energy-Related Applications

CS benefits conductive surfaces and energy components. Copper (Cu) and Cu-based deposits support conductivity, limit oxidation, and promote bonding [5].

1.2.5 Cold Spray Additive Manufacturing

CS supports layer-by-layer build-up, near-net-shape deposition, and feature additions, requiring control of track width, trajectory, footprint, coating uniformity, gas-particle flow, nozzle design, and dispersion [6].

1.2.6 Protective and Functional Coatings

CS creates protective and functional coatings to improve wear resistance, corrosion resistance, hardness, and surface integrity, depending on compatibility, deformation, and bonding conditions [7], [8].

1.3 Fundamentals of the CS Process

The components of a CS system include a gas supply system, a heater, a powder feeder, pre-chamber, convergent-divergent (CD) nozzle, and a substrate, as illustrated in Figure 1.3. The gas expands through the nozzle. At the throat, its velocity equals the speed of sound. In the diverging portion, the gas exceeds that speed, creating high-velocity particles directed to impact the substrate.

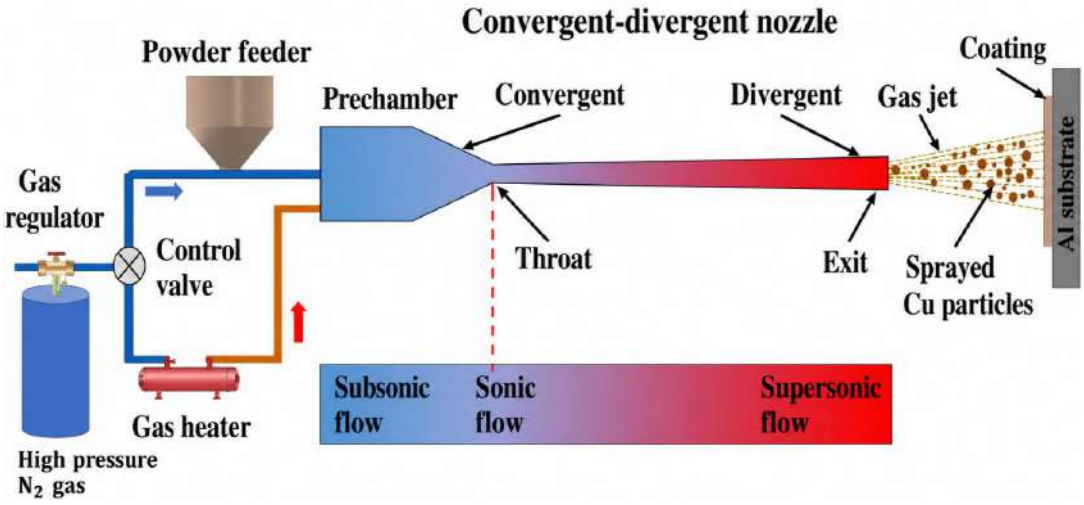

Figure 1.3 Schematic of CS system

1.3.1 Deposition Principle and CS System Classification

When the impact velocity of a particle is above the critical velocity (V_{cr}), it causes significant plastic deformation at the particle-substrate bond area and thus improves the bond contact and adhesion [9]. Below this limit, rebound is the dominant process and coating formation is reduced [10]. CS has been categorized into high-pressure cold spray (HPCS) and low-pressure cold spray (LPCS), as shown in Figure 1.4 and Figure 1.5. HPCS typically operates at pressures ranging from 15−40 bar and at temperatures up to 1000°C; LPCS operate at pressures from 5−10 bar and at temperatures up to 500°C. A summary of the operating conditions for both processes can be seen in Table 1.1 [11]. The spray angles also affects the continuity of the coating and deposition efficiency (DE); 90° is the most favorable angle of impact, and as the angle decreases, the normal component of PV decreases, and deposition becomes less effective [12].

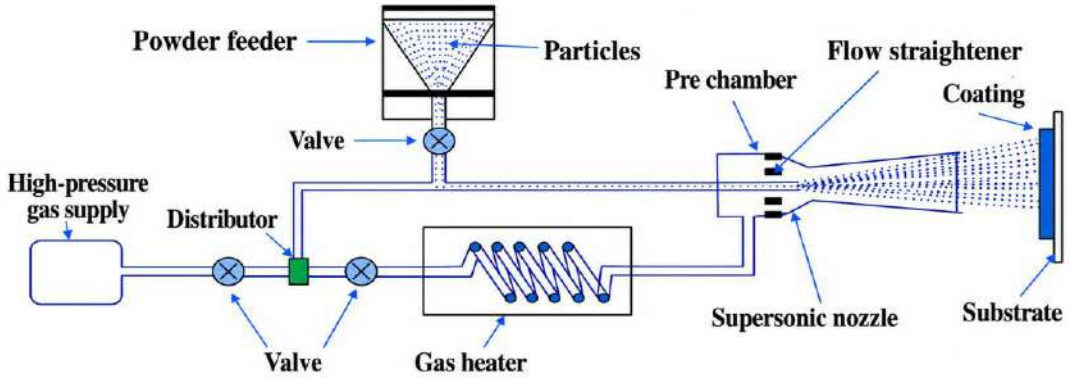

Figure 1.4 High-pressure cold spray (HPCS) working cycle

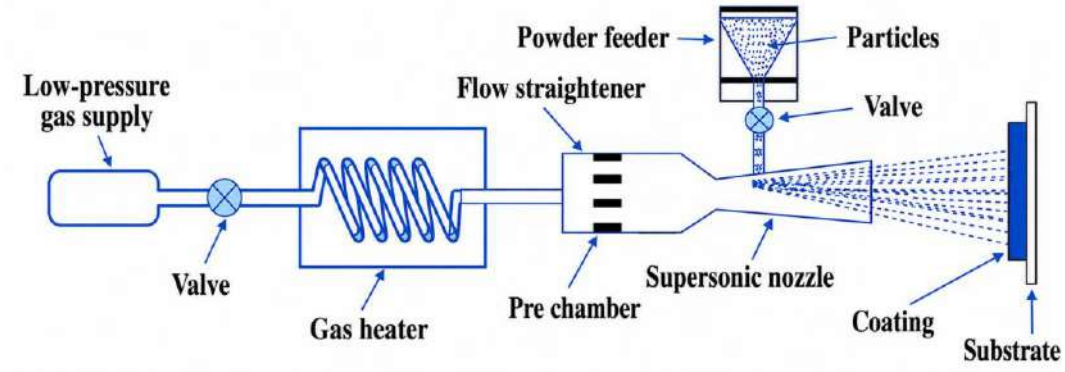

Figure 1.5 Low-pressure cold spray (LPCS) working cycle

Table 1.1 Major difference between the two methods

HPCS	**LPCS**
Pressure 15−40 bars	Pressure 5−10 bars
Axial injection of powder with carrier gas	Radial injection of powder at the nozzle throat
Carrier gases (He, N_2, or Air) up to 1000 °C	Carrier gases (He or N_2) up to 500 °C
Efficiency 90%	Efficiency 50%
Powder feed rate (kg/h) 1.1−13.5	Powder feed rate(kg/h) 0.3−3
Spraying materials Al, Cu, Ni, Cr, Ta, and Ti	Spraying materials Sn, Zn, Al, Cu, and Ni
Electric power (KW) 17−47	Electric power (KW) 3.3
Particle size (μm) 5–50	Particle size (μm) 5−30
Spraying distance (mm) 10−50	Spraying distance (mm) 5−15

1.3.2 Main Components and Their Roles in the Deposition Process

The main components of a CS system control the final impact state of particles. Among these, the CD nozzle is the most critical component as it determines particle acceleration, momentum transfer, and particle condition prior to impact. The pressure, temperature, and expansion characteristics control the acceleration and heating of particles. Drag, heating, and acceleration are influenced by powder size (D_p), morphology, and material properties, while deformation, bonding, and the rebound-to-deposition transition are influenced by substrate conditions [13], [14].

1.4 Nozzle and Gas-Particle Flow Physics

The in-flight particle condition before impact is determined by nozzle and gas-particle flow physics, thus controlling deposition quality. Therefore, CS is considered a nozzle-driven compressible-flow and particle-transport process controlling final impact condition.

1.4.1 Convergent-Divergent Nozzle and Gas Expansion

The CD nozzle consists of a converging section, throat area, and a diverging section. With gas expansion, pressure and static temperature decrease while gas velocity increases toward nozzle exit as shown in Figure 1.6. Enthalpy of propellant gas is converted into kinetic energy, producing a high-velocity gas stream that transfers momentum to particles injected into the nozzle. Due to particle inertia, particles cannot instantly reach gas velocity. Therefore, acceleration depends on local flow field, particle characteristics and residence time in the nozzle [15].

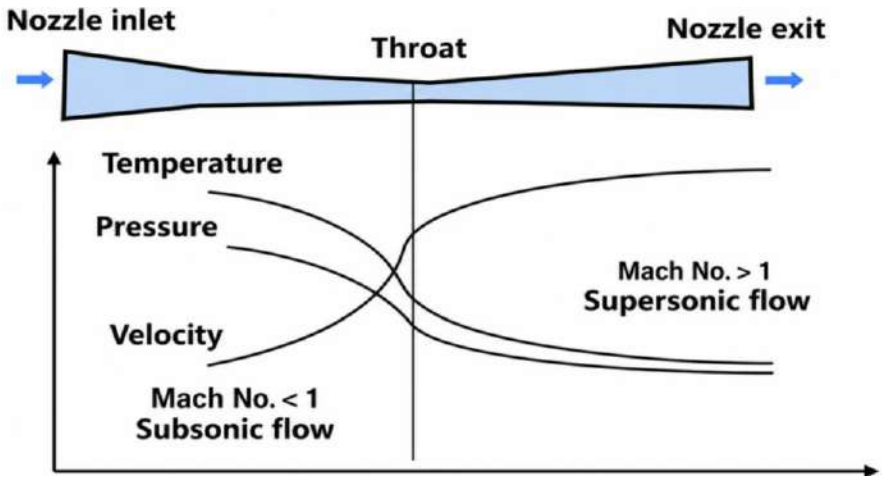

Figure 1.6 Flow characteristics of De Laval nozzle

1.4.2 Gas-Particle Interaction and the Effect of Nozzle Geometry

The interaction in the nozzle between gas and particles determines how particles respond to increasing flow velocities while moving from the nozzle inlet to the exit. This depends on powder injection location, nozzle geometry, velocity field, pressure gradient, and internal flow distribution. Poor gas-particle interaction causes non-uniform acceleration, unstable trajectories, and increased particle dispersion before substrate contact. In addition to influencing PV, particle temperature (PT), and spray quality, by controlling gas expansion, nozzle geometry also affects heat flux (HF) and surface pressure (SP) near the substrate. Therefore, gas-particle interaction and nozzle flow physics must be analyzed for deposition performance.

1.5 Need for Numerical Investigation and Optimization

The CS process is complex, with gas flow and particle dynamics occurring in the CD nozzle and free-jet near the substrate, where direct measurements are not possible. PV, PT, and impact conditions are affected by gas pressure (G_p), gas temperature (G_t), particle size (D_p), nozzle geometry, powder injection, and standoff distance (SoD). Numerical

investigation is needed for nozzle design, process optimization and coating quality improvement, as shown in Figure 1.7.

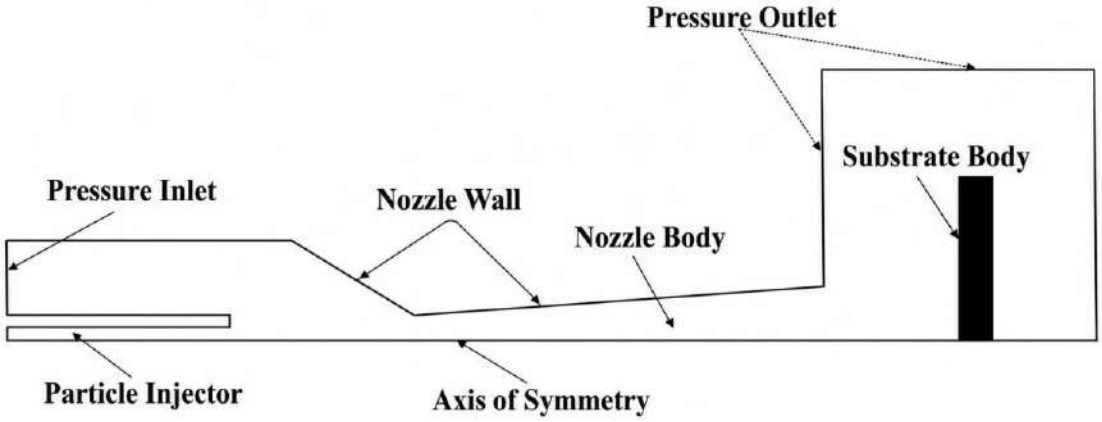

Figure 1.7 Schematic representation of the computational domain and boundary conditions

1.6 Key Parameters Influencing CS Performance

CS behavior is controlled by interacting parameters that determine the in-flight condition of particles and impact conditions. PV, PT, and radial dispersion (RD) determine overall performance. Hence, the combined effect of G_p, G_t, D_p, particle sphericity (ψ), SoD, powder injection conditions, and nozzle geometry should be considered when evaluating performance.

1.6.1 Gas Pressure and Gas Temperature

G_p is a highly influential CS parameter, controlling compressible gas expansion and particle acceleration. When conditions are favorable, increasing G_p increases gas density, momentum transfer, and PV. G_p remains a control variable for coating quality, as deposition depends on achieving a suitable impact state. G_t affects gas expansion and thermal conditions of particles. Increasing G_t can increase gas velocity and PT, improving deformability during impact. However, G_t should be considered with G_p and nozzle-flow

development because its effect depends on coupled gas-particle acceleration and heat transfer.

1.6.2 Effects of Particle Characteristics and SoD on Particle Impact Conditions

D_p affects the ability of particles to respond to drag forces within the nozzle free jet. Larger particles need greater amounts of momentum transfer than smaller particles to reach the same impact conditions. Due to their lower inertia, smaller particles can accelerate faster than larger particles. These factors make D_p and size distribution critical factors for achieving good deposition quality. Spherically shaped particles exhibit consistent aerodynamics during flight. Non-spherical particles experience varied drag forces, acceleration and dispersion patterns. This variation in drag and acceleration results in variations in the dispersion of non-spherical particles. Therefore, ψ affects the way spherical particles focus, disperse uniformly throughout the spray and ultimately affect the deposition response. The SoD determines particle conditions before impact and influences impact velocity, near-substrate flow behavior and DE.

1.6.3 Injector Geometry and Nozzle Design Parameters

Injector geometry and powder injection conditions control how particles enter the accelerating gas stream and how effectively they move through the nozzle. Particle entry location, residence time, gas-particle contact, and transport stability are influenced by injector inner diameter (D_{id}), injector position, and injector length (L_i). If the injection conditions are not suitable, particles may show poor focusing, lower acceleration, or unstable motion before reaching the nozzle exit. Therefore, injector design is important for controlling spray uniformity and particle dynamics. The nozzle design parameters introduced in Section 1.4 interact with injector conditions to jointly determine particle acceleration path, thermal history, and final impact condition. The roles of these parameters are as follows:

- Throat diameter (D_t) controls the minimum flow area and affects choking, mass flow, and downstream PV.
- Exit diameter (D_e) influences the final gas expansion, outlet flow structure, and particle release conditions.
- Convergent length (L_c) affects the inlet-to-throat flow development.
- Divergent length (L_d) controls the supersonic acceleration distance after the throat.

1.7 Performance Measures for CS Deposition

The quality of the CS deposition is judged by measurable parameters that describe the condition of the particles in flight and the quality of the deposit. The primary response variables include PV, PT, RD, HF, SP, DE, coating thickness uniformity, bonding quality and surface integrity [16]. PV is the most critical performance measure since it determines if the impact condition falls within the deposition window. Too low PV can cause particles to rebound or create weak interfacial bonds, while too high PV can cause erosion or excessive deformation. Therefore, suitable PV is required for successful coating formation. PT controls particle deformability at impact and should be considered in conjunction with PV, which together control the thermomechanical state at impact. HF and SP represent substrate-level thermal and mechanical loading, which are important for assessing particle softening, bonding conditions, and surface response. RD measures lateral spreading of the particle stream before impact; lower RD focuses the deposition footprint and increases coating uniformity. DE is a measure of process efficiency and parameter suitability and is defined as the ratio of deposited powder mass to injected powder mass [17]. Coating thickness uniformity indicates spatial uniformity of the deposited layer, while bonding quality is determined by contact mechanics after impact. Surface integrity indicates coating continuity and stability under repeated impact loading. Thus, CS deposition quality is related to PV, PT, RD, DE, coating uniformity, bonding conditions and surface response, which are related to process parameters and nozzle design studied in the present work.

CHAPTER 2 LITERATURE REVIEW

2.1 Literature Review

This section provides an overview of the main research trends in CS, such as experimental studies, gas-particle flow modeling, nozzle design, process parameters, particle characteristics, optimization methods, and coating-quality indicators. The reviewed studies collectively indicate that CS performance is not controlled by any one variable, but by the combined effect of gas expansion, particle acceleration, heat transfer, impact behavior, and substrate interaction.

2.2 Research Progression

To understand the early deposition mechanism in CS, Dykhuizen et al. [18] studied the impact behavior of Cu particles on a stainless-steel substrate. The study showed that coating was formed by high velocity solid particle impact and not by melting and solidification. The particle and substrate were severely plastically deformed during impact and the depth of the crater was found to increase with impact velocity. The sizes of the splat and crater were also observed to be dependent on D_p.

Grujicic et al. [10] created a computational impact model to explore particle-substrate bonding mechanisms during CS deposition. Analysis was conducted for a single spherical particle impacting a semi-infinite substrate, and the deformations of particle and substrate, contact pressure and contact area were investigated. A typical example is a 20 μm Aluminum (Al) particle striking a Cu substrate at 650 m/s and the deformation process is followed at 5, 20, 35 and 50 ns after impact. The numerical results indicated that the plastic deformation of the particle at the particle-substrate interface was fast, and the local pressure was high. The model revealed that the interfacial contact area and contact pressure were greater for Cu deposition on Al than for Al deposition on Cu.

Schmidt et al. [19] suggested a generalized deposition window for CS, based on the correlation between particle impact velocity, temperature, size and material response. Only when PV is greater than the V_{cr} will deposition occur, and if the velocity is too high, erosion will occur. The V_{cr} for Cu particles decreased with increasing D_p, with 15 µm, 25 µm, and 50 µm particles bonding at about 600 m/s, 500 m/s and 450 m/s respectively, whereas a 5 µm particle did not bond under feasible impact conditions. These results showed that PV, PT, and D_p should be considered together and PV alone should not be used as the main indicator of coating quality.

15

Assadi et al. [20] reviewed CS as a deposition and additive manufacturing process in which micron-sized powder particles are deposited on the substrate by high velocity impact and severe plastic deformation. The review described how particles are accelerated by the expansion of gas through a CD nozzle and how heated process gas enhances the acceleration and thermal softening. V_{cr}, particle deformability, oxide-layer rupture, adiabatic shear instability and metallurgical bonding were associated with successful deposition. The study also highlighted the importance of material properties, PT, substrate compatibility and impact conditions on the coating response, establishing PV and PT as critical parameters for CS process control.

Rokni et al. [21] demonstrated the relationship between particle deformation, coating microstructure and mechanical properties in HPCS. This study conclude that CS usually uses powder particles of 5–50 µm and high-pressure carrier gas to accelerate the particles to speeds of about 300–1400 m/s. It was demonstrated that the coating density, hardness, strength and bonding quality were related to the particle deformation, inter-particle contact and microstructural development during repeated impacts. The performance of HPCS coatings was placed in a process–microstructure–property context, highlighting the fact that spray parameters are not enough to characterize coating behavior.

Guo et al. [3] reviewed over 30 years of CS development, from the first concept of solid-state powder deposition to repair, coating and additive manufacturing applications. The

review showed that CS research has evolved from the feasibility of deposition to process control, nozzle design, material expansion and manufacturing oriented applications. The study further highlighted that gas flow, nozzle geometry, D_p, impact conditions, coating properties and optimization are now considered as interrelated aspects of coating-performance development.

2.2.1 Bibliometric Trends

Beginning with the study of R. T. Li et al. [22], a bibliometric study was performed to quantify the development of literature in CS, including publication trends, subject areas, contributions of organizations, contributions of nations, and topics represented through topic modeling. The results indicated an increase in annual published papers; while there were approximately 252 papers in 1991, this number grew to about 1,141 papers in 2014. As such, it is clear that the literature has grown rapidly over time in the area of spray coating. It also appeared that the majority of coating research falls under the categories of materials science, engineering, and physics, which indicates that the behavior of the material, the physical processes involved in the deposition process, and the engineering properties of the coatings themselves are likely to be among the top priorities in terms of determining how to further develop CS as a technology.

Abu Bakar et al. [23] conducted a CS literature review using a large dataset from Scopus from 1994 to 2022. Their bibliometric analysis of the 1,944 documents received 41,267 citations, 21.23 citations per document, 1473.82 citations per year, an h-index of 89 and a g-index of 142. As demonstrated by the steady increase in published papers from 160 in 2017 to 183 in 2020, there is also an increase in research activity in CS. Materials Science was the most frequent subject area with 1551 documents, Physics and Astronomy was second with 1170 documents, while Engineering was third with 770 documents. Modeling, additive manufacturing, PV, and CFD were found to be recurring research themes in CS through keyword mapping.

Vaz et al. [6], used a bibliometric approach to assess trends analysis of cold spray additive manufacturing (CSAM) using Scopus data from 2012 to 2022. The authors began by identifying over 450 studies and then screened out to retain 439 studies. Over time the number of studies published annually grew from 4 in 2012 to 84 in 2022. Publications remained somewhat consistent in both 2020 and 2021 at an approximate annual rate of 81. Based on the study's findings, the most prolific author was Halin Liao (35 documents), while the Journal of Thermal Spray Technology was the most frequently cited publication source (48 documents). This evidence suggests that there is a growing interest among researchers in applying CS technology to solid-state-deposition, repairing materials, creating near-net-shape manufactured parts, and building coatings without melting.

2.2.2 Major Research Clusters and Publication Directions

W.-Y. Li, Liao, et al. [24] numerically designed a convergent-barrel CS nozzle and examined the influence of barrel length, barrel diameter, accelerating gas, G_p, G_t, and D_p on PV and PT. The results showed that, compared with a CD nozzle, the convergent-barrel nozzle produced lower PV but higher PT under the same G_p. Cu powder deposition experiments confirmed that coating formation was possible at lower G_p using the designed nozzle.

W. Y. Li et al. [25] optimized a CS nozzle by combining numerical prediction of PV with experimental validation using 316L stainless steel powder. The study revealed that the optimum ER depends on G_p, G_t, D_p, D_t, and L_d. ER was found to increase with increasing G_p and L_d, while decreasing with the increase in G_t, D_p, and D_t. An optimized nozzle was used to spray a 316L stainless steel coating with a dense structure and high microhardness with air as the accelerating gas.

Katanoda et al. [26] numerically investigated the gas-particle flow in CS for Tungsten Carbide with 12 wt.% Cobalt (WC-12Co), Cu and Titanium (Ti) particles, using nitrogen

(N_2) and helium (He) as process gases. The particle diameter was changed from 0.1 to 30 µm to investigate PV and PT. Two material-independent combination parameters were introduced: particle diameter × density for velocity and particle diameter² × density × specific heat for temperature. The combination parameter values for maximum impact velocity were 0.020 kg/m² for N_2 and 0.0065 kg/m² for He.

Tabbara et al. [27] studied process optimization in CS by examining nozzle cross-section, D_p, and process gas. The simulations used about 1000 Cu particles, with 11 µm particles carried by N_2 at 29 bar and 298 K. Circular and square nozzles produced the least dispersed particle distributions, with 99% of particles in the 460–465 m/s range, while the elliptical nozzle showed slightly lower velocity, with a maximum reduction of about 20 m/s. The study also showed that 5 µm particles had higher velocities and greater dispersion than 30 µm particles, and He produced higher PV and wider dispersion than N_2.

Lupoi & O'Neill [14] investigated the powder-stream characteristics for CS nozzles as well as how particle trajectory, powder-injection position, injector geometry and carrier gas flow control affected the form of deposition tracks. Their results indicated that a wide range of track widths was possible track widths (i.e., about 1 to 8 mm), demonstrating that both particle focusing and particle lateral spreading are highly sensitive to injection and flow conditions. In addition, they stressed that the powder-stream behavior depends not only on the nozzle-exit-flow but also on the particle entry from upstream and interaction with the carrier gas.

Yin, Liu, et al. [28] investigated the influence of injection pressure on particle acceleration, dispersion, and deposition in CS using CFD and experimental validation. Higher injection pressure increased injection flow rate, and powder feed rate, which resulted in thicker coatings, but also wider particle dispersion on the substrate. The particle impact velocity-to-critical velocity ratio and deposition range decreased with increasing injection pressure, indicating that the DE and bonding strength decreased.

Pathak & Saha [2] reviewed CS coatings and CSAM for repair and production purposes. The review defined CS as a low-temperature deposition technique in which small powder particles, approximately 1–50 μm in diameter, were accelerated by a de Laval nozzle to velocities of approximately 300–1200 m/s and then deposited onto a surface approximately 25 mm from the nozzle. The authors identified repair, remanufacture, thick coating applications, and the production of three-dimensional (3D) freeform components as the primary research directions that should be addressed through publications related to CS.

2.3 Experimental Studies

Experimental investigations of CS deposition provide the physical basis for particle impact, bond formation and coating build-up. PV, PT, D_p, substrate conditions, and powder-substrate compatibility are important factors. The numerical optimization of G_p, G_t, nozzle geometry, SoD, and particle characteristics should ultimately be linked to coating quality.

2.3.1 Particle Impact and Bonding Conditions

Gilmore et al. [29] experimentally studied the relationship between PV and DE in CS process using Cu powder. The in-flight particle velocities were measured using a laser-two-focus system under various G_p, G_t, and powder feed rate conditions. The study found a DE of up to 95% on Al substrates and the V_{cr} for deposition was found to be around 640 m/s. The results indicated that the formation of the coating was highly dependent on the ability of the particles to attain a high impact velocity prior to impact with the substrate.

Raletz et al. [30] determined the critical PV in CS using particle imaging and DE-based calculations. N_2 was used as the propellant gas, the D_t of the de Laval nozzle was 2.6 mm, the powder feed rate was 5–10 g/min, and the SoD was 30 mm. The critical velocities reported in the literature were 571 m/s for Cu on Cu, 574 m/s for Cu on 316L stainless

steel, and 576 m/s for Nickel (Ni) on Cu, while DE-based predictions gave 538, 555, and 585 m/s, respectively. The results indicated that the coating formation starts only when the velocity of the particles is greater than the V_{cr}, which depends on the material.

Champagne et al. [31] compared theoretical PV predictions with experimental measurements for Al particles accelerated by N_2. The study validated the ability to predict the particle acceleration using the one-dimensional (1D) gas-dynamic analysis, one-dimensional (2D) CFD modeling and experimental PV measurements. The results indicated that PV increased with G_p, and the nozzle design controls the acceleration history before impact. The study verified the need to validate the flow model with experiments since the bonding of particles is strongly depends on the actual velocity of the particles when they impact the substrate rather than only on the inlet gas conditions.

W. Y. Li et al., Yin et al. [32], [33] studied heating and heat transfer during CS. Both studies employed hot compressed air conditions of 2.7 MPa and 673 K and also investigated inlet temperatures of 473, 673, and 873 K. The highest substrate temperature and HF were found near the impact center and decreased along the radial direction. Increasing SoD or decreasing the inlet temperature reduced substrate temperature, while the maximum nozzle-wall temperature appeared near the throat. Initial bonding and coating formation are strongly affected by substrate thermal conditions, HF, and bow-shock effect.

Xie et al. [34] examined the formation of metallurgical bonding in CSAM by comparing single-particle impact with full coating deposition. Ni splats and coatings were produced on Al substrates at different propelling G_p. The results showed that clear metallurgical bonding was not observed in single-particle impact, even at 3.7 MPa, whereas full coating deposition showed bonding after repeated impacts and heat treatment. The study indicated that successive particle impacts created a strengthened peening effect, which improves coating densification, interparticle contact, and metallurgical bonding.

Nastic et al. [35] studied the effect of PT on soft Al particle deposition on a hard steel substrate in CS. The study varied particle impact temperature while keeping particle impact velocity comparable and examined three particle diameters. At a low impact temperature of about 50 °C, adhesion was mainly controlled by in situ peening. With increasing PT, bonding became more dependent on the in-flight particle condition, expressed through the velocity ratio. Higher PT improved deformation, DE, and adhesion, while smaller particles showed stronger bonding at elevated temperature.

2.3.2 Powder and Substrate Combinations in Coating Formation

Q. Wang et al. [7] investigated Al-Al_2O_3 composite coatings on the AZ91D magnesium alloy substrate using kinetic metallization, a CS variant based on a convergent-barrel nozzle. The effects of Aluminum oxide (Al_2O_3) particle content and spray temperature on coating microstructure, hardness, DE, and bond strength were studied. The addition of Al_2O_3 increased coating density and enhanced DE up to an optimum value. Bond strength at the coating-substrate interface was improved, and higher Al_2O_3 content shifted failure from adhesive failure to cohesive failure.

Meyer & Lupoi [36] compared three different de Laval nozzle designs using Ti deposition on Al 6082-T6 and CFD simulation to analyze the particle flow in CS nozzles. The nozzle throat behavior had a significant effect on DE under constant process conditions, with N1 yielding a DE of approximately 16.3% and N3 yielding a DE of approximately 33.3%. One-way particle tracking was not able to reproduce this trend, while two-way coupling indicated that the PV decreased by approximately 4.4% to 511.9 m/s. Nozzle design, particle loading and particle-flow coupling have an influence on coating build-up.

Akisin et al. [37] investigated the single-particle impact of CoCrFeNiMn High-entropy alloy (HEA) particles on commercially pure aluminum (CP-Al), Al6082, SS304, and Titanium alloy (Ti6Al4V) substrates using experimental and numerical analyses. The impact morphology revealed adiabatic shear instability in the HEA particle and harder

substrates, and mechanical interlocking through localized substrate deformation in soft Al substrates. The V_{cr} was about 800 m/s for HEA/SS304 and 700 m/s for HEA/Ti6Al4V. The highest interfacial heating rate for CP-Al was around 65 × 10^9 K/s at 550 m/s. Deformation and bonding are influenced by hardness, density, and thermal conductivity.

2.4 Numerical Modeling of Gas and Particle Flow

Numerical simulation is an important research trend in CS because the process involves compressible gas expansion, powder injection, particle acceleration, heat transfer, turbulent spreading and interaction with the substrate. Particles do not follow the gas velocity because the motion depends on D_p, density, drag force (F_d), residence time, local gas velocity, and local gas temperature. Particle tracking estimates PV, PT, and particle dispersion through the computed gas field.

Park et al. [38] numerically studied particles in a supersonic nozzle and investigated the influence of shock waves, nozzle geometry, ambient pressure, and substrate location. The simulations were carried out at a stagnation pressure of 6 bar and a stagnation temperature of 300 K and an ambient pressure ranging from 1 bar to 0.01316 bar. The results indicated that shock structures were reduced as the nozzle was moved closer to the optimal expansion condition. A greater diverging angle was needed at low ambient pressure.

Suo et al. [39] examined particle distribution by changing the exit height, throat height, and powder injector height while keeping the ER constant. Their numerical cases used Magnesium (Mg) particles with D_p values of 20–120 μm, air as the process gas, SoD of 30 mm, G_p of 2 MPa, and G_t of 227 °C. The results showed that increasing exit height broadened and flattened the particle distribution, whereas increasing throat height reduced the mean PV from 572 ± 36 m/s to 531 ± 39 m/s. These values show that nozzle dimension changes both the gas-flow field and particle distribution.

Yin et al. [40] numerically investigated the effect of total pressure (Po) and L_d on gas-flow behavior and particle impact velocity. The study used CFD to predict the nozzle-exit Mach number and particle acceleration. The results showed that increasing Po increased particle impact velocity because higher gas density increased F_d, although the rate of increase became lower. The nozzle-exit Mach number first increased with Po and then became stable after reaching a critical pressure level. Increasing L_d reduced nozzle-exit Mach number, but particle impact velocity reached a maximum at an optimal L_d.

Tang et al. [41] numerically examined the interaction between hot propulsion gas and cold powder carrier gas inside a CS nozzle. Their model used N_2 and Cu particles, with about 400,000 structured cells**,** D_{id} of 1.8 mm**,** D_t from 2 to 4.4 mm, L_c of 20 mm, L_d of 150 mm**,** expansion ratio (ER) of 9, and SoD of 30 mm. The propulsion gas conditions were 2.0 MPa and 773 K, while the carrier gas temperature (T_c) was 300 K and the pressure differential (ΔP) varied from 0 to 0.4 MPa**.** Increasing ΔP reduced gas velocity and particle impact velocity, whereas increasing L from 0 to 50 mm improved mixing and particle acceleration. These numerical results show that carrier-gas pressure, L, and D_t control the internal gas mixing and particle acceleration before deposition.

Zahiri et al. [42] developed a holistic 3D CFD model to predict supersonic jet behavior from the injection region to the substrate surface. The model used N_2 as the gas flow with a two-equation $k-\varepsilon$ turbulence approach and was calibrated using Ti substrate temperature measurements. The results showed good agreement with the experimental temperature history, while the predicted gas velocity and pressure fields were satisfactory for describing jet expansion, off-axis flow, and substrate-region gas behavior.

Faizan-Ur-Rab et al. [43] validated a 3D multicomponent CFD model using two particle image velocimetry (PIV) experiments. The model was created for spherical Ti particles and validated in supersonic flow fields with N_2 and He. The results indicated that the 3D model predicted lower PV than the PIV measurements for irregular particles, and showed better agreement for spherical Ti powder. The study also estimated PT and particle impact

locations, revealing that the finer particles were more concentrated nearer to the jet center. This work validated the need for 3D CFD modeling in order to interpret PV, temperature and deposition behavior.

Alonso et al. [44], compared an analytical model with experiments and Fluent simulations. Their validation included ZK61 particles with a D_p of 58 µm, Al particles with D_p of 15 µm, and Cu particles with D_p values of 9.6 µm and 32.6 µm. The analytical model showed differences below 8% for ZK61 and below 5% for Al when compared with experimental data, while the difference compared with Fluent prediction was below 2%. These values show that PV can be estimated accurately when gas conditions, particle density, D_p, and nozzle geometry are properly included.

Kowalski et al. [45] numerically studied a modified CS process-flow technique using CFD, and compared the basic, vortex, and combined gas-supply techniques with the same de Laval nozzle geometry. Air was used as the working gas with spherical Cu particles were used, and the spraying process was simulated for approximately 0.05 s. The combined-flow method yielded the highest accretion rate of 33.6, and the vortex method yielded the lowest value 10.7. The combined case also resulted in a concentration of particles in the center of the sprayed surface, creating a cone-shaped deposit pattern, while the basic case resulted in a more uniform pattern. The results demonstrate that the stability of the jet, particle focusing, and deposition behavior can be modified by changing the gas-flow arrangement.

Wan et al. [46] developed a non-axisymmetric 3D numerical model for CSAM to study gas-flow behavior, particle acceleration, and nozzle-clogging tendency. The model examined the effects of L, powder-injector length difference (Pl), and D_{id}. The results showed that gas vortex distribution and particle acceleration were strongly affected by L and D_{id}, while Pl had limited influence. Particle backflow near the injector increased the likelihood of particle-wall collision and nozzle clogging. Using L = 190 mm, D_{id} = 1 mm, and Pl = 10 mm prevented nozzle clogging during 9 min of spraying.

16

2.5 Nozzle Design Studies

CS nozzle design controls gas expansion, particle acceleration, heating, and particle impact distribution. In a CD nozzle, L_c and D_t affect inlet-to-throat acceleration and choking, while L_d and D_e control supersonic expansion and nozzle-exit flow. Powder injector geometry governs particle entry, residence time, focusing, and spreading.

2.5.1 Effect of Convergent Length and Throat Diameter

W. Y. Li & Li, [47] optimized a novel CS gun nozzle for limited-space spraying and treated the nozzle design as a constrained gas-acceleration problem. The study considered D_i, D_t, D_e, L_c, and L_d as coupled design parameters. The results showed that the throat region must maintain choking and a pressure drop, while the convergent section should guide the gas smoothly before supersonic expansion. This work showed that nozzle geometry should be selected according to the available deposition space and particle acceleration requirements, rather than only using a standard de Laval profile.

Buhl et al. [48] optimized a de Laval nozzle for energy-efficient acceleration of microparticles by comparing standard and modified nozzle-flow geometries through numerical simulation. The results showed that nozzle-channel geometry strongly affected particle trajectories and impact velocity. Compared with the standard nozzle, the modified nozzle increased the impact velocity of Al particles by 14.6% and that of Ni particles by 12% under the same initial conditions. This shows that small-particle acceleration depends strongly on the local gas-flow gradient, throat-region control, and residence time, making nozzle geometry important for improving impact velocity without simply increasing pressure or temperature.

Cao et al. [13] numerically studied the coupled effects of powder-carrier gas and powder characteristics. The results showed that larger inlet diameter (D_i) and longer L_c increased mixed-gas temperature and PT before the throat because heat exchange became more stable inside the nozzle. The study also showed that particle impact velocity decreased

with increasing D_p and particle density. Therefore, heavier particles required a longer acceleration distance and a larger ER to obtain sufficient kinetic energy before impact.

2.5.2 Effect of Divergent Length and Exit Diameter

Varadaraajan & Mohanty [49] optimized a rectangular divergent CS nozzle for 316 stainless steel powder by varying radial injection angle, ER, and traverse speed. Three injection schemes and four nozzle geometries were compared, and numerical particle tracking was performed with approximately 12,000 particles. The injection angle affected particle distribution and injection pressure, whereas ER controlled exit-flow conditions and deposition response. Very low traverse speeds below 6 mm/s were investigated. Particle spreading, coating footprint, and DE were controlled by the nozzle exit design.

Cao et al. [50] designed and experimentally validated a special de Laval nozzle for CSAM of Ti6Al4V. The study showed that nozzle geometry improved particle heating, kinetic energy, deposit continuity, and single-pass build-up. With the improved nozzle configuration, the maximum single-pass deposit thickness increased to 1179 μm and microhardness increased to 324 HV. The deposit width also increased, and the edges became smoother, showing that nozzle-exit flow and particle impact conditions strongly affect deposition continuity in CSAM.

Zavalan & Rona [51] developed method-of-characteristics based nozzle design workflow for CSAM. Their optimized nozzle used a convergent inlet angle of 11.1°, a throat radius of curvature normalized by throat radius of 2.9, and a divergent section inflection angle of 9°. The optimized design used a D_e of 8 mm and a divergent axial length 3.6 mm shorter than that of the baseline nozzle. Their simulations predicted 8–9% higher mass-averaged PV, 3.8% lower velocity variability, 22.6% more radially uniform particle deposition, and about 150% higher DE.

Sharma et al. [52] numerically investigated a co-flow nozzle for CSAM to reduce nozzle clogging during long-duration spraying. The study used high-pressure N_2 gas at 6 MPa

and 1273 K with Inconel 718 particles with sizes of 15–35 µm. By replacing the solid divergent-wall boundary with an annular co-flow gas boundary, the shortened nozzle with a reduced L_d preserved primary-flow momentum and maintained higher PV after the nozzle exit. The co-flow design compensated for PV loss and provided acceleration performance comparable to the original longer nozzle.

2.5.3 Effect of Powder Injector Geometry

Sova et al. [53] numerically studied the influence of powder-injection position on powder preheating efficiency in CS. The study compared subsonic and supersonic powder injection conditions and showed that injection location affects particle residence time, heat exchange, and thermal preparation before impact. The results indicated that powder preheating efficiency depends on injection type because particles introduced at different nozzle regions experience different G_t and velocity histories, affecting particle thermal conditions and deposition readiness.

Wan et al. [54] numerically investigated the effects of powder injector D_{id} and overhang length on particle acceleration in CSAM. The results showed that particle dispersion increased with higher initial ΔP and larger injector D_{id}, while smaller D_{id} and lower ΔP concentrated particles near the nozzle axis and reduced the clogging tendency. Particle impact velocity decreased with increasing ΔP, overhang length, and injector D_{id}. Particles with diameters of 20–40 µm were suggested for smaller footprint and better CSAM accuracy, while 15–45 µm particles showed greater temperature sensitivity to injector geometry.

Khan et al. [55] investigated the effect of particle injector length (L_i) using a 2D axisymmetric CFD model. The study evaluated particle impact velocity, PT, and substrate surface temperature for Ti powder on a steel substrate. The results showed that L_i changes the residence path of particles before they enter the main acceleration zone, which affects particle heating and impact conditions. Among the studied cases, an L_i of 15 mm was

found to be optimal. He produced the highest PV, while pure N_2 produced higher particle and substrate temperatures under the same operating conditions. Overall, nozzle design studies show that CS performance depends on the coordinated selection of L_c, D_t, L_d, D_e, and injector geometry.

2.6 Effects of Process Parameters

CS performance depends on operating parameters because gas-particle conditions before impact control PV, PT, DE, coating thickness, porosity, and bonding quality. G_p, G_t, SoD, powder feed conditions, traverse velocity, and substrate geometry determine whether particles reach the deposition window without excessive rebound, erosion, dispersion, or thermal degradation. The discussion is divided into the effects of G_p, G_t, SoD, and coupled operating parameters.

2.6.1 Effect of Gas Pressure and Temperature

Xie et al**.** [56] investigated the effect of substrate preheating on the adhesive strength of 316L stainless steel cold-sprayed coatings. The study used a G_p of 2.5 MPa and a G_t of 645 °C, while substrate preheating temperatures were varied as 400, 600, and 700 °C. Adhesive strength increased to 31.0 ± 6.4 MPa at 400 °C and reached a maximum of 63.2 MPa at 600 °C. The results showed that higher substrate temperature improved plastic deformation at the interface, disrupted oxide films more effectively, and increased coating-substrate bonding.

Ozdemir et al. [57] investigated high-rate deposition of tantalum (Ta) using He gas. Their study used Ta powder with an average D_p of about 23 µm, a 4140-steel substrate, SoD of 20 mm, a G_p of 5 MPa, and a G_t of 570 °C. The powder-to-gas mass flow ratio was increased from 5 to 14%, and the simulations predicted only minor changes in particle bonding conditions. Experimentally, increased powder stream loading allowed the same amount of Ta to be deposited in nearly one-third of the time. These results show that G_p

and G_t provide the particle acceleration environment, while powder loading controls productivity and coating build-up rate.

W. Li et al. [58] investigated the effects of spray parameters and heat-treatment temperature on single-pass and single-layer cold-sprayed Cu coatings on Al 6061-T6 aluminum alloy. The results indicated that the coating thickness, surface roughness, porosity, microstructure, shear strength, and microhardness were significantly influenced by G_p and G_t. Higher G_p resulted in rougher but less porous coatings, while higher G_t resulted in a smoother coating surface and reduced porosity. The lowest surface roughness of 8.03 µm was achieved at 800 °C and 4.0 MPa, while the lowest porosity of 0.26% was achieved at 800 °C and 5.5 MPa. A heat-treatment condition of 400 °C was determined to be the most appropriate condition to enhance the coating properties.

2.6.2 Effect of Standoff Distance

Pattison et al. [59] investigated the effect of SoD and bow-shock formation on PV and DE in CS. The experiments used Al, Cu, and Ti powders with He and N_2 as process gases. The results showed a strong relationship between SoD and DE, because a short SoD strengthened the bow shock near the substrate and reduced particle impact velocity. At SoD below 60 mm, the bow shock reduced DE by up to 40%. This shows that SoD must be selected to limit bow-shock deceleration and maintain effective particle impact conditions.

W. Y. Li et al. [60] investigated the influence of SoD on coating deposition using Al, Ti, and Cu powders. The maximum PV was obtained at approximately 50–100 mm from the nozzle exit. DE values for Al and Ti decreased as SoD increased from 10 mm to 110 mm, and Cu exhibited the maximum DE at 30 mm and then decreased with increasing SoD. SoD controls the balance between particle acceleration and coating build-up.

Moreno-Murguia et al. [61] studied the deposition of LPCS Cu coatings by varying air pressure and SoD. The study used Cu powder on Al substrates and compared experimental

PV with CFD results. The highest DE of 36–37.5% was obtained at 7 bar for SoD of 5–12.5 mm, while increasing pressure to 8 bar reduced DE to 6–11%. SoD and pressure must be selected together to maintain effective particle impact velocity and DE.

Garmeh et al. [62] examined CS deposition on discontinuous substrate geometries, including holes, steps, and off-axis features. The study used Cu powder with particle sizes of 17–77 μm with N_2 gas, SoD of 10 mm, G_p of 2 and 4 MPa, and G_t of 400 and 800 °C. Deposition rate decreased as hole diameter decreased or hole depth increased. Local geometry also affects near-wall gas flow and edge-focused deposition.

2.7 Particle Characteristics and Deposition Quality

Particle characteristics strongly affect CS deposition because D_p, morphology, density, surface condition, and ψ control acceleration, heating, dispersion, and impact with the substrate. Smaller particles usually accelerate faster due to lower inertia. Therefore, D_p and ψ must be considered together when evaluating PV, PT, RD, and coating uniformity.

Özdemir et al**.** [63] combined particle velocimetry, schlieren imaging, and 3D CFD to examine the role of ψ in CS. The study used Al6061 and Cu powders with helium, nitrogen, and air as process gases, showed that ψ strongly affects PV and velocity scatter. When particles were assumed perfectly spherical ($\psi = 1$), CFD underestimated the measured PV, while using measured D_p and sphericity data improved prediction accuracy. For most particles larger than 20 μm in the Al6061-N_2 case, the prediction error remained below 10%. Lower ψ increased PV, and particles below 10 μm entered the slip-flow regime, showing that both D_p and morphology must be included in CS particle-flight analysis.

Ardeshiri Lordejani et al. [64] developed a comprehensive numerical framework to assess how feedstock features affect deposit quality. The study considered D_p, morphology, extent of oxidation, and impact angle, and evaluated deposit indicators such as V_{cr}, particle flattening, and porosity. Lagrangian and coupled Eulerian-Lagrangian methods were

identified as robust approaches for single-and multi-particle impact analysis. The results showed that feedstock characteristics control impact deformation and deposit quality, indicating that feedstock characteristics must be evaluated collectively

Ozdemir & Muftu [65] developed a 1D analytical model to predict DE by incorporating ψ. The model used measured size and sphericity distributions of Al, Cu, Ti, and Ta powders to predict particle impact velocity, PT, and DE. The results showed that ψ changes drag behavior and deposition probability, so particles with similar nominal sizes can produce different impact conditions when their shapes differ. This study confirms that ψ should be included with D_p in particle-flight analysis and DE prediction.

Sinnwell et al. [66] studied the effect of particle morphology on spray characteristics in LPCS with three Cu powders of 1–40 μm. The study employed 2D image analysis and X-ray micro-computed tomography to determine circularity, sphericity, surface area, and volume distributions. The results showed that irregular particles had lower circularity and ψ than spherical particles, while PV and spray dispersion were higher. Spherical particles produced lower maximum velocity and wider spray dispersion. Drag response, plume focusing, and deposition footprint are influenced by particle morphology. First, D_p controls inertia and acceleration; second, ψ controls drag response; third, RD controls coating footprint.

2.8 Coating Quality Indicators

Coating quality in CS is evaluated through a combination of in-flight, impact, and deposit-based indicators rather than using a single response variable. Assadi et al., Schmidt et al. [1], [20] explained that PV is one of the most important coating-quality indicators, because successful deposition occurs only when particle impact velocity exceeds the V_{cr} required for plastic deformation and bonding. This concept directly supports the present research, where PV was maximized to improve impact energy, deformation capability, and bonding probability. In this study, PV was treated as the main response because higher PV

improves coating build-up, DE, and interfacial quality provided that erosion limits are not exceeded. Therefore, maximizing PV provides a direct measure of nozzle and process performance. This approach is consistent with the present CFD-based methodology, where nozzle geometry and operating conditions were selected to enhance particle acceleration before impact.

Kamaraj & Radhakrishnan [67] **e**xplained that coating quality in CS is mainly governed by the combined effect of impact velocity (V_p) and particle temperature (T_p), because deposition occurs within the useful window of (V_{cr}) < V_p < (V_{er}), where $V_{er} \approx 2V_{cr}$. For Cu, with a melting temperature (T_m) = 1356 K, they showed that V_{cr} decreases from about 500 m/s at room temperature to 250 m/s at 800 °C, confirming the thermal sensitivity of the deposition window. In the present research, PT was controlled at around 415 K, yielding $T_p/T_m \approx 0.31$, which remained within the solid-state adhesion region while supporting particle softening and deformation. Therefore, PT was assessed together with PV to maintain stable bonding and coating quality.

Yin et al. [32] demonstrated that the surface heating, near-wall temperature, and bonding conditions in CS are affected by substrate preheating and gas-particle thermal interaction. This helps to justify the use of HF as a coating quality response, as it is a measure of the thermal energy transferred toward the substrate impact region. HF enhances the local thermal state at the substrate surface, facilitates the deformation of particles, and enhances the interfacial contact during deposition without particle melting. Hence, HF should be evaluated in conjunction with PV and PT as coating quality depends on both mechanical impact and controlled thermal assistance. W. Y. Li et al. [33] also demonstrated that the temperature distribution within the substrate and the nozzle wall varies with SoD and inlet temperature, which indicates that the thermal response of the substrate should be taken into account in the analysis of the process for coating applications.

Pattison et al. [59] examined SoD and bow-shock formation in CS and showed that the near-substrate flow field can reduce particle impact velocity and DE when the SoD is not

properly selected. This supports the use of surface pressure (SP) as a substrate-level response variable because SP reflects the pressure build-up in front of the nozzle exit and its influence on particle deceleration near the impact zone. Zavalan & Rona [51] further showed that nozzle contour and exit condition influence PV, radial uniformity, and DE in CSAM. Therefore, SP should be minimized to reduce adverse near-wall flow resistance, weaken the bow-shock barrier, maintain effective PV at the substrate, and improve coating uniformity

Raletz et al., Wan et al. [30], [54] demonstrated that the geometry of the powder injector and the value of ΔP significant influence particle acceleration and RD in CSAM. Their results support the present research because RD was minimized to improve spray focusing, coating uniformity, and deposition accuracy. A smaller RD indicates that more particles are concentrated near the jet centerline where PV is higher and particle trajectories are more stable. This enhances coating build-up and minimizes off-axis spreading, which is crucial for coating width and material utilization. Overall, coating quality in CS should be assessed through the combined responses of DE, coating uniformity, and bonding quality.

2.9 Optimization Approaches

Optimization approaches have developed because process variables and responses do not improve. Higher PV can improve impact energy, but excessive velocity may increase rebound, erosion, or radial spreading. CS optimization moved from single-response selection toward multi-factor and multi-response frameworks.

Deb et al. [68] proposed NSGA-II, a Pareto-based multi-objective optimization (MOO) algorithm to deal with conflicting responses. NSGA-II is a multi-objective genetic algorithm that produces a diverse Pareto front of balanced non-dominated solutions, unlike a conventional genetic algorithm (GA) that typically finds a single optimum solution. This is applicable in CS optimization as PV, PT, and RD do not improve under the same process condition. Increasing PV can increase impact energy, but can also increase RD or move the particle condition out of the desired thermal window. Hence, NSGA-II can be applied

to optimize G_p, G_t, D_p, D_t, and SoD to simultaneously improve PV, control PT, and reduce RD.

Shojaeefard & Zare [69] applied modified NSGA-II and TOPSIS and demonstrated that Pareto optimization can be used to select a practical solution among the competing alternatives by applying MCDM ranking. Yang et al. [70] also used NSGA-II and entropy-weighted TOPSIS to demonstrate that objective weighting enhances the reliability of the ranking when multiple responses are considered simultaneously. In CS optimization, this route is suitable because PV, PT, and RD often conflict with each other, so the Pareto front obtained from NSGA-II still requires a decision-making stage. TOPSIS ranks alternatives according to their closeness to the ideal response, while VIKOR determines a compromise solution by utility and regret measures. AHP can incorporate engineering priority using pairwise comparison, while EWM can give data-based objective weighting. Hence, the hybrid NSGA-II and MCDM approach is more effective than a single optimization approach as it enables the selection of the coating-oriented conditions with high PV, controlled PT and reduced RD.

Canales et al. [71] used machine-learning methods to describe the deposition window and predict DE in cold spraying. Their model classified whether particles adhered or rebounded by linking the prediction with cumulative particle size distribution and DE data. This data-driven approach is useful when deposition response is difficult to describe through a simple analytical equation because adhesion depends on PV, D_p distribution, material response, and impact condition together. The machine-learning route therefore introduced a faster predictive method for identifying whether a given particle condition lies inside or outside the deposition window.

Z. Wang et al. [72] applied feature selection and ANN to predict V_{cr} in CS. Their analysis showed that mechanical material parameters had stronger influence on V_{cr} than thermal parameters, especially those related to plastic deformation. The nonlinear ANN model achieved 95.24% prediction accuracy on the original dataset and 96.45% accuracy on the

new dataset, outperforming the linear ANN and empirical formula. These values show that ANN can capture nonlinear material-response effects that are difficult to represent through direct empirical equations, especially when the response is controlled by combined mechanical and thermal material properties.

Mohankumar et al. [73] used central composite rotatable design with 3 variables and 5 levels to optimize CS process inputs for AA2024/Al_2O_3 coatings on AZ31B magnesium alloy. RSM and analysis of variance were applied to minimize porosity and maximize hardness. Their optimized condition of 500 °C gas temperature, 10 mm SoD, and 20 g/min powder feed rate produced minimum surface porosity of 3.31 vol.% and hardness of 137.21 HV. The RSM converted the broad process window into a specific parameter combination, showing that porosity and hardness require simultaneous treatment because both responses do not necessarily improve under the same setting.

Shorinov et al. [74] optimized LPCS Ni + Al_2O_3 coating on VT3-1 titanium alloy using central composite design (CCD), RSM, and ANOVA to maximize adhesion strength and DE. Their study varied nozzle inlet temperature from 450 to 550 °C, powder feed rate from 0.2 to 0.8 g/s, and SoD from 5 to 15 mm, while G_p was fixed at 0.9 MPa. The regression models showed high reliability, with R^2 values of 0.9911 for adhesion and 0.9893 for DE. The optimized condition was at G_t of 537 °C, SoD at 11 mm, and feed rate of 0.6 g/s, giving adhesion strength of 34.78 MPa and DE of 29.46%.

Ashokkumar et al. [75] optimized CS parameters for AA2024/Al_2O_3 coating on AZ31B Mg alloy using RSM and ANOVA. Their study considered temperature of 470–570 °C, SoD of 7–17 mm, powder feed rate of 17–27 g/min, and constant pressure of 12 bar. The experimental minimum porosity was 2.0 vol.% at 520 °C, 12 mm SoD, and 22 g/min feed rate. RSM predicted an improved porosity of 1.845 vol.% at 527.77 °C, 9.59 mm SoD, and 22.58 g/min, with less than 7.5% prediction error.

Singhal & Murtaza [76] optimized CGDS DE using 2D axisymmetric CFD with RSM and CCD. Their model used N_2 gas, Copper-Zinc alloy C93200 particles, steel substrate, 132,334 quadrilateral cells, gas inlet pressure of 3.0 MPa, injection pressure of 3.1 MPa, and gas inlet temperature of 923 K. The study varied D_p, SoD, and T_c to predict V_{cr}, erosion velocity (V_{er}), and DE. ANOVA confirmed model significance with $R^2 = 0.9423$. The optimized condition was D_p of 23.57 µm, SoD of 50 mm, and T_c of 623 K, giving DE of 82.97%.

Kun et al. [77] optimized CS nozzle conditions using RSM by treating G_t, D_p, and G_p, as interacting variables. Their regression model predicted PV at the Laval-nozzle exit and before substrate deposition with an error of less than 1.6% compared with the simulated value. For Al particles, the optimized condition was G_t = 550 °C, D_p = 20 µm, and G_p = 1.0 MPa, giving V_{er} of 502.5 m/s and PV of 494.5 m/s. For Cu particles, the optimized condition was G_t = 700 °C, D_p = 15 µm, and G_p = 1.5 MPa, giving V_e = 478.4 m/s and V_p = 478.8 m/s. These values show that RSM can be used not only for coating properties but also for predicting particle flight responses.

Eberle et al. [78] applied machine learning to optimize Ti deposition by predicting PV distribution and DE. Their work used 62 spray-plume experiments with N_2 gas, CP Ti powder of about 32 µm average size, powder feed rate of about 0.4–4.5 kg/h, and 135,996 measured particles. Support vector regression and neural network (NN) models predicted average PV with RMSE close to 41 m/s. The velocity-distribution model was then combined with a deposition-window approach to predict DE from nine coupon samples, giving RMSE values of 3.2% for SVR and 5.5% for NN. This supports data-driven PV and DE optimization.

Gutiérrez de Frutos et al. [79] developed a 3D-CFD and design of experiments (DOE) based nozzle optimization approach for PV improvement. Their model used N_2 gas at 5 MPa and 500 °C, Al6061 and pure Cu powders with mean D_p of 40 µm, and a reference nozzle with L_c of 31 mm, L_d of 130 mm, 5.7 mm² throat area, and ER of 5.5. The study

varied L_d from 80 to 200 mm, throat area from 3 to 8 mm², and ER from 4 to 10 using about 2 million mesh cells. L_d was the most influential factor, supporting CFD-based nozzle-geometry optimization for PV improvement.

2.10 Research Gaps

In the field of CS coating, bibliometric analysis is one of the important quantitative methods for understanding the current state of research. However, limited studies have used suitable keywords to identify research gaps within CS coating and prioritize specific research areas. On the other hand, many studies are available on deposition, process parameters, and nozzle design and gas-particle flow, but limited work has been found on the combined optimization of 2D-CD nozzle design and process parameters for improved coating quality. Critical factors such as throat diameter, convergent length, divergent length, exit diameter, inner injector diameter, gas velocity, pressure, temperature, powder size, and standoff condition still require systematic CFD-based analysis. Therefore, there is a need to develop an integrated numerical and optimization framework considering particle size distribution, particle shape, sphericity, deposition, and coating uniformity.

2.11 Research Objectives

Based on the identified research gaps, the objectives of the present study are as follows:

i. Employ quantitative analysis to identify research gaps within the realm of cold spray coating and prioritize specific areas for further investigation.
ii. Analyse and optimize the 2D-CD nozzle for different design parameters by CFD.
iii. Utilize CFD to analyse and optimize the 2D-CD nozzle across different process parameters.
iv. Explore various sizes and shapes of particle deposition through simulation, and determine the most effective process parameters for improving coating quality.

CHAPTER 3 RESEARCH METHODOLOGY AND MODELING

3.1 Research Methodology

The present research work was conducted using bibliometric analysis, CFD modelling and optimization of the CS coating process. 2D axisymmetric nozzle configurations were designed and simulated using CFD to study gas-particle flow, particle acceleration, particle heating, and substrate level responses. Numerical results were used to optimize nozzle design, process parameters, and particle characteristics for performance evaluation. Using this methodology, the following studies were carried out:

- Bibliometric analysis was conducted using Scopus data and VOSviewer software to analyze publication trends, keyword co-occurrence, research clusters, and influential sources.
- Geometry, mesh, boundary conditions, material properties, and the turbulence model were defined to develop 2D axisymmetric CD nozzle configurations with the substrate region.
- Gas velocity, gas temperature, pressure distribution, particle velocity, particle temperature, heat flux, surface pressure, and radial dispersion were analysed using the CFD model.
- Nozzle design parameters were varied, and response data were used to optimize the 2D-CD nozzle using RSM with a desirability function (RSM-DF) and an ANN-genetic algorithm (ANN-GA).
- The selected nozzle model was subjected to various process parameters.
- Multi-objective optimization was carried out using NSGA-II, followed by AHP, EWM, TOPSIS and VIKOR.
- GRA integrated particle velocity and particle temperature into a single performance response.
- Particle size and sphericity effects were analysed by numerical simulation.

3.2 Methodology for Bibliometric Analysis

The bibliometric analysis was performed to define the general structure of the CS research field and to give a quantitative foundation for interpreting the development of the field, influential themes, and research gaps. The methodology was carried out through a sequential process, as illustrated in Figure 3.1, which includes bibliographic data retrieval from the Scopus database, data processing, network extraction, mapping, visualization, and analytical interpretation. Scopus was chosen because it offers relevant bibliographic records, citation information, and metadata for bibliometric mapping.

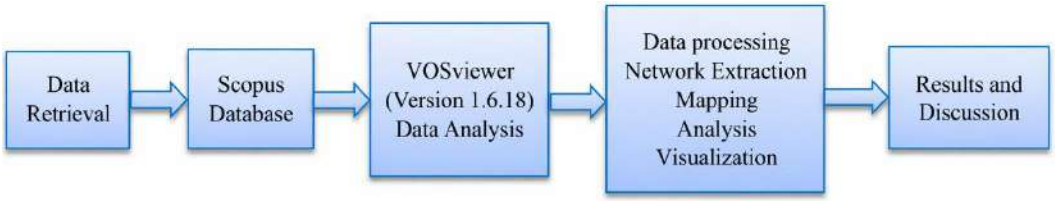

Figure 3.1 Steps involved in data assessment and bibliometric analysis

3.2.1 Data Source and Search Strategy

The bibliometric data were retrieved from the Scopus database, which was used as the main source for identifying and organizing published studies on CS. The search strategy was TITLE-ABS-KEY (“COLD SPRAY” AND “DEFORMATION” AND “COATINGS”), and publications from 1999 to 2022 were retrieved. This search framework provided a focused and structured dataset and a suitable basis for comparative bibliometric assessment and structured analysis [80]. Document inclusion was based on direct relevance to the selected bibliometric theme. After applying the search query and relevant filters, the final dataset consisted of 387 documents. For data extraction, the selected records were downloaded from Scopus in comma-separated values (.csv) format, containing full records and cited references for bibliographic mapping, network generation, and further analytical assessment.

3.2.2 Bibliometric Mapping and Analysis Procedure

This dataset was analyzed using VOSviewer (Version 1.6.18) as the core software for scientometric evaluation and the generation of maps in the context of bibliometric mapping. The software was implemented to create bibliometric maps to explore the structural relationship within the CS research field and to help with visual interpretation. Network visualization and density visualization were employed to interpret the maps produced and to analyze clustering patterns, strength of links, and relative concentration of research activity. The parameters used for the bibliometric evaluation were the number of publications, cumulative publications, publication year, total citations, average citations, author's document citations, and the co-occurrence of keywords. The results were interpreted in a theme-based manner across various output categories: publication growth, source distribution, author output distribution, subject-based output distribution, document distribution, keyword co-occurrence, and keyword density visualization, in order to examine thematic concentration and research relationships.

3.3 Technical Screening and Selection of Study Variables

The study variables were selected through technical screening to maintain a focused and technically connected framework. The selection was restricted to variables that directly influence compressible gas flow, particle acceleration, thermal behavior, impact conditions, and deposition-related characteristics in a CS process. In this way, the variable set was organized around nozzle-related, process-related, particle-related, and response variables, so that the subsequent analysis could proceed systematically from nozzle design and operating conditions toward particle-based behavior and coating performance [6], [40]. The principal nozzle-related variables were D_t, L_c, L_d, D_{id}, L_i, and D_e. These variables were considered relevant because the convergent section affects gas acceleration and velocity distribution, the divergent section controls gas expansion and supersonic flow, the injector dimensions influence particle acceleration and PT, and the exit section affects Mach number and particle dynamics. The process-related variables G_p, G_t, D_p, and

SoD were retained because they control particle acceleration, thermal response, and impact conditions in HPCS. In addition, ψ was selected for morphology-sensitivity analysis because it alters drag response, in-flight motion, substrate impact conditions, and dispersion. These variables were finally used to evaluate PV, PT, and RD to improve coating quality, bonding condition, and deposition performance.

3.4 Development of the CFD Model

To analyze nozzle design, optimize process parameters, and investigate the behavior of particles, a CFD model was developed. The model was developed for a 2D axisymmetric compressible gas-flow CD nozzle, with Eulerian-Lagrangian tracking of Cu particles accelerated by N_2 gas toward the substrate. PV, PT, RD, HF, and SP were evaluated by solving the gas phase using continuity, momentum, and energy equations, while the particle phase was modeled using the discrete phase model (DPM). The geometry, assumptions, turbulence model, boundary conditions, and solution procedure are described in Sections 3.4.1−3.4.4.

3.4.1 Nozzle Geometry and Computational Domain

A 2D axisymmetric computational domain was used to represent the CS system. Pressurized N_2 was divided into a preheated working-gas stream and a carrier-gas stream transporting Cu particles. Both streams merged in the prechamber before entering the CD nozzle, where the flow accelerates toward the substrate. Figure 3.2 shows the optimized computational geometry used for the CFD simulations. The optimized geometry consisted of a 35 mm prechamber, a 22.85 mm convergent section**,** and a 231.21 mm divergent section. The inlet, throat, and exit diameters were fixed at 19 mm, 2.5 mm, and 7.93 mm, respectively. The nozzle exit was placed 25 mm from the substrate.

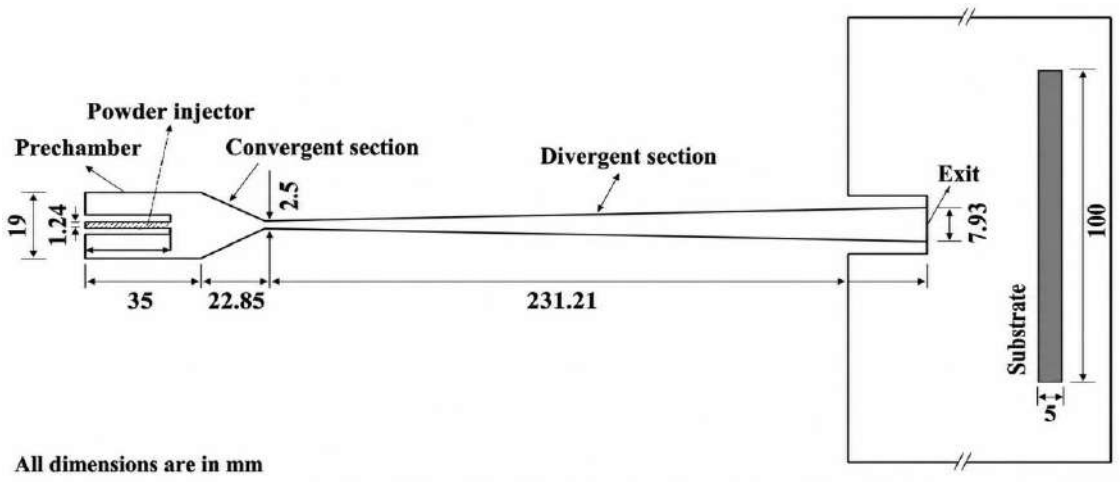

Figure 3.2 Schematic of 2D geometry of nozzle and substrate used in the CFD simulations

Figure 3.3 shows the baseline CD nozzle used for nozzle geometry optimization, while Table 3.1 presents its detailed geometric and operating parameters. Under baseline conditions, N_2 was used as both the propulsion gas and the carrier gas, 25 μm Cu particles were used as feedstock, G_p was fixed at 3 MPa**,** G_t was set at 773 K, and the particle injection pressure was set at 3.1 MPa, which was 0.1 MPa higher than the main G_p, resulting in $\Delta P = 0.1$ MPa to ensure stable particle entrainment [41].

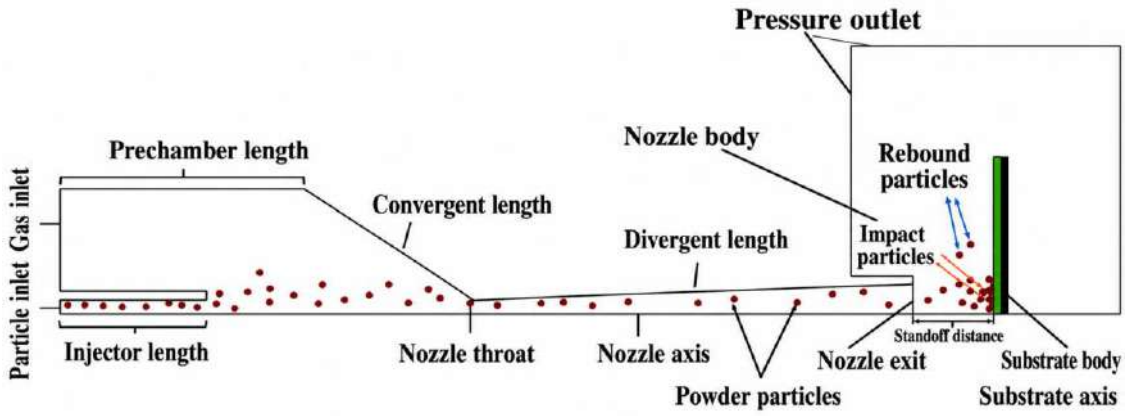

Figure 3.3 Detailed illustration of key geometric parameters in an axisymmetric 2D CD nozzle (not to scale)

Table 3.1 Detailed geometric and operating parameters

Baseline nozzle design parameters				Operating parameters	Value
Fixed parameters	**Value (mm)**	**Critical parameters**	**Value (mm)**		
D_i	19	L_c	20	gas inlet pressure	3 MPa
L	35	L_d	200	gas temperature	773 K
D_t	2.5	D_{id}	1.8	particle injection pressure	3.1 MPa
SoD	25	L_i	20	particle temperature	300 K
D_{od}	4	D_e	7	outlet pressure	0.1 MPa

3.4.2 Governing Assumptions and Gas Flow Equations

The CFD model was developed based on governing assumptions to capture the dominant compressible-flow and particle-dynamic features of HPCS while maintaining numerical stability and computational efficiency. The principal assumptions adopted in the present work are summarized as follows [81]:

1. The computational domain was treated as 2D and axisymmetric.
2. The gas phase was assumed to be steady, compressible, and turbulent.
3. The working gas was treated as an ideal gas with Newtonian behavior.
4. The nozzle and injector walls were treated as adiabatic no-slip boundaries.
5. The gas phase was solved within a Reynolds-averaged turbulence framework.
6. The particle phase was treated using an Eulerian-Lagrangian formulation with DPM.
7. One-way coupling was assumed.
8. Particle-particle interactions were neglected.
9. The dominant force acting on the particles was taken as aerodynamic drag.
10. Particles were initially treated as spherical, and later analysis introduced ψ explicitly.
11. Particle temperature within each particle was assumed to be spatially uniform.
12. Particle impacts with the nozzle wall were treated as elastic reflections.

These assumptions provided a stable and consistent numerical basis for nozzle design optimization, process-parameter optimization, and particle-based analysis. They were selected to preserve the dominant thermo-fluid and particle-dynamics features. Based on these assumptions, the gas phase was solved using the steady Reynolds-averaged Navier-Stokes (RANS) equations for compressible gas flow. The continuity, momentum, and energy equations were used to describe the compressible gas flow through the CD nozzle and the free-jet region up to the substrate. The governing equations are written as:

$$\frac{\partial}{\partial x_i}(\rho u_i) = 0 \tag{3.1}$$

$$\frac{\partial}{\partial x_i}\left(\rho u_i u_j\right) = -\frac{\partial P}{\partial x_i} + \frac{\partial \tau_{ij}}{\partial x_i} \tag{3.2}$$

$$\frac{\partial}{\partial x_i}(\rho e u_i) = -\frac{\partial P u_i}{\partial x_i} + \frac{\partial\left(u_j \tau_{ij} - q_i\right)}{\partial x_i} \tag{3.3}$$

where ρ is the gas density, u_i represents the velocity components, P is the static pressure, e is the internal energy, τ_{ij} is the viscous stress tensor, and q_i is the conductive heat flux.

Since the nozzle flow is highly compressible during supersonic acceleration, the gas density was evaluated by the ideal-gas equation of state,

$$\rho = \frac{P}{RT} \tag{3.4}$$

where R is the gas constant and T is the gas temperature.

The gas phase in the present CFD model was solved within a Reynolds-averaged turbulence framework, and the standard k–ε turbulence model was adopted for simulations because previous CS studies have shown that k–ε type turbulence closure can reproduce nozzle wall pressure and in-flight PV trends in close agreement with experimental measurements, as validated in Section 4.4.1. To represent the near-wall flow properly,

enhanced wall treatment was employed, and the y^+ value was maintained in the range of 30–50 [41].

The transport equations for turbulent kinetic energy (k) and turbulent dissipation rate (ε) are written as follows:

$$\frac{\partial}{\partial x_i}(\rho k u_i) = \frac{\partial}{\partial x_j}\left[\left(\mu + \frac{\mu_t}{\sigma_k}\right)\frac{\partial k}{\partial x_j}\right] + G_k + G_b - \rho\varepsilon - Y_m + S_k \tag{3.5}$$

$$\frac{\partial}{\partial x_i}(\rho \varepsilon u_i) = \frac{\partial}{\partial x_j}\left[\left(\mu + \frac{\mu_t}{\sigma_\varepsilon}\right)\frac{\partial \varepsilon}{\partial x_j}\right] + C_{1\varepsilon}\frac{\varepsilon}{k}(G_k + G_{3\varepsilon}G_b) - C_{2\varepsilon}\rho\frac{\varepsilon^2}{k} + S_\varepsilon \tag{3.6}$$

The eddy viscosity is calculated as:

$$\mu_t = \rho C_\mu \frac{k^2}{\varepsilon} \tag{3.7}$$

where k is the turbulent kinetic energy, ε is its dissipation rate, μ is the molecular viscosity, μ_t is the eddy viscosity, G_k is the production of turbulent kinetic energy due to mean velocity gradients, G_b is the buoyancy production term, Y_m is the compressibility dissipation term, and S_k and S_ε are source terms. The standard constants used in the solver were $C_{1\varepsilon} = 1.44$, $C_{2\varepsilon} = 1.92$, $C_\mu = 0.09$, $\sigma_k = 1.0$, and $\sigma_\varepsilon = 1.3$.

3.4.3 Particle Tracking and Heat Transfer Modeling

The particle phase was treated using the DPM within an Eulerian-Lagrangian framework, where the gas phase was solved in the Eulerian frame and particle trajectories were calculated in a Lagrangian frame. This treatment was adopted because CS deposition requires the solution of the gas phase flow together with particle motion, and the particle dynamics prior to impact directly govern PV, impact conditions, and deposition-related behavior. In the present simulations, the particle phase was treated with one-way coupling, and turbulence-induced particle dispersion was represented by the Discrete Random Walk (DRW) model. Approximately 1200 particle streams per cas**e** were tracked with a time-scale constant of 0.15 to obtain stable particle trajectories [54]. The particle motion was

computed using the high-Mach-number drag law, while heat transfer was evaluated using the convective heat-transfer formulation. Particle Mach number was greater than 0.4, and the particle Reynolds number was above 20 [82].

The particle motion was governed by the standard force-balance equation:

$$\frac{du_p}{dt} = F_d(u - u_p) + \frac{g_x(\rho_p - \rho)}{\rho_p} + F_x \tag{3.8}$$

where u_p is the particle-phase velocity, u is the gas-phase velocity, ρ_p is the particle density, g_x is the gravitational component in the x direction, and F_x is the additional acceleration term. The drag term (F_d) per unit particle mass was expressed as

$$F_d = \frac{18\mu}{\rho_p D_p^2}\frac{C_D Re}{24} \tag{3.9}$$

where μ is the gas viscosity, D_p is the particle size, C_D is the drag coefficient, and Re is the relative Reynolds number. The particle Reynolds number was evaluated as:

$$Re = \frac{\rho(u - u_p)D_p}{\mu} \tag{3.10}$$

To justify the one-way coupled Eulerian-Lagrangian treatment, the mass loading ratio, particle volume fraction, and Stokes number were also evaluated as:

$$\Phi_m = \frac{\dot{m}_p}{\dot{m}_g} \tag{3.11}$$

$$\Phi_v = \frac{\Phi_m\, \rho}{\rho_p\left(1+\Phi_m\, \rho/\rho_p\right)} \tag{3.12}$$

$$St = \frac{\tau_p U_e}{D_e} \tag{3.13}$$

where $\dot{m}_p$ and $\dot{m}_g$ are the particle and gas mass flow rates, $\tau_p = \rho_p D_p^2/(18\mu)$ is the particle time scale, U_e is the mean exit velocity magnitude, and D_e is the nozzle exit diameter. The reported values confirmed dilute loading and highly inertial particle motion,

which justified neglecting particle-particle interactions and momentum feedback from the particle phase to the gas phase [83].

The drag force acting on the particles was evaluated through the drag coefficient (C_D), and separate drag laws were used for spherical and non-spherical particles. In the optimization framework, where the injected particles were initially treated as spherical, C_D was determined using the Morsi-Alexander correlation [84], written as:

$$C_D = a_1 + \frac{a_2}{Re} + \frac{a_3}{Re^2} \tag{3.14}$$

where a_1, a_2, and a_3 are empirical constants dependent on the Reynolds number regime. In the later morphology-sensitive analysis, the spherical-particle assumption was relaxed and the C_D for non-spherical particles was computed using the Haider-Levenspiel model [85], expressed as

$$C_D = \frac{24}{Re}(1 + ARe^B) + \frac{C}{1 + \frac{D}{Re}} \tag{3.15}$$

where the empirical constants A, B, C, and D are functions of ψ, given by

$$A = \exp(2.3288 - 6.4581 + 2.4486\psi^2) \tag{3.16}$$

$$B = 0.0964 + 0.5565\psi \tag{3.17}$$

$$C = \exp(4.905 - 13.8944\psi + 18.4222\psi^2 - 10.2599\psi^3) \tag{3.18}$$

$$D = \exp(1.4681 + 12.2584\psi - 20.7322\psi^2 + 15.8855\psi^3) \tag{3.19}$$

For the morphology-sensitive simulations, ψ was defined as:

$$\psi = \frac{Surface\ Area\ of\ a\ Spherical\ Particle\ of\ Equivalent\ Volume}{Surface\ Area\ of\ the\ Actual\ Particle} \tag{3.20}$$

The particle heat transfer model was used to predict the particle thermal response of the injected particles during their motion through the CS nozzle and the free-jet region. Because the gas temperature changes continuously during compressible expansion, PT

was calculated through a transient convective energy balance between the surrounding gas and the particle. The transient energy balance for each particle was written as:

$$m_p c_{p,p} \frac{dT_p}{dt} = hA_{sp}(T_g - T_p) \tag{3.21}$$

where m_p is the particle mass, $c_{p,p}$ is the specific heat capacity of the particle, T_g and T_p are the gas-phase and particle-phase temperatures, respectively, A_{sp} is the surface area of the spherical particle, and h is the convective heat-transfer coefficient. The heat-transfer coefficient was defined as:

$$h = \frac{Nu\lambda_g}{D_p} \tag{3.22}$$

where λ_g is the thermal conductivity of the gas and D_p is the particle size. The Nusselt number was evaluated using the Ranz-Marshall correlation as

$$Nu = 2.0 + 0.6Re^{1/2}Pr^{1/3} \tag{3.23}$$

and the Prandtl number was written as:

$$Pr = \frac{\mu c_{p,g}}{\lambda_g} \tag{3.24}$$

where μ is the gas viscosity and $c_{p,g}$ is the specific heat capacity of the gas. These equations provided the common heat-transfer formulation for predicting PT in the present CFD model.

3.4.4 Material Properties and Numerical Setup

The detailed material and particle-property specifications are summarized below, while the corresponding thermophysical properties of the gas and materials used in the simulation are presented in Table 3.2 [25], [86].

1. Gas phase material: N_2 was selected as both the propellant gas and the carrier gas, and in the numerical framework its density was evaluated using the ideal gas law, while the specific heat capacity was represented using a piecewise-polynomial formulation.
2. Powder material: Cu particles were used as the discrete phase.
3. Substrate material: Al was used as the substrate.
4. Particle size specification: A reference D_p of 25 μm was used for baseline evaluation, while later stages considered $D_p = 5$–45 μm and $D_p = 2$–75 μm.
5. Particle shape specification: Particles were initially treated as spherical, and later $\psi = 1.0$ to 0.6 was introduced.
6. Particle injection state: Particles were introduced with an injection velocity of 10 m/s, and the reference particle temperature at injection was 300 K.

Table 3.2 Thermophysical properties of the gas and materials used in the simulation

Properties	**Cu**	**N_2**	**Al**
Density, kg/m^3	8978	Ideal gas law	2719
Specific heat capacity, J/ (kg·K)	381	Piecewise-polynomial	871
Thermal conductivity, W/ (m·K)	387.6	0.0242	202.4

The boundary conditions were prescribed to reproduce the operating environment of an HPCS system with axial powder injection, compressible nozzle flow, and particle impingement on a flat substrate. The boundary-condition layout of the 2D axisymmetric model, including the gas inlet, particle inlet, nozzle and injector walls, outlet, substrate region, and response locations, is shown in Figure 3.4. The boundary conditions are stated as follows [83], [87].

1. Gas inlet condition: The main working-gas inlet was treated as a pressure inlet. In the baseline and process-parameter studies, the principal baseline condition was 3 MPa

and 773 K, while the broader optimization window covered G_p = 2–4 MPa and G_t = 633–913 K.

2. Carrier-gas and particle-inlet condition: The carrier-gas inlet was also treated as a pressure inlet and was maintained at a pressure slightly higher than the working-gas pressure, with ΔP = 0.1 MPa. The particles were injected at 300 K with an initial velocity of 10 m/s.

3. Outlet condition: The downstream boundary was specified as a pressure outlet with 0.1 MPa and 300 K. The outlet was placed sufficiently downstream of the nozzle exit to reduce non-physical back-pressure and shock reflection.

4. Wall boundary conditions: The nozzle and injector walls were treated as adiabatic no-slip boundaries.

5. Axisymmetric boundary: The centerline was assigned an axisymmetric boundary.

6. Turbulence inlet specification: Both inlets and the outlet were assigned 1% turbulence intensity, with the turbulence length scale taken as 20% of the nozzle throat diameter.

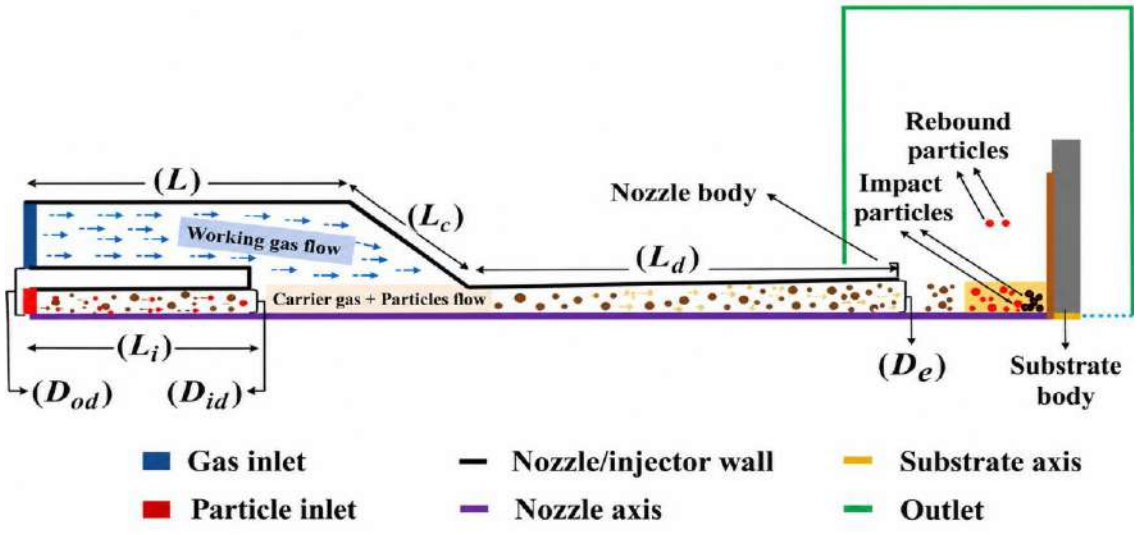

Figure 3.4 Boundary conditions for coupled gas and particle flow in the 2D axisymmetric nozzle model (not to scale)

The numerical solution procedure was implemented in ANSYS Fluent using a solver setup appropriate for compressible, high-velocity, supersonic nozzle flow with discrete particle tracking. The procedure was standardized so that nozzle-design, process-parameter, and morphology-sensitive simulations could be compared on a common numerical basis. The numerical solution procedure can be summarized as follows:

1. A density-based implicit solver was used for highly compressible CS nozzle flow with supersonic acceleration;
2. Double-precision calculations were adopted in the simulations;
3. The governing equations were discretized using a second-order upwind scheme, with gradients evaluated using the least-squares cell-based method;
4. Roe-FDS was used to improve the resolution of compressible flow and shock-related features
5. Iterations were continued until the normalized residuals fell below 10^{-5}
6. High-order term relaxation (HOTR), convergence acceleration, and full multigrid (FMG) initialization were used.

A structured quadrilateral mesh was adopted to ensure numerical accuracy, stable convergence, and mesh-independent prediction of the major CS responses. The mesh was generated for the 2D axisymmetric computational domain, and the final mesh was selected after grid-independence verification. A higher mesh density was used in the powder injector/prechamber, nozzle throat, and exit region to resolve choking, strong pressure, temperature, velocity gradients, jet development, and shock structures. The overall computational domain and mesh details are presented in Figure 3.5.

The nozzle geometry used in the present simulations was first prepared in SolidWorks by defining the axisymmetric CD nozzle, powder injector, and substrate configuration. The overall computational domain is shown in Figure 3.5(a). After completing the geometric definition, the model was transferred to the numerical platform for mesh generation and further CFD analysis, which helped maintain dimensional consistency of the nozzle, injector, and substrate arrangement before discretization of the computational domain. A

structured quadrilateral mesh was then created using ANSYS Meshing, and the final mesh was selected after mesh-independence tests. Local mesh refinement was applied in the injector region, nozzle throat, and substrate-facing zone, and the refined mesh zones used in the present work are shown in Figure 3.5(b-d). This localized refinement improved the numerical prediction of velocity, pressure, temperature, and particle-trajectory fields without unnecessarily increasing the total cell count in the complete domain.

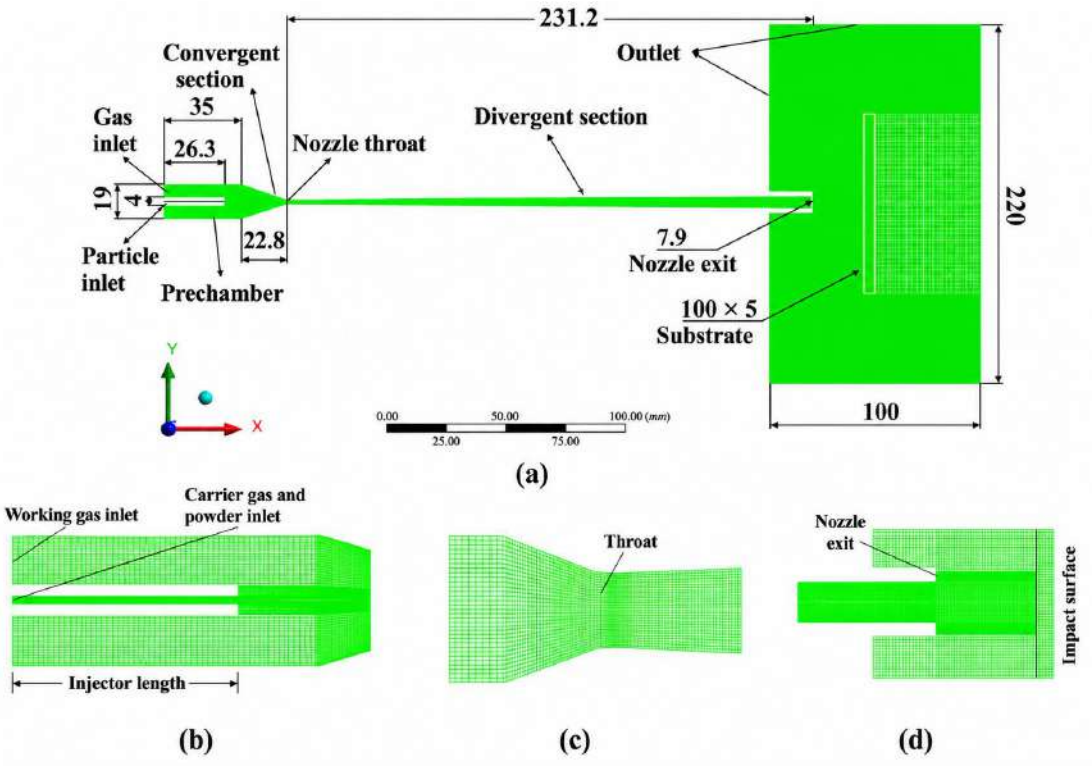

Figure 3.5 Computational domain and mesh details: (a) full 2D nozzle mesh, (b) prechamber, (c) upstream and throat zones, and (d) nozzle exit and expansion region

The grid-independence analysis was carried out using a reference case of $G_p = 3$ MPa, $G_t = 773$ K, $D_p = 25$ µm, $D_t = 2.5$ mm, and SoD = 25 mm. A total of nine structured meshes, G1−G9, were examined, with grid sizes ranging from 6.35×10^4 to 26.28×10^4 elements, as summarized in Table 3.3. Progressive mesh refinement increased PV and decreased PT toward asymptotic values. Beyond mesh G6 (20.90×10^4 elements), PV

and PT variations were limited to $\leq 0.006\%$ and $\leq 0.123\%$, respectively. Therefore, G6 was selected as the reference grid.

Table 3.3 Grid-independence results corresponding to $G_p = 3$ MPa, $G_t = 773$ K, $D_p = 25$ μm, $D_t = 2.5$ mm, and SoD = 25 mm

Grid	No. of elements ($\times 10^4$)	PV (m/s)	PT (K)	Change on refinement (%)	
				PV	PT
G1	6.35	604.8	415.7	1.035	1.516
G2	8.18	611.1	409.4	0.896	0.513
G3	10.61	616.5	408.3	0.524	0.294
G4	13.89	619.7	407.1	0.373	0.197
G5	16.60	622.1	406.3	0.191	0.197
G6	20.90	623.2	405.5	0.003	0.049
G7	22.81	623.2	405.3	0.006	0.099
G8	25.01	623.3	404.9	0.002	0.123
G9	26.28	623.1	405.4	--	--

The mesh-quality behavior of the grid is presented in Figure 3.6(a), where orthogonality remained high, while skewness decreased with increasing grid refinement. In Figure 3.6(b), velocity contours for three representative meshes, G1, G6, and G9, show that the jet structure and shock-cell pattern were already well resolved at G6, with negligible change up to G9. Thus, the selected mesh was considered sufficiently refined for the subsequent simulations.

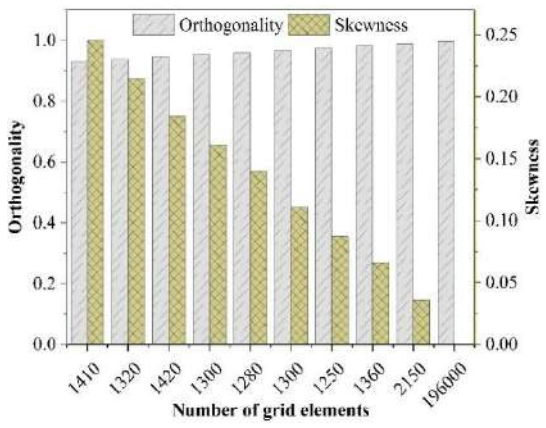

(a)

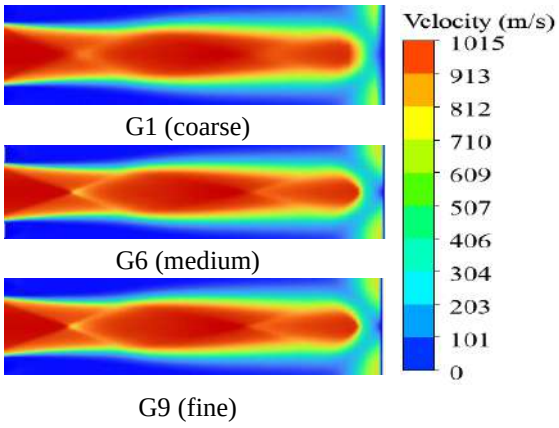

(b)

Figure 3.6 (a) Mesh quality metrics and (b) shock resolution with refinement

For the subsequent numerical simulations, a moderately refined structured quadrilateral mesh, generally in the range of $1.71 - 2.18 \times 10^4$ elements depending on the selected geometric configuration, was retained as the final mesh level. This mesh range preserved the grid-independent behavior established by the reference case while maintaining an effective balance between numerical accuracy and computational cost. It was also sufficient to provide stable predictions of the principal responses under variations in nozzle dimensions and operating conditions. The numerical model was validated against reported experimental measurements under comparable operating conditions. The validation was carried out in a stepwise manner so that the gas-phase flow field, substrate-side thermal response, particle-velocity trend, and particle thermal response could all be examined before using the model for further numerical analysis. The complete validation set is presented in Figure 3.7.

1. Gas-phase validation: In the first step, the gas-phase supersonic jet structure was validated by comparing the predicted shock and expansion features with a reported flow-visualization study. As shown in Figure 3.7(a), the predicted nozzle-jet field reproduced the main oblique-shock, expansion-fan, Mach-disk, and jet-boundary features in close agreement with the reported pattern.

2. Substrate thermal validation: In the second step, the predicted substrate thermal response was validated by comparing the surface temperature at the center and edge locations for SoD = 10, 30, and 50 mm in Figure 3.7(b). The maximum deviation for substrate temperature was reported as 4.7%.

3. Particle-velocity validation under different operating conditions: In the third step, the validation was extended to the particle phase by comparing PV trends for a fixed representative particle size and a polydisperse injection defined through the Rosin-Rammler function. As shown in Figure 3.7(c), the predicted PV trends followed the

experimentally reported variation with gas pressure, with maximum deviations of 4.2% for the polydisperse case and 9.1% for the monodisperse case.

4. Particle velocity and particle temperature validation across different particle sizes: In the last step, the predicted PV and PT were compared with the corresponding experimental measurements as a function of particle size. As shown in Figure 3.7(d), the numerical model reproduced both trends satisfactorily, with deviations of 2.7% for PV and 6.8% for PT. Overall, the adopted CFD model provides a reliable numerical basis for the subsequent analysis.

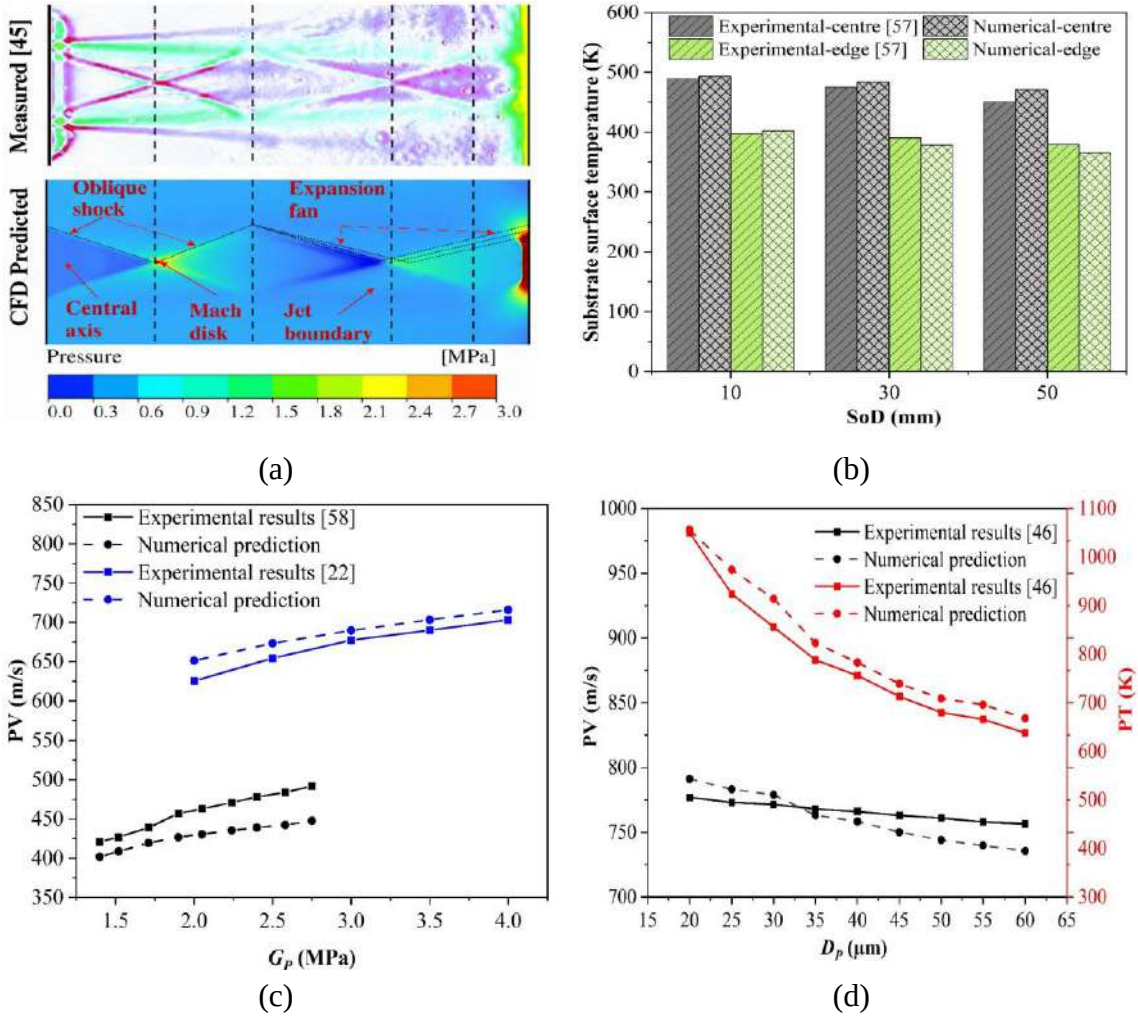

Figure 3.7 Model validation against literature measurements: (a) comparison of supersonic jet/shock features [88], (b) substrate surface temperature at different SoD

values [32], (c) PV at various G_p values under comparable conditions [29], [79], and (d) PV and PT across different D_p values compared with experiments [89]

3.5 Methodology for Nozzle Design Optimization

The nozzle-design optimization in the present work was carried out using a MOO methodology to improve the performance of the CD nozzle in CS. The procedure involved CFD simulations, FCCD, RSM, ANN, and NSGA-II using GA in an optimization framework. The key nozzle geometric parameters were chosen as design parameters. The major performance responses were obtained from CFD results, and the data were used to develop predictive models and determine the optimum nozzle design, as illustrated in Figure 3.8. The methodology was structured into two optimization approaches. The first approach involved the use of FCCD design points and response surface models for prediction and optimization by the RSM-DF method. In the second approach, the same CFD data set was used to train the ANN model and was then coupled with NSGA-II for the MOO of PV, PT, HF, and SP.

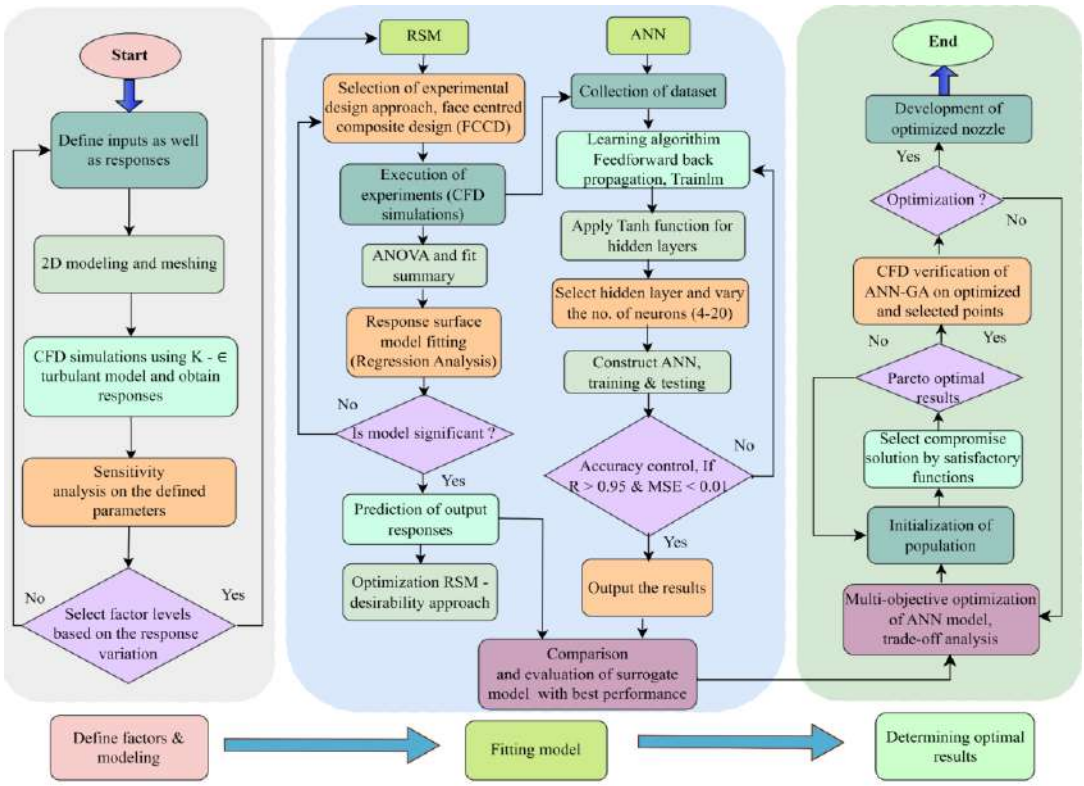

Figure 3.8 Flowchart detailing the optimization process for nozzle design

3.5.1 Selection of Input Variables and Sensitivity Analysis

The nozzle design variables were selected to represent the geometric parameters that most strongly affect gas expansion, flow development, particle acceleration, particle temperature, and near-substrate responses in the CD nozzle. Therefore, L_c, L_d, D_{id}, L_i, and D_e were retained as the principal design variables. The convergent section affects gas acceleration and pressure distribution, the divergent section controls gas expansion and supersonic flow, injector dimensions influence particle acceleration and temperature, and the nozzle exit affects Mach number and particle dynamics. The selected geometric parameters and associated responses are illustrated in Figure 3.9.

To preserve a common baseline configuration during optimization, the remaining geometric parameters, D_i, L, D_t, D_{od}, and SoD, were retained as fixed parameters. Before

defining the final design levels for the DOE, a one-at-a-time sensitivity analysis was carried out. Each design variable was sequentially divided into eleven equal segments, while the remaining parameters were kept fixed at the baseline condition. Range selection was made primarily on the basis of PV [44], [90]. During this screening stage, the mean of the maximum and minimum values of each geometric parameter was taken as the center value for the subsequent FCCD.

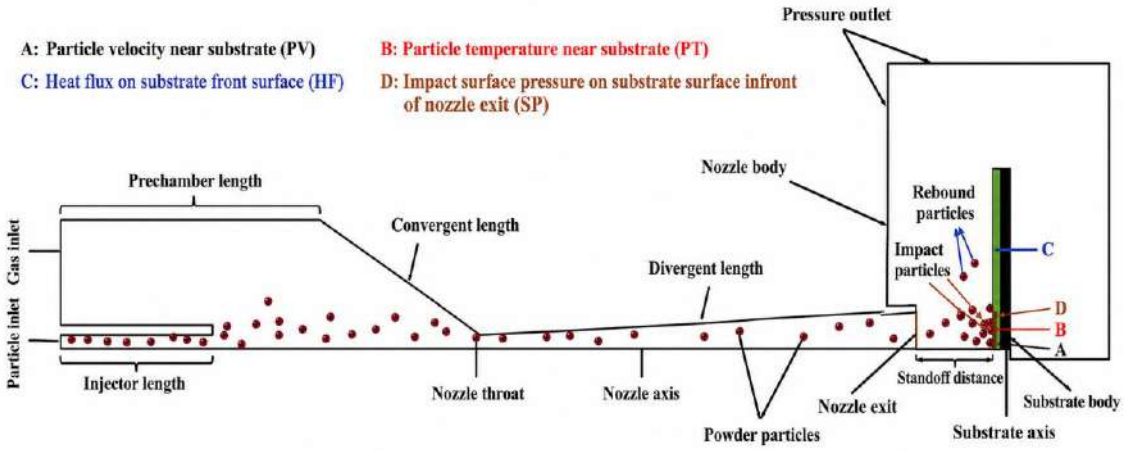

Figure 3.9 Detailed illustration of key geometric parameters and associated responses in an axisymmetric 2D CD nozzle

3.5.2 FCCD and CFD Data Generation

A three-level FCCD was used to define the design space for nozzle optimization. FCCD was chosen because it maintains the design points within realistic geometric boundaries and is efficient in capturing linear, quadratic, and interaction effects. The center values were determined from the sensitivity analysis and the chosen nozzle design variables were set at three levels as shown in Table 3.4. These levels maintained a practically bounded geometric range and provided the numerical design matrix for the subsequent CFD simulations.

Table 3.4 RSM factor levels for key nozzle design parameters at three levels

	L_c (mm)	L_d (mm)	D_{id} (mm)	L_i (mm)	D_e (mm)
Level 1	20	70	1	10	6.4

Level 2	55	185	2	20	7.25
Level 3	90	300	3	30	8.1

Once the FCCD design matrix was created, numerical responses for each design point were obtained by using CFD simulations in ANSYS Fluent. The design variables were varied at the coded levels of the FCCD, while the other nozzle parameters and operating conditions were kept at their baseline values. PV, PT, HF, and SP near the substrate surface were extracted for each design point. The generated CFD dataset consisted of 50 design points, and this response set was used for the subsequent RSM-DF and ANN-GA optimization stages. The complete FCCD matrix with corresponding CFD-generated responses is included as Supplementary Table A1 in Appendix A.

3.5.3 Optimization Framework

The CFD-generated dataset was used to develop surrogate models for nozzle-design optimization. In the first approach, RSM was used to establish regression-based relationships between the selected nozzle design variables and the corresponding responses. The general second-order polynomial model was used because it can represent linear, quadratic, and interaction effects among the design variables [81], [91]. The model is expressed as:

A second-order model was applied and expressed as

$$Y = f(x_1, x_2, \cdots, x_n) + \epsilon \tag{3.25}$$

The second-order polynomial model is written as

$$Y = \beta_0 + \sum_{i=1}^{k} \beta_i X_i + \sum_{i=1}^{k} \beta_{ii} X_i^2 + \sum_{i=1}^{k} \sum_{j=i+1}^{k} \beta_{ij} X_i X_j + \epsilon \tag{3.26}$$

where Y is the response, $x_1, x_2, \ldots, x_n$ are the design parameters, ε represents the random error term, β_0 is the intercept, β_i is the linear coefficient, β_{ii} is the quadratic coefficient, β_{ij} is the interaction coefficient, and X_i and X_j are the coded values of the design variables.

Thus, the RSM formulation converted the CFD response dataset into a predictive mathematical framework for subsequent analysis of nozzle-design effects and optimum-design determination.

The ANN model was developed to establish a nonlinear predictive relationship between the selected nozzle design variables and the CFD-generated responses. In the present study, the MATLAB neural network fitting tool was used to model and validate the numerical dataset obtained from the FCCD design points. The ANN structure, which works similarly to brain neurons, was used to predict the responses by analyzing the CFD-generated outcomes, and the architecture mapping structure is presented in Figure 3.10.

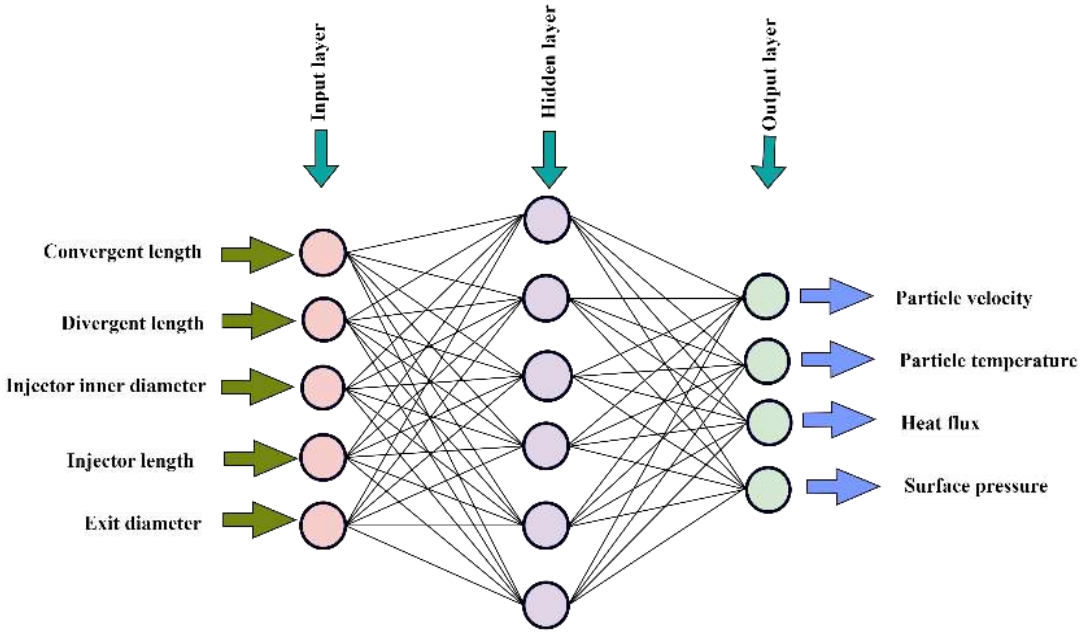

Figure 3.10 ANN architecture mapping structure

The neurons are linked through synaptic weights and trained using suitable transfer and training functions to predict the responses. The ANN selection procedure and the resulting network topology are shown in Figure 3.11(a-b).

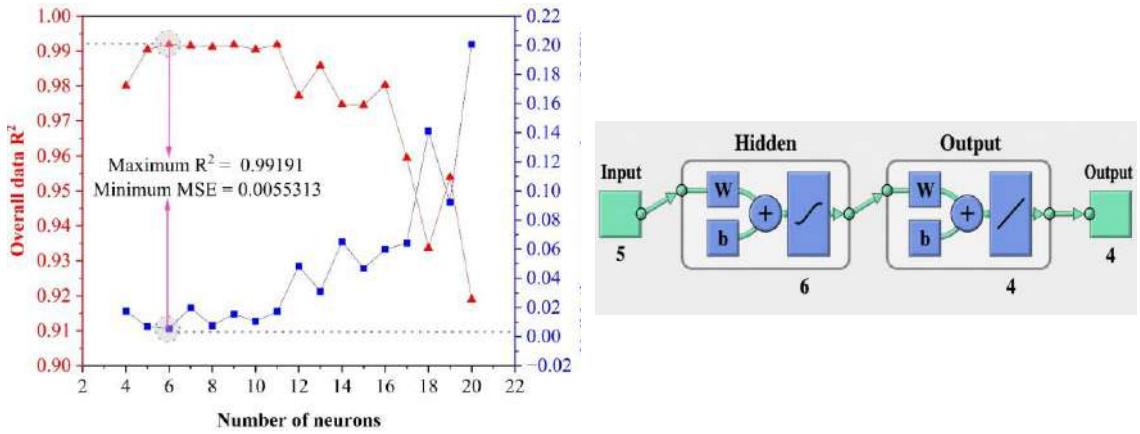

(a) (b)

Figure 3.11 Graphs representing the ANN model (a) MSE and overall R^2 with the number of neurons in the hidden layer, (b) ANN topology

As summarized in Table 3.5, the developed ANN model consisted of five input variables, four output responses, and one hidden layer. The number of neurons in the hidden layer was varied from 4 to 20, and the model was optimized by starting with the minimum number of neurons and then gradually increasing the number of neurons while examining the mean square error (MSE) and correlation coefficient at each stage. The best number of neurons for the trainlm algorithm was found to be 6. Therefore, the final network topology was retained as 5-6-4. The dataset was randomly divided into 70% for training, 15% for testing, and 15% for validation. The training function was Levenberg-Marquardt (trainlm), the adaptation learning function was LEARNGDM, the transfer function was Hyperbolic Tangent Sigmoid (tansig), and the performance function was MSE.

Table 3.5 Detailed specification of the ANN structure

Network	5 inputs, 4 output, and one hidden layer with 6 neurons (5-6-4)
Training algorithms	Feedforward back propagation
Data (randomly selected)	Training: 70%; Test: 15%; Validation: 15%
Training function	Levenberg- Marquardt (Trainlm) training function
Adaptation learning function	LEARNGDM
Transfer function	Hyperbolic Tangent Sigmoid (Tanh):

Performance function	MSE
Stopping criteria	Stop the network training when the validation error starts increasing

Before training, the data were normalized in the range of −1 to 1 so that all input features had similar scales. The normalized data relationship used in the present work is given as:

$$\text{Normalized data} = \frac{2(X_A - X_{min})}{(X_{max} - X_{min})} - 1 \tag{3.27}$$

where X_A is the actual value, $X_{\min}$ is the minimum value, and $X_{\max}$ is the maximum value of the selected factors and responses.

The maximum number of epochs was set to 1000, while training was stopped earlier if the validation error began to increase to prevent overfitting and improve generalization [91]. In this way, the ANN model provided a nonlinear surrogate framework for the subsequent optimization stage.

The predictive performance of the developed RSM and ANN models was evaluated by comparing the model-predicted values with the corresponding CFD-computed values. The statistical error metrics used for this comparison were mean absolute error (MAE), root mean square error (RMSE), mean absolute percentage error (MAPE), correlation coefficient (R), coefficient of determination (R^2), and Nash-Sutcliffe efficiency (NSE), as defined in Eqs. (3.28−3.33) [92].

$$\text{MAE} = \frac{1}{n}\sum_{i=1}^{n}\left|u_{i,predicted} - u_{i,simulated}\right| \tag{3.28}$$

$$\text{RMSE} = \sqrt{\frac{\sum_{i=1}^{n}\left(u_{i,predicted} - u_{i,simulated}\right)^2}{n}} \tag{3.29}$$

$$\text{MAPE} = \left[\sum_{i=1}^{n}\left|\frac{u_{i,simulated} - u_{i,predicted}}{u_{i,simulated}}\right|\right] \times \frac{100}{n}\ \% \tag{3.30}$$

$$R = \sqrt{\left[1 - \frac{\sum_{i=1}^{n}\left(u_{i,simulated} - u_{i,predicted}\right)^2}{\sum_{i=1}^{n}\left(u_{i,predicted}\right)^2}\right]} \quad (3.31)$$

$$R^2 = \left[1 - \frac{\sum_{i=1}^{n}\left(u_{i,simulated} - u_{i,predicted}\right)^2}{\sum_{i=1}^{n}\left(u_{i,predicted}\right)^2}\right] \quad (3.32)$$

$$NSE = \left[1 - \frac{\sum_{i=1}^{n}\left(u_{i,simulated} - u_{i,predicted}\right)^2}{\sum_{i=1}^{n}\left(u_{i,simulated} - u_{mean,simulated}\right)^2}\right] \quad (3.33)$$

where $u_{i,\text{predicted}}$ and $u_{i,\text{simulated}}$ are the predicted and CFD-computed values of the i^{th}data point, n is the total number of data points, and $\bar{u}_{\text{simulated}}$ is the mean of the CFD-computed values.

The comparative analysis across all response variables was performed to examine how closely the RSM and ANN predictions matched the CFD values under all design-point cases. In this framework, lower values of MAE, RMSE, and MAPE, together with higher values of R, R^2, and NSE, indicated better predictive agreement with the CFD data and supported the selection of a suitable model for nozzle-design optimization

After the ANN model had achieved satisfactory prediction accuracy, it was integrated with the GA for MOO of the nozzle design variables. In the present work, NSGA-II was used to identify non-dominated solutions under conflicting response conditions. The trained ANN model was used as a surrogate, and optimization was carried out to obtain improved combinations of L_c, L_d, D_{id}, L_i, and D_e.

The NSGA-II algorithm was implemented using a double-vector population type, a population size of 1000, a uniform creation function, crossover fraction of 0.8, adaptive feasible mutation function, intermediate crossover function, and a maximum generation of 1000**.** The lower and upper bounds for the selected design variables were taken as [20, 70, 1, 10, 6.4] and [90, 300, 3, 30, 8.1]**,** respectively. The adopted ANN-GA framework was used to optimize PV, PT, HF, and SP simultaneously. Since these responses do not

improve in the same direction, NSGA-II was employed to generate Pareto-optimal solutions, and a total of 350 solutions were identified.

3.5.4 Selection of Optimum Nozzle Design

The optimum nozzle design was selected on the basis of multi-objective criteria in which PV and HF were maximized [20], [32], [45], SP was minimized [51], and PT was controlled with respect to the 415 K reference for 25 μm Cu particles [19], [35], [67]**.** The final design was not selected on the basis of a single response; rather, it was determined by considering the combined influence of all selected responses. For the RSM approach, the solution was identified through the desirability function (DF) method, whereas for the ANN-based approach, the trained ANN model was integrated with NSGA-II to generate non-dominated solutions. The selected design was then retained for further numerical verification, while the detailed optimum values, comparative performance, and response improvements are presented in Section 4.3.

3.6 Methodology for Process Parameter Optimization

The methodology for process parameter optimization was developed to identify the operating and nozzle-design conditions that provide high PV, controlled PT and reduced RD in HPCS. In this stage, G_p, G_t, D_p, D_t, and SoD were studied within an acceptable CS parameter range using Cu powder. The process-parameter optimization was established as a multi-objective framework as the selected responses do not improve in the same direction under all operating conditions; therefore, a compromise-based optimization method was required [93]. The overall process-optimization framework started with the selection of input variables and objective functions, FCCD to generate design points, CFD simulations for response generation, and RSM for surrogate-model development. The statistically adequate response models were then optimized by NSGA-II to obtain the Pareto-optimal solutions, and the best compromise solution was obtained using TOPSIS and VIKOR with a hybrid AHP-EWM weighting scheme. The entire methodological

sequence followed in the present process-parameter optimization is shown in Figure 3.12 [81].

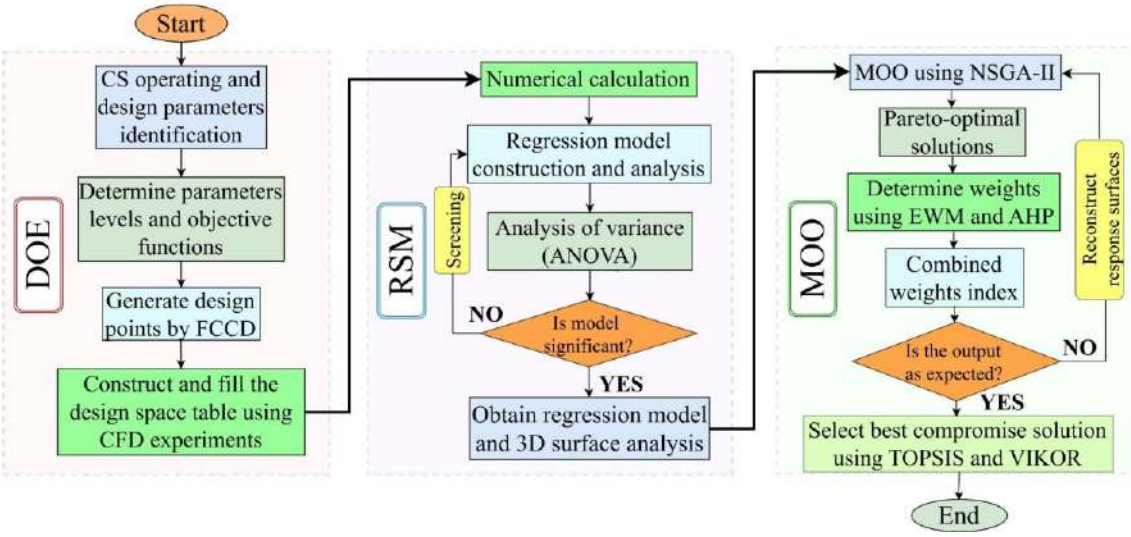

Figure 3.12 Multi-objective optimization flowchart

3.6.1 Selection of Input Variables and Design Matrix

The process variables were selected to represent the key operating and design conditions that govern gas-particle dynamics near the substrate. Accordingly, G_p, G_t, D_p, D_t, and SoD were considered as the principal variables in the present study. These variables were selected because G_p and G_t control particle acceleration and thermal conditions, D_p governs particle inertia and heat-transfer response, D_t affects gas-jet expansion and particle focusing, and SoD controls near-substrate interaction and plume spreading. The HPCS system considered in the present work, together with the key operating and design parameters, is illustrated in Figure 3.13, whereas the coupled gas-particle flow field, boundary conditions, and near-substrate computed responses are shown in Figure 3.14. The response variables were selected in accordance with the objective of obtaining high PV, controlled PT, and reduced RD.

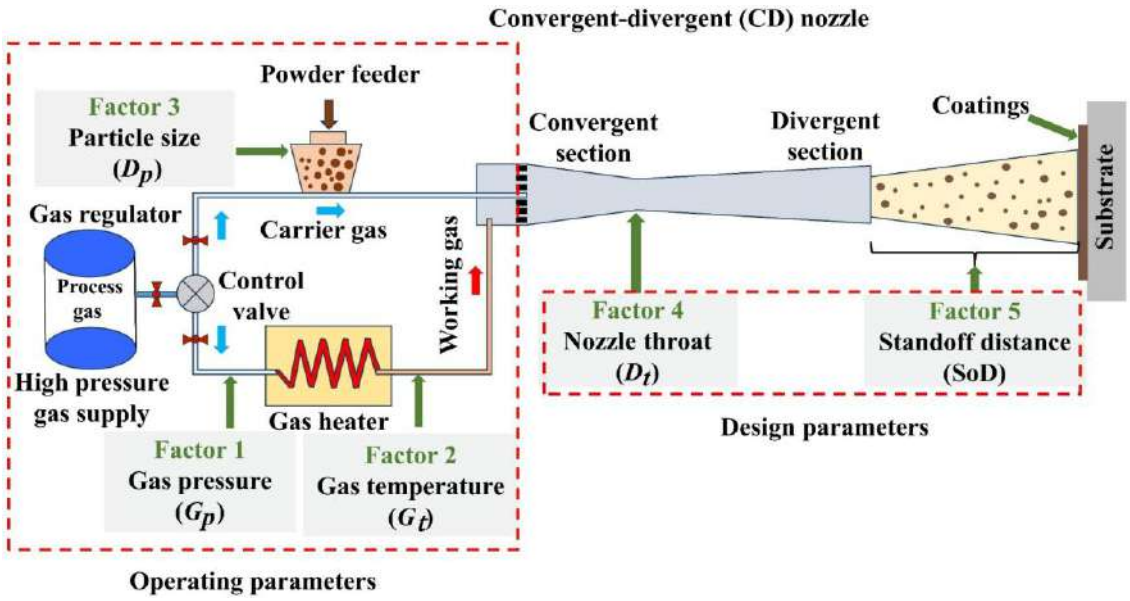

Figure 3.13 Schematic of the HPCS system highlighting the key operating parameters and design parameters

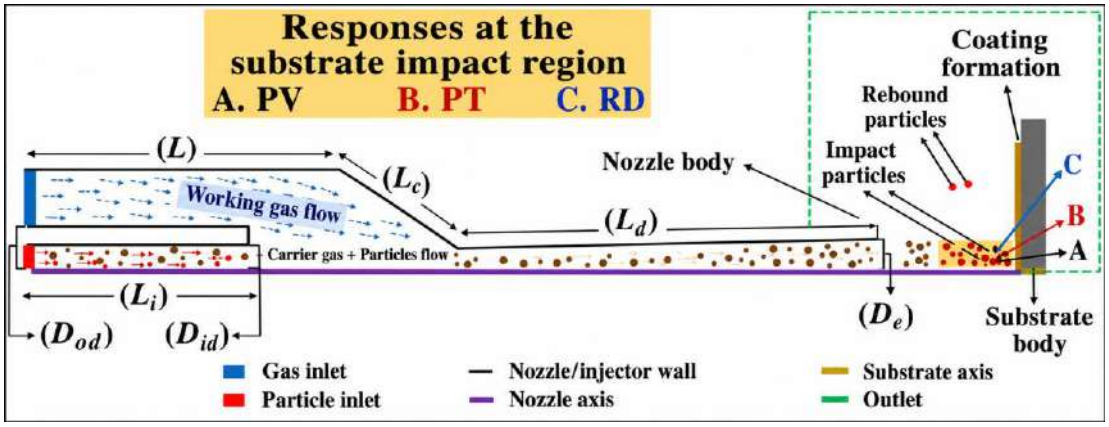

Figure 3.14 2D axisymmetric nozzle's boundary conditions for coupled gas-particle flows and responses (not to scale)

A reference case was defined to establish a consistent basis for the subsequent process-parameter optimization. In the present study, the reference condition was taken as $G_p = 3$ MPa, $G_t = 773$ K, $D_p = 25$ µm, $D_t = 2.5$ mm, and SoD $= 25$ mm, because these values represent mid-range operating conditions capable of producing stable supersonic flow and

effective particle acceleration. This condition was used as the reference for comparing optimized cases so that the changes in PV, PT, and RD could be interpreted.

For the process-optimization stage, the particle phase was represented in two forms. First, a fixed representative D_p was used in the FCCD design matrix, where $D_p = 5, 25, \text{and } 45$ μm were retained as the three monodisperse levels. Second, the particle-size distribution was represented by a Rosin-Rammler distribution over the range of $2 - 75$ μm. As summarized in Table 3.6, the three factor levels were defined to maintain practically bounded process ranges while preserving the significant response window of each parameter. On this basis, the FCCD generated the numerical design matrix used for the subsequent CFD simulations and later RSM modeling of PV, PT, and RD [81].

Table 3.6 Levels of input parameters used for the FCCD design

S. No.	Input parameters	Level		
		-1	0	1
1	Gas inlet pressure, MPa	2	3	4
2	Gas inlet temperature, K	633	773	913
3	Particle size, μm	5	25	45
4	Nozzle throat diameter, mm	2.5	3.25	4
5	Standoff distance, mm	10	25	40

3.6.2 CFD Data Generation and Response Surface Modeling

After establishing the FCCD for the selected process parameters, numerical data corresponding to the design points were generated through CFD simulations in ANSYS Fluent**.** In this stage, the input variables were varied according to the coded levels of the FCCD, while the remaining boundary conditions, material system, and numerical settings were retained at the baseline values. For each design point, PV, PT, and RD were extracted as response variables. In this way, the process design matrix was converted into a numerical response dataset for the later RSM, NSGA-II, and MCDM stages.

The generated CFD dataset consisted of 50 design points, including factorial, face-centered, and center points. The corresponding simulation results were used to build regression models for PV, PT, and RD**.** The complete FCCD matrix with the CFD-generated responses is presented as Supplementary Table A2 in Appendix A.

RSM was then used to develop regression models for the three selected responses from the FCCD-CFD dataset. Separate response models were fitted for PV, PT, and RD as functions of G_p, G_t, D_p, D_t, and SoD, so that the linear, quadratic, and interaction effects of the process parameters on particle acceleration, thermal response, and dispersion could be captured.

Before fitting the regression model for RD, the radial spread of particles at the substrate plane was defined from the DPM particle-tracking coordinates. As illustrated in Figure 3.15, RD represents the lateral spread of particles from the jet centerline at the substrate and is directly related to coating-footprint uniformity, deposition precision, and overspray control [94]. The RD was calculated as:

$$\mathrm{RD} = \left[\frac{1}{N}\sum_{i=1}^{N}\{R_i(x) - R_i(0)\}^2\right]^{1/2} \tag{3.34}$$

where $i = 1,2,3,\ldots,N$, $R_i(x)$and $R_i(0)$ denote the radial positions of the ith particle at distance x and at injection, respectively, and N is the total number of tracked particles.

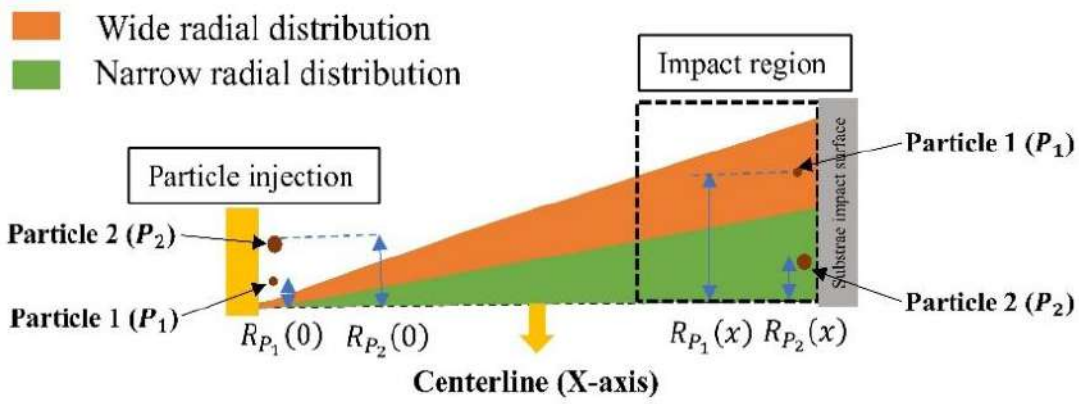

Figure 3.15 Schematic of particle RD showing trajectories from injection to the substrate plane (not to scale)

Thus, the FCCD-CFD dataset combined with the second-order response model provided the predictive basis for the later ANOVA-based model adequacy assessment, NSGA-II optimization, and TOPSIS- and VIKOR-based compromise ranking [69].

3.6.3 Optimization and Ranking Procedure

After the regression models for PV, PT, and RD had been established, the MOO was carried out using NSGA-II. This algorithm was adopted because it provides an effective trade-off between solution diversity and convergence and is capable of handling conflicting responses that cannot be optimized concurrently using a single-objective method. In the present work, the optimization framework was implemented in MATLAB, and the adopted procedure is illustrated in Figure 3.16. The objective problem was formulated as:

$$\text{Minimize: } F(x) = [-PV(x), |PT(x) - 415|, RD(x)] \quad (3.35)$$

$$\text{Subject to: } x = [G_p, G_t, D_p, D_t, \text{SoD}] \quad (3.36)$$

with parameter ranges as:

$$(2 \le G_p \le 4)\ \text{MPa},\ (633 \le G_t \le 913)\ \text{K},\ (5 \le D_p \le 45)\ \mu\text{m}, \quad (3.37)$$

$(2.5 \le D_t \le 4)$ mm, and $(10 \le \text{SoD} \le 40)$ mm.

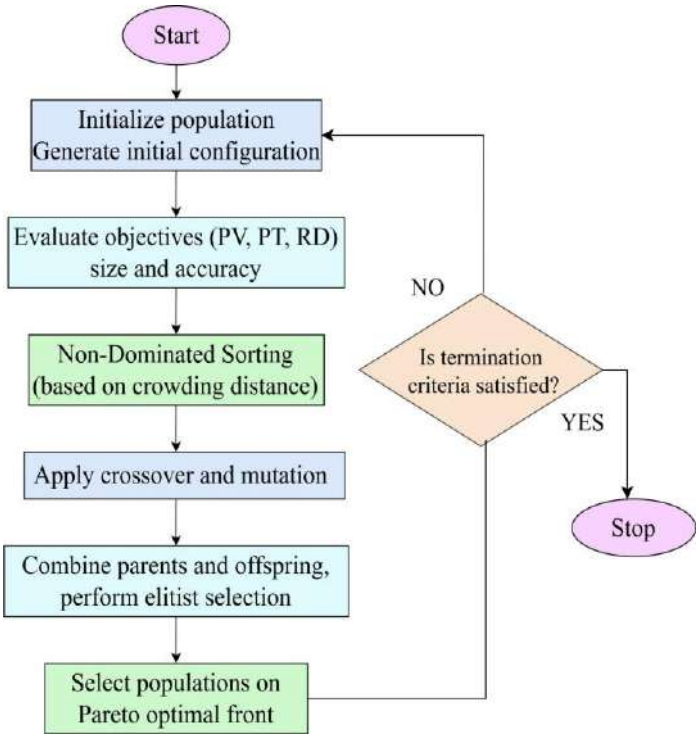

Figure 3.16 NSGA-II workflow used in this study

Before fixing the final algorithm settings, the convergence and diversity of the NSGA-II search were examined through a generation test up to **1**000 generations. As illustrated in Figure 3.17, the average distance between individuals stabilized after approximately 400–500 generations, indicating that 500 generations were sufficient to obtain stable results. Accordingly, the final NSGA-II settings were retained as population size = 500, Pareto fraction = 0.35, crossover rate = 0.8, mutation rate = 0.2, and stall generation limit = 500. In this way, the NSGA-II stage captured the trade-offs between PV, PT, and RD and generated the Pareto-optimal solution set for the selected process parameters. The obtained Pareto solutions were then carried forward for TOPSIS, VIKOR, and hybrid AHP-EWM based compromise ranking, where the combined criteria weights (ω_{Mi}) were applied before ranking the alternatives.

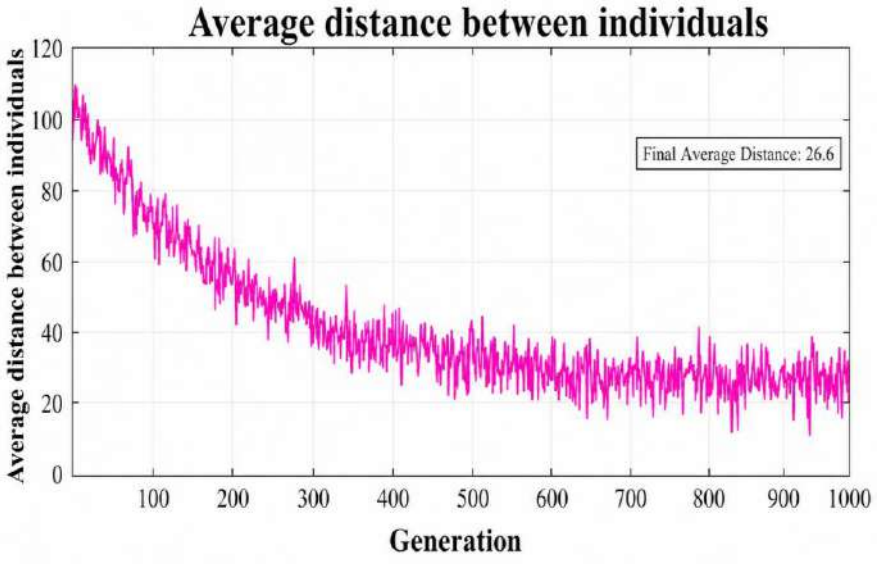

Figure 3.17 Average distance convergence over generations

In the TOPSIS procedure, the decision matrix for m alternatives and n objectives were first defined as

$$X = \left(x_{ij}\right)_{m\times n} \{i = 1,2, \dots \dots m; j = 1,2, \dots \dots, n\} \quad (3.38)$$

The matrix was then normalized as

$$r_{ij} = \frac{x_{ij}}{\sqrt{\sum_{i=1}^{m} x_{ij}^2}} \quad (3.39)$$

and the weighted normalized matrix was written as

$$v_{ij} = \omega_{Mi} r_{ij} \{i = 1,2, \dots \dots m; j = 1,2, \dots \dots, n\} \quad (3.40)$$

where ω_{Mi} is the weight of the jth element and $\sum \omega_{Mi} = 1$.

The positive ideal solution (PIS) and negative ideal solution (NIS) were then determined as

$$A_j^+ = \left\{\langle min\left(v_{ij}|i = 1,2, \dots., m|\right) j \in J_-\rangle, \langle max\left(v_{ij}|i = 1,2, \dots., m|\right) j \in J_+\rangle\right\} \quad (3.41)$$

$$A_j^- = \{\langle max(v_{ij}|i = 1,2, \dots ., m|)\, j \in J_-\rangle, \langle min(v_{ij}|i = 1,2, \dots ., m|)\, j \in J_+\rangle\} \quad (3.42)$$

where J^- and J^+ denote the cost and benefit criteria, respectively. The Euclidean distances from the PIS and NIS were calculated as

$$d_i^+ = \sqrt{\sum_{j=1}^{n} \left(v_{ij} - A_j^+\right)^2} \quad i = 1,2, \dots \dots, m \quad (3.43)$$

$$d_i^- = \sqrt{\sum_{j=1}^{n} \left(v_{ij} - A_j^-\right)^2} \quad i = 1,2, \dots \dots, m \quad (3.44)$$

and the relative closeness to the ideal solution was obtained from

$$s_i = \frac{d_i^-}{d_i^+ + d_i^-} \quad (3.45)$$

Accordingly, the best compromise solution in TOPSIS was identified as

$$A_{final} = A \in max(s_i) \quad (3.46)$$

Thus, the TOPSIS method ranked the Pareto solutions according to their closeness to the ideal response combination.

In the VIKOR procedure, the Pareto alternatives were evaluated using the utility measure (S_i), regret measure (R_i), and compromise index (Q_i). These were written as

$$S_i = \sum_{j=1}^{n} \omega_{Mi} \frac{x_j^+ - x_{ij}}{x_j^+ - x_j^-} \quad (3.47)$$

$$R_i = \max_j \left(\omega_{Mi} \frac{x_j^+ - x_{ij}}{x_j^+ - x_j^-} \right) \quad (3.48)$$

$$Q_i = \mathrm{v}. \frac{S_i - S^*}{S^* - S^-} + (1 - v). \frac{R_i - R^*}{R^* - R^-} \quad (3.49)$$

where S^*, S^-, R^*, and $R^-$are the best and worst values of S_i and R_i, respectively, and v is the weight factor satisfying $0 < v < 1$.

In this way, the VIKOR method evaluated the compromise among the conflicting objectives and identified a practically balanced solution from the Pareto set. Therefore, TOPSIS and VIKOR provided the decision-analysis stage of the present process-parameter optimization framework.

The criteria weights used in the decision-analysis stage were determined by combining AHP and EWM. This hybrid weighting procedure was adopted to obtain a balanced weighting mechanism for the three selected responses. In this framework, AHP was used to assign the subjective weights through pairwise comparison of the criteria, whereas EWM was used to assign objective weights on the basis of data dispersion. By combining both approaches, the final weighting scheme reduced excessive subjectivity and improved the reliability of the ranking procedure used in TOPSIS and VIKOR [95].

In the AHP procedure, the problem was first organized into a hierarchy and pairwise comparisons were made using the Saaty scale (1–9) [96]. A judgment matrix was then established and the criteria weights were calculated as

$$\omega_{Ai} = \frac{1}{n}\sum_{j=1}^{n} \frac{a_{ij}}{\sum_{k=1}^{n} a_{kj}} (j = 1, 2, \dots\dots\dots, n) \tag{3.50}$$

where ω_{Ai}, n, and a_{ij} are the weight for criterion i, the number of criteria, and the judgment-matrix element, respectively. The consistency of the judgment matrix was assessed through the consistency ratio (CR), and $\mathrm{CR} < 0.1$ was taken as acceptable consistency for the present weighting procedure.

In the EWM procedure, the criteria weights were assigned objectively from the variation in the decision data. The entropy of each criterion was written as:

$$E_j = -k\sum_{i=1}^{m} p_{ij} ln(p_{ij}) (j = 1, 2, \dots\dots\dots, n) \tag{3.51}$$

and the corresponding entropy weight was determined as:

$$\omega_{Ei} = \frac{1 - E_j}{\sum_{j=1}^{n}(1 - E_j)} \tag{3.52}$$

where p_{ij}, E_j, ω_{Ei}, and k are the normalized value of the ith alternative for the jth criterion, the entropy of the criterion, the weight of criterion j, and the constant $k = 1/\ln(m)$, respectively. Since the entropy weight depends on the degree of information provided by the criterion values, this method minimized bias and reflected the actual variations.

To improve the objectivity of the index weights, the EWM-based objective weights were used to modify the AHP-derived subjective weights. The final combined weight was calculated as:

$$\omega_{Mi} = \frac{\sqrt{\omega_{Ai} \times \omega_{Ei}}}{\sum_{i=1}^{n}\sqrt{\omega_{Ai} \times \omega_{Ei}}} \tag{3.53}$$

where ω_{Mi} is the combined weight of the ith criterion. In this way, the final hybrid weights retained both expert preference and data-driven variation, and these combined weights were then used in the subsequent TOPSIS and VIKOR procedures for ranking the Pareto-optimal solutions and identifying the best-compromise process condition.

3.6.4 Selection of Optimum Process Condition

The optimum process condition was selected after the Pareto-optimal solutions generated using NSGA-II were ranked through TOPSIS and VIKOR using the combined criterion weights obtained from the AHP-EWM procedure. In the present work, the final selection was not based on a single response; rather, it was carried out by considering the combined requirement of high PV [20], controlled PT [19], [67], and low RD [30]. In this way, the optimum condition was identified as a best-compromise solution within the Pareto set [81]. The preferred alternatives obtained from TOPSIS and VIKOR were then used for further numerical verification under the same CFD framework, as presented in Section 4.4.

3.7 Grey Relational Analysis (GRA) Based Optimization

The methodology adopted in this stage was developed to identify the most favorable process condition by considering PV and PT simultaneously in HPCS. In this approach, ΔP, D_p, ER, and T_c were treated as the principal process parameters, because these factors directly govern particle acceleration, gas expansion, particle heating, and in-flight thermal-kinetic behavior. Since high PV and controlled PT do not necessarily occur at the same parameter combination, a multi-response optimization framework was required. Therefore, the process optimization was carried out by integrating CFD simulations, FCCD, GRA, and RSM in a logically connected sequence [97]. In this framework, PV and PT were combined into a single performance index through the GRG [67].

3.7.1 Selection of Parameter Levels and Response Generation

The factors selected for the present process optimization were ΔP, D_p, ER, and T_c. These factors were selected because ΔP affects powder injection, D_p strongly influences particle acceleration and thermal response, ER controls gas expansion and shock structure, and T_c governs particle heating. Thus, these parameters represent the main thermal-fluid and particle-related conditions required to examine the combined effects of process variables on CS performance. The response variables were selected as PV and PT because high PV and adequate PT are critical for achieving favorable particle bonding without melting. The factor levels used in the present study are summarized in Table 3.7 and provide the basis for the subsequent FCCD, CFD simulations, GRA, and RSM-based optimization.

Table 3.7 Parameters and their levels

Parameters	**ΔP (MPa)**	**D_p (μm)**	**ER**	**T_c (K)**
Level 1	0.1	5	6	300
Level 2	0.2	25	8	450
Level 3	0.3	45	10	600

The CFD response data were generated using the 2D axisymmetric numerical framework described in Section 3.4.1. In this stage, ΔP, D_p, ER, and T_c were varied according to the adopted design matrix, and a total of 32 numerical cases were solved. The complete design matrix with the corresponding CFD-generated PV and PT values is presented as Supplementary Table A3 in Appendix A.

3.7.2 Data Normalization and GRA Formulation

The CFD-generated values of PV and PT were first converted into dimensionless form before applying GRA. This normalization step was necessary because the two responses have different units and optimization requirements. In the present study, PV was treated by the higher-the-better criterion because higher PV enhances impact energy and bonding strength, whereas PT was treated by the target-the-better criterion with a desired value of $x_{\text{target}} = 415$ K to achieve sufficient thermal softening without oxidation or thermal degradation.

For PV, higher-the-better the normalized value was calculated as

$$x_1^* = \frac{x_i - min(x)}{max(x) - min(x)} \tag{3.54}$$

For PT, the target-the-better normalization was written as

$$x_k^* = 1 - \frac{|x_i - x_{target}|}{max(|x_i - x_{target}|)} \tag{3.55}$$

where x_i is the original response value.

Thus, both responses were scaled between 0 and 1, and values closer to 1 represented more favorable conditions. After normalization, the GRC values were computed using the distinguishing coefficient $\zeta = 0.5$ as:

$$\xi_i(k) = \frac{\Delta_{min} + \zeta.\Delta_{max}}{\Delta_i(k) + \zeta.\Delta_{max}} \tag{3.56}$$

where $\Delta_i(k)$ is the absolute deviation between the reference sequence and the normalized data, and Δ_{min}, Δ_{max} are the minimum and maximum values of the deviation sequence, respectively. In this way, normalization and GRC calculation converted PV and PT comparable grey relational values for subsequent GRG formulation.

After calculating the GRC for PV and PT, the overall performance of each design point was expressed through the GRG. In the present study, GRG was taken as the arithmetic mean of the individual GRC values of the selected responses, so that the multi-response problem could be converted into a single performance index. The GRG was calculated as

$$\mathrm{GRG} = \frac{1}{n}\left(\sum_{i=1}^{n} \mathrm{GRC}\right) \tag{3.57}$$

where n is the total number of responses and $\mathrm{GRC_i}$ is the grey relational coefficient of the ith response. Since two responses were considered in the present work, the computed GRG represented the combined effect of PV and PT for each simulation run. Higher GRG values indicate closer proximity to the ideal response condition and therefore reflect more favorable process performance.

After computing the GRG for all the design points, the runs were arranged in descending order of GRG, while the corresponding raking sequence was expressed as the grey order. Further, RSM was applied to establish the predictive relationship between the selected process factors and the combined grey response, so that the two-response problem involving PV and PT was converted into a single-response optimization framework through the GRG-RSM approach.

3.7.3 Selection of Favorable Parameter Combination

The favorable parameter combination was selected based on the GRG obtained for each design point. In the present work, the run having the highest GRG and the first grey order was treated as the most favorable parameter combination, representing the closest approach to high PV and controlled PT. The detailed values of the best, average, and worst combinations are discussed separately in Section 4.5.

3.8 Methodology for Particle Size and Morphology Analysis

The methodology adopted in this stage was developed to quantify the coupled effects of D_p, G_p, and ψ on PV, substrate impact velocity footprint, and RD during Cu deposition in HPCS using N_2. In this stage, the same CFD framework was used, while the analysis was extended toward morphology-sensitive particle behavior. Accordingly, the methodology focused on the D_p range of $2 - 75$ µm, G_p range of $2 - 4$ MPa, and ψ range of $1.0 - 0.6$ to examine how realistic particle morphology affects particle in-flight acceleration, substrate impact conditions, and lateral spreading [1], [63]. Thus, the present section establishes the methodological basis for evaluating axial PV, substrate velocity footprint, and RD under different combinations of D_p, G_p, and ψ.

3.8.1 Selection of Morphology Analysis Parameters

The selection of D_p, G_p, and ψ in the present stage was made to isolate the coupled influence of particle inertia, jet momentum, and particle morphology on the in-flight and near-substrate behavior of Cu particles in HPCS. Unlike the previous optimization stages, the purpose here was not to rank operating conditions through a design matrix, but to examine how particle dynamics change when D_p, G_p, and ψ are varied together within a morphology-sensitive simulation. The comparative analysis was carried out using $G_p = 2, 3, 4$ MPa, representative D_p values of 5, 25, 45, and 75 µm, and ψ values of 1.0, 0.8, 0.7, and 0.6, where $\psi = 1.0$ represents spherical particles and lower values

represent progressively non-spherical morphologies. The corresponding morphology classification is summarized in Table 3.8.

Table 3.8 Particle morphology classification based on sphericity

ψ (sphericity)	Particle Morphology Classification	Ref.
1.0	Spherical particle	[63]
0.8	Near-spherical / slightly non-spherical particle	[63]
0.7	Moderately non-spherical particle	[94]
0.6	Highly non-spherical / irregular particle	[94]

3.8.2 Design of Particle Simulation Cases

The morphology-sensitive simulation cases were defined by combining the selected levels of G_p, D_p, and ψ within the CFD framework. These cases were organized under fixed geometric and numerical conditions to isolate the effects of G_p, D_p, and ψ on particle motion. The defined cases were grouped to evaluate axial in-flight particle response, substrate velocity footprint, and RD.

3.8.3 Evaluation of Velocity Footprint and Radial Dispersion

The evaluation in this stage was carried out through three connected response measures, namely axial PV, substrate velocity footprint, and RD. First, the axial evolution of PV was examined along the nozzle axis to assess the effect of D_p and ψ on in-flight acceleration under selected pressure conditions. Second, the substrate velocity footprint was evaluated from the radial distribution of PV at the substrate plane, because this distribution reflects how incoming particles spread across the impact zone and indicates footprint width and impact localization. In this way, the methodology links in-flight particle acceleration with the velocity field reaching the substrate under morphology-sensitive conditions. For the present analysis, particle trajectories computed through the DPM-based CFD framework were used to extract axial PV and substrate-side PV distribution for each selected case. The evaluation of RD under different sphericities was carried out to examine how particle

morphology modifies the lateral spreading of particles at the substrate, while the detailed variation in RD is presented in Section 4.6.

3.8.4 Particle Shape Classification and Preferred Condition Selection

For the present morphology-sensitive analysis, the particle shapes were classified on the basis of ψ so that the simulated cases could be interpreted in a physically consistent manner. The selected ψ values, defined in Section 3.8.1, were used to represent a gradual transition from spherical particles to highly irregular particles. This classification was adopted to relate the numerical cases directly with the expected variation in aerodynamic drag, particle acceleration, substrate velocity footprint, and RD, as described through the drag model introduced in Section 3.4.3 [63]. Accordingly, the morphology categories were interpreted as spherical, near-spherical, sightly non-spherical, moderately non-spherical, and highly non-spherical/irregular particles. The preferred morphology condition was identified by jointly considering PV, substrate velocity footprint, and RD under the selected combinations.

CHAPTER 4 RESULTS AND DISCUSSION

4.1 Introduction

This section presents the results and discussion progressively, beginning with field-level understanding and moving toward detailed numerical investigation, optimization, and particle-based analysis. The results are organized as a logically connected sequence in which publication growth, source contribution, collaboration structure, thematic evolution, and research gaps are examined first, followed by response-oriented numerical investigation of nozzle design, process conditions, and particle behavior. Thus, the chapter shows how bibliometric assessment, nozzle-related investigation, process optimization, and morphology-sensitive analysis together contribute to improved CS performance and coating quality.

4.2 Bibliometric Structure

The bibliometric analysis was carried out to establish the overall structure of the CS research field and to provide a quantitative basis for interpreting its development and influential themes. The results are presented through growth-oriented, contributor-oriented, and theme-oriented outputs, including the annual publication trend, subject-area distribution, authorship, source contribution, collaboration maps, document-citation mapping, keyword co-occurrence, and density visualizations. Therefore, the bibliometric results provide the field-level basis for identifying research concentration and gaps before moving on to the numerical and optimization studies.

4.2.1 Publication Growth and Subject Evolution

The complete bibliometric dataset consisted of 387 Scopus-indexed documents retrieved using the selected search query. For the publication-growth analysis, a filtered research-paper subset of 248 papers was used to examine annual and cumulative publication trends. The first relevant publication appeared in 1999. The annual publication output remained

limited during the initial stage of CS coating research, while clearer growth started after 2004. From 2008 onward, the number of publications increased steadily, indicating growing research attention toward CS coatings. The maximum annual output was observed in 2020, with around 34 publications, whereas 14 articles were recorded in 2022 at the time of data extraction. From 2008 to 2013, the annual output remained below 10 articles per year, showing that the field was still in an early development stage. Figure 4.1 depicts the research trend based on annual and cumulative publications. The increase after 2013 indicates stronger research activity related to CS coating structure, powder-substrate interaction, and material properties [21]. This trend reflects the continued development of CS technology and its application to engineering materials and industrial sectors [3].

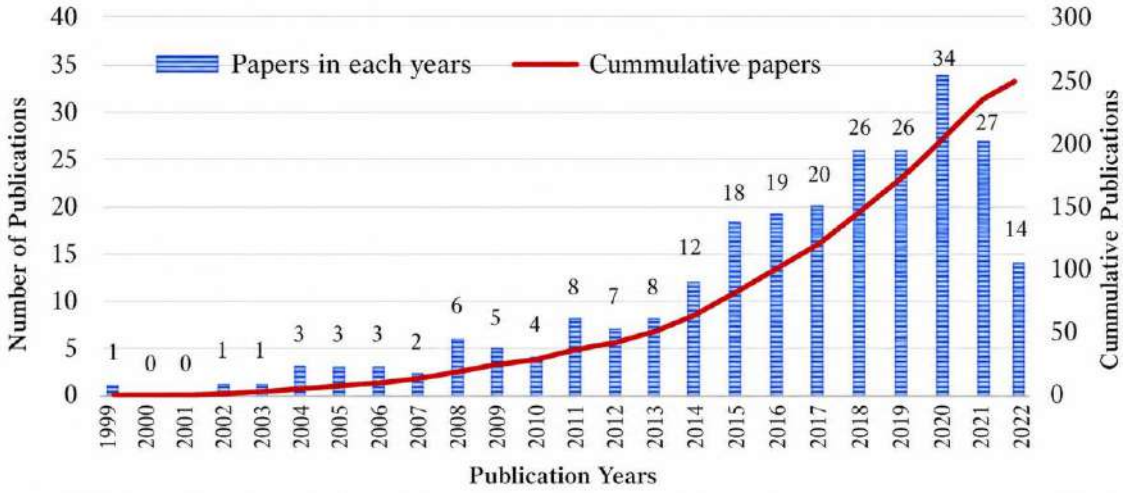

Figure 4.1 Level of development of research on cold spray coatings

The subject-area distribution of CS research shows that the field is mainly concentrated in material science and engineering. As depicted in Figure 4.2, materials science and engineering are the two leading subject areas, contributing approximately 45% and 25% of publications, respectively. This distribution shows that CS research is strongly linked with material behavior, coating development, and engineering performance, while the contribution of other subject areas remains comparatively smaller.

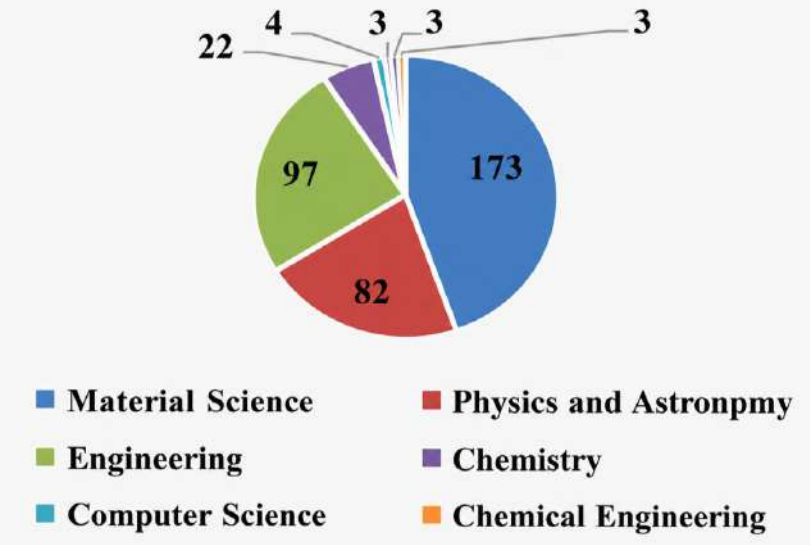

Figure 4.2 Subject areas of in the cold spray study

4.2.2 Research Contributors and Citation Structure

The influential authors and their pioneering research in the CS field were identified based on the number of citations received and collaborative contributions, which indicate knowledge transfer, research influence, and conceptual development. Out of 748 authors, 27 met the requirement of having at least 5 publications. The highest number of publications was by Jodoin b. (13) articles, followed by Liao h. (10) and Xie y. (10), while Assadi h. and Champagne v.k. (9) also contributed significantly. In terms of total citations, Assadi h. ranked first with 1347 citations, followed by Gartner f. (1308) and Klassen t. (465). Moreover, when average citations were considered, Assadi h. ranked highest with 149.7 citations per document, followed by Yue s. (55.1) and Li c.-j. (47.1), as mentioned in Table 4.1. Liao h, Lic-j., and Yue s. were also among the top authors in terms of h-index values greater than 40. These results show that the leading authors mainly contributed to metallic powder deposition, composite coatings, microstructure analysis, bonding mechanisms, and corrosion behavior in CS research.

Table 4.1 Leading authors of the topic cold spray

Author	Institutions	Country	Documents	Total citations	Average citations	Total h index
jodoin b.	University of Ottawa	Canada	13	255	19.6	41
liao h.	ICB UMR 6303	France	10	376	37.6	61
xie y.	National Engineering Laboratory	China	10	191	19.1	21
assadi h.	Brunel University London	UK	9	1347	149.7	33
li c.-j.	State Key Laboratory	China	9	424	47.1	64
yin s.	Trinity College Dublin	Ireland	9	379	42.1	35
champagne v.k.	U.S. Army Research Laboratory	USA	9	229	25.4	32
ogawa k.	Tohoku University	Japan	8	207	25.9	24
chromik r.r.	McGill University	Canada	8	170	21.3	36
yue s.	McGill University	Canada	7	386	55.1	56

The author and co-author relationships through citation visualization are shown in Figure 4.3. However, it is critical to identify developing authors based on their average annual publications with co-authors. It was discovered that the three most recent authors in this discipline were all from China. However, two of them (Sun. w. and Xie. y) were from the same institution National Engineering Laboratory for Modern Materials Surface Engineering Technology and one author (Chen. c) was from the State Key Laboratory of Advanced Special Steels, whose research is generally around 2016–2021.

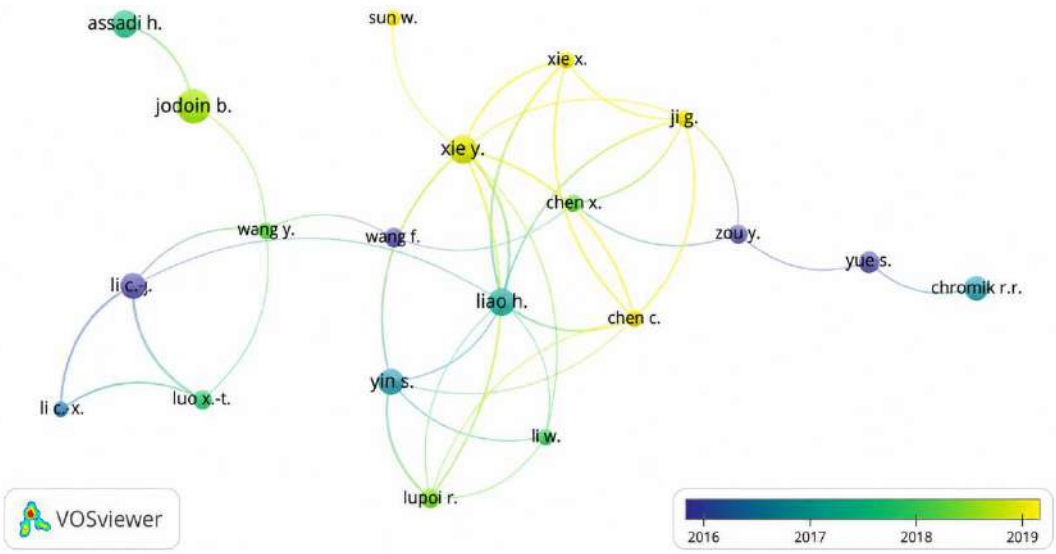

Figure 4.3 Overlay Visualization of Co-authorship analysis

The most prestigious authors share their findings along with citations and source references. Researchers may also quickly and simply select the best sources for publishing their studies based on their research, the journal's reputation, and citations [23]. The statistics for the five main sources of publications from 2015 onward are shown in Figure 4.4. 'Surface and Coatings Technology' has shown a dramatic increase since 2017 and almost steady publications on average afterwards. With an increase in the number of publications in 'Coatings' and 'Acta Materialia' which are emerging sources and the 'Journal of Thermal Spray Technology' and 'Applied Surface Science' the quantity published is lower and has shown a declining trend. Out of 75 sources, 19 met the requirement of having at least 3 documents published. The same journal cluster and node size signify higher citations. Overall, five sources contributed to 72% of publications. The main sources of CS research in the period 1999–2022 are summarized in Table 4.2.

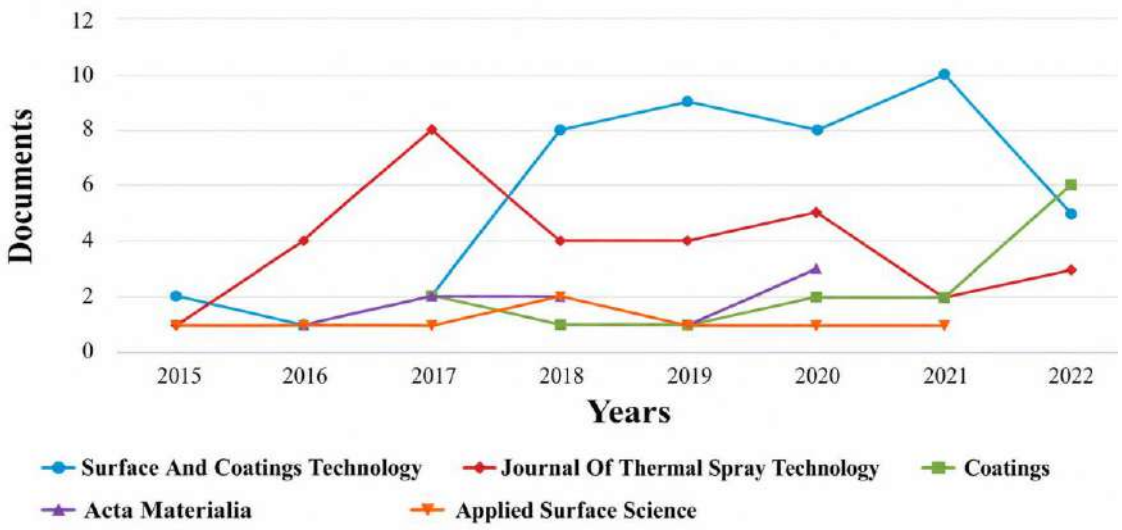

Figure 4.4 The number of publications by source

Table 4.2 List of main sources of cold spray research in the period 1999–2022

Source	Publications	Citations	Citations per documents	Total link strength (TLS)
surface and coatings technology	59	1797	30.46	221
journal of thermal spray technology	37	1346	36.38	194
applied surface science	13	785	60.38	84
acta materialia	12	1916	159.67	215
coatings	11	70	6.36	31
surface engineering	8	154	19.25	32
materials science and engineering	6	197	32.83	29
international journal of advanced manufacturing technology	5	74	14.8	15
scripta materialia	5	377	75.4	64

The assessment showed that ‘surface and coatings technology’ is ranked first, and is highly popular among researchers, followed by ‘Journal of Thermal Spray Technology’, ‘Applied Surface Science’ and ‘Acta Materialia’ in terms of the number of publications. A higher citation count indicates a lot of dynamic research on CS accepted by particular sources. In this study, ‘Surface and Coatings Technology’ is at the top in terms of citations (1797). The number of citations per document reveals the importance of the journal articles and reflects that ‘Acta Materialia’, ‘Scripta Materialia’ and ‘Applied Surface Science’ are the

top three journals and their average citations per document are 159.67, 75.4, and 60.38 respectively. Although 'Acta Materialia' emerges as a high-impact source due to the maximum number of citations per document and a large TLS. The journals are divided into seven groups: red (5 journals), green (3 journals), blue (3 journals), yellow (3 journals), violet (3 journals), cyan (1 journal), and orange (1 journal), as shown in Figure 4.5. The stronger the connection between two journal nodes, the shorter their link.

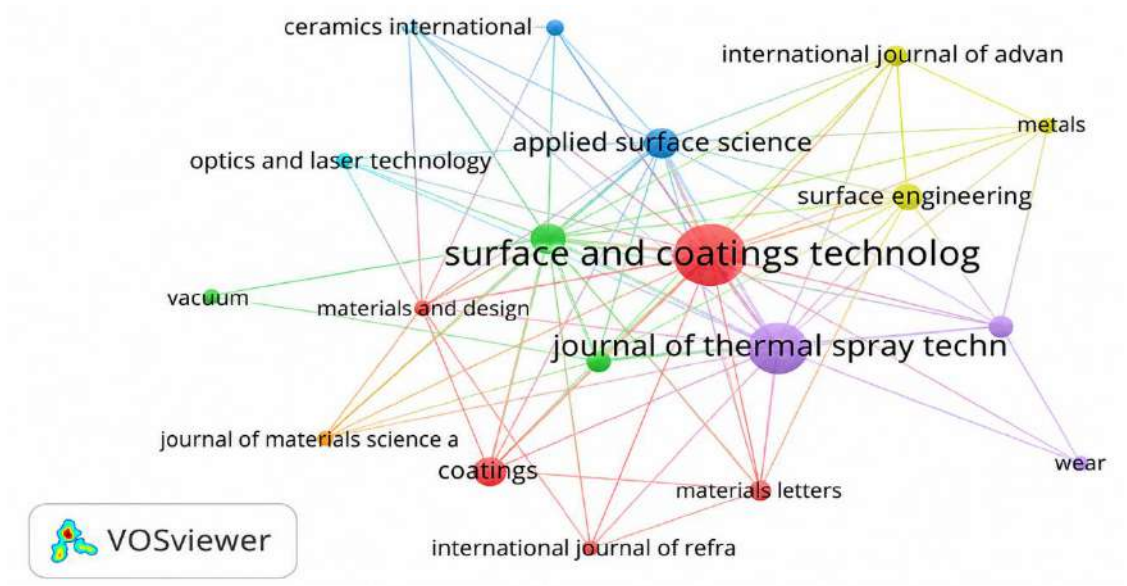

Figure 4.5 The Network Visualization of sources

The most influential publications in CS research were identified through citation-based assessment, because the number of citations helps in recognizing those studies that have shaped the development of the field. In this section, the 10 most-cited studies found in the Scopus database are summarized in Table 4.3, while the citation-based relationship among influential documents is presented in Figure 4.6. Most researchers cite documents with higher citation counts because the work is highly relevant and suitable for academic use. The most-cited paper, by Schmitt T. (2006), published in Acta Materialia with a total of 856 citations, analyzed Adiabatic shear instability (ASI) on Cu and 316L (steel) using D_p ranges of 25–50 μm with a decreased V_{cr} of 600 m/s, resulted in larger particles, at or beyond 500 m/s caused high-rate deformation due to different material properties and D_p.

The second most cited paper is by Assadi h. (2016) in again Acta Materialia with a total of citations 432 highlights CS is two-fold: (a) surface technology and (b) solid-state additive manufacturing process, offering an alternative to selective laser melting or electron beam melting methods, uses a high-pressure supersonic jet at critical velocities (500–1200) m/s, the kinetic energy rupture surface oxide and deforms particles plastically. This study reveals that ASI may be consider a prerequisite for bonding on metals. The third paper, by Grujicic M. (2003), had a total of 411 citations, published in Applied Surface Science, studies the impact of Al particle with the incident velocity of 650 m/s and a flat infinite Cu substrate.

Table 4.3 List of the top ten influential papers on the topic of cold spray obtained up to July 2022

Rank	Total citations	Title	Author	Journal	Ref.	Cluster
1	856	Development of a generalized parameter window for cold spray deposition	Schmidt t. (2006)	Acta Materialia	[19]	2
2	432	Cold spraying – A materials perspective	Assadi h. (2016)	Acta Materialia	[20]	5
3	411	Computational analysis of the interfacial bonding between feed-powder particles and the substrate in the cold-gas dynamic-spray process	Grujicic m. (2003)	Applied Surface Science	[10]	6
4	358	Impact of high velocity cold spray particles	Dykhuizen r.c. (1999)	Journal of Thermal Spray Technology	[18]	3
5	336	Aluminum coatings via kinetic spray with relatively large powder particles	Steenkiste t.h.v. (2002)	Surface and Coatings Technology	[9]	3
6	180	Dynamic recrystallization in the particle/particle interfacial region of cold-sprayed nickel coating: Electron backscatter diffraction characterization	Zou y. (2009)	Scripta Materialia	[16]	2
7	175	Residual stress and thermo-mechanical properties of cold spray metal coatings	Luzin v. (2011)	Acta Materialia	[98]	7
8	145	Review of Relationship Between Particle Deformation, Coating Microstructure, and Properties in High-Pressure Cold Spray	Rokni m.r. (2017)	Journal of Thermal Spray Technology	[21]	4
9	130	Microstructure and mechanical property of Ti and Ti6Al4V prepared by an *in-situ* shot peening assisted cold spraying	Luo x.-t. (2015)	Materials & Design	[17]	5

10	130	The effects of heat treatment on the mechanical properties of cold-sprayed coatings	Huang r. (2015)	Surface and Coatings Technology	[8]	7

The citation structure further shows that the early highly cited studies are mainly centered on high-velocity particle impact, interfacial bonding, and parameter-window identification, which indicates that the initial growth of CS research was strongly influenced by deposition physics and impact mechanics. Three publications before Schmitt T. in 1999, 2002, and 2003 on CS focus on the impact of high-velocity powder using ductile materials such as copper, aluminum, stainless steel, and silver both as powder and substrate characterization, and these relationships are reflected in Figure 4.6. It was also observed that out of the ten most cited papers worldwide, one influential study was by Luo x.-t. on Microstructure and mechanical property of *Ti* and *Ti6Al4V* prepared by an in-situ shot peening assisted cold spraying, which showed that the plastically deformed layer was enhanced and porosity decreased on large-sized particles. However, many researchers have investigated metallic materials such as Cu, Ti, steel, and high-entropy alloy, to develop and optimize the spray parameter feedstock properties, and substrate conditions to understand the bonding mechanism of CS [20].

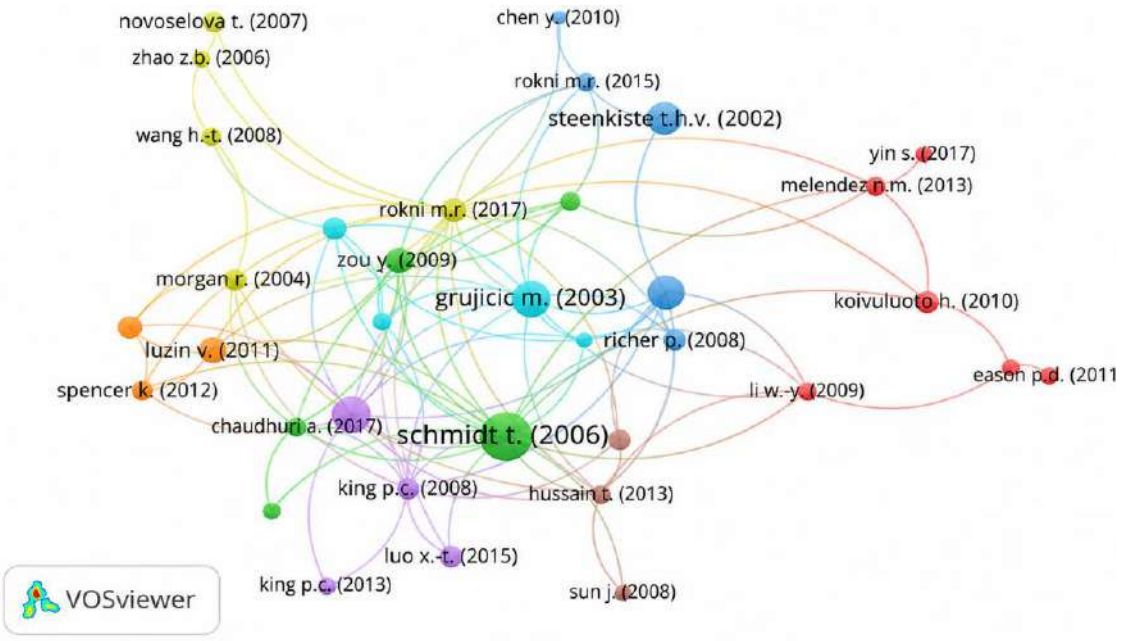

Figure 4.6 The Network Visualization of documents based on citations

4.2.3 Keyword Networks and Research Directions

Density visualization was interpreted using the font size of keywords and the background color of the density map. The sequence represents the TLS in the order of yellow > green > blue. The distance between each keyword indicates how closely the research topics are related. Co-occurrence analysis was performed using two criteria; I: considered keywords appearing in the title, abstract, and keyword list, II: considered author-provided keywords. In criteria I, out of 2142 keywords, 341 were selected based on a threshold on a minimum of three co-occurrences, as shown in Figure 4.7(a). In criteria II, 661 keywords were generated, and 28 met the threshold of five occurrences, as shown in Figure 4.7(b). Terms often associated with CS like “grain refinement”, “spray nozzle”, “substrate” and “binary alloy” do not appear, due to different occurrences of keywords and TLS. The keyword ‘CS’ is also associated with other parameters such as “bonding mechanism”, “residual stresses”, “recrystallization”, and “numerical simulation”. Figure 4.7(b) concludes that the

occurrence of these types of keywords is the lowest in terms of their TLS, and research publications in the past years have not diversified yet.

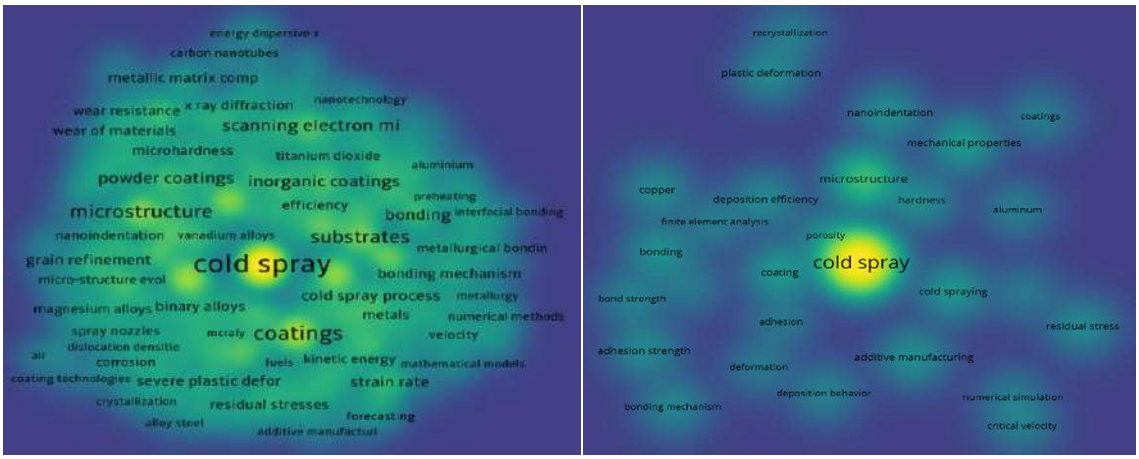

(a) (b)

Figure 4.7 Density visualization of keyword co-occurrence: (a) in the title, abstract, and keyword list, minimum 3 occurrences, (b) in author-provided keywords, minimum 5 occurrences

Furthermore, the study is required to identify proper material selection, powder refinement procedures and their toxicity, and the use of CFD for analysis and design of geometries that help this field reach a highly advanced level and could be suitable for other applications [4]. The CS process works well for automotive and aircraft material coatings and their maintenance; however, this method is still not properly investigated in the biomedical field, so far, the thermal spray method has only been used with limitations. Some of the important keywords such as “metal matrix composite”, “numerical simulation”, “residual stresses”, “composite coatings”, and “recrystallization” have the lowest TLS values of 7, 8, 10, 11, and 12, respectively. “Metal matrix composite” is useful for providing favorable properties due to constituent phases such as ductile intermetallic materials and hard ceramic particles that offer thermal and mechanical treatments in coatings to improve properties and macrostructure. “Numerical simulation” is useful to optimize and synthesize coatings on various powder-substrate combinations and could predict CS process characteristics and properties, minimize expensive experiments, and save time. Moreover, it can be used to extract more accurate information from coating

synthesis conditions and parameters [99]. Another important term to investigate is "residual stresses," which can affect coating microstructures, bonding mechanism, and repair quality. The evaluation of residual stress would benefit materials in a variety of engineering applications in various environments by improving fatigue life. Residual stresses in Cu and its alloys extend coating life [74]. The inclusion of these keywords in research could improve CS technology on a wider level and perform coatings on other substrates with the help of different materials and analysis techniques.

4.3 Nozzle Design Responses and Optimization Results

The MOO of the CD nozzle for the CS process is presented, and the effects of five important nozzle design parameters are explored. A 2D axisymmetric baseline nozzle was optimized using FCCD, CFD simulation, RSM, ANN, and GA. Four response variables, PV, PT, HF, and SP were optimized to evaluate the nozzle performance. Comparative analysis revealed that the RSM models were more accurate on average than the ANN models, while the ANN models provided a better understanding of complex nonlinear interactions. Therefore, the combination of CFD, RSM, ANN, and GA provide an effective method to optimize CD nozzle parameters and enhance coating-oriented performance.

4.3.1 Sensitivity and Design Space Selection

To use FCCD within RSM, it is necessary to understand the range of significant parameters that require a sensitivity analysis as shown in Figure 4.8. The crucial geometrical parameters, such as L_c, L_d, D_{id}, L_i, and D_e were considered and divided into eleven equal segments, selected for the CFD analysis. For each analysis, all the responses were observed and decisions were made based on PV, since PV determines the success and efficiency of the CS process [44]. PV directly affects particle deformation and bonding, which are essential for achieving high coating density and adhesion strength [90]. Therefore, PV values ranging from minimum to maximum and vice versa for each parameter, along with corresponding parametric dimensions at local minima and maxima, were noted. Parametric dimensions where PV variation was considered insignificant were

ignored, and the mean of the maximum and minimum values of each geometric parameter was chosen as the central value for FCCD. For the sensitivity analysis, the initial baseline CD nozzle model was used with the fixed and variable parameters listed in Table 3.1. The same boundary conditions were applied for both the sensitivity analysis and the RSM design-space simulations.

The effect of L_c, L_d, D_{id}, L_i, and D_e on nozzle responses shows that each design parameter contributes differently to PV, PT, HF, and SP. As shown in Figure 4.8(a), PV significantly increases, as L_c increases from 20 to 90 mm. There is an optimal range of L_c for maximizing PV after which the behavior in PV starts to almost flatten with further increases in L_c. PT also shows a similar trend as PV, this indicates that L_c influences the thermal dynamics of the particles due to longer residence time. But, beyond a certain length of L_c probably around 90 to 100 mm, PT slightly reduces due to the cooling effect of expansion in the divergent section, it is necessary to obtain a balance between heat gain and heat loss. HF and SP also follow a similar trend, initially increasing and with a sufficiently large L_c of approximately 90 mm, both either stabilize or slightly decrease, due to longer L_c allowing more efficient transfer of heat between the nozzle and the particles, and increasing friction and resistance faced by the accelerating particles. Based on the results, an average L_c value of 55 mm is taken for further investigation. Different L_d values plotted against the response variables in Figure 4.8(b), indicate that initially PV rises with L_d and reaches a maximum close to 300 mm, further increases in L_d show no significant PV improvement. This peak represents the optimal L_d for maximizing PV near 300 mm, which provides sufficient kinetic energy for a strong impact bond. PT steadily declines as L_d increases, indicating that particles lose thermal energy and become less ductile, which affects deformation upon impact. HF remains relatively stable across varying L_d and decreases slightly, while SP decreases significantly as L_d increases and lower SP corresponds to higher L_d, suggesting that the force exerted by the gas and particles on the substrate is diminished, which could reduce the potential for substrate damage [48]. Therefore, an average L_d of 185 mm was taken for further analysis.

The impact of D_{id} on response variables indicates that PV variation is significant for D_{id} ranges of 1 to 3 mm, suggesting that a smaller D_{id} is favorable for higher PV. PT decreases with an increase in D_{id}, leading to a loss of ductility and thermal energy as shown in Figure 4.8(c). HF also initially decreases with D_{id} and stabilizes at around 3.3 mm, whereas SP increases with D_{id}. Therefore, an optimal D_{id} should consider the effect of PT, HF, and SP to ensure sufficient heat is transferred to the substrate without causing excessive SP, which impacts the process efficiency and overall cost of coatings [54]. Thus, an average D_{id} of 2 mm was selected.

PV increases with L_i up to 30 mm, beyond which PV shows a stabilized trend, as shown in Figure 4.8(d). This suggests that longer L_i can positively influence the acceleration of particles, by enhancing PV due to longer travel time. However, further increases in L_i show a limited effect on PV, as the additional length does not significantly contribute to PV. It is also confirmed that PT decreases with an increase in L_i, due to the cooling effect over the longer travel distance inside the injector. HF shows a decrease with increasing L_i but then stabilizes, whereas SP increases with L_i, and the longer L_i causes particles to impact the substrate with greater force, thus increasing pressure at the point of contact, therefore, an average L_i value of 20 mm was taken for further analysis

The effect of D_e shows that PV increases, as D_e increases from a minimum value of 6.4 mm to the maximum value of 8.1 mm, beyond this, no significant changes are observed in Figure 4.8(e). As D_e increases, PT decreases, suggesting that a larger nozzle D_e allows the gas and particles to expand and cool, leading to lower PT at the point of impact. Additionally, HF shows a significant decrease with the increase in D_e, while SP significantly declines as D_e increases. This is likely because a larger D_e reduces the resistance to the gas flow, leading to lower back pressures within the nozzle. The optimal D_e should therefore be selected to maximize PV while considering the implications on PT, HF, and SP to ensure a high-quality coating process [25]. Therefore, the average value of D_e was taken as 7.25 mm for further analysis. These results established the center levels of the five critical nozzle design parameters for the later FCCD-based optimization.

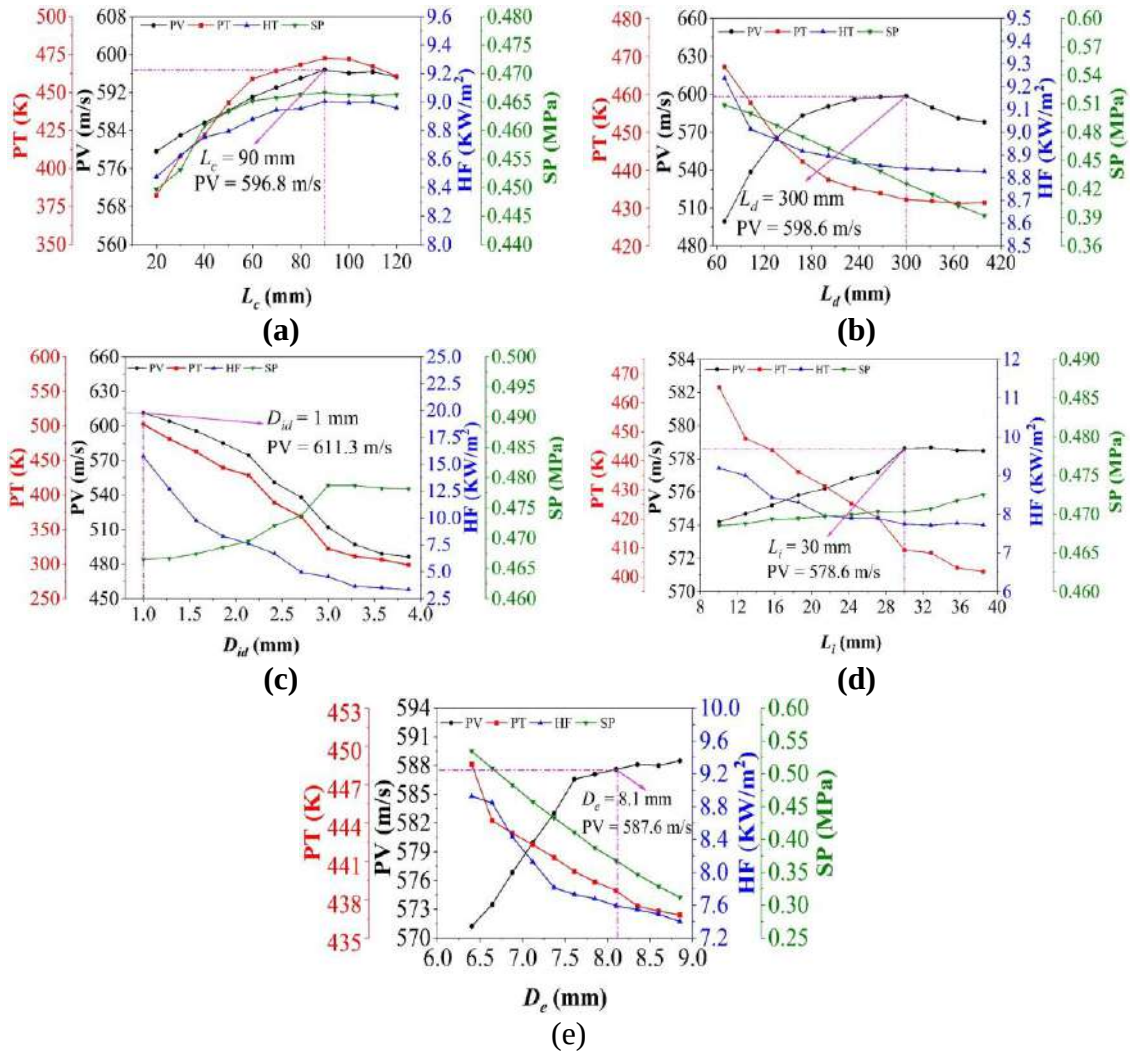

Figure 4.8 Sensitivity analysis of key nozzle parameters (a) L_c, (b) L_d, (c) D_{id}, (d) L_i, and (e) D_e

4.3.2 Response Modeling and Pareto Results

The summary and analysis of ANOVA for PV, PT, HF, and SP are given in Table 4.4. By using RSM, the standard deviation, mean, R^2, predicted R^2, model F, p-values, and adjusted R^2 were determined for all the selected responses. The mean values of these parameters are 544.19 m/s, 423.39 K, 7.70 kW/m², and 0.441 MPa, respectively, with relatively lower standard deviations. The R^2 and model p-values are important for evaluating the model accuracy, with an R^2 value above 0.80 being acceptable for the

correlation between the variables. In the present study, the R^2 values confirm that PV explains 99.57% of the changes. However, the R^2 values for PT, HF, and SP are 0.9809, 0.9827, and 0.9981, respectively, indicating they are important too. The models are reliable because of the small difference, less than 0.2, between adjusted R^2 and predicted R^2 [91]. Regarding model significance, the p-value must be under 0.05. In the present study, all response variables have p-values below 0.05, and the model p-values are even below 0.0001. This demonstrates the reliability and efficacy of the model, confirmed by substantial F-values.

Table 4.4 Detailed ANOVA and fit statistics across multiple response variables

Responses	**PV**	**PT**	**HF**	**SP**
Standard deviation	4.10	11.91	0.3314	0.0038
Mean	544.19	423.39	7.70	0.4411
C.V	0.7542	2.81	4.31	0.8523
R^2	0.9957	0.9809	0.9827	0.9981
Adjusted R^2	0.9946	0.9759	0.9815	0.9976
Predicted R^2	0.9923	0.9632	0.9794	0.9965
Adequate precision	108.5820	47.9453	65.4054	151.9747
Model F value	902.75	199.79	869.41	1827.56
Model p-value	0.0001	0.0001	0.0001	0.0001
Suggested model	quadratic	quadratic	quadratic	quadratic
Model remark	significant	significant	significant	significant
Lack of fit remark	not significant	not significant	not significant	not significant

The results of modeling the CS nozzle by considering its design parameters and responses gave mathematical equations that relate the responses to the independent variables in terms of their actual values. In each equation, the p-value approach was employed to verify significance, if ($p < 0.05$) as well as 0.001 models show statistically significant or highly accurate modeled terms, if ($p > 0.05$) are considered as not significant, therefore, the nonsignificant terms are ignored [73]. The simplified model equations in the actual form are given below in Eq. (4.1) – (4.4).

$$PV = 518.83881 + 0.308172L_c + 0.677474L_d + 19.32481D_{id} + 0.479449L_i - 18.84414D_e - 0.004375L_cL_i - 0.061033L_dD_{id} + 0.139642L_d - 0.003178L_d^2 - 10.92389D_{id}^2 \quad (4.1)$$

$$PT = 492.10653 + 3.43921L_c + 0.186813L_d - 62.80907D_{id} - 3.71182L_i - 0.002964L_cL_d - 0.429732L_cD_{id} + 0.019438L_cL_i - 0.045299L_dD_{id} + 0.750938D_{id}L_i - 0.012912L_c^2 \quad (4.2)$$

$$HF = 10.62080 + 0.005741L_c + 0.132749D_{id} - 0.749365D_{id}^2 \quad (4.3)$$

$$SP = 1.68724 + 0.001653L_c - 0.001363L_d + 0.007855D_{id} + 0.000678L_i - 0.226885D_e - 4.87554E\text{-}07L_cL_d - 0.000051L_cD_{id} - 8.27420E\text{-}06L_cL_i + 0.000140L_dD_e - 9.01735E\text{-}06L_c^2 + 0.007482D_e^2 \quad (4.4)$$

The comparison between actual (CFD-observed) and predicted values for all responses is presented in Figure 4.9. The diagonal line represents the fit, indicating the best predictions when the points lie on it. Points above the line imply overpredictions, while those below indicate underpredictions. Most points closely align with the 45-degree line, indicating closeness to actual values and evenly distributed errors across the model. In Figure 4.9(a), (b), and (d), comparisons are made between values for PV, PT, and SP calculated by CFD and those predicted by the regression model. The differences between R^2 and adjusted R^2 values are minimal at $1.1e^{-3}$, $5e^{-3}$, and $5e^{-4}$, respectively, suggesting that only a small portion of the data remains unexplained. Additionally, the gaps between adjusted R^2 and predicted R^2 values for these responses are also small at $2.3e^{-3}$, $1.3e^{-3}$, and $1.1e^{-3}$ respectively; with R^2 values close to 1, the regression model represents a good fit. In Figure 4.8(c), data points cluster in three regions, which is attributed to the nature of the data and does not suggest a systematic error in the model, with the error between the data value and predicted value remaining low and the R^2 value close to 1, which suggests that the regression model fits well for all responses. The model's Adequate Precision, which reflects the signal-to-noise ratio, exceeds 4 in all instances and ensures high predictive

accuracy. The coefficient of variation (CV), which assesses model reproducibility, is extremely low at 0.99%, and a CV below 10% is considered satisfactory [77].

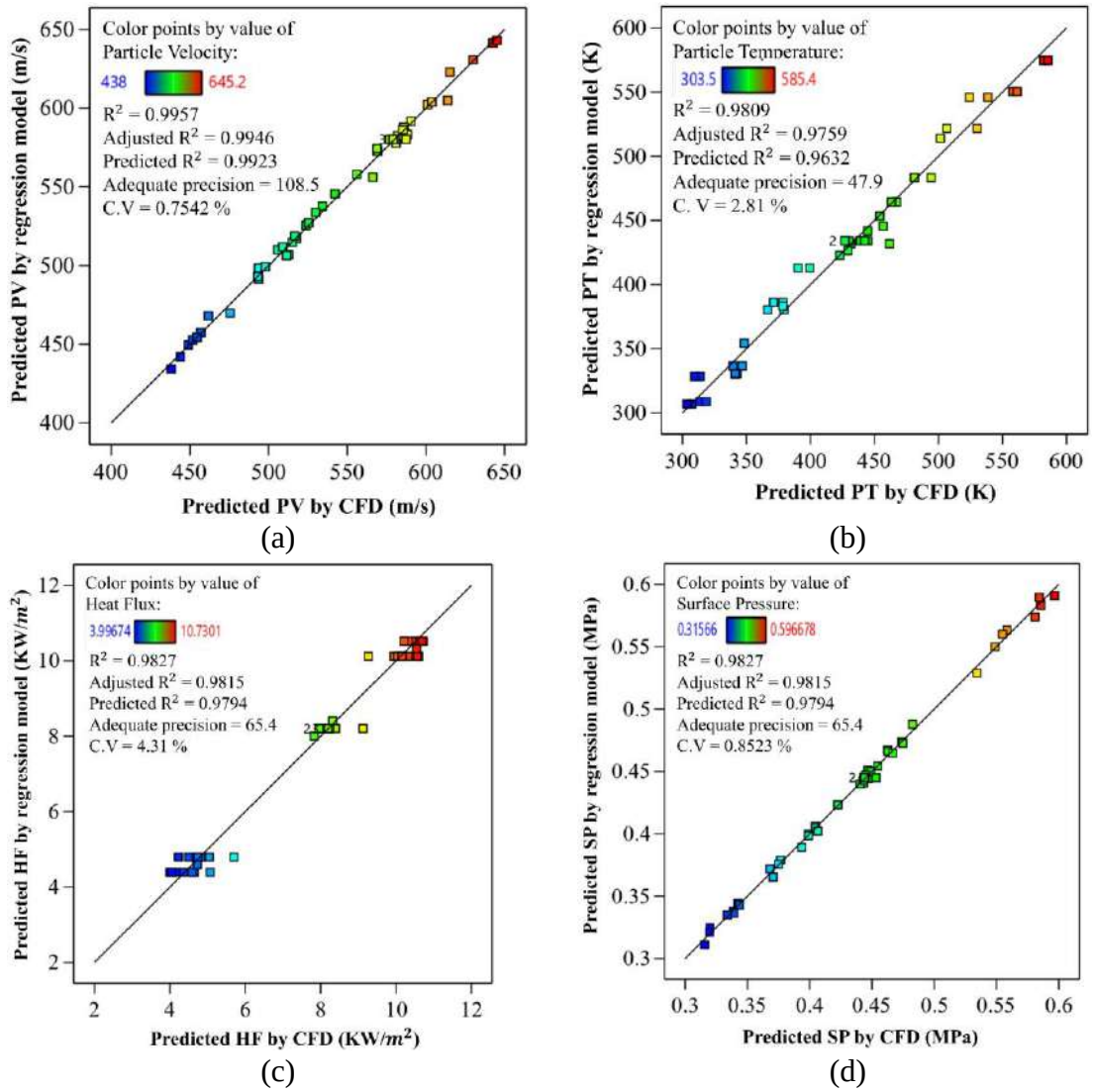

Figure 4.9 The predicted vs. actual plots for all responses (a) PV, (b) PT, (c) HF, and (d) SP

To visualize the single and combined effects of independent variables on all responses, 3D response surface contour plots and 2D lines were generated, as shown in Figure 4.10. For each plot, two independent factors were considered with the other factors kept at their centre values. The interaction between the noticeable factors on PV is given in **F**igure 4.10(a–c). The effect of L_c and L_i on PV, as shown in Figure 4.10(a), suggests that the impact of these factors is less significant. Maximum PV is achieved as L_c increases,

whereas L_i has a negligible impact on the contribution of PV. Figure 4.10(b) represents the combined effect of L_d and D_{id} on PV, the curved contours of both factors across the entire coordinate range indicate that PV is highly sensitive to variations in these factors. An increase in velocity occurs when L_d increases and D_{id} decreases. The maximum PV of 620 m/s is achieved when L_d increases up to 254 mm, and a further increase shows a minimal effect on PV [44]. The nozzle D_e also influences PV, with larger L_d resulting in higher PV, while maintaining almost consistent behavior as the nozzle D_e varies. However, D_{id} seems to have a more remarkable impact on PV as its value changes from maximum to minimum, and the PV also fluctuates between 530–620 m/s. This indicates that D_e has a remarkable impact on PV, especially for sufficiently large L_d, as shown in Figure 4.10(c) [40].

Figure 4.10(d–h) shows the impact of nozzle design parameters on PT, showing how these factors have contributed significantly. Figure 4.10(d) suggests that PT increases with L_c and decreases with an increase in L_d, indicating that the optimal range of temperature can be achieved with smaller L_c and larger L_d [50]. As shown in Figure 4.10(e), the almost steep contour of PT suggests that variation in D_{id} contributes significantly to PT especially for larger L_c, with a maximum PT of around 540 K. Therefore, the optimal selection of D_{id} is always necessary for the effective coating of Cu material. Figure 4.10(f) describes the interaction between L_i and L_c toward PT. It can be seen that variation of L_i has an almost negligible impact on PT for large L_c. However, a slight fall in PT is observed as L_i increases over the entire coordinate corresponding to small L_c. The interaction effect of L_d and D_{id} on PT is shown in Figure 4.10(g), where an upward slope indicates that there is an increase in PT as D_{id} decreases. Also, an upward trend between L_i and D_{id} is shown in Figure 4.10(h), where variation in L_i shows a significant change toward PT when D_{id} is small. SP is one of the desirable response factors that should be considered to investigate the effect of design parameters that ideally influence the back pressure and should be minimized to prevent undesirable effects such as bouncing back or damage to the substrate. Lower SP enhances coating adhesion and quality by improving bond

strength and controlling impact dynamics for uniform thickness [51]. The interaction between L_d and L_c affecting SP is shown in Figure 4.10(i), indicating that a minimum SP occurs at larger L_d and smaller L_c. The interaction between L_c and D_{id}, as shown in Figure 4.10(j), indicates that D_{id} ensures consistent flow dynamics and maintains steady particle acceleration and gas expansion, which results in minimal variation in SP. A similar trend is observed in the interaction plot between L_i and L_c, as shown in Figure 4.10(k). The injector length primarily affects the acceleration and velocity of the particle, and does not show any significant contribution to SP. In the interaction plot between L_d and D_e on SP, shown in Figure 4.10(l), larger dimensions are suitable for achieving minimum SP on the substrate surface by allowing expanded gas flow and particle deacceleration that minimizes the reflected force and particle rebound upon impact with the substrate.

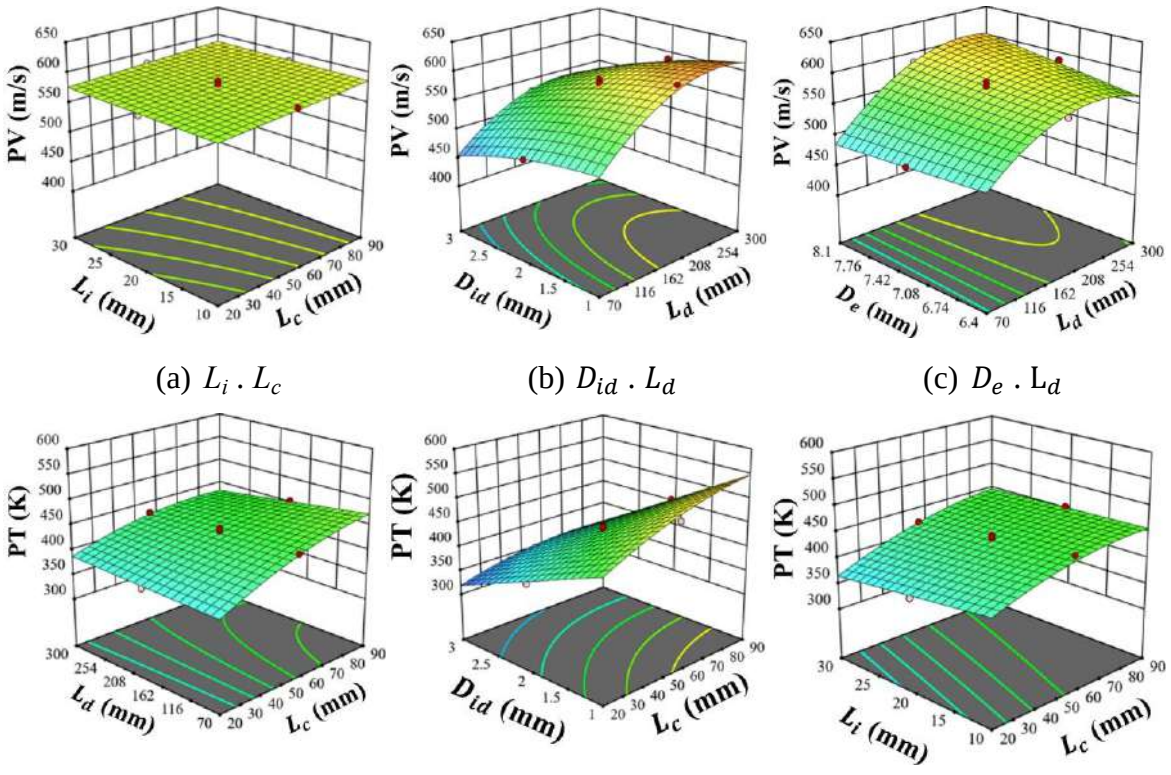

(a) L_i . L_c (b) D_{id} . L_d (c) D_e . L_d

(d) L_d . L_c (e) D_{id} . L_c (f) L_i . L_c

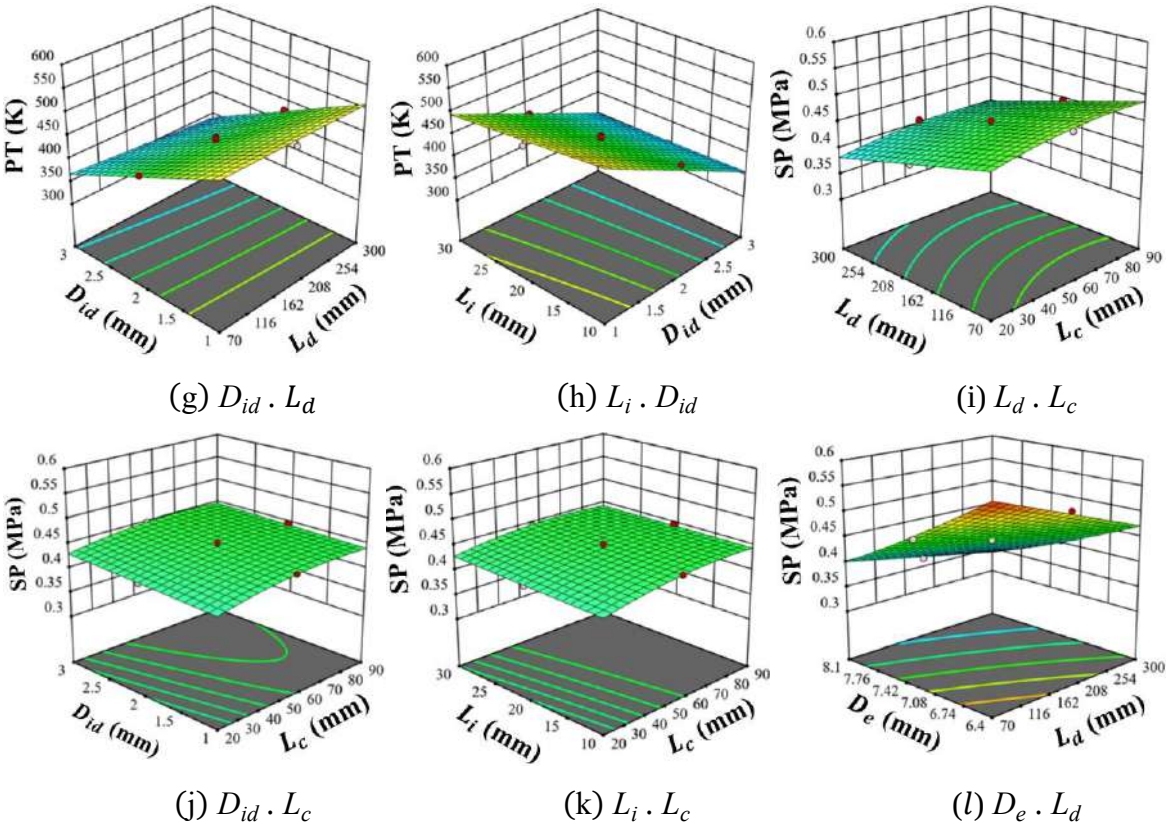

(g) D_{id} . L_d (h) L_i . D_{id} (i) L_d . L_c

(j) D_{id} . L_c (k) L_i . L_c (l) D_e . L_d

Figure 4.10 Multivariate response surface analysis

The ANN-based prediction of nozzle responses shows that the developed neural network provided a reliable nonlinear relationship between the selected nozzle design variables and the corresponding CFD-generated responses. During the regression training process, there was a decrease in the MSE down to 0.0055313. The error reduction pattern follows a curve that starts to level off around 25 epochs (iterations). After this point, increasing the number of iterations did not further reduce the error, which aligns with conclusions drawn from research on using ANN for modeling and prediction, as shown in Figure 4.11. The regression behavior further confirms that the ANN model predicted the nozzle responses with strong reliability. As shown in Figure 4.12, the model is reliable based on an R value of 0.9971 for training data, 0.94883 for testing data, 0.99114 for validation data, and 0.99191 for all combined datasets. These results indicate that the ANN model captured the relationship between the nozzle design variables and the responses, with a high level

of predictive agreement. Thus, the ANN-based prediction provided a strong surrogate framework for the subsequent optimization stage.

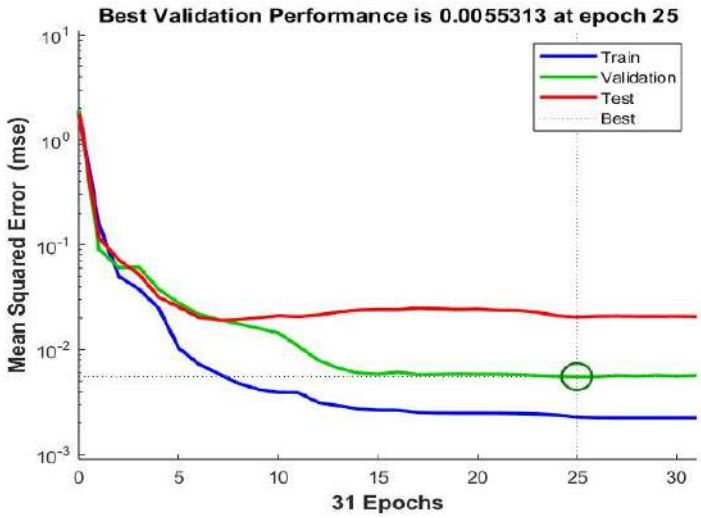

Figure 4.11 ANN model training performance representing MSE vs. test periods

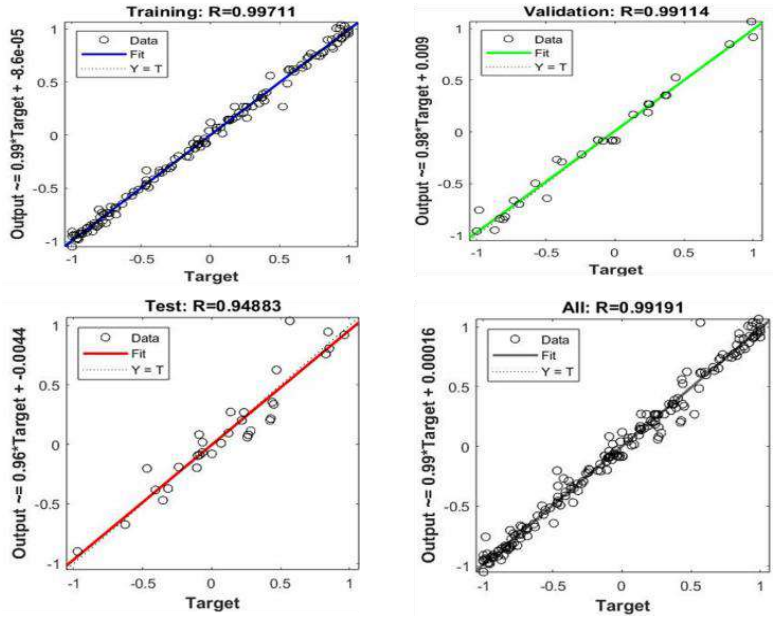

Figure 4.12 Regression plots representing overall correlation coefficients (R)

4.3.3 Optimum Configuration and Comparative Performance

To evaluate the effectiveness of the RSM and ANN models, the predicted outcomes from the RSM-DF and ANN-GA models were compared with those computed by CFD for all

responses. The detailed comparative analysis of RSM and ANN model metrics across all response variables is presented in Table 4.5 using Eqs. (3.28−3.33). The comparison of CFD, RSM, and ANN predictions for key performance metrics is shown in Figure 4.13. The comparison across all test scenarios indicates that the predictions of both models closely correspond with the CFD values for all parameters. Examining error metrics and correlation matrices is vital for an evaluation of the model performance. This process not only quantifies errors but also scrutinizes the strength and nature of relationships between predicted and observed values [71].

The comparison of model metrics shows that RSM typically provides lower MAE, RMSE, and MAPE for the PV and HF datasets, demonstrating its superior performance. On the other hand, in the case of PT, ANN delivers accurate predictions based on error and correlation metrics, reducing the performance gap and indicating its effectiveness in specific scenarios. Despite the error metrics for SP, ANN still shows strong predictive ability, with high correlation and determination coefficients. In Figure 4.13(a–d), the predicted responses from both models remain close to the CFD values for PV, PT, HF, and SP, which confirms that both surrogate models are capable of representing the nozzle-response behavior with acceptable precision. The overall comparison highlights that RSM might be more precise under many conditions, whereas ANN performance indicates its potential for strong predictive capabilities, particularly in complex scenarios where the relationship between variables might not be straightforward. Despite slightly higher error metrics, the ANN model was also retained because it can model nonlinear relationships among the variables. Therefore, RSM was preferred for statistical accuracy and interpretability, while ANN was useful for nonlinear prediction and subsequent GA-based optimization.

Table 4.5 Detailed comparative analysis of RSM and ANN model metrics across all response variables

Metrics	**Parameters**	**PV**		**PT**		**HF**		**SP**	
		RSM	**ANN**	**RSM**	**ANN**	**RSM**	**ANN**	**RSM**	**ANN**
	MAE	2.6799	5.4549	8.5672	6.1362	222.38	229.18	2565.1	4332.8

Error	RMSE	3.6241	7.8980	10.517	9.0082	317.89	355.14	3282.1	6032.2
	MAPE	0.4957	0.9832	2.0852	1.4770	2.0852	3.2624	2.0852	1.9356
Correlation	R	0.9978	0.9904	0.9903	0.9931	0.9912	0.9895	0.9990	0.9968
	R^2	0.9957	0.9802	0.9808	0.9861	0.9826	0.9791	0.9981	0.9936
	NSE	0.9955	0.9812	0.9806	0.9860	0.9823	0.9784	0.9979	0.9933

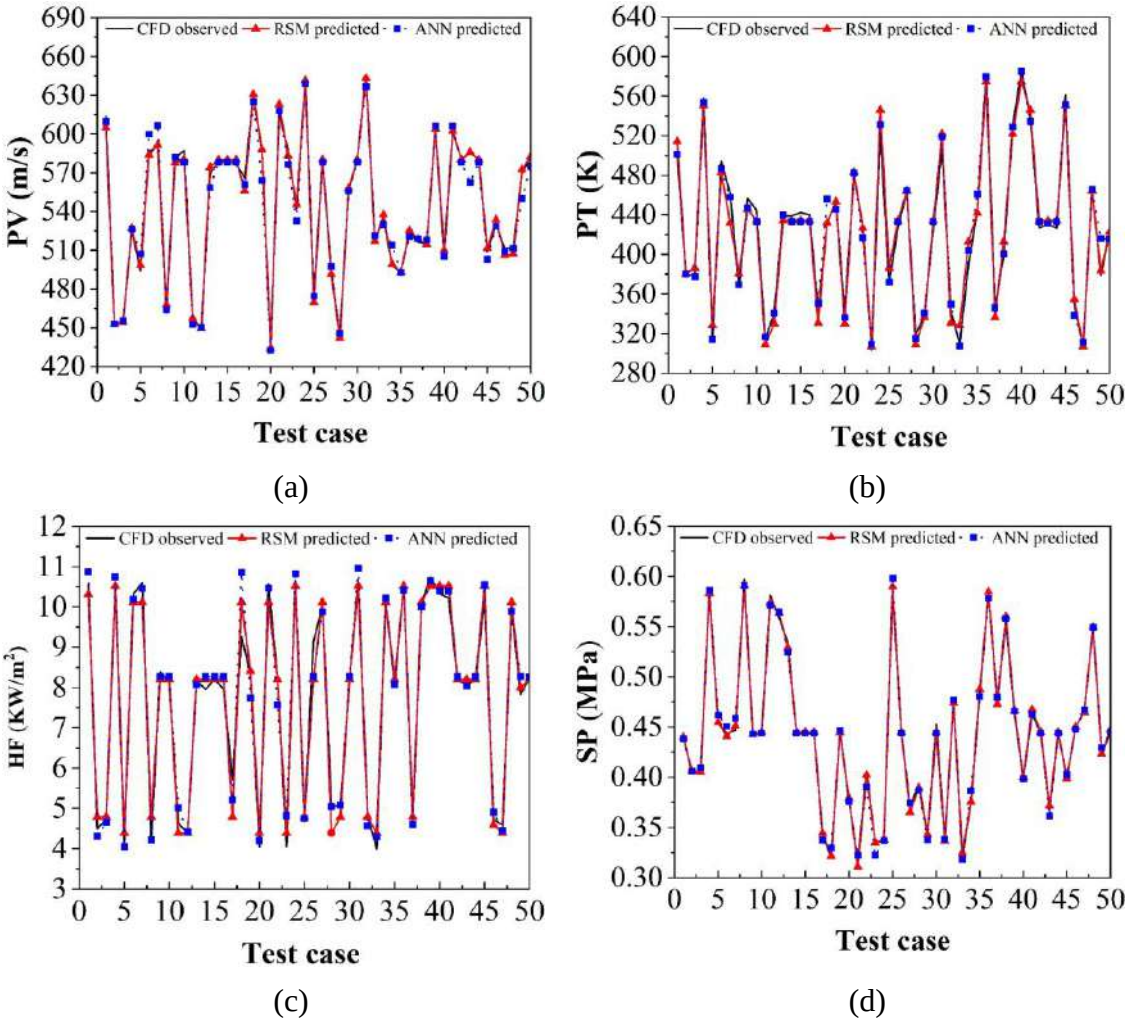

Figure 4.13 Comparative analysis of CFD, RSM, and ANN predictions for key performance metrics (a) PV, (b) PT, (c) HF, and (d) SP

Using RSM-based numerical optimization, all factors were set to “within the range” and the four responses were assigned according to the required optimization criteria. For Cu particle deposition, PV was maximized to enhance particle kinetic energy, which promotes

significant plastic deformation, stronger mechanical interlocking, and the formation of denser and more durable coatings. For 25 μm Cu particles, PT was controlled with respect to the 415 K reference condition to improve particle ductility and minimize oxidation. Maximizing HF ensures efficient heat distribution due to the high thermal conductivity of Cu. In addition, SP was minimized to reduce excessive mechanical loading on the substrate, particle rebound, and deposition nonuniformity, thereby improving adhesion, coating durability, process stability, and cost-effectiveness.

On this basis, the ramp plot shown in Figure 4.14 presents the optimal nozzle parametric conditions and their corresponding responses obtained through the desirability-function (DF) approach. The desirability value of 0.931 indicates that the selected combination of geometric parameters provides a highly favorable compromise among PV, PT, HF, and SP under the imposed optimization criteria. Thus, the RSM-DF provided an effective multi-objective framework for identifying improved nozzle conditions before the subsequent GA-based NSGA-II based optimization.

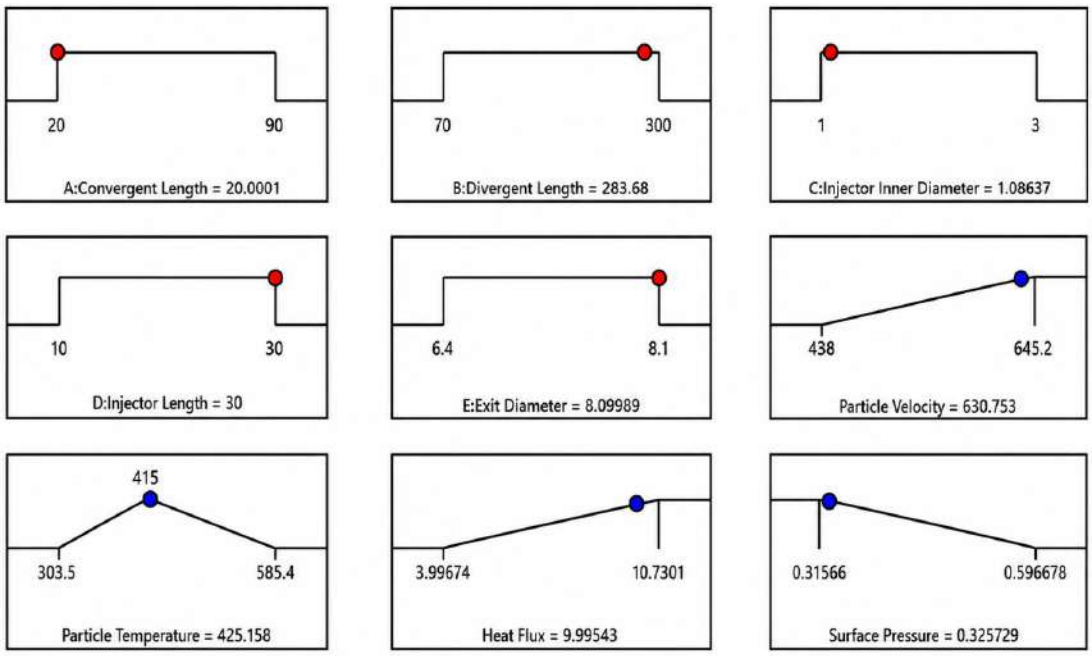

Figure 4.14 Ramp plots demonstrating optimal geometric and performance parameters via RSM-DF

For MOO analysis, the use of ANN-GA emerges as a powerful and effective method for optimizing complex processes [91]. This approach achieved optimal results in 112 iterations, with function values meeting the desired tolerance limit. By comparing the performance of ANN-GA in terms of its ability to determine the Pareto-optimal front from 350 solutions among all the responses, the optimization behavior is represented in Figure 4.15, where the analysis is focused on three pairwise comparisons of objective functions, namely Objective 1 (PV) and Objective 2 (PT), Objective 2 (PT) and Objective 3 (HF), and Objective 3 (HF) and Objective 4 (SP).

The Pareto front in MOO illustrates optimal trade-offs between conflicting objectives such as PV and PT in CS, assisting decision-makers in selecting balanced solutions based on specific preferences. The Pareto front depicted in Figure 4.15(a) shows a set of optimal points that represent the best trade-offs between Objective 1, particle velocity, and Objective 2, particle temperature. The correlation suggests that enhancements in PV result in proportional increases in PT within the optimal solutions. Therefore, any decision that

involves a trade-off between PV and PT should take into account the application and the desired equilibrium between these two factors. The Pareto front illustrates that, as the solution moves from left to right with increasing PV, there is an elevation in PT among the optimal points. The normal points also exhibit this pattern and are not part of the Pareto front, indicating fewer effective trade-offs. The plot highlights specific points of interest (A-E), each presenting a unique set of solutions. Point A, characterized by high PV and PT values, might necessitate higher pressure levels leading to excessive substrate erosion and poor coating adhesion. Point E, which has the lowest PV value, suggests that particles may not deform adequately, resulting in weak mechanical bonding and porosity within the coating [90]. With the annotation of point C as an optimized point, notable solutions are indicated within the context of the optimization problem. The overall behavior of the plot indicates a defined optimization process offering a visual representation of potential trade-offs between the two conflicting objectives. During the CS process, the Cu particles are accelerated in a supersonic jet, which imparts significant kinetic energy to the particles. Below around 525 m/s, close to the V_{cr} of 505 m/s, there is a minimum PT lower than 300 K [19]. However, after 525 m/s model predictions align closely, indicating a strong consistent correlation between them, due to more uniform heat transfer and acceleration effects. By fine-tuning at lower velocities for uniform temperature and leveraging the predictable relationship at higher velocities, critical optimization of the CS process can be achieved. This optimization ensures strong particle bonding and superior coating quality.

In Figure 4.15(b), Objective 2, particle temperature, and Objective 3, heat flux, exhibit a generally upward trend, suggesting that as PT increases, so does HF. The spread indicates slight variability after the temperature reaches around 490 K in model predictions. Before this temperature, a more pronounced and cohesive upward trend is observed. This directly proportional trend suggests that, as the PT increases, there is a corresponding increase in the HF on the substrate surface. The clustering of points, particularly at higher temperatures, demonstrates the ability to predict a consistent and strong relationship between the two variables. As PT increases, the particle capacity for heat transfer upon impacting the substrate also enhances, and intensifies particle deformation, facilitates

better bonding and potentially increases thermal conductivity at the interface, which contributes to high HF.

The scattered plot in Figure 4.15(c) presents a comparison between Objective 3, heat flux, and Objective 4, surface pressure, and also presents two sets of data points, optimal points and normal points. The data points are scattered across the plot indicating the absence of a trade-off curve that is typically observed in a Pareto front for low HF values. This suggests that the relationship between HF and SP is complex, where an increase in one does not necessarily have a direct impact on the other. This observation indicates a multi-dimensional optimization scenario involving various influencing factors, resulting in a wider distribution of both optimal and normal solutions. However, there is a distinct cluster of optimal points representing the best solutions for maximizing HF and minimizing SP. These optimal points exhibit a pattern at the higher HF values, whereas HF increases there seems to be a slight upward trend in SP. The optimal points identified represent the best conditions for maximizing HF while aiming to minimize SP, reflecting a balanced approach within the imposed constraints. A slight increase in SP is observed with higher HF values, indicating a complex interdependency between these parameters. This increase is predictable due to intensified particle impacts and dynamic gas interactions inherent in higher HF. Despite this, the conditions remain optimal, enhancing particle energy and bonding while maintaining SP at safe levels, with a maximum of 0.405 MPa, which is 47.32% lower than the upper bound and 22.07% higher than the lower bound, respectively, aligning closely with the stated objectives. This indicates a possible correlation between the two objectives at these higher HF values, indicating a more complex relationship, with perhaps multiple local optima. The slight upward trend in SP with higher HF values among the optimal points suggests that there may be an increase in stress within the material as the HF increases. This could be related to the higher particle impact velocities or temperatures that reduce porosity and increase bond strength but also may introduce residual stress into the coating [100].

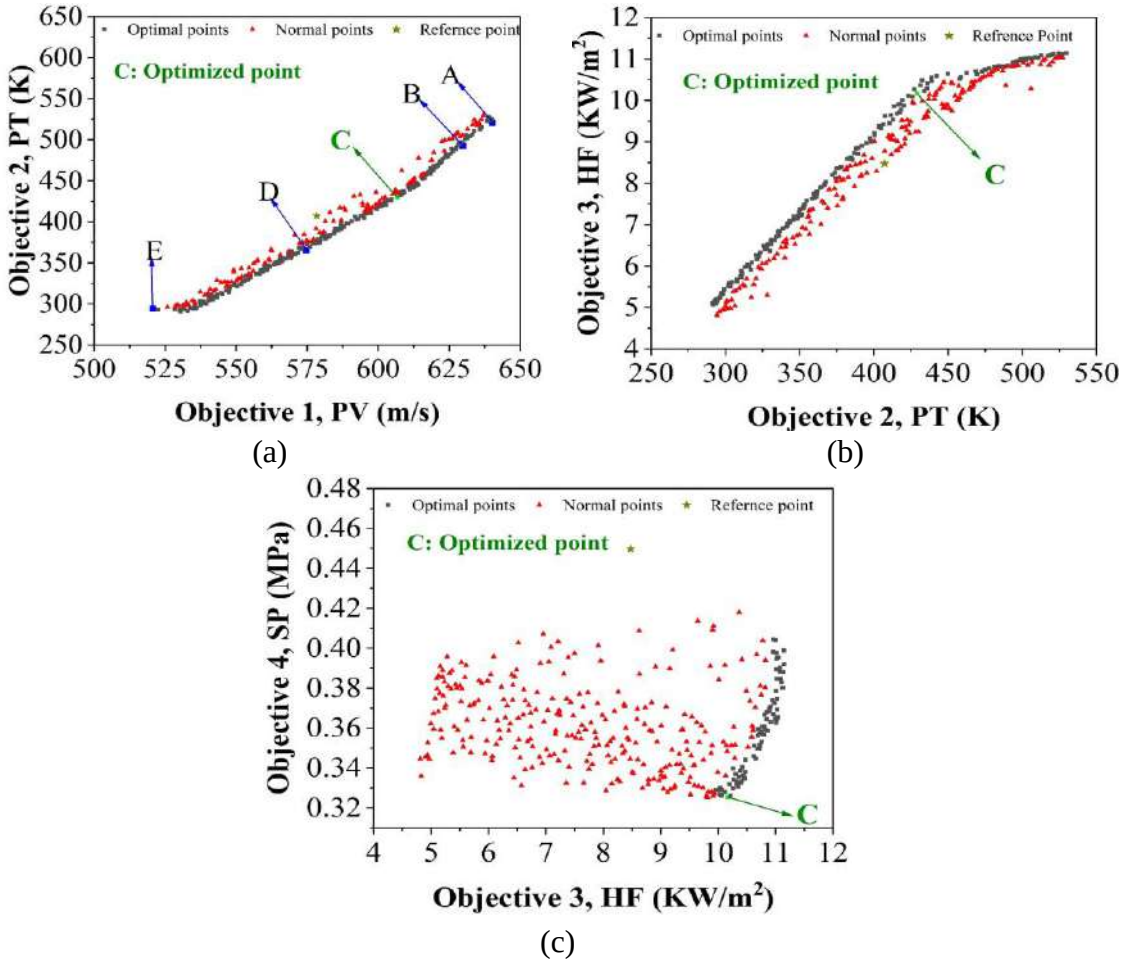

Figure 4.15 Pareto fronts in three pairwise comparisons (a) Objective 1 (PV) and Objective 2 (PT), (b) Objective 2 (PT) and Objective 3 (HF), and (c) Objective 3 (HF) and Objective 4 (SP)

To confirm whether the RSM-DF and ANN-GA optimization results are accurate or not, CFD simulations were performed on the optimized geometric parameters and compared with the baseline nozzle. The comparison of baseline and optimized nozzle geometric and response parameters is summarized in Table 4.6. The baseline nozzle was defined by $L_c = 20$ mm, $L_d = 200$ mm, $D_{id} = 1.8$ mm, $L_i = 20$ mm, and $D_e = 7$ mm, whereas the RSM-DF and ANN-GA produced modified geometric combinations with improved response behavior. The CFD results show that the baseline nozzle gives PV = 578.38 m/s, PT = 407.2 K, HF = 8.477 kW/m^2, and SP = 0.450 MPa, while the optimized configurations improve the overall nozzle performance. In particular, the ANN-GA nozzle gives PV =

620.7 m/s, PT = 409.3 K, HF = 9.807 kW/m^2, and SP = 0.356 MPa, whereas the RSM-DF nozzle gives PV = 630.12 m/s, PT = 408.9 K, HF = 10.365 kW/m^2, and SP = 0.325 MPa. These results show that the optimized nozzle dimensions produce a clear improvement over the baseline nozzle in terms of particle acceleration, thermal response, and substrate-side behavior.

Table 4.6 Comparison of baseline and optimized nozzle geometric and response parameters

	Design parameters				
	L_c **(mm)**	L_d **(mm)**	D_{id} **(mm)**	L_i **(mm)**	D_e **(mm)**
Baseline	20	200	1.8	20	7
RSM-DF	20	283.68	1.08	30	8.09
ANN-GA	22.85	231.21	1.24	26.27	7.93

	Optimized results				**CFD results**			
	PV (m/s)	**PT (K)**	**HF (KW/m^2)**	**SP (MPa)**	**PV (m/s)**	**PT (K)**	**HF (KW/m^2)**	**SP (MPa)**
Baseline	--	--	--	--	578.38	407.2	8.477	0.450
RSM-DF	630.7	425.2	9.995	0.326	630.12	408.9	10.365	0.325
ANN-GA	606.8	429.2	10.168	0.325	620.7	409.3	9.807	0.356

The reproducibility of the selected Pareto solutions was further examined by analyzing five different design points, namely A, B, C, D, and E, taken from the ANN-GA Pareto-optimal front as shown in Figure 4.15(a). The absolute error (%) associated with these reproductions is summarized in Table 4.7. The comparison between GA results and CFD results shows that the optimized points remain in acceptable agreement, which confirms that the selected Pareto solutions are numerically reliable. Among these points, Point C represents the optimized solution retained for further interpretation, with GA values of PV = 606.8 m/s, PT = 429.2 K, HF = 10.168 kW/m^2, and SP = 0.325 MPa, while the corresponding CFD values are PV = 620.7 m/s, PT = 409.3 K, HF = 9.807 kW/m^2, and SP = 0.356 MPa. Thus, the selected optimum point remains physically meaningful and computationally reproducible within the nozzle-design framework.

Table 4.7 Detailed validation of the selected Pareto-optimal front for CD nozzle optimization

Point	GA results				CFD results				Error (%)			
	PV (m/s)	PT (K)	HF (KW/m^2)	SP (MPa)	PV (m/s)	PT (K)	HF (KW/m^2)	SP (MPa)	PV (m/s)	PT (K)	HF (KW/m^2)	SP (MPa)
A	640.2	520.5	10.9	0.352	640.8	506.2	10.5	0.349	0.09	2.75	3.67	0.85
B	629.8	492.7	10.8	0.346	636.2	479.2	10.7	0.349	1.01	2.74	0.93	0.87
C	606.8	429.2	10.168	0.325	620.7	409.3	9.807	0.356	2.30	4.63	3.55	9.53
D	574.7	365.1	7.76	0.347	592.5	352.3	7.89	0.352	3.09	3.5	1.68	1.44
E	520.6	294.4	5.20	0.386	503.9	307.2	4.85	0.409	3.2	4.34	6.73	5.95

The improvement rate of each factor and response is depicted in Figure 4.16, where the positive and negative signs indicate overall reduction and enhancement when compared to the baseline model. Optimizing L_c to 22.85 mm using the ANN-GA model markedly improves PV to 620.7 m/s and HF to 9.807 kW/m^2, showing enhanced particle acceleration and heating efficiency. This optimization results in significant performance benefits, as L_d increases PV by up to 80 m/s and DE by up to 50 mm/s under identical gas conditions [25]. The ANN-GA model achieves more stable enhancements in nozzle design with minimal variation in dimensions, showing only a 15.6% change from the baseline. This contrasts with the RSM-DF model, which exhibits a maximum variation of 50% in L_i and 41.8% in L_d, and therefore shows that the ANN-GA approach is more stable in terms of geometric refinement. ANN-GA shows significant improvement in all four responses, and consequently it can be considered an effective model to achieve the desired objectives.

To verify the accuracy of these models further, the comparison analysis of PV and PT for different D_p values from 5 to 60 μm between the baseline nozzle and the optimized nozzles is shown in Figure 4.17. The baseline and optimized nozzles show a uniform reduction in PV as D_p increases, serving as a standard comparison. However, both RSM-DF and ANN-GA performed well and gave consistently higher PV in comparison with the baseline nozzle. Unlike PV, the PT values initially increase around 20 μm and then start decreasing in all cases, and ANN-GA provides the maximum PT compared with the baseline nozzle. It is shown that the PV and PT for 60 μm improved by 8.91% and 5.32% for RSM-DF,

and by 2.75% and 1.59% for ANN-GA, respectively, in comparison with the baseline model. These comparisons show that the optimized nozzle conditions remain effective even when the D_p is varied over a wider range.

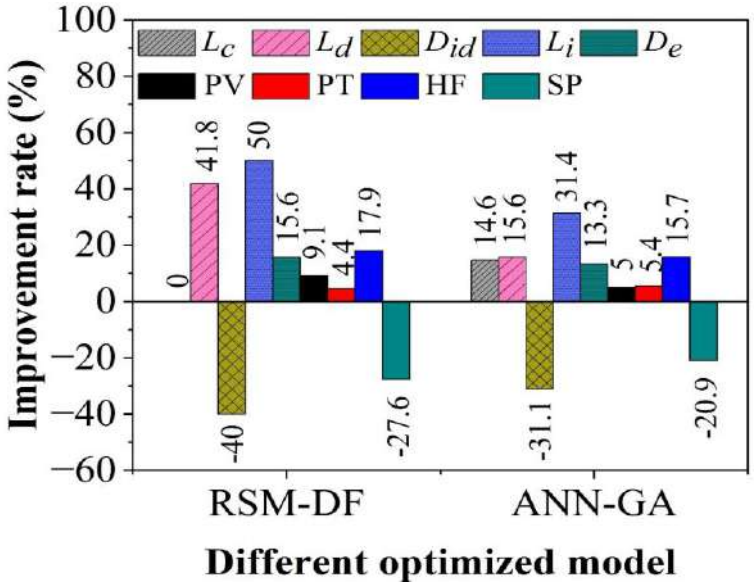

Figure 4.16 Model performance comparison: RSM-DF vs. ANN-GA

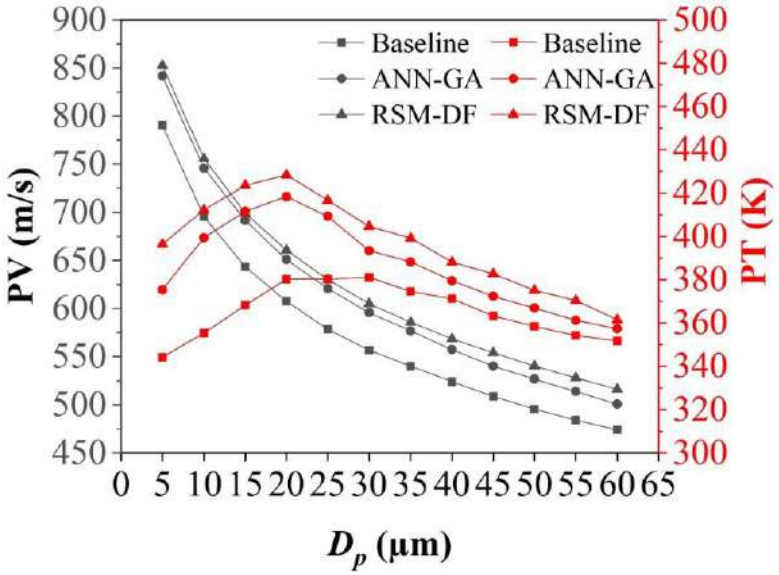

Figure 4.17 Impact of particle diameter on PV and PT

Figure 4.18 presents the particle behavior ranging from 5 to 60 μm in the velocity contour of the baseline and ANN-GA optimized nozzle. Ideally, both nozzles minimize flow

separation and the resulting shockwaves, as these can affect PV and direction. The gas velocities in the baseline range up to around 930 m/s, while in ANN-GA they reach up to 1004 m/s, and therefore accelerate the particles to higher speeds, which could be beneficial for the CS process. The ANN-GA optimized nozzle, with its extended L_d of 231.21 mm and increased D_e of 7.93 mm, compared to the baseline model of 200 mm and 7 mm, achieves gas velocities significantly higher than the baseline. This configuration minimizes turbulence and maximizes kinetic energy transmission, leading to accelerated particle velocities, improved uniformity in particle distribution, and enhanced coating efficiency [25]. In the baseline nozzle, the particles are clustered in certain areas, whereas ANN-GA shows a slightly more uniform distribution toward the nozzle exit. A more uniform particle distribution can lead to a more consistent coating.

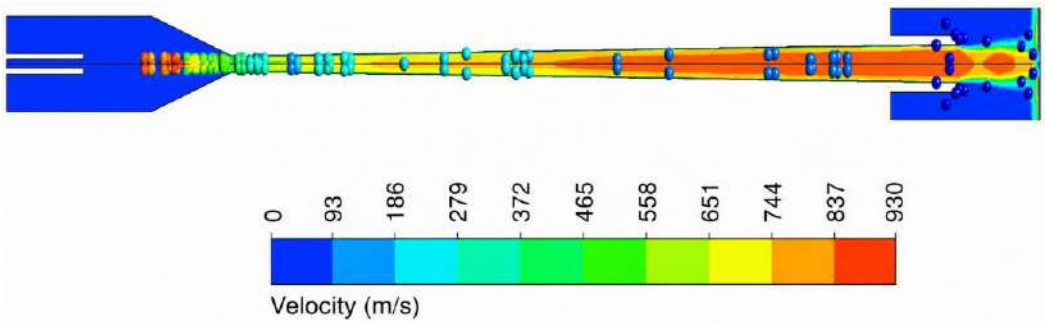

(a)

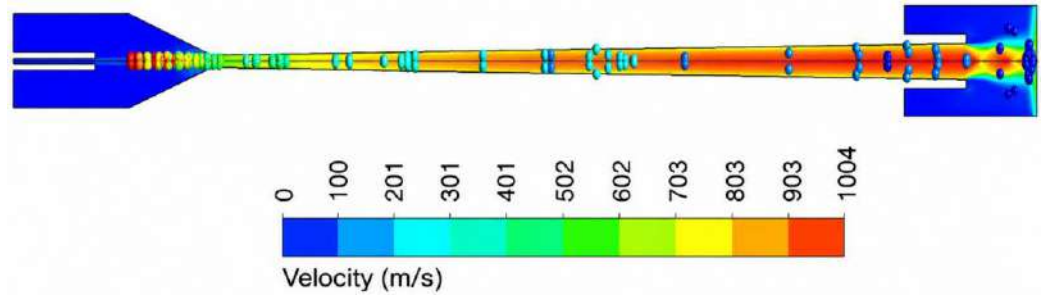

(b)

Figure 4.18 The behavior when the particles of different sizes 5 to 60 (μm) are injected along with gas velocity contour (a) Baseline nozzle, (b) Optimized ANN-GA nozzle

The gas temperature distribution comparison is shown in Figure 4.19. The peak temperatures are localized near the throat and the initial segment of the expansion area,

with a progressive reduction toward the exit. The optimized ANN-GA nozzle shows a comparatively more uniform temperature throughout the expansion section, which might be important for coating materials [101]. This observation indicates that the gas and particles undergo efficient heating in the most critical area and are then allowed to cool slightly. This mechanism potentially prevents excessive heating, while still ensuring that the temperatures remain sufficiently high to facilitate the effective deformation of particles upon impact [90].

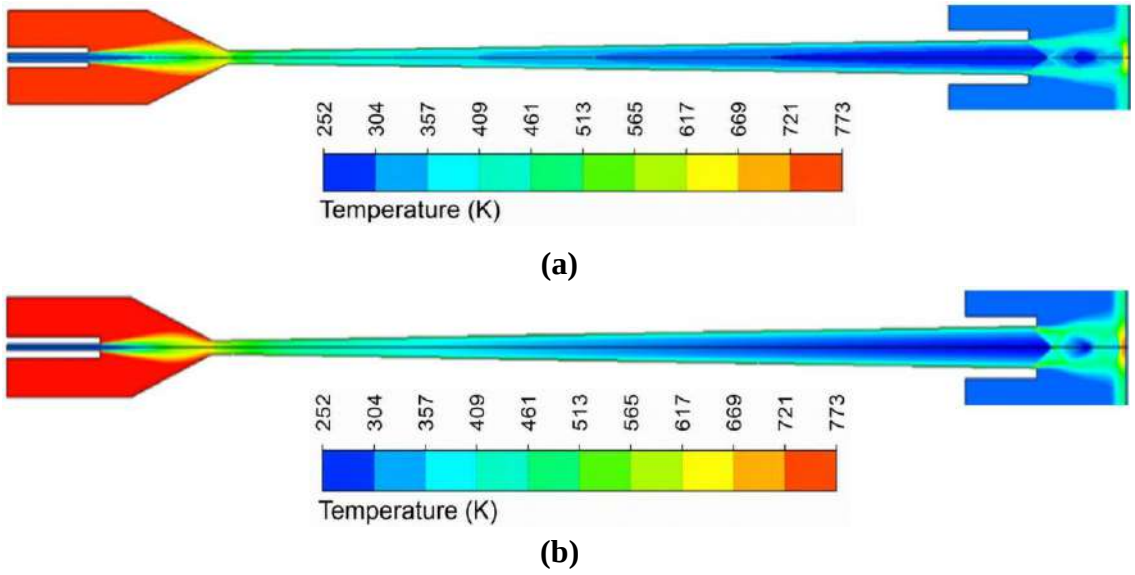

Figure 4.19 Gas temperature distribution comparison (a) Baseline nozzle, (b) Optimized ANN-GA nozzle

The comparison between the baseline and optimized nozzles at different particle injection pressures is shown in Figure 4.20. The propulsion gas enters at pressure of 3 MPa and 4 MPa, with a constant temperature of 773 K. The pressure of the carrier gas changes such that the pressure differential (ΔP) ranges from 0 to 0.5 MPa at equal intervals, while the other conditions were selected the same as in the previous case. It is clear that PV increases for the optimized nozzle. The average PV for the baseline nozzle is 568.4 m/s and 599.6 m/s, and the values for the RSM-DF optimized nozzle are 626.2 m/s and 657.7 m/s, while those for ANN-GA are 612.4 m/s and 643.6 m/s corresponding to 3 MPa and 4 MPa. Hence, the overall improvement rate suggests that PV is approximately 9.93% higher for

RSM-DF and 7.54% higher for ANN-GA. In the baseline model, based on the average results obtained at pressures 3 MPa and 4 MPa, PT is 4.3% lower than the target temperature of 415 K, while for the optimized RSM-DF model, PT is 11.03% higher and for ANN-GA, the variation is only 0.54%. HF on the substrate surface is 55.26% higher for the RSM-DF nozzle and 34.2% higher for the ANN-GA nozzle than the baseline nozzle, whereas SP is significantly reduced by 24.3% and 18.6% on average for the RSM-DF and ANN-GA models. Based on the results and overall analysis of four responses under 3 MPa and 4 MPa, ANN-GA is considered the best optimized model because it more accurately fulfills the objectives of this study. This is likely because, while RSM-DF shows better performance in terms of PV and HF, ANN-GA provides a more balanced optimization across all metrics. Particularly, its precise PT control is crucial for ensuring the quality of the coating without damaging the substrate or the particles.

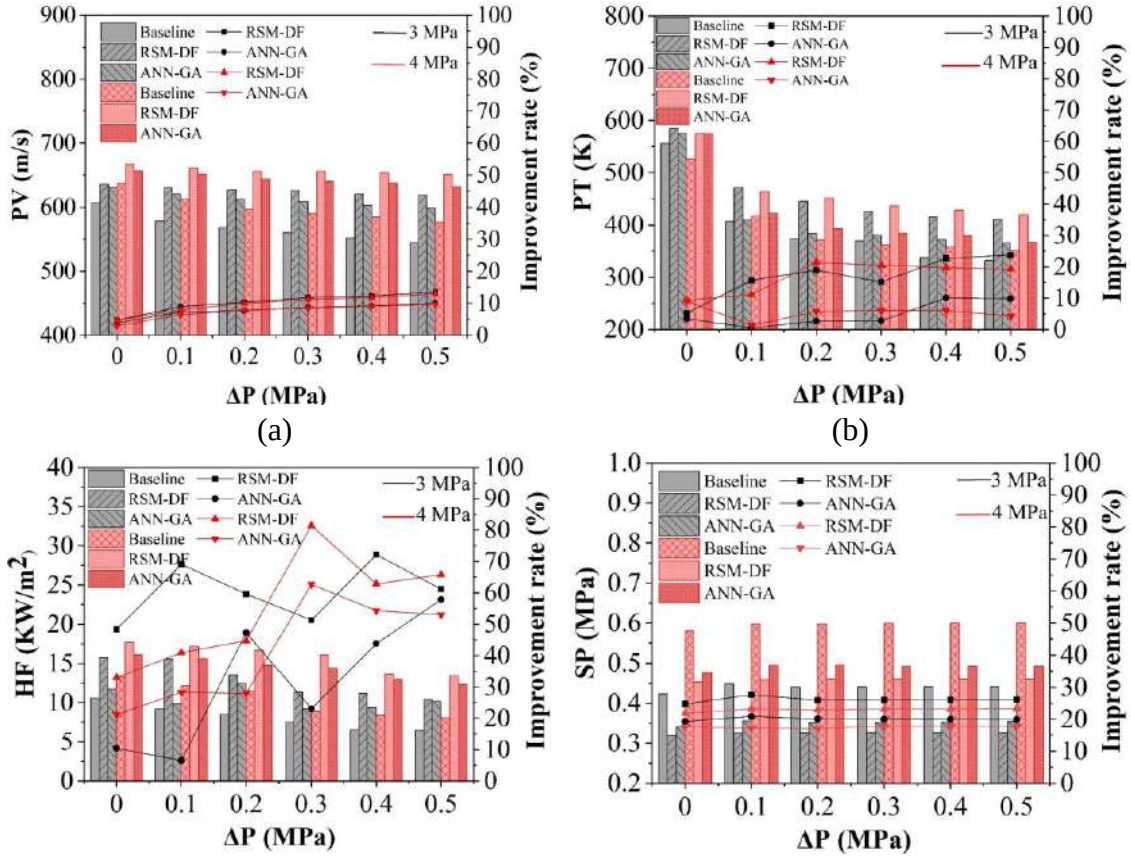

Figure 4.20 Comparison of results between the baseline and optimized nozzle for different particle injection pressure corresponds to 3 MPa and 4 MPa gas inlet pressure for (a) PV, (b) PT, (c) HF, and (d) SP

The axial comparison of the baseline and optimized nozzles is shown in Figure 4.21. Gas velocity is an important factor in determining the particle impact velocity, which is essential for the quality of coatings [102]. As the gas moves through the nozzle, its velocity increases significantly from the convergent section to the divergent section after passing the throat. The ANN-GA nozzle design shows the highest peak in gas velocity compared to the baseline and RSM-DF nozzle designs, which suggests that ANN-GA is optimized for better performance in particle acceleration. The ANN-GA nozzle particle impact velocity is approximately 5% higher than the baseline nozzle, and this improvement in PV can lead to better adhesion and performance. The gas temperature rises sharply in the convergent section, reaches a maximum near the throat, and then falls in the divergent section. With a constant D_t, longer L_c leads to higher axial G_t due to better heat exchange [50]. The ANN-GA method keeps the PT at the throat about 5.4% higher than the standard nozzle and maintains this elevated G_t to the substrate surface. However, RSM-DF maintains the highest gas temperature compared with ANN-GA and the baseline nozzle over a greater distance due to its longer L_d. ANN-GA maintain a similar temperature distribution to RSM-DF despite having a shorter L_d. This suggests that the ANN-GA nozzle is more effective in retaining heat, which is critical for ensuring the particles remain sufficiently malleable for effective coating during CS [100]. For PV along the axial distance, the ANN-GA nozzle seems to maintain the highest velocities across the span, closely followed by RSM-DF, with the baseline exhibiting the lowest velocities. For PT along the same axial distance, the ANN-GA nozzle is very close to RSM-DF, and both are above the baseline, which suggests that both optimized nozzles manage to heat the particles more effectively than the baseline nozzle, but the ANN-GA nozzle's consistency and peak in both metrics suggest that it may provide the best results for the CS process.

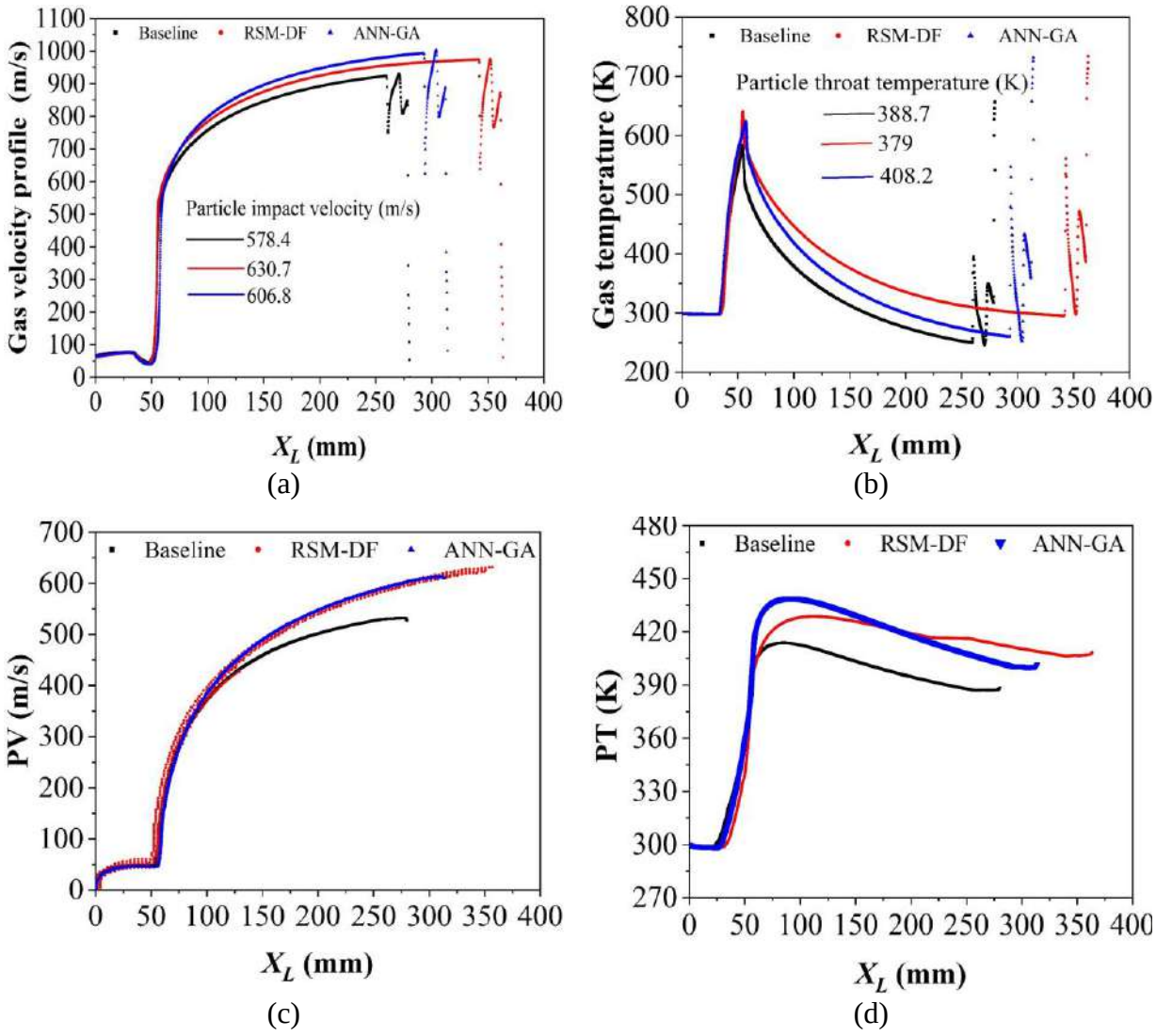

Figure 4.21 Axial comparison of baseline and optimized nozzle (a) Gas velocity, (b) Gas temperature, (c) PV, and (d) PT

The radial comparison of baseline and optimized nozzle is presented in Figure 4.22. HF is highest at the center and decreases sharply along the radial direction, which means heat intensity decreases with distance due to dispersion and cooling [32]. ANN-GA shows a higher distribution of HF in comparison with the baseline model, and this might be more stable and efficient for nozzle performance. SP is also higher at the center of the nozzle and decreases as the distance from the center increases. This trend is typical for fluid flow

exiting a nozzle, where the pressure is greatest at the center and decreases toward the edges due to the flow expansion and interaction with the ambient environment.

Both optimized nozzle conditions show an almost similar pattern of rapid decrease in SP as the distance from the nozzle center increases. However, there are large variations in the pressure values between the optimized nozzles and the baseline nozzle. Based on the area-weighted average, the reduction in SP for RSM-DF is 27.6%, and that for ANN-GA is 20.9% compared with the baseline model. RSM-DF uses a large L_d of 283.68 mm and a larger D_e of 8.09 mm, which contributes to a smoother and more expanded gas flow. This reduces the SP by allowing the gas to decelerate and cool effectively before exiting the nozzle. Similarly, ANN-GA extends L_d to 231.21 mm and uses a minimal D_e of 7.93 mm, compared with RSM-DF, and optimizes the flow dynamics further to achieve efficient particle acceleration with a moderately reduced SP, which is critical for reducing particle bounce-back and ensuring a denser, more uniform coating deposition on the substrate. In summary, both RSM-DF and ANN-GA nozzles are designed to optimize flow dynamics, with RSM-DF focusing on a smoother gas flow and ANN-GA further enhancing particle acceleration efficiency while maintaining a reduced SP for improved coating deposition quality [98].

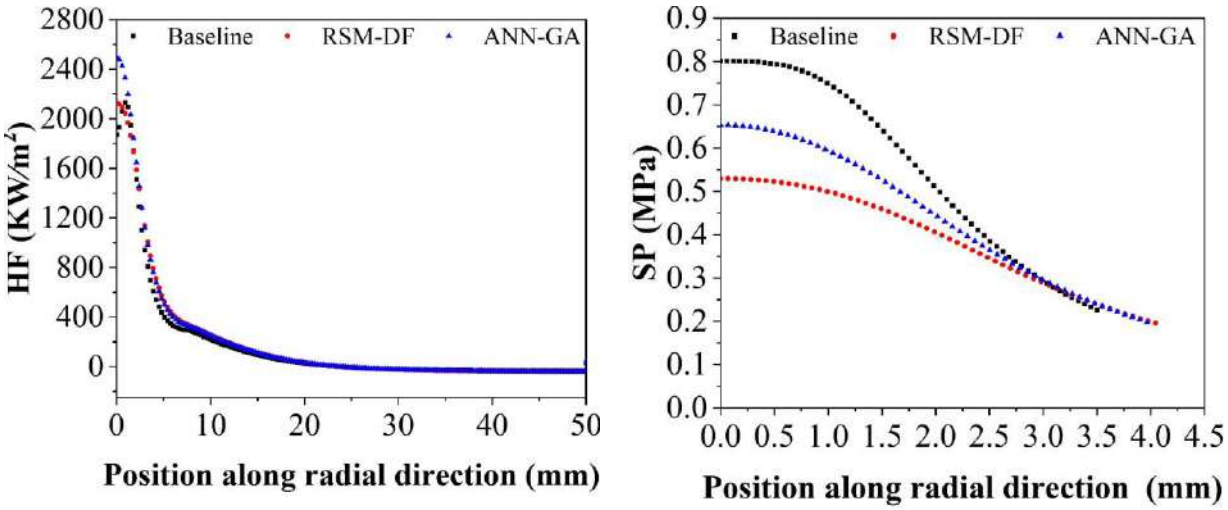

(a) (b)

Figure 4.22 Radial comparison of baseline and optimized nozzle (a) HF and (b) SP

4.4 Process Parameter Effects and Optimization

CFD-based MOO was carried out for the HPCS process by combining CFD simulations with FCCD, RSM, and NSGA-II. The final compromise solutions were selected using TOPSIS and VIKOR with hybrid AHP-EWM weighting. In this stage, G_p, G_t, D_p, D_t, and SoD were considered as the selected input parameters, while PV, PT, and RD were retained as the desired responses for Cu deposition. This formulation was required because high PV, controlled PT, and low RD do not necessarily occur under the same process conditions. A sufficient PV is necessary to surpass the V_{cr} and cause severe plastic deformation and interfacial jetting to enhance metallurgical bonding with the substrate. PT is equally important because too-cold particles will bounce instead of bonding, while hot particles will oxidize or undergo softening and damage the integrity of the coating. At the same time, limiting RD can be used to create a narrower and more uniform particle footprint, which reduces overspray and improves deposition precision. Therefore, the selected process parameters were optimized together to obtain improved particle impact conditions and coating-oriented performance.

Gas-particle dynamics in CS affect how the acceleration of particles in a supersonic flow is calculated, which in turn affects PV as well as the impact behavior on the substrate. Figure 4.23 shows the gas velocity and PV profiles along the nozzle axis for $D_p = 25$ µm with different combinations of G_p and G_t. The gas velocity profiles for G_p (2–4 MPa) and G_t (633–913 K) are shown in Figure 4.23(a-c). Increasing G_p enhances isentropic expansion, which generates higher Mach numbers and exit velocities. The flow is slightly under-expanded at 2 MPa, which results in weak shock structures near the exit. Distinct shock cells were developed at 3 MPa, indicating stronger shock structures associated with under- expanded flow conditions. A higher exit velocity at 4 MPa provides a collimated jet with reduced shock-cell height. An increase in G_t raises the velocity, according to $v = M\sqrt{\gamma RT}$, where v is the gas velocity, M is the Mach number, γ is the ratio of specific heats, R is the gas constant, and T is the gas temperature, which increases the exit velocity at a given Mach number [103]. Figure 4.23(d-f) shows that the PV of 25 µm Cu particles

increases with G_p and G_t due to a stronger drag force, and PV follows the gas-phase velocity pattern directly.

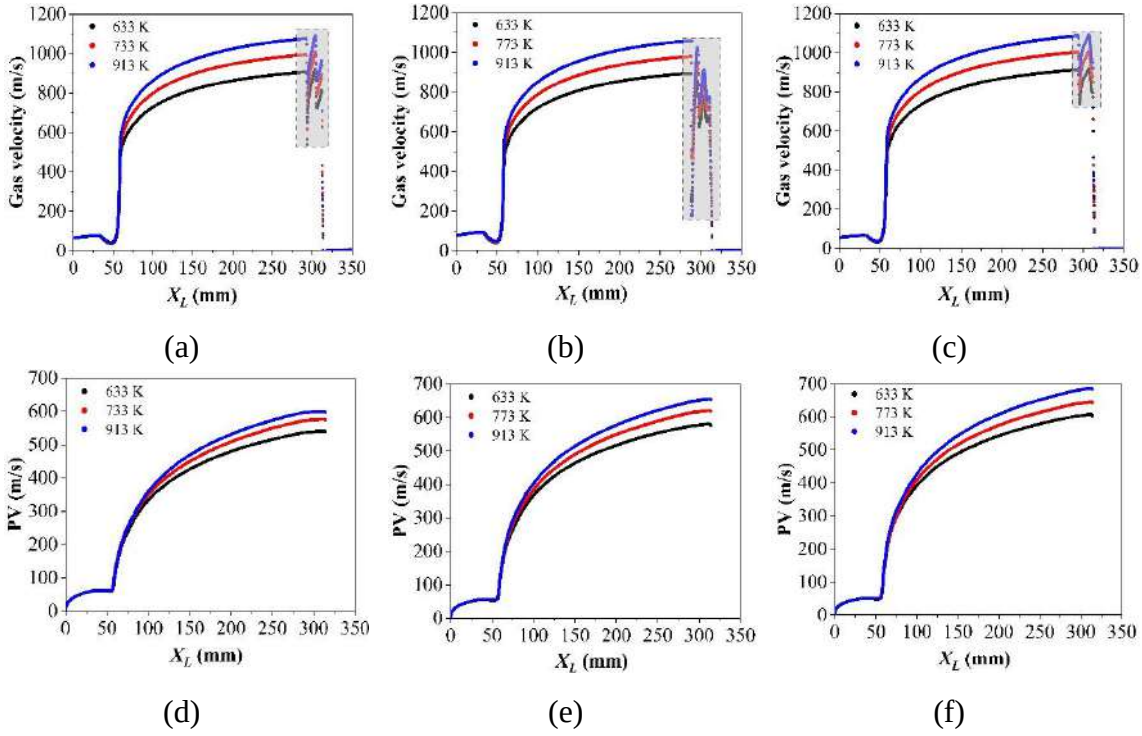

Figure 4.23 Gas velocity (a−c) and PV (d−f) along X_L at different G_p: (a, d) 2 MPa, (b, e) 3 MPa, (c, f) 4 MPa for various G_t

Figure 4.24 shows the particle dispersion in the radial direction by illustrating how PV varies. PV is enhanced by increasing G_p and G_t, but jet widening further decreases the uniformity of the coating along the radial direction at the substrate surface, as depicted in Figure 4.24(a-c).

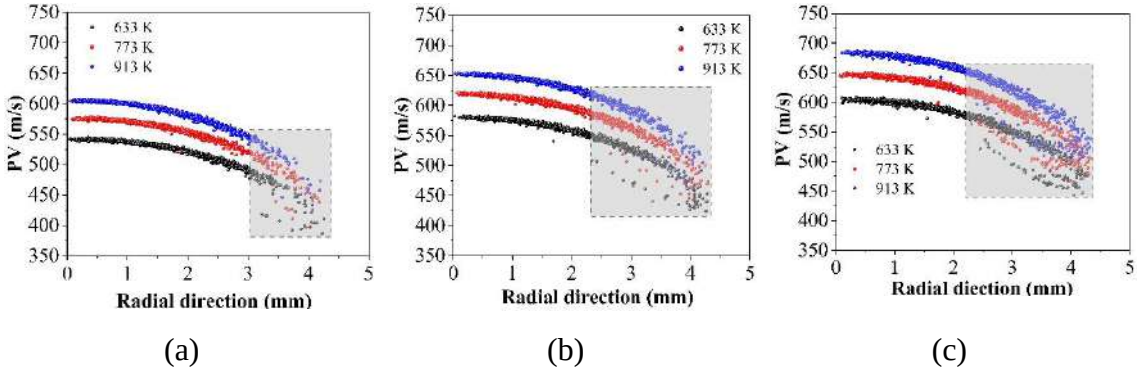

Figure 4.24 Variation of PV along the radial direction at different G_p: (a) 2 MPa, (b) 3 MPa, (c) 4 MPa for various G_t

4.4.1 Numerical Justification and Model Adequacy

To validate the one-way coupled Eulerian-Lagrangian treatment in HPCS, the mass loading (Φ_m), particle volume fraction (Φ_v), and Stokes number (St) were evaluated under different combinations of G_p, G_t, and D_t using Eqs. (3.11−3.13). The computed Φ_v lies between 8.5 and 9.9×10^{-7}, which means that particles do not contribute significantly to the carrier-gas turbulence (i.e.,<10^{-6}) [104]. The mass loading remains dilute ($\Phi_m \approx 0.6 - 1.1\%$), which is consistent with typical HPCS operations. In addition, the St is much greater than 1 when $D_p = 5$, 25, and 45 µm, which is a strong indication that the particles are highly inertial and that the momentum feedback to the gas is negligible. Consequently, there is no need to introduce additional source terms, S_k in Eq. (3.5) and S_ε in Eq. (3.6), which were therefore neglected [94]. The corresponding values of Φ_v, Φ_m, and St are summarized in Table 4.8.

Table 4.8 Mass loading, volume fraction, and Stokes number for different combinations

G_p (MPa)	G_t (K)	D_t (mm)	Volume fraction (10^{-7})	Mass loading (%)	Stokes number (St)		
			Φ_v	Φ_m	5 µm	25 µm	45 µm
2	773	4	9.26	0.94	61	1546	5009
	913	3.25	8.55	1.02	66	1657	5371
3	633	4	9.91	0.57	57	1430	4635
	913	2.5	9.01	1.07	64	1621	5254
4	633	2.5	9.37	1.04	60	1517	4915
	773	3.25	8.64	0.71	65	1649	5345

The values reported in Table 4.8 further show that the selected gas-particle flow remained within the dilute loading regime throughout the investigated cases. This confirms that the adopted one-way coupling assumption is acceptable for the present HPCS simulations, because the gas phase governs particle motion, while the feedback from the particle phase to the gas phase remains negligible. In this way, the evaluated Φ_v, Φ_m, and St provide the physical basis for retaining the one-way coupled Eulerian-Lagrangian framework in numerical investigation.

A comprehensive literature review on CFD modeling and validation of HPCS nozzle-jet flow has shown that $k-\varepsilon$ type turbulence closure can reproduce nozzle wall-pressure and in-flight PV trends in close agreement with experimental measurements [43]. In the study, the turbulence model was selected by directly comparing numerical predictions with the experimental data of Li et al. [87]. Four models, viz. Standard $k-\varepsilon$, Realizable $k-\varepsilon$, RNG $k-\varepsilon$, and SST $k-\omega$ were evaluated under two test conditions, as presented in Table 4.9, for a G_p of 2 MPa using N_2 gas. For both cases, the Standard $k-\varepsilon$ model resulted in the lowest PV deviation from the measured values ($|\Delta|$=14.68 and 4.73, respectively), followed by the RNG $k-\varepsilon$ model and the other models. Therefore, the Standard $k-\varepsilon$ model was adopted for all subsequent simulations in this study [41], [54].

Table 4.9 Comparison of predicted PV (m/s), using different turbulence models with experimental result [87]

G_t (K) / D_p (µm)	Li et al. [87]	Standard $k-\varepsilon$	Realizable $k-\varepsilon$	RNG $k-\varepsilon$	SST $k-\omega$
503 / 9.6	552.76	567.44	582.92	578.94	581.61
538 / 32.6	432.11	427.37	424.68	437.17	437.81

The validation of the developed models was based on the agreement between the simulated and predicted values of PV, PT, and RD, while the regression modeling was used to obtain predictive equations within the specified design-parameter range. In this way, the statistical validation establishes the reliability of the developed response models, and the regression formulations provide the numerical basis for the subsequent sensitivity analysis, response-surface interpretation, and MOO of the selected parameters. The ANOVA was used in this study to determine the statistical significance of the process parameters and to assess the statistical adequacy of the RSM regression models. The values of the coefficient of determination (R^2) for PV, PT, and RD were 0.9998, 0.9919, and 0.9820, respectively. This implies that the unexplained variance is 0.02%, 0.81%, and 1.8%, which are very small, so there is a high level of similarity between the simulated and predicted values. The small differences between the adjusted and predicted R^2 values, all below 0.20, further confirming the robustness of the models. The RD model exhibited

a lower fit than the PV and PT models, but it still exceeds the 85% standard [75]. As shown in Table 4.10, all three models are statistically significant, as indicated by p-values < 0.0001 and high F-values of 6546.09, 177.31, and 79.24 for PV, PT, and RD, respectively. It can be observed that for PV, all the single-factor terms, G_p, G_t, D_p, D_t, and SoD are statistically significant factors ($p < 0.001$). G_p^2, G_t^2, and D_p^2 have statistically significant quadratic effects, whereas $G_p * G_t$, $G_p * D_p$, $G_p * D_t$, $G_p *$ SoD, $G_t * D_p$, $G_t * D_t$, $D_p * D_t$, and $D_t *$ SoD have statistically significant effects among the two-factor interaction terms. The ranking of individual terms by significance can be determined using the F-value, which leads to the following order:$D_p > G_t > G_p > D_p^2 > G_t * D_p > G_p * D_p >$ SoD $> D_p * D_t > G_p * G_t > G_p * D_t > D_t *$ SoD $> D_t > G_p *$ SoD $> G_t^2 > G_p^2 > G_t * D_t$.This indicates that D_p is the most dominant factor influencing PV. For PT, it can be observed that among the single-factor linear terms, G_p, G_t, D_p, and D_t are statistically significant. In the quadratic term only D_p^2 is significant. In the two-factor interaction terms, $G_p * D_p$, $G_p * D_t$, $G_t * D_p$, $G_t * D_t$, $D_p * D_t$, and $D_p *$ SoD are significant. By analyzing the F-values, the significance order of the factors can be determined as follows: $G_t > G_t * D_p > D_p^2 > D_p > D_t > G_p * D_p > G_t * D_t > D_p * D_t > G_p * D_t > G_p > D_p *$ SoD. From these results, it is evident that G_t is the most significant factor influencing PT. Based on the F-values, the order of significance within the RD model can be determined as follows: $D_t > D_p > G_p * D_t > G_p > D_t^2 > D_p^2 > G_p * D_p > G_t * D_t >$ SoD $>$ SoD$^2 > G_p^2 > G_p * G_t$. This suggests that D_t remains the most significant factor affecting RD. Overall, the ANOVA results confirm that the developed models are statistically robust and that D_p and D_t play key roles in influencing particle kinematics and coating uniformity in the CS process.

Table 4.10 ANOVA results across multiple response variables

Source	**Responses**					
	PV		**PT**		**RD**	
	F-value	**p-value**	**F-value**	**p-value**	**F-value**	**p-value**
Model	6546.09	< 0.0001	177.31	< 0.0001	79.24	< 0.0001
G_p	6089.46	< 0.0001	7.95	0.0086	37.43	0.0002

G_t	8939.60	< 0.0001	2732.53	< 0.0001	3.37	0.0478
D_p	107895.2	< 0.0001	86.98	< 0.0001	475.20	< 0.0001
D_t	34.26	< 0.0001	64.83	< 0.0001	721.60	< 0.0001
SoD	197.22	< 0.0001	3.83	0.0600	18.87	0.0082
$G_p * G_t$	93.87	< 0.0001	0.5334	0.4710	4.42	0.1800
$G_p * D_p$	210.18	< 0.0001	60.08	< 0.0001	17.55	0.0052
$G_p * D_t$	38.86	< 0.0001	10.21	0.0034	210.47	< 0.0001
G_p * **SoD**	19.03	0.0001	2.08	0.1604	1.65	0.6546
$G_t * D_p$	1223.62	< 0.0001	285.30	< 0.0001	1.17	0.7839
$G_t * D_t$	6.03	0.0203	38.77	< 0.0001	22.67	0.0043
G_t * **SoD**	2.78	0.1065	0.0602	0.8079	0.0051	0.8307
$D_p * D_t$	116.92	< 0.0001	13.42	0.0010	0.0153	0.9914
D_p * **SoD**	2.55	0.1212	7.57	0.0101	0.4026	0.4454
D_t * **SoD**	37.27	< 0.0001	0.0784	0.7814	0.6740	0.7931
G_p^2	10.28	0.0033	0.6978	0.4103	8.31	0.3055
G_t^2	10.52	0.0030	0.6556	0.4247	0.1616	0.1102
D_p^2	1935.69	< 0.0001	44.60	< 0.0001	20.64	0.0005
D_t^2	1.91	0.1771	0.3347	0.5674	39.58	0.0006
SoD²	1.07	0.3091	2.49	0.1252	7.80	0.0612
PV	R^2 = 0.9998		adjusted R^2 = 0.9996		predicted R^2 = 0.9992	
PT	R^2 = 0.9919		adjusted R^2 = 0.9863		predicted R^2 = 0.9720	
RD	R^2 = 0.9820		adjusted R^2 = 0.9696		predicted R^2 = 0.9455	

The predicted and actual values of PV, PT, and RD show close agreement, with most data points lying along the regression line, confirming that the RSM models adequately represent the responses, as shown in Figure 4.25. Minor deviations appear in a few cases; however, the overall prediction accuracy remains high. The residual plots in Figure 4.26 show all residuals within ±3.6218 and are randomly scattered, confirming the reliability and consistency of the developed models.

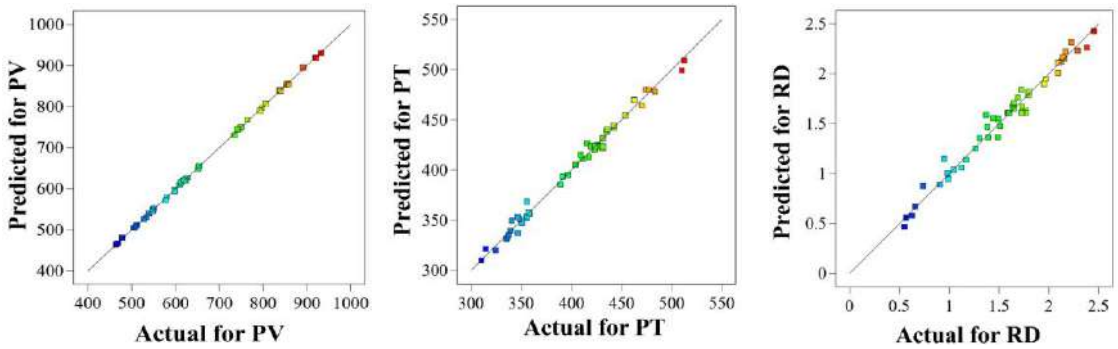

(a) (b) (c)

Figure 4.25 Comparison of predicted and actual values: (a) PV, (b) PT, and (c) RD

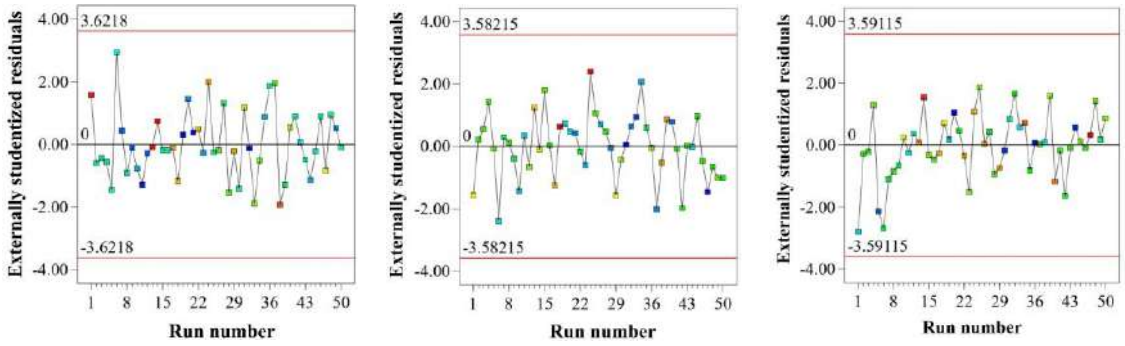

(a) (b) (c)

Figure 4.26 Residual distribution of the regression model: (a) PV, (b) PT, and (c) RD

The following equations were developed to predict the three responses within the specified design space, and the corresponding model coefficients are presented as follows.

$$\begin{aligned}\text{PV} = {} & 354.05 + 50.13G_p + 0.84G_t - 13.9D_p - 14.8D_t - 0.79\text{SoD} + 0.03G_pG_t \\ & + 0.33G_pD_p - 3.81G_pD_t + 0.133G_p\text{SoD} - 0.006G_tD_p + 0.01G_tD_t \\ & + 0.33D_pD_t + 0.25D_t\text{SoD} - 6.53G_p^2 - 0.0003G_t^2 + 0.18D_p^2\end{aligned} \quad (4.5)$$

$$\begin{aligned}\text{PT} = {} & 113.81 + 1.54G_p + 0.35G_t + 5.7D_p - 31.12D_t - 0.38\text{SoD} + 0.42G_pD_p \\ & - 4.61G_pD_t - 0.006G_tD_p + 0.06G_tD_t + 0.26D_pD_t + 0.0099D_p\text{SoD} - 0.07D_p^2\end{aligned} \quad (4.6)$$

$$\begin{aligned}\text{RD} = {} & -4.48 + 1.84G_p - 0.00134G_t - 0.06D_p + 3.77D_t - 0.0305\text{SoD} - \\ & 0002G_pG_t + 0.0031G_pD_p - 0.2893G_pD_t + 0.0006G_tD_t - 0.15G_p^2 + \\ & 0006D_p^2 - 0.594D_t^2 + 0.0006\text{SoD}^2\end{aligned} \quad (4.7)$$

These regression equations show that the three responses were predicted directly in terms of the selected process parameters. Thus, Eqs. (4.5−4.7) provide the predictive basis for the subsequent analysis, 3D response-surface interpretation, and MOO.

In this study, a sensitivity analysis was performed to evaluate the relative influence of process parameters on the three response variables. The sensitivity index was determined using the following relation for each response:

$$\text{sensitivity index} = \frac{\max(k) - \min(k)}{\text{ave}(k)} \tag{4.8}$$

where $\max(k)$ and $\min(k)$ represent the maximum and minimum response values, and $\text{ave}(k)$ denotes the mean value of the response.

The sensitivity histogram shown in Figure 4.27 presents the relative effects of the input parameters G_p, G_t, D_p, D_t, and SoD on PV, PT, and RD. In the case of PV, the sensitivity and ANOVA results indicate that D_p is the strongest factor with a negative sensitivity, which means that larger particles cause a significant decrease in velocity. Conversely, G_p and G_t exhibit moderate positive sensitivities, whereas D_t and SoD show weak sensitivities for PV. In the case of PT, G_t remains the most influential factor with a strong positive sensitivity, followed by G_p and D_p, which supports the dominant role of G_t in increasing PT. D_t has a weak negative effect on PT. In the case of RD, D_t shows positive sensitivity and has the greatest influence on particle dispersion, whereas D_p exhibits negative sensitivity. G_p and SoD show smaller but noticeable positive effects. In general, such a sensitivity analysis provides valuable guidance for design and process parameter selection, which can enhance coating quality in practical CS applications.

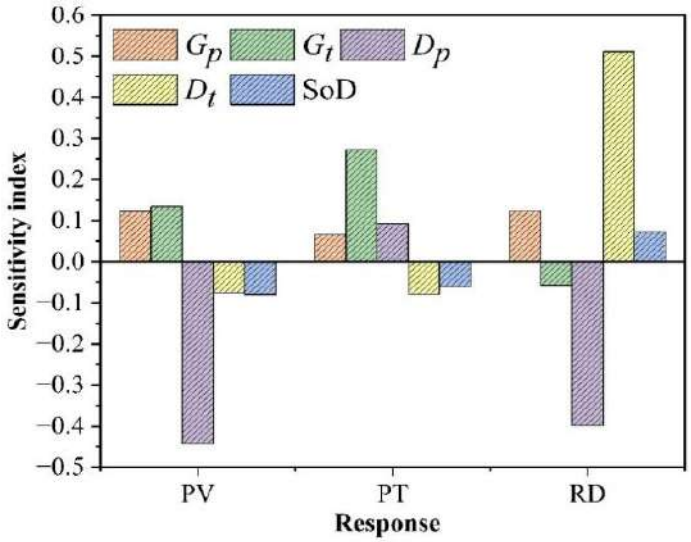

Figure 4.27 Parameter sensitivity histogram

4.4.2 Parametric Effects on Particle Responses

The 3D response surface plots were used to provide a visual analysis to reveal the cumulative effects of process parameters on the output responses using 3D response surface plots. Two parameters were varied while the others were maintained at their central values to observe the interaction effects on the responses. This approach provides useful information regarding the effect of parameter combinations on the dynamics and deposition behavior of particles.

The interactive effect of the significant process parameters on PV is shown in Figure 4.28. Overall, PV tends to increase with G_p and G_t, as shown in Figure 4.28(a), because higher pressure and temperature enhance drag and momentum transfer to the particles. The interactions between $G_p * D_p$ and $G_t * D_p$ are nonlinear, as indicated in Figure 4.28(b) and Figure 4.28(e). PV increases rapidly with increasing G_p and G_t and decreases with increasing D_p due to higher particle inertia and reduced acceleration under drag forces within the nozzle. These curvatures show that smaller particles (<25 μm) obtain greater velocities, particularly with a large G_p (4 MPa) and elevated G_t (~913 K). Figure 4.28(c), Figure 4.28(d), and Figure 4.28(f) indicate that factors involving D_t and SoD have less

significant effects on PV. A small rise in D_t decreases PV, since a larger throat decreases the ratio of the gas expansion and the gas velocity. Similarly, a small SoD increases PV, however, a very short SoD may create bow-shock effects, which decrease particle momentum before collision. Figure 4.28(g) demonstrates the combined effect of D_p and D_t, which indicates that PV decreases with increasing D_p and D_t, and the effect is more pronounced for smaller particles. This indicates that the acceleration efficiency is strongly influenced by particle inertia as well as nozzle geometry. Conversely, the D_t and SoD interaction in Figure 4.28(h) reveals only a slight variation and does not significantly influence PV within the investigated range.

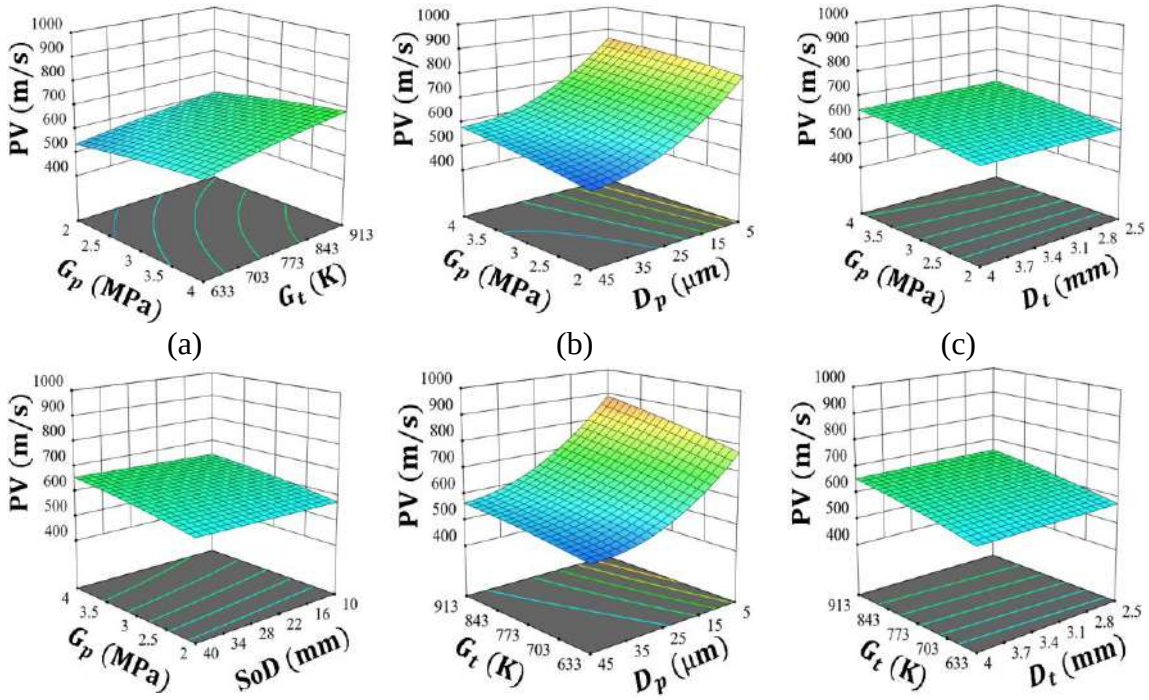

(a) (b) (c)

(d) (e) (f)

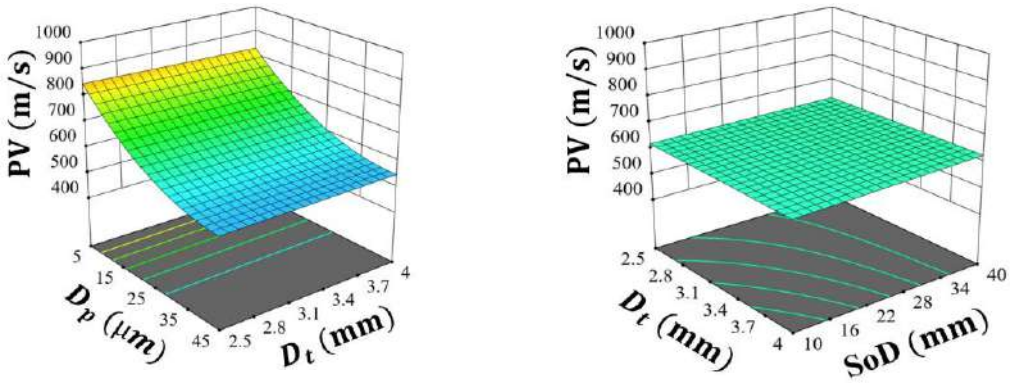

(g) (h)

Figure 4.28 Combined effects of interactions between parameters on PV

The interactive effects of the process parameters on PT are shown in Figure 4.29. Figure 4.29(a) and Figure 4.29(b) reveal that variations in G_p and D_t do not have a significant influence. However, increasing G_p has a minor impact on reducing PT since it accelerates particle motion and decreases the residence time. On the other hand, Figure 4.29(c) indicates that the effects of G_t and D_p on PT are highly nonlinear, with PT increasing at higher G_t and decreasing with larger D_p, since smaller particles (<25 μm) absorb heat more effectively from the gas stream, especially at 850 K. Figure 4.29(d) shows that PT increases steadily with G_t, whereas the impact of D_t is relatively weak. Increasing D_t values result in slight increases in PT due to increased heat-transfer interaction time between the gas and the particle, however, G_t remains the most dominant variable governing heat transfer. Figure 4.29(e) tends to indicate a weak curvature in the D_p and D_t interaction, and the highest PT was recorded with medium-sized particles (~20–25 μm). Larger particles take more time to reach thermal equilibrium, whereas smaller particles heat up rapidly and also cool rapidly. Lastly, Figure 4.29(f) suggests that PT increases moderately at intermediate D_p and moderate SoD (~25–30 mm), whereas very large D_p or extreme SoD values reduce PT due to inefficient heat transfer or excessively rapid cooling.

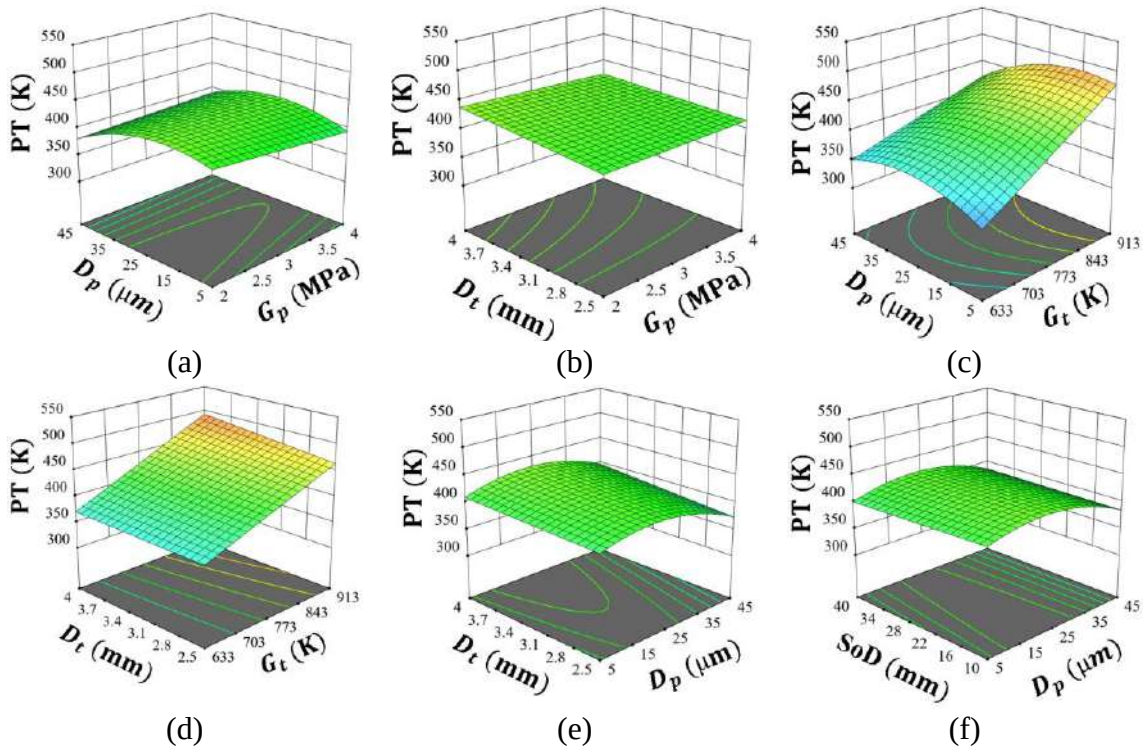

Figure 4.29 Combined effects of interactions between parameters on PT

The interactive effect of the parameters on RD is shown in Figure 4.30. As demonstrated in Figure 4.30(a), RD is almost constant in the tested range, which means that the simultaneous variation of G_p and G_t does not significantly impact particle spread. This stability may be attributed to the combined effects of jet momentum and thermal conditions at the nozzle exit. In Figure 4.30(b), RD rises gradually with reductions in D_p and G_p, which indicates that smaller particles are subjected to greater aerodynamic drag and will tend to deviate more from the core jet. On the other hand, larger particles tend to exhibit reduced dispersion due to increased inertia. Figure 4.30(c), which shows the interaction between G_p and D_t, depicts a slight reduction in RD at larger D_t, which may improve flow uniformity and reduce turbulence. Similarly, Figure 4.30(d) shows that RD is slightly reduced at higher G_t and larger D_t, suggesting improved particle focusing at elevated G_t. Thus, the combined response-surface analysis shows that PV, PT, and RD are governed by different interaction patterns, and the improvement of coating quality requires a balanced combination of particle acceleration, thermal control, and dispersion reduction.

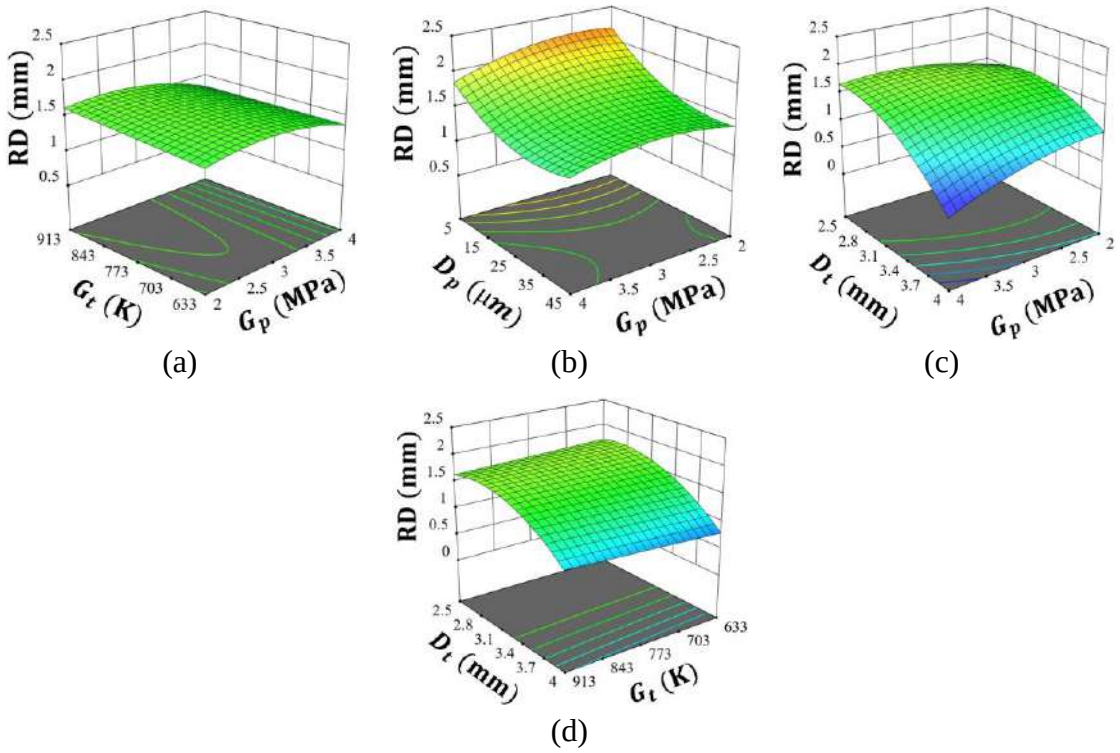

Figure 4.30 Combined effects of interactions between parameters on RD

4.4.3 Pareto Ranking and Optimum Process Window

The NSGA-II algorithm was used to capture the trade-offs between the three objectives and to generate a well-distributed Pareto front. Convergence and diversity were first investigated using a generation test with 1000 generations. As shown in Figure 3.17, the average distance between individuals stabilized after about 400–500 generations at approximately 26.6, indicating that 500 generations were sufficient to obtain stable results.

The Pareto-optimal solutions obtained from NSGA-II for the tri-objective problem are shown in Figure 4.31, where the 3D distribution is presented in Figure 4.31(a) and the 2D projections are presented in Figure 4.31(b–d). The Pareto front clearly shows the competing behavior among PV, PT, and RD, and illustrates the optimization direction required to obtain improved CS performance. Three selected points are denoted as A, B, and C corresponding to the solutions $(PV)_{max}$, $(PT)_{target}$, and $(RD)_{min}$, respectively.

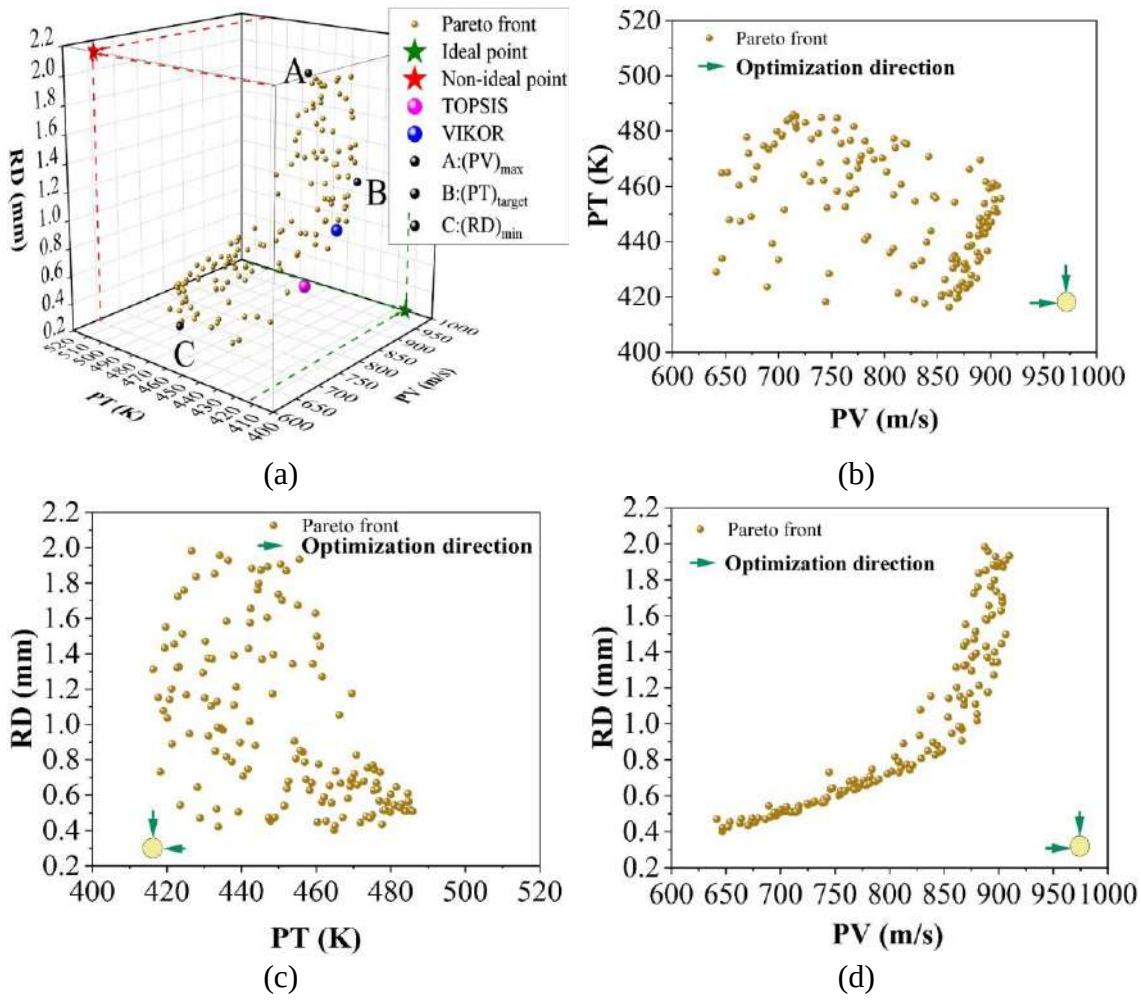

Figure 4.31 Pareto-optimal solutions obtained from NSGA-II for the tri-objective: (a) 3D Pareto front with marked special points and (b–d) 2D projections illustrating trade-offs among objectives and the optimization direction

The criteria weights were determined using the Analytic Hierarchy Process (AHP) and the Entropy Weight Method (EWM). The AHP technique was used to determine the relative importance of the responses as PV, PT, and RD, through pairwise comparisons based on Saaty's scale, and the corresponding scale used for judgment is presented in Table 4.11 [96]. The corresponding AHP pairwise comparison matrix and weights are presented in Table 4.12. PV was rated much higher than PT because it directly contributes to bonding formation through impact energy, and it is moderately higher than RD because DE is strongly influenced by PV. RD was given more importance than PT in regard to its impact

on coating uniformity. To minimize subjective bias, EWM was used to compute data-driven entropy weights, and the combined weights (ω_{Mi}) are summarized in Table 4.13. TOPSIS and VIKOR were then applied using ω_{Mi} to identify compromise solutions on the Pareto front.

Table 4.11 Saaty's scale for AHP scores

Importance	**Score**
Equal	1
Moderate	3
Strong or essential	5
Very strong	7
Extreme	9
Values for intermediate comparison	2,4,6,8

Table 4.12 AHP pairwise comparison matrix and weights

Index	**PV**	**PT**	**RD**
PV	1	5	3
PT	1/5	1	1/3
RD	1/3	3	1

Table 4.13 Weight distribution of indexes

Weights method	**PV**	**PT**	**RD**
AHP (ω_{Ai})	0.6333	0.1062	0.2605
EWM (ω_{Ei})	0.2946	0.4148	0.2906
Combined (ω_{Mi})	0.4711	0.2289	0.3001

The optimal solutions obtained from TOPSIS and VIKOR, as well as the special points A, B, C, and the reference case intended for comparative analysis, are presented in Table 4.14. The Pareto-optimal solutions obtained from the MOO algorithm were validated using CFD simulations with the same design variables. In the case of TOPSIS, the CFD results showed close agreement with the MOO predictions, with errors of 4.05% for PV, 3.41% for PT, and 4.11% for RD. VIKOR exhibited even smaller deviations of 1.24%, 0.28%, and 3.85%, respectively. These results support that integrating NSGA-II with

TOPSIS and VIKOR can be used to identify practical operating conditions for the CS process with good predictive accuracy.

Table 4.14 Representative objective functions and corresponding variable values

		G_p (MPa)	G_t (K)	D_p (µm)	D_t (mm)	SoD (mm)	PV (m/s)	PT (K)	RD (mm)
Reference case		3.0	773	25	2.5	25	623.4	404.5	1.7367
A: PV_{max}		3.9	894	5	3.16	29	910	455.6	1.9327
B: PT_{target}		3.9	809	5	3.74	25	861.2	416.4	0.4326
C: RD_{min}		3.9	867	29	4	22	646.8	464.8	0.4021
TOPSIS	**MOO results**	3.9	780	14	3.94	27	744.7	418.2	0.7303
	CFD results						714.9	435.6	0.7603
	Error (%)						4.05	3.41	4.11
VIKOR	**MOO results**	3.9	823	6	3.96	25	857.1	426.1	0.9466
	CFD results						846.5	424.9	0.9830
	Error (%)						1.24	0.28	3.85

Among the representative selections, Point A: $(\mathrm{PV})_{\max}$, has $G_p = 3.9$ MPa, $G_t = 894$ K, $D_t = 3.16$ mm, and SoD = 29 mm with the maximum PV and a relatively higher RD for $D_p = 5$ µm. Although PT is higher, Point A exhibits 45.97% and 11.28% increases in PV and RD, respectively, relative to the reference case, indicating that the higher PV resulting from increased G_p and G_t leads to RD widening. Point B: $(\mathrm{PT})_{\mathrm{target}}$, with PT close to 415 K, yields $G_p = 3.9$ MPa, $G_t = 809$ K, $D_t = 3.74$ mm, and SoD = 25 mm. Compared with Point A, PV decreases by 5.36% and RD drops by 77.61%. Relative to the reference case, PV increases by 38.14% while RD decreases by 75%. Lastly, Point C: $(\mathrm{RD})_{\min}$, has $G_p = 3.9$ MPa, $G_t = 867$ K, $D_t = 4$ mm, and SoD = 22 mm, resulting in the lowest RD and an increase in PV of 3.75%. These trade-offs can be summarized as: (a) higher PV enhances bonding but reduces uniformity, and (b) lower RD improves uniformity but may reduce bonding strength. Since no single set of operating and design parameters fully satisfies all objectives, TOPSIS and VIKOR were used to select the best compromise solution along the Pareto front. To enable a wider comparison of the reference case with the selected solutions, additional flow simulations were performed using a Rosin-Rammler particle-

size distribution of 2–75 μm. As shown in Figure 4.32(a), the optimized cases have a higher PV of (~610 m/s) and PT of about 418 K than the reference case, which gives 558 m/s and 380 K, respectively. These values are consistent with the experimental findings of a 600–650 m/s velocity and 443 K temperature, and such conditions allow efficient Cu deposition [19]. Figure 4.32(b) depicts the axial variation of RD and shows that RD is significantly reduced for TOPSIS and VIKOR, especially after the nozzle exit. The high particle concentration and reduced plume width are used to enhance the uniformity of coating along the nozzle outflow and on the substrate surface.

Overall, the optimized case performed better than the reference case, with PV increased by 9.16%, PT increased by 10%, and RD was reduced by 52.57%. Consequently, the optimized process parameters are practically useful in minimizing RD and preserving high PV and PT, thereby promoting the formation of dense, uniform, and well-bonded coatings. The selection of the preferred solution was done in the MCDM stage, where the performance requirements of the coating are prioritized. Point A is most optimal when the goal is to maximize PV and consequently improve the DE, but the VIKOR-selected solution implies a moderate compromise of the objectives. Point B is ideal in cases where particle plasticity is required for bonding, but oxidation and substrate heating should be minimized. To minimize RD as the primary objective, both TOPSIS and Point C are preferable, as they enhance homogeneous and steady coatings. The final decision must therefore be taken based on a compromise between the demands of engineering, the performance goals of the coating, and the concerns of the decision-makers.

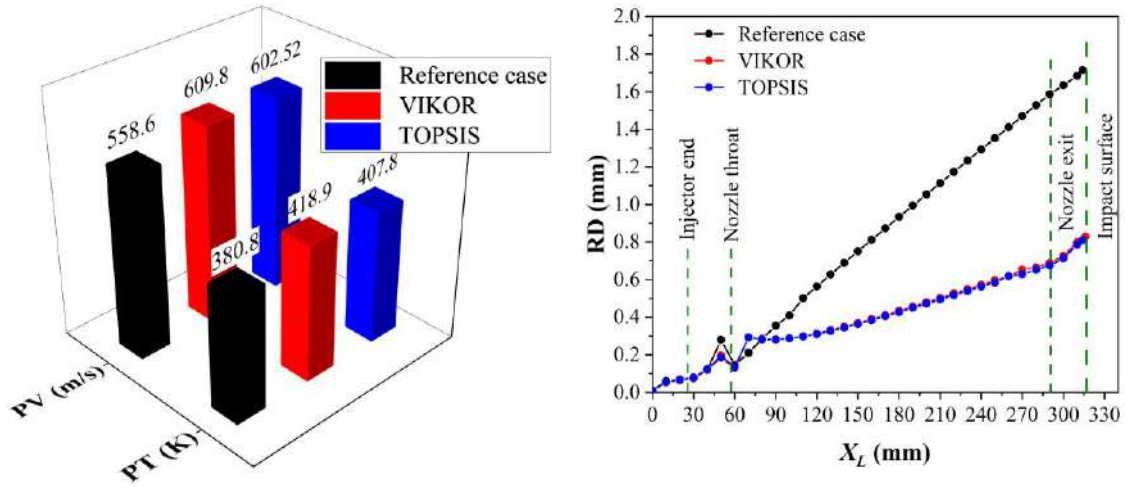

(a) (b)

Figure 4.32 Comparison between reference and optimized cases: (a) PV and PT at substrate surface and (b) variation of RD along nozzle axis

The CFD-predicted PV was compared with the size-dependent V_{cr} and V_{er} to define the deposition window over the particle-size range of $D_p = 2 - 75$ µm [105]. The V_{cr} represents the minimum impact velocity required for particle adhesion, whereas the V_{er} represents the upper velocity limit beyond which particle impact may cause erosion of the substrate or previously deposited material. In this analysis, PV was primarily compared with V_{cr} to identify whether particle bonding could occur, while $V_{er}$was calculated only to confirm that the predicted PV remained within the safe deposition window between V_{cr} and erosion velocity. In the present analysis, V_{cr} and V_{er} were calculated using the hybrid formulation based on the Assadi and Moridi models, in which the weight porosity (WP) of the powder is included to improve the prediction for very small particles. The value of WP was taken as 0.25. The critical and erosion velocities were calculated as:

$$V_{cr} = (707 + 90\ln(WP))\frac{0.42\left(\frac{d_p}{d_{ref}}\right)^{0.5}\sqrt{1-\frac{T_p}{T_m}} + 1.19\sqrt{1-0.73\frac{T_p}{T_m}}}{0.65 + \left(\frac{d_p}{d_{ref}}\right)^{0.5}} \quad (4.1)$$

$$V_{er} = (1364 + 218\ln(WP)) \frac{0.42\left(\frac{d_p}{d_{ref}}\right)^{0.5}\sqrt{1-\frac{T_p}{T_m}} + 1.19\sqrt{1-0.73\frac{T_p}{T_m}}}{0.65+\left(\frac{d_p}{d_{ref}}\right)^{0.5}} \quad (4.2)$$

where T_p is the particle temperature at impact, T_m is the melting temperature of the material, d_p is the particle diameter, and d_{ref} is the reference particle diameter of 25 μm. These parameters were used to determine V_{cr} and V_{er}, which are essential for evaluating whether the predicted particle impact condition lies within the deposition window.

PV exceeds the V_{cr} and bonding is expected to occur, as shown in Figure 4.33. Under the reference condition, the PV and V_{cr} curves intersect twice, indicating that only an intermediate particle-size band meets the deposition criterion. As D_p increases, the predicted PV decreases because of the reduced acceleration of higher inertia particles, which reduces the margin between PV and V_{cr} at the coarse end. On the other hand, finer particles are more sensitive to shock-induced deceleration effects. Thus, particles <5 μm and >60 μm remain below the deposition limit, indicating a limited deposition window [19], as shown in Figure 4.33(a). In contrast, the optimized TOPSIS and VIKOR conditions, which correspond to $G_p = 3.9$ MPa, $D_t \approx 3.95$ mm, and higher $G_t =$ 780–823 K, cause the PV curve to shift upward, leading to a wider deposition window, thus improving the robustness to variations in D_p, as shown in Figure 4.33(b-c). Given that particles adhere when the impact PV exceeds the V_{cr}, only finer to medium D_p are expected to bond at $G_p = 3$ MPa and $G_t = 773$ K in the reference case. On the other hand, a much larger fraction of the D_p range satisfies $\mathrm{PV} > V_{cr}$, when G_p and G_t are increased. However, an excessive increase in G_p intensifies the bow-shock effect, which limits the impact PV of the finest particles [59]. Therefore, increasing G_p alone does not necessarily broaden the deposition window, even at high G_t [106].

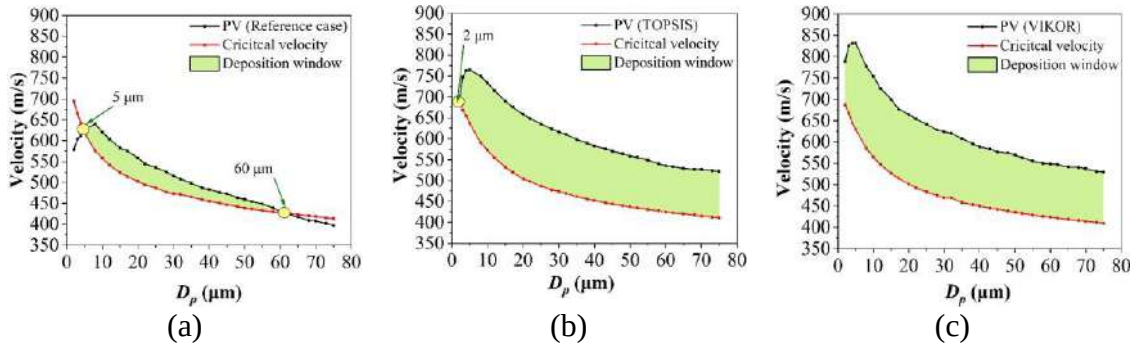

(a) (b) (c)

Figure 4.33 The predicted relationship between the PV at impact and the V_{cr} in terms of D_p: (a) Reference case, (b) TOPSIS, and (c) VIKOR

Particle trajectories were also calculated for the D_p range considered, in order to evaluate particle focusing at the substrate. RD was assessed based on particle impact locations by using Eq. (3.34). The reference operating point resulted in the widest dispersion ($\mathrm{RD} = 1.71$ mm), while the optimized solutions selected by TOPSIS and VIKOR resulted in the most focused particle stream with $\mathrm{RD} = 0.829$ mm and 0.811 mm, respectively, as shown in Figure 4.34. Overall, both optimized conditions improve particle focusing compared to the reference case, in agreement with the literature, which suggests that widening of particle streams is largely dominated by near-throat turbulence and particle-wall deflections, whereas appropriate nozzle and injector parameters together with operating conditions can decrease dispersion [14]. Further, the reference case exhibits clear radial non-uniformity in PT at the substrate, with particles arriving at different temperatures across the plume radius, that is, a cooler core and warmer outer layers [29]. In the optimized cases, the impact region is more uniform, indicating a significant reduction in radial PT variation. Thus, the optimized operating conditions not only widen the deposition window in terms of D_p but also improve particle focusing and thermal uniformity at the substrate, which is favorable for obtaining dense, uniform, and well-bonded coatings.

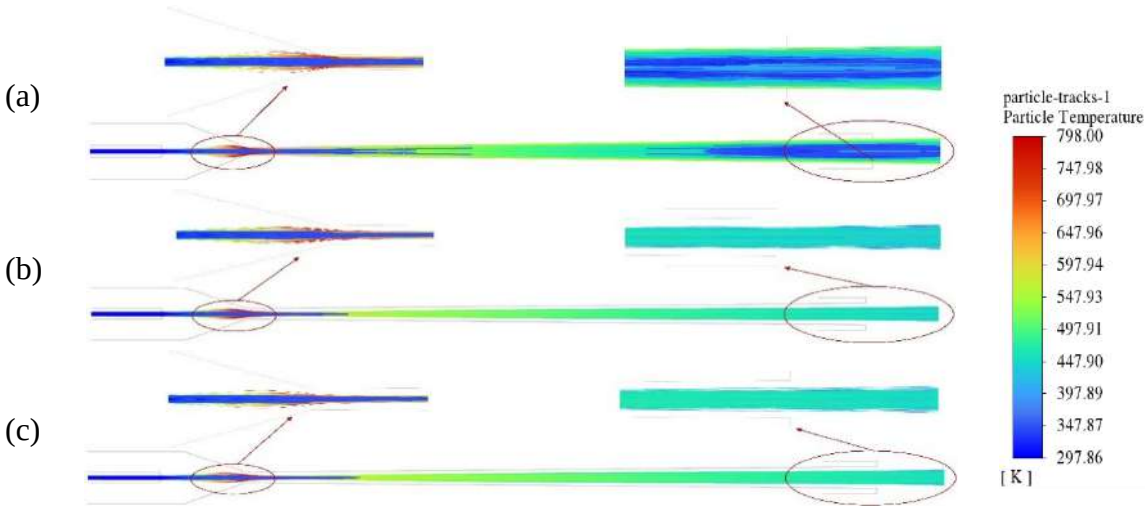

Figure 4.34 Particle tracks colored by PT for the D_p range using a Rosin-Rammler distribution: (a) Reference case, (b) TOPSIS, and (c) VIKOR

4.5 GRA-Based Optimization Results

The grey relational process optimization was carried out to evaluate the combined effect of PV and PT in Cu-based CS. In this stage, ΔP, D_p, ER, and T_c were considered as the selected process parameters, as defined in Table 3.7. The CFD-generated PV and PT values were normalized and converted into a single grey relational grade (GRG) using GRA, so that the kinetic and thermal responses could be assessed together.

Higher PV was preferred because it improves particle impact energy and bonding, while PT was controlled near the 415 K reference condition to support particle softening without melting. The calculated GRG values were used to rank all parameter combinations through grey order. The best, average, and worst combinations were then compared to identify the most favorable process condition for Cu particle deposition. The results are discussed through GRG variation, grey order, temperature contours, radial PT distribution, ANOVA of the GRG model, and interaction effects of ΔP, D_p, ER, and T_c. In this way, the selected cold spray conditions are interpreted on the basis of overall grey relational performance rather than PV or PT alone.

4.5.1 Grey Relational Grade and Response Integration

Complete details of the CFD run pattern, calculated responses, grey relational coefficient, grey relational grade, and ranking are given in Supplementary Table A3. The grey-relational ranking separated the selected parameter combinations in terms of their combined PV and PT performance. Run 27 achieved the highest GRG of 0.9474, corresponding to the grey order 1, and represented the most favorable parameter combination. Under this condition, the selected parameters were ER = 10, T_c = 300 K, ΔP = 0.1 MPa, and D_p = 5 µm, which produced a PV of 844.47 m/s and a PT of 421 K. This condition provided high particle impact velocity while keeping PT close to the target value of 415 K. Run 5 also performed well, with a higher PV of 858.53 m/s and PT of 425 K, but its PT was slightly farther from the target value than Run 27. Run 22 produced the maximum PV of 865.22 m/s; however, its PT of 434 K reduced the combined grey relational performance. In contrast, Run 17 showed the lowest GRG of 0.3839 because of a low PV of about 532 m/s and a high PT of about 493 K. Overall, Runs 27, 10, and 17 represent the best, average, and worst trade-offs between particle impact energy and thermal load. This ranking converts the two-response problem into a single performance sequence and provides a clear basis for comparing all parameter combinations before examining the statistical significance and interaction effects of the selected parameters.

As shown in Figure 4.35, temperature contours in the divergent section exhibit limited variation between the best and average cases because both have the same ER of 10, showing the dominant role of ER in downstream gas expansion. However, comparing the best, average, and worst cases highlights the coupled influence of ER, D_p, ΔP, and T_c on thermal-core development [54]. The worst case, Run 17, shows a less favorable thermal field because low ER weakens expansion, while larger particles respond slowly to the accelerating gas. Thus, higher T_c alone does not improve performance unless sufficient gas expansion and particle acceleration are maintained. These findings are consistent with CS physics, where suitable ER and particle response promote efficient expansion, controlled heating, and stable thermal-kinetic conditions for deposition [13]. The radial

PT distribution at the nozzle throat for the selected grey orders shown in Figure 4.36. PT strongly correlates with particle dispersion, which is influenced by particle inertia and local flow dynamics. Particles farther from the axis exhibit higher temperatures due to interaction with hotter surrounding gas. Smaller particles (5 μm), with lower inertia, disperse more widely, and many exceed the injector semi-diameter. Larger particles (45 μm) maintain tighter trajectories and remain within a 0.62 mm radius. Interestingly, the worst case (45 μm) exhibits higher PT than the average case (25 μm), due to higher T_c and lower ER, which slow the flow and enhance heat transfer. In addition, low ΔP (0.1 MPa) prolongs particle residence in the thermal core, increasing PT. Therefore, while D_p controls dispersion, elevated PT in the worst case arises from the combined effects of low ΔP, low ER, and high T_c, highlighting PT as a function of coupled thermal-fluid behavior, not size alone.

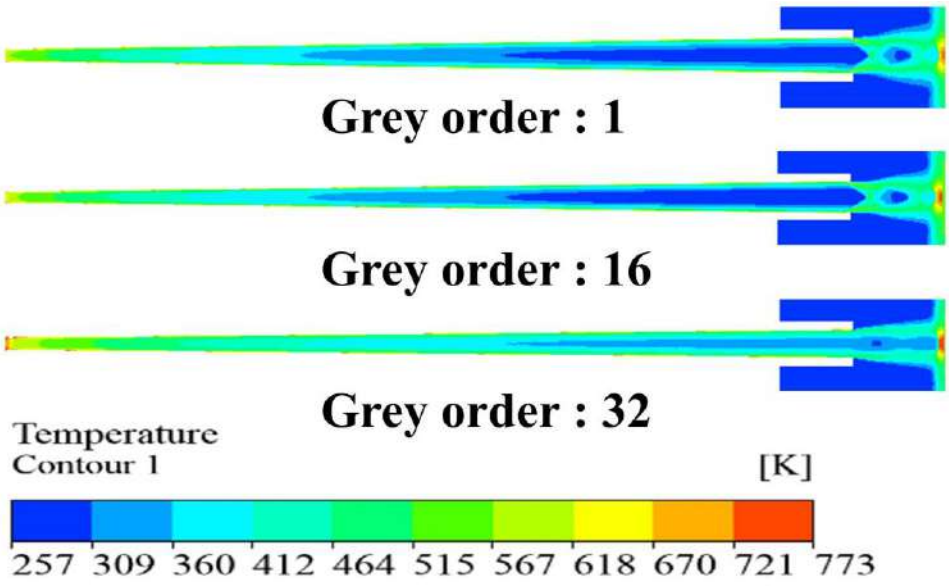

Figure 4.35 Temperature contours in the nozzle divergent section for best, average, and worst cases

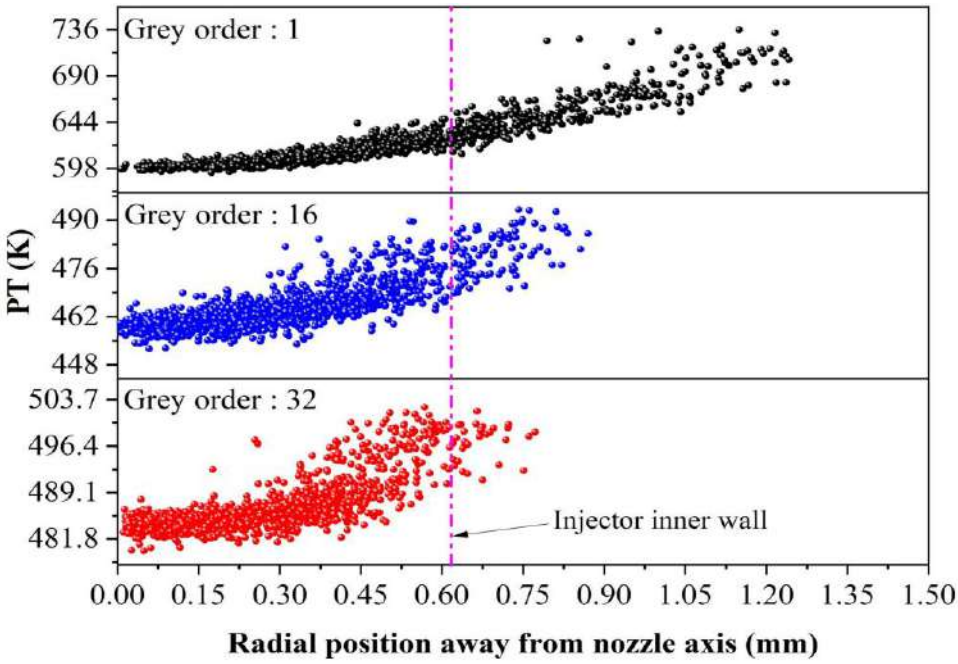

Figure 4.36 Radial PT distribution at the nozzle throat for grey orders 1, 16, and 32, showing their influence on dispersion and heating

The ANOVA results given in Table 4.15 confirm that the quadratic model is statistically significant ($p < 0.0001$). Significant terms include B, C, D, BC, CD, and B^2 ($p < 0.05$). Factor contribution was assessed using the sum of squares. The model showed strong reliability with a high adjusted R^2 of 0.9404 and predicted R^2 of 0.8632, indicating strong model reliability. Among all factors, D_p exhibited the highest influence with 59.42% contribution, with an F-value of 309.17 for D_p and 28.87 for ER, indicating that both are highly significant. ΔP showed minimal impact, with an F-value and a p-value of 0.4244 and 0.5235, respectively. A smaller D_p(5 μm) consistently yields the highest PV and favorable PT, making it the most effective. Higher ER further enhanced flow acceleration, but slightly increased particle heating. T_c has a negligible effect on PV but strongly influenced PT, indicating its thermal-control role [107].

Table 4.15 ANOVA table

Source	Sum of squares	df	Mean square	F-value	p-value	
Model	0.7361	14	0.0526	35.95	< 0.0001	significant
A- ΔP	0.0006	1	0.0006	0.4244	0.5235	
B- D_p	0.4522	1	0.4522	309.17	< 0.0001	
C- ER	0.0422	1	0.0422	28.87	< 0.0001	
D- T_c	0.0179	1	0.0179	12.26	0.0027	
AB	1.345E-7	1	1.345E-7	0.0001	0.9925	
AC	0.0008	1	0.0008	0.5181	0.4814	
AD	0.0055	1	0.0055	3.78	0.0687	
BC	0.0511	1	0.0511	34.94	< 0.0001	
BD	0.0001	1	0.0001	0.0920	0.7653	
CD	0.0148	1	0.0148	10.14	0.0054	
A^2	0.0011	1	0.0011	0.7185	0.4084	
B^2	0.0745	1	0.0745	50.91	< 0.0001	
C^2	0.0023	1	0.0023	1.55	0.2294	
D^2	0.0001	1	0.0001	0.0407	0.8426	
Residual	0.0249	17	0.0015			
Lack of Fit	0.0196	10	0.0020	2.60	0.1088	not significant
Pure Error	0.0053	7	0.0008			
Cor Total	0.7610	31				
R^2 (96.73%)		adjusted R^2 (94.04%)			predicted R^2 (86.32%)	

The interaction plots shown in Figure 4.37 indicate that the GRG response mainly increases at smaller D_p and higher ER, confirming that particle size and nozzle expansion are the dominant controls for the combined PV–PT performance. Finer particles ($D_p \leq 30$ μm), especially around 5 μm, give higher GRG because their lower inertia allows faster acceleration and stronger response to gas expansion. At ER = 10, the expanded gas provides higher velocity and better momentum transfer, which improves the thermal-kinetic balance. This trend remains visible under all ΔP and T_c combinations. For coarser particles near 45 μm, GRG decreases because larger particles require greater momentum transfer and respond more slowly to the gas stream. In these cases, the favorable region

shifts toward intermediate ER, suggesting that excessive expansion may weaken gas-particle coupling for heavier particles, as also reported in cold spray nozzle optimization studies [13], [25]. At ΔP = 0.1 MPa and T_c = 300 K, Figure 4.37(a) shows a high GRG region for small D_p and high ER, indicating stable acceleration with controlled particle heating. When T_c increases to 600 K at the same ΔP, Figure 4.37(c) shows reduced GRG in some regions because added thermal energy increases PT without a proportional velocity gain. At higher ΔP, Figure 4.37(b, d) shows that the increased carrier-gas driving effect can support particle heating and acceleration, particularly near ER = 10. Overall, this confirms that the optimum condition is controlled mainly by a small D_p and high ER, while ΔP and T_c modify the final GRG through gas mixing, residence time, and particle heating.

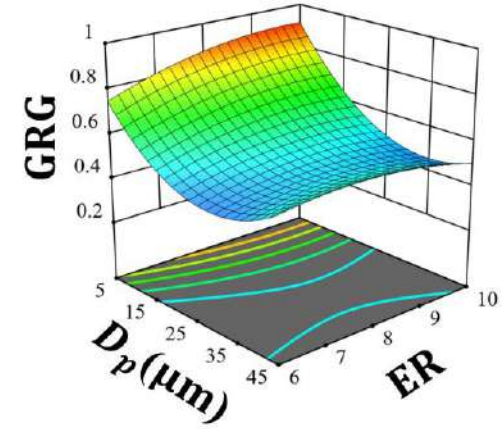

(a)

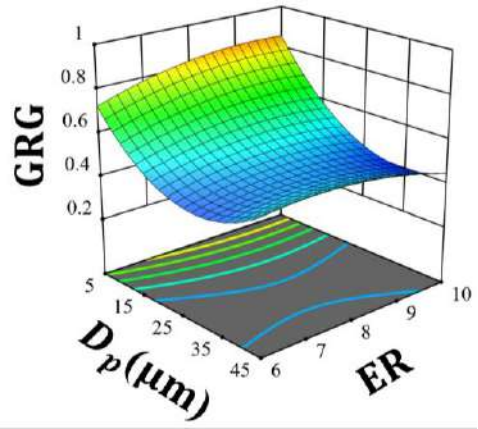

(b)

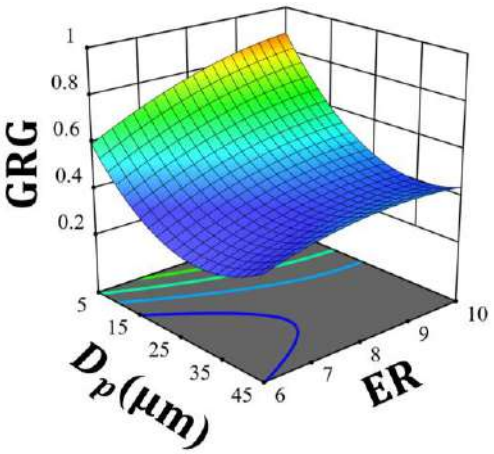

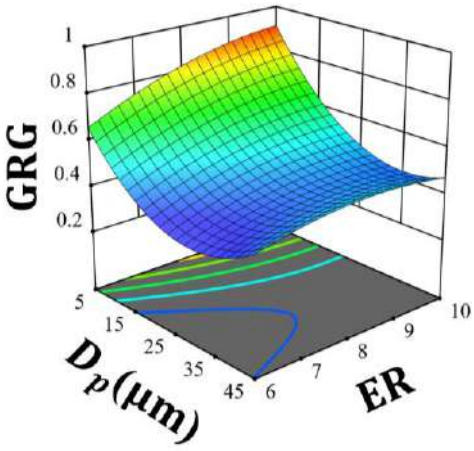

(c) (d)

Figure 4.37 GRG variation with D_p and ER for: (a) ΔP = 0.1 MPa, T_c = 300 K, (b) ΔP = 0.3 MPa, T_c = 300 K, (c) ΔP = 0.1 MPa, T_c = 600 K, and (d) ΔP = 0.3 MPa, T_c = 600 K

4.5.2 Favorable Parameter Combination

The selected Run 27 condition was favorable because it balanced high PV with controlled PT, instead of choosing maximum velocity alone. A fine D_p improved acceleration due to lower inertia, while higher ER enhanced gas expansion and momentum transfer. Lower T_c kept PT closer to the target value, avoiding excessive heating. Thus, the first grey order provided the best thermal-kinetic condition for Cu deposition.

4.6 Particle Size and Morphology Effects

The coupled influence of D_p, G_p, and ψ on PV and RD was examined for Cu particles in HPCS using N_2 as the working gas. In this morphology-sensitive analysis, spherical and non-spherical particles were modeled using Eqs. (3.14)−(3.19). The non-spherical drag formulation was implemented through a user-defined function in Fluent to account for morphology-dependent drag in the HPCS supersonic flow.

4.6.1 Axial Particle Acceleration and Substrate Velocity Footprint

As shown in Figure 4.38, PV decreases monotonically with increasing D_p, because larger particles have higher inertia and are less effectively accelerated in the supersonic jet. At a given D_p, PV is higher at G_p values ranging from 2 to 4 MPa, reflecting the stronger expansion of the gas and the higher jet momentum available for particle acceleration at higher inlet pressure. A consistent morphology effect is also evident, where PV increases with decreasing values of ψ from 1.0 to 0.6. This behavior suggests that non-spherical or irregular particles experience a change in drag and flight characteristics, which affects the dynamics of acceleration. For the very small particles below 5 μm, the sphericity effect is less significant, whereas the influence of morphology becomes more significant in the larger D_p regime. Thus, the morphology effect on PV is not uniform across all particle sizes. Instead, its influence strengthens as particle size increases, which indicates that a

realistic prediction of Cu-particle dynamics in HPCS requires particle shape to be considered together with particle inertia and the G_p level rather than through spherical assumptions alone.

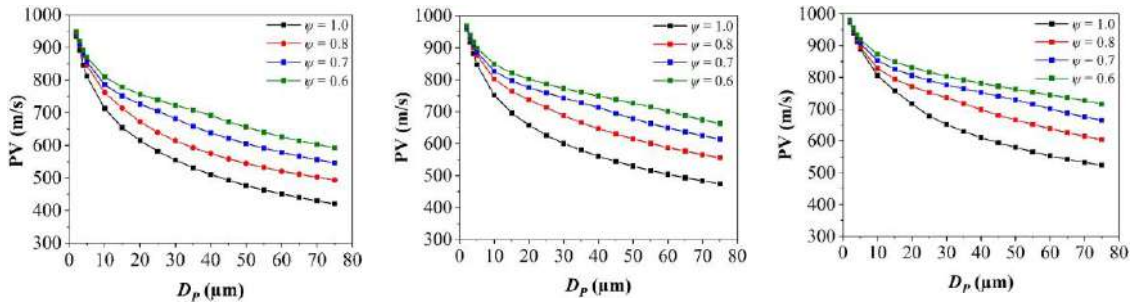

(a) (b) (c)

Figure 4. 38 Effect of D_p on PV for different particle sphericities at G_p of (a) 2 MPa, (b) 3 MPa, and (c) 4 MPa

Figure 4.39 displays PV evolution along the nozzle axis at 3 MPa for different particle sizes (5, 25, 45, 75 um) and sphericities in the range of (1.0−0.6). In all cases, PV increases strongly after the convergent-throat region and then approaches a plateau downstream, which is typical of particle acceleration by a supersonic jet formed in a CD nozzle. A clear morphology trend is observed for all particle sizes, with higher PV for lower sphericity values ($0.6 > 0.7 > 0.8 > 1.0$), which is consistent with the view that particle shape has a strong influence on in-flight acceleration and measured velocities. The separation between the axial PV curves becomes more pronounced when D_p increases from 25 to 75 μm, which indicates that morphology effects are stronger for larger particles. In contrast, for very small particles around 5 μm, the curves remain closer and the ψ effect is comparatively weak. This behavior shows that the acceleration history of large particles is more sensitive to morphology than that of very fine particles. Therefore, under the same pressure condition, particles with lower ψ attain higher axial PV, but the magnitude of this benefit depends strongly on particle size. The axial results thus confirm that D_p and ψ act together in controlling in-flight acceleration in HPCS.

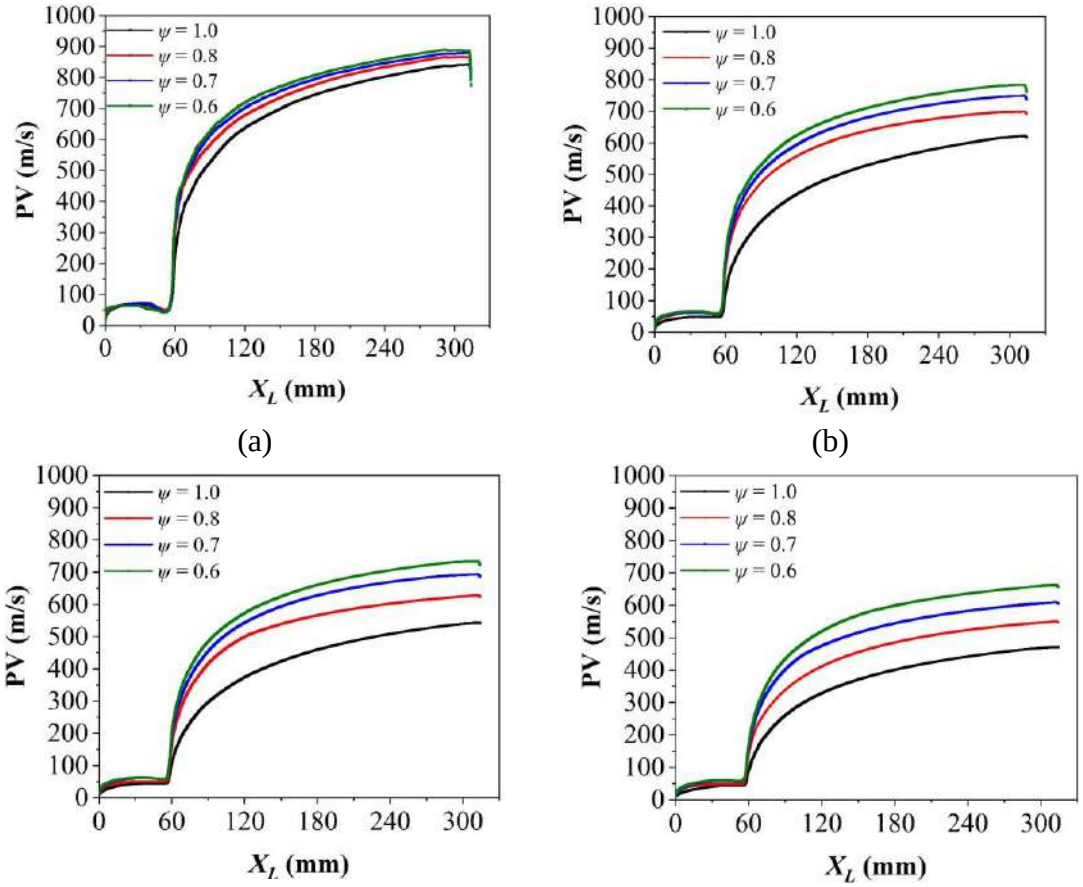

Figure 4.39 Particle tracks at 3 MPa for different D_p and ψ values (a) 5 μm, (b) 25 μm, (c) 45 μm, and (d) 75 μm

The radial distribution of PV at the substrate for G_p from 2 to 4 MPa, across D_p of 5, 25, 45, and 75 μm, and sphericities from 1.0 to 0.6, is shown in Figure 4.40. For each given D_p and ψ, PV reaches a maximum close to the jet core and reduces with increasing radial distance, which is consistent with the spreading of the jet and a reduction in the transfer of momentum away from the axis. A clear pressure effect can be observed whereby the gains in PV as G_p increases from 2 to 4 MPa shift the PV distributions upward, indicating an increase in in-flight and impact velocities at higher G_p, in agreement with experimental and modeling studies of CS. Comparing the different cases in Figure 4.40(a-d), a reduction in ψ is seen to consistently increase PV over the entire radius, proving that particle morphology can modify the drag and flight behavior and increase particle acceleration or

retention of velocity. Size effects are also evident, since smaller particles (5 μm) reach a higher PV with a stronger radial drop, while larger sizes (45–75 μm) show lower PV with a comparatively smoother radial variation, reflecting the combined effect of inertia and gas-particle coupling [39]. Thus, the radial PV footprint at the substrate is governed jointly by G_p, D_p, and ψ.

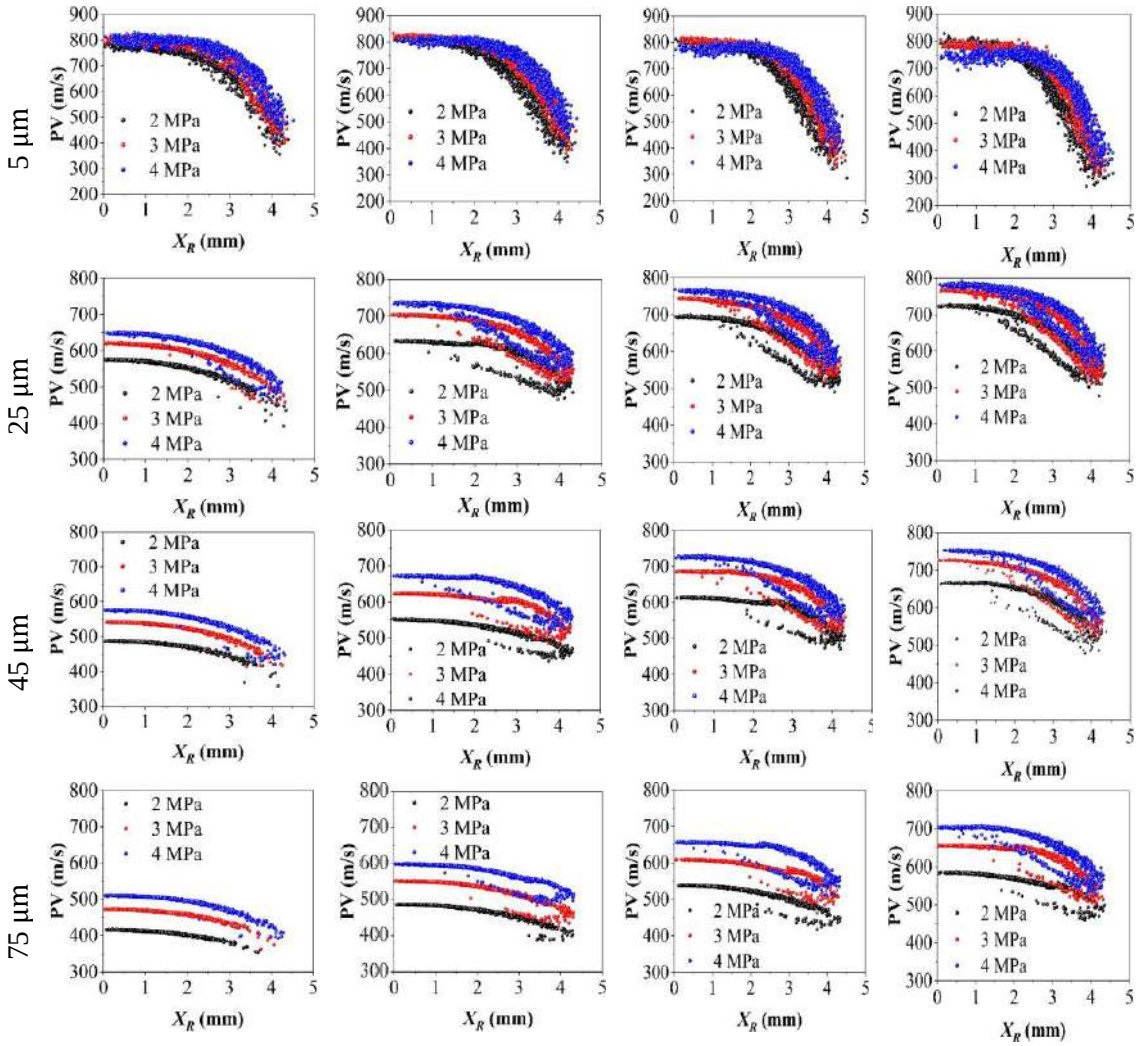

Figure 4.40 Radial distribution of PV on the substrate at G_p values of 2−4 MPa for D_p of 5, 25, 45, and 75 μm, comparing sphericities values of (a) $\psi = 1.0$, (b) $\psi = 0.8$, (c) $\psi = 0.7$, and (d) $\psi = 0.6$

4.6.2 Radial Dispersion and Preferred Condition

The variation of RD along the nozzle axial direction for 5 μm and 75 μm particles with different sphericities is shown in Figure 4.41. RD remains very small upstream, but then increases rapidly after the throat and through the divergent section as the jet expands and the particle spreading due to turbulence increases toward the substrate. This axial growth of particle spreading and the formation of a wider impact footprint are consistent with earlier CFD and diagnostic studies for particle spatial distributions and their downstream evolution [81]. A distinct morphology effect can be observed, with RD increasing as the value of ψ reduces, suggesting that off-axis migration is more intense and the impact footprint becomes broader because of shape-dependent aerodynamic response. This agrees with ψ-based CS analyses that show that particle shape significantly alters in-flight behavior [63]. Comparing sizes, RD for 5 μm particles is higher than for 75 μm particles because small particles couple more strongly with turbulent eddies and follow the expanding jet more closely, whereas large particles behave more ballistically and are less sensitive to lateral turbulent fluctuations. These results indicate that lower ψ values provide higher PV, but they also increase RD and widen the impact footprint along the jet.

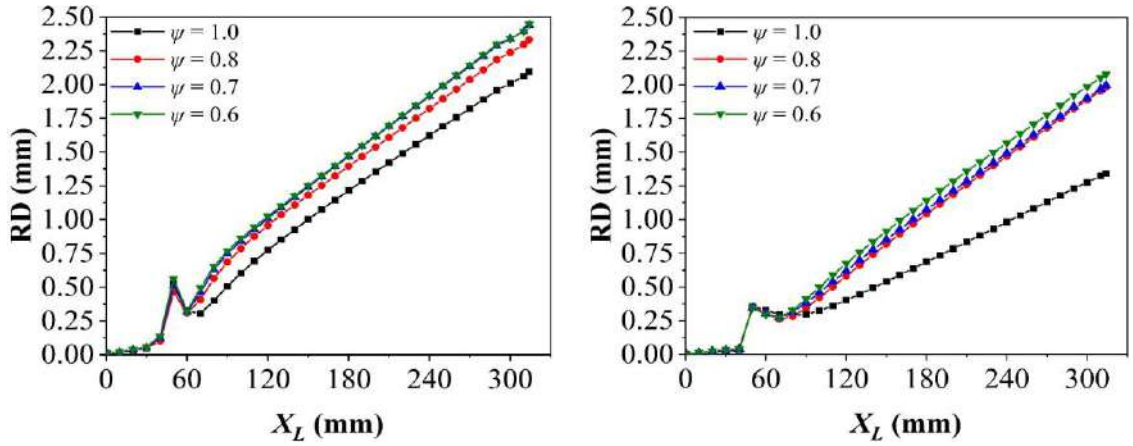

Figure 4.41 Radial dispersion of Cu particles at the substrate for different sphericities: (a) 5 μm and (b) 75 μm

The comparative analysis shows that D_p, G_p, and ψ act together in controlling the in-flight and impact behavior of Cu particles in HPCS. Across the investigated range, PV increased with increasing G_p and decreased with increasing D_p, which confirms the dominant roles of jet momentum and particle inertia in controlling particle acceleration. An increase in G_p from 2 to 4 MPa systematically increased PV and shifted the substrate PV footprint upward, whereas increasing D_p reduced acceleration under the same spraying conditions because larger particles possess higher inertia. These results indicate that G_p promotes acceleration, while D_p governs the resistance of particles to that acceleration.

ψ introduced an additional and consistent trend in the particle dynamics. Decreasing the value of ψ from 1.0 to 0.6 increased PV both along the nozzle axis and at the substrate, which indicates that non-spherical particles experience modified drag and flight behavior under identical spray conditions. At the same time, lower sphericity also increased RD and widened the impact footprint, showing that the gain in PV is accompanied by stronger off-axis spreading. This morphology effect became more pronounced for larger particles, whereas very small particles exhibited comparatively low sensitivity to sphericity. Thus, the influence of particle morphology is not independent but is amplified when particle inertia becomes larger. A comparison of the combined trends further shows that smaller particles are accelerated more effectively and respond more strongly to the expanding jet, while larger particles are less effectively accelerated but show stronger morphology-dependent differences. Similarly, higher G_p enhances particle acceleration for all particle sizes and sphericities, but it does not remove the fundamental effect of D_p and shape on the final impact condition. Therefore, D_p remains the main inertial control, G_p provides the momentum driving force, and ψ modifies the aerodynamic response and radial spreading of the particles. In this way, the particle dynamics of Cu in HPCS are governed by the coupled action of D_p, G_p, and ψ, rather than by any one of these parameters alone.

CHAPTER 5 CONCLUSIONS AND FUTURE SCOPE

5.1 Conclusions

The present research established a connected CS research pathway in which bibliometric assessment, technical parameter review, CFD-based nozzle analysis, process-parameter optimization, grey-relational optimization, and morphology-aware particle prediction were integrated in accordance with the overall research direction. The overall outcomes show that CS performance cannot be interpreted through one variable alone, because PV, PT, HF, SP, and RD are all interrelated responses of the same gas-particle-substrate system. Careful evaluation of bibliometric development, nozzle behavior, optimized process conditions, grey-relational performance, and morphology-sensitive particle dynamics revealed the following key findings:

- The bibliometric paper established the broad contours and overall structure of the CS field by examining the literature development, publication trends, influential contributors, and major research gaps. It showed that bibliometric analysis is a practical method for establishing a broad framework for a specific area of scientific inquiry, and that the CS field has moved well beyond a limited early-stage deposition topic toward a broader and more active scientific area.
- A thorough examination of 387 documents found in the Scopus database from 1999 to 2022 was carried out, and the mapped publication analysis showed that the total number of research papers was 248, the first literature document was published in 1999, and from 2008, the number of publications in each year grew exponentially till the current year. In 2020, the maximum number of published papers was around 34, while 14 articles had already been published in 2022. Material science and engineering were the two leading areas of research with 45% and 25% of the articles, respectively, and five sources contributed 72% of the

publications. Despite several successful experiments, brittle materials have received little attention, highlighting the need for research in this area.

- The technical review established the general scientific and engineering basis of CS by organizing the field through its working principle, system types, major parameters, applications, and challenges. It showed that CS is a feasible low-temperature coating process that is increasingly economical and environmentally friendly, with relevance to aeronautical, medical, marine, defense, petrochemical, nuclear, agriculture, oil-and-gas, and turbine applications. It summarized HPCS and LPCS, identified G_p, G_t, SoD, spraying angle, substrate temperature, nozzle design, and substrate preparation as the major technical parameters. It also classified CS applications into metallic, metal-matrix composite, ceramic, nanocrystalline, and polymer coatings, while highlighting weak adhesion in brittle ceramic and hard-material systems as a major challenge.
- The nozzle-design optimization established that the performance of the CD nozzle can be improved significantly through a combined framework of FCCD, CFD simulations, RSM, ANN, and GA. It showed that nozzle design parameters do not act independently, and that L_c, L_d, D_{id}, L_i, and D_e all contribute to particle acceleration, thermal behavior, and near-substrate response.
- Comparative analysis showed that both RSM and ANN models were highly accurate, with $R^2 = 0.9893$ for RSM and $R^2 = 0.9848$ for ANN. Both models are more accurate on average, while ANN captured the complex interactions with an overall correlation coefficient of 0.99191. Optimization using RSM coupled with numerical simulation improved PV, PT, HF, and SP by 9.1%, 4.4%, 17.9%, and 27.6%, respectively. Further optimization with a 5–6–4 ANN and GA (NSGA−II) improved PV by 5%, PT by 5.4%, HF by 15.7%, and reduced SP by 20.9%. Based on the results and overall analysis of four responses under 3 MPa and 4 MPa, ANN-GA was considered the best optimized model because it more accurately fulfilling the objectives of the study.

- The process-parameter optimization established that HPCS process conditions can be improved through an MOO that combines CFD simulations with FCCD, RSM, NSGA-II, and MCDM analysis using TOPSIS and VIKOR with a hybrid AHP-EWM weighting. It showed that the key operating and design parameters G_p, G_t, D_p, D_t, and SoD must be treated together because high PV, controlled PT, and low RD do not necessarily occur under the same parameter combination.
- The performance of the RSM models showed high predictive accuracy ($R^2 > 0.94$), with residual values within the range of ±3.6218. The sensitivity analysis revealed that D_p and G_t were the most significant parameters affecting PV and PT, while D_t had a significant effect on RD. The optimized TOPSIS solution produced PV = 744.7 m/s, PT = 418.2 K, and RD = 0.7303 mm, whereas the VIKOR solution produced PV = 857.1 m/s, PT = 426.1 K, and RD = 0.9466 mm. CFD validation showed errors of 4.05%, 3.41%, and 4.11% for TOPSIS and 1.24%, 0.28%, and 3.85% for VIKOR in PV, PT, and RD, respectively. Overall, the optimized case performed better than the reference case, with PV maximized by 9.16%, PT increased by 10%, and RD reduced by 52.57%, thereby promoting the formation of dense, uniform, and well-bonded coatings.
- The GRA further established that high PV and adequate PT are critical for achieving strong bonding without melting, and that these two responses can be integrated into one performance index through the GRG. It showed that the combined effects of ΔP, D_p, ER, and T_c can be treated through a CFD-based multi-parameter optimization linked with GRA and RSM.
- The best case (grey order 1) conditions were obtained at ER = 10, $T_c = 300$ K, ΔP = 0.1 MPa, and $D_p = 5$ µm, with PV of 844.47 m/s, PT of 421 K, and the highest GRG of 0.9474. This condition was selected because fine particles accelerated effectively at higher ER, while lower T_c kept PT closest to the target value. Run 5 and Run 22 produced higher PV, but their PT values moved farther from the target, reducing the combined grey-relational balance. The quadratic model was

statistically significant ($p < 0.0001$), with adjusted $R^2 = 0.9404$ and predicted $R^2 = 0.8632$, and factor contribution analysis showed that D_p contributed 59.42%. These conditions ensure sufficient impact energy with controlled thermal softening.

- The morphology-sensitive analysis established that the performance of HPCS depends on D_p, G_p, and ψ, and that the coupled effects on the dynamics of Cu particles cannot be ignored in realistic modeling. It showed that a CFD-based Eulerian-Lagrangian model can be used to investigate the effects of D_p in the range of $2 - 75$ µm, N_2 pressure of $2 - 4$ MPa, and ψ in the range of $1.0 - 0.6$ on in-flight behavior and impact conditions on an aluminum substrate.
- The results showed that PV increased with increasing G_p and decreased with increasing D_p due to enhanced jet momentum and high particle inertia. Decreasing the value of ψ produced higher values of both axial and substrate impact velocities, and also resulted in higher RD. This influence increased for larger particles, but very small particles exhibited low sensitivity to the effect of ψ. The results suggested that non-spherical Cu particles achieve higher impact velocities under identical spray conditions, whereas spherical particles are more suitable for obtaining a narrower impact footprint and a more uniform coating.

Overall, this integrated bibliometric-numerical-optimization framework establishes a coherent understanding of HPCS for Cu deposition on Al substrates. The study not only clarifies the coupled roles of nozzle geometry, process parameters, and particle morphology, but also demonstrates that improved coating-oriented performance depends on their combined optimization. The outcomes provide a reliable basis for further development of uniform, well-bonded, and application-oriented CS coatings.

5.2 Future Scope

- Future studies may experimentally validate the optimized CS conditions obtained through CFD-based analysis. The predicted PV, PT, RD, and nozzle performance can be confirmed by measuring DE, coating porosity, adhesion strength, coating thickness uniformity, residual stress, and surface quality under actual CS operating conditions.
- The present numerical and optimization framework may be further extended by combining nozzle design parameters and process parameters in a single optimization model. Parameters such as G_p, G_t, D_p, D_t, SoD, ER, D_{id}, L_c, L_d, and D_e can be simultaneously optimized for improved coating quality.
- Future research may include more realistic powder characteristics such as particle size distribution, non-spherical particle morphology, powder feed rate, mass loading, and particle-particle interaction. Since D_p and ψ strongly influence PV and RD, their combined optimization can help achieve higher impact velocity with better coating uniformity and reduced overspray.
- The proposed methodology can be applied to different powder-substrate combinations and advanced materials. Future investigations may consider ceramics, metallic glasses, biomedical materials, polymers, high entropy alloys, and metal matrix composites to expand the application of CS in aerospace, automobile, defense, energy, repair, and additive manufacturing sectors.
- Future numerical models may be improved by using 3D simulations, two-way coupling, advanced turbulence models, non-adiabatic wall conditions, and detailed shock-wave and near-substrate interaction analysis. Such high-fidelity modelling will provide deeper understanding of particle acceleration, impact behavior, bonding mechanism, and V_{cr} for different conditions.

REFRENCES

[1] T. Schmidt *et al.*, "From particle acceleration to impact and bonding in cold spraying," *J. Therm. Spray Technol.*, vol. 18, no. 5–6, pp. 794–808, 2009, doi: 10.1007/s11666-009-9357-7.

[2] S. Pathak and G. C. Saha, "Development of sustainable cold spray coatings and 3D additive manufacturing components for repair/manufacturing applications: A critical review," *Coatings*, vol. 7, no. 8, 2017, doi: 10.3390/coatings7080122.

[3] D. Guo *et al.*, "Cold Spray: Over 30 Years of Development Toward a Hot Future," *J. Therm. Spray Technol.*, vol. 31, no. 4, pp. 866–907, 2022, doi: 10.1007/s11666-022-01366-4.

[4] S. Kumar, M. Kumar, and N. Jindal, "Overview of cold spray coatings applications and comparisons: a critical review," *World J. Eng.*, vol. 17, no. 1, pp. 27–51, 2020, doi: 10.1108/WJE-01-2019-0021.

[5] P. Petrovskiy, M. Doubenskaia, A. Sova, and A. Travyanov, "Analysis of copper-tungsten cold spray coating: Kinetics of coating formation and its thermal properties," *Surf. Coatings Technol.*, vol. 385, 2020, doi: 10.1016/j.surfcoat.2020.125376.

[6] R. F. Vaz, A. Garfias, V. Albaladejo, J. Sanchez, and I. G. Cano, "A Review of Advances in Cold Spray Additive Manufacturing," *Coatings*, vol. 13, no. 2, 2023, doi: 10.3390/coatings13020267.

[7] Q. Wang, K. Spencer, N. Birbilis, and M. X. Zhang, "The influence of ceramic particles on bond strength of cold spray composite coatings on AZ91 alloy substrate," *Surf. Coatings Technol.*, vol. 205, no. 1, pp. 50–56, 2010, doi: 10.1016/j.surfcoat.2010.06.008.

[8] R. Huang, M. Sone, W. Ma, and H. Fukanuma, "The effects of heat treatment on the mechanical properties of cold-sprayed coatings," *Surf. Coatings Technol.*, vol. 261, pp. 278–288, 2015, doi: 10.1016/j.surfcoat.2014.11.017.

[9] T. H. V. Steenkiste, J. R. Smith, and R. E. Teets, "Aluminum coatings via kinetic spray with relatively large powder particles," *Surf. Coatings Technol.*, vol. 154, no.

2–3, pp. 237–252, 2002, doi: 10.1016/S0257-8972(02)00018-X.

[10] M. Grujicic, J. R. Saylor, D. E. Beasley, W. S. DeRosset, and D. Helfritch, "Computational analysis of the interfacial bonding between feed-powder particles and the substrate in the cold-gas dynamic-spray process," *Appl. Surf. Sci.*, vol. 219, no. 3–4, pp. 211–227, 2003, doi: 10.1016/S0169-4332(03)00643-3.

[11] H. Singh, T. S. Sidhu, S. B. S. Kalsi, and J. Karthikeyan, "Development of cold spray from innovation to emerging future coating technology," *J. Brazilian Soc. Mech. Sci. Eng.*, vol. 35, no. 3, pp. 231–245, 2013, doi: 10.1007/s40430-013-0030-1.

[12] C.-J. Li, W.-Y. Li, Y. Y. Wang, and H. Fukanuma, "Effect of Spray Angle on Deposition Characteristics in Cold Spraying," *Therm. Spray 2003 Adv. Sci. Appl. Technol.*, pp. 91–96, 2003.

[13] C. Cao, T. Han, Y. Xu, W. Li, X. Yang, and K. Hu, "The associated effect of powder carrier gas and powder characteristics on the optimal design of the cold spray nozzle," *Surf. Eng.*, vol. 36, no. 10, pp. 1081–1089, 2020, doi: 10.1080/02670844.2020.1744297.

[14] R. Lupoi and W. O'Neill, "Powder stream characteristics in cold spray nozzles," *Surf. Coatings Technol.*, vol. 206, no. 6, pp. 1069–1076, 2011, doi: 10.1016/j.surfcoat.2011.07.061.

[15] A. Mehmood, M. Zunaid, and A. K. Madan, "A Brief Review of Technical Parameters and Its Applications Used in Cold Spray Process," *Lect. Notes Mech. Eng.*, pp. 243–255, 2023, doi: 10.1007/978-981-99-2921-4_23.

[16] Y. Zou, W. Qin, E. Irissou, J. G. Legoux, S. Yue, and J. A. Szpunar, "Dynamic recrystallization in the particle/particle interfacial region of cold-sprayed nickel coating: Electron backscatter diffraction characterization," *Scr. Mater.*, vol. 61, no. 9, pp. 899–902, 2009, doi: 10.1016/j.scriptamat.2009.07.020.

[17] X. T. Luo, Y. K. Wei, Y. Wang, and C. J. Li, "Microstructure and mechanical property of Ti and Ti6Al4V prepared by an in-situ shot peening assisted cold spraying," *Mater. Des.*, vol. 85, pp. 527–533, 2015, doi:

10.1016/j.matdes.2015.07.015.

[18] R. C. Dykhuizen, M. F. Smith, D. L. Gilmore, R. A. Neiser, X. Jiang, and S. Sampath, “Impact of high velocity cold spray particles,” *J. Therm. Spray Technol.*, vol. 8, no. 4, pp. 559–564, 1999, doi: 10.1361/105996399770350250.

[19] T. Schmidt, F. Gärtner, H. Assadi, and H. Kreye, “Development of a generalized parameter window for cold spray deposition,” *Acta Mater.*, vol. 54, no. 3, pp. 729–742, 2006, doi: 10.1016/j.actamat.2005.10.005.

[20] H. Assadi, H. Kreye, F. Gärtner, and T. Klassen, “Cold spraying – A materials perspective,” *Acta Mater.*, vol. 116, pp. 382–407, 2016, doi: 10.1016/j.actamat.2016.06.034.

[21] M. R. Rokni, S. R. Nutt, C. A. Widener, V. K. Champagne, and R. H. Hrabe, “Review of Relationship Between Particle Deformation, Coating Microstructure, and Properties in High-Pressure Cold Spray,” *J. Therm. Spray Technol.*, vol. 26, no. 6, pp. 1308–1355, 2017, doi: 10.1007/s11666-017-0575-0.

[22] R. T. Li, K. A. Khor, and L. G. Yu, “Identifying Indicators of Progress in Thermal Spray Research Using Bibliometrics Analysis,” *J. Therm. Spray Technol.*, vol. 25, no. 8, pp. 1526–1533, 2016, doi: 10.1007/s11666-016-0445-1.

[23] I. A. Abu Bakar, N. I. Omar, Y. Yusuf, and T. Abdul Rahim, “Reflection and Future Perspectives in Cold Spray Technology: A Bibliometric Analysis,” *J. Therm. Spray Technol.*, vol. 32, no. 6, pp. 1576–1595, 2023, doi: 10.1007/s11666-023-01612-3.

[24] W.-Y. Li, H. L. Liao, G. Zhang, C. Coddet, H.-T. Wang, and C.-J. Li, “Optimal Design of a Convergent-Barrel Cold Spray Nozzle by Numerical Method,” *Therm. Spray 2006 Proc. from Int. Therm. Spray Conf.*, vol. 83669, pp. 259–264, 2006, doi: 10.31399/asm.cp.itsc2006p0259.

[25] W. Y. Li, H. Liao, G. Douchy, and C. Coddet, “Optimal design of a cold spray nozzle by numerical analysis of particle velocity and experimental validation with 316L stainless steel powder,” *Mater. Des.*, vol. 28, no. 7, pp. 2129–2137, 2007, doi: 10.1016/j.matdes.2006.05.016.

[26] H. Katanoda, M. Fukuhara, and N. Iino, “Numerical study of combination

parameters for particle impact velocity and temperature in cold spray," *J. Therm. Spray Technol.*, vol. 16, no. 5–6, pp. 627–633, 2007, doi: 10.1007/s11666-007-9087-7.

[27] H. Tabbara, S. Gu, D. G. McCartney, T. S. Price, and P. H. Shipway, "Study on process optimization of cold gas spraying," *J. Therm. Spray Technol.*, vol. 20, no. 3, pp. 608–620, 2011, doi: 10.1007/s11666-010-9564-2.

[28] S. Yin, Q. Liu, H. Liao, and X. Wang, "Effect of injection pressure on particle acceleration, dispersion and deposition in cold spray," *Comput. Mater. Sci.*, vol. 90, pp. 7–15, 2014, doi: 10.1016/j.commatsci.2014.03.055.

[29] D. L. Gilmore, R. C. Dykhuizen, R. A. Neiser, T. J. Roemer, and M. F. Smith, "Particle velocity and deposition efficiency in the cold spray process," *J. Therm. Spray Technol.*, vol. 8, no. 4, pp. 576–582, 1999, doi: 10.1361/105996399770350278.

[30] F. Raletz, M. Vardelle, and G. Ezo'o, "Critical particle velocity under cold spray conditions," *Surf. Coatings Technol.*, vol. 201, no. 5, pp. 1942–1947, 2006, doi: 10.1016/j.surfcoat.2006.04.061.

[31] V. K. Champagne, D. J. Helfritch, S. P. G. Dinavahi, and P. F. Leyman, "Theoretical and experimental particle velocity in cold spray," *J. Therm. Spray Technol.*, vol. 20, no. 3, pp. 425–431, 2011, doi: 10.1007/s11666-010-9530-z.

[32] S. Yin, X. F. Wang, W. Y. Li, and X. P. Guo, "Examination on substrate preheating process in cold gas dynamic spraying," *J. Therm. Spray Technol.*, vol. 20, no. 4, pp. 852–859, 2011, doi: 10.1007/s11666-011-9623-3.

[33] W. Y. Li, S. Yin, X. Guo, H. Liao, X. F. Wang, and C. Coddet, "An investigation on temperature distribution within the substrate and nozzle wall in cold spraying by numerical and experimental methods," *J. Therm. Spray Technol.*, vol. 21, no. 1, pp. 41–48, 2012, doi: 10.1007/s11666-011-9685-2.

[34] Y. Xie *et al.*, "Strengthened Peening Effect on Metallurgical Bonding Formation in Cold Spray Additive Manufacturing," *J. Therm. Spray Technol.*, vol. 28, no. 4, pp. 769–779, 2019, doi: 10.1007/s11666-019-00854-4.

[35] A. Nastic, B. Jodoin, D. Poirier, and J. G. Legoux, “Particle temperature effect in cold spray: A study of soft particle deposition on hard substrate,” *Surf. Coatings Technol.*, vol. 406, 2021, doi: 10.1016/j.surfcoat.2020.126735.

[36] M. Meyer and R. Lupoi, “An analysis of the particulate flow in cold spray nozzles,” *Mech. Sci.*, vol. 6, no. 2, pp. 127–136, 2015, doi: 10.5194/ms-6-127-2015.

[37] C. J. Akisin, C. J. Bennett, F. Venturi, H. Assadi, and T. Hussain, “Numerical and Experimental Analysis of the Deformation Behavior of CoCrFeNiMn High Entropy Alloy Particles onto Various Substrates During Cold Spraying,” *J. Therm. Spray Technol.*, vol. 31, no. 4, pp. 1085–1111, 2022, doi: 10.1007/s11666-022-01377-1.

[38] J. J. Park *et al.*, “Supersonic nozzle flow simulations for particle coating applications: Effects of shockwaves, nozzle geometry, ambient pressure, and substrate location upon flow characteristics,” *J. Therm. Spray Technol.*, vol. 20, no. 3, pp. 514–522, 2011, doi: 10.1007/s11666-010-9542-8.

[39] X. K. Suo, T. K. Liu, W. Y. Li, Q. L. Suo, M. P. Planche, and H. L. Liao, “Numerical study on the effect of nozzle dimension on particle distribution in cold spraying,” *Surf. Coatings Technol.*, vol. 220, pp. 107–111, 2013, doi: 10.1016/j.surfcoat.2012.09.029.

[40] S. Yin, M. Zhang, Z. Guo, H. Liao, and X. Wang, “Numerical investigations on the effect of total pressure and nozzle divergent length on the flow character and particle impact velocity in cold spraying,” *Surf. Coatings Technol.*, vol. 232, pp. 290–297, 2013, doi: 10.1016/j.surfcoat.2013.05.017.

[41] W. Tang, J. Liu, Q. Chen, X. Zhang, and Z. Chen, “The effects of two gas flow streams with initial temperature and pressure differences in cold spraying nozzle,” *Surf. Coatings Technol.*, vol. 240, pp. 86–95, 2014, doi: 10.1016/j.surfcoat.2013.12.019.

[42] S. H. Zahiri, T. D. Phan, S. H. Masood, and M. Jahedi, “Development of holistic three-dimensional models for cold spray supersonic jet,” *J. Therm. Spray Technol.*, vol. 23, no. 6, pp. 919–933, 2014, doi: 10.1007/s11666-014-0113-2.

[43] M. Faizan-Ur-Rab, S. H. Zahiri, S. H. Masood, M. Jahedi, and R. Nagarajah, “PIV

Validation of 3D Multicomponent Model for Cold Spray Within Nitrogen and Helium Supersonic Flow Field," *J. Therm. Spray Technol.*, vol. 26, no. 5, pp. 941–957, 2017, doi: 10.1007/s11666-017-0567-0.

[44] L. Alonso, M. A. Garrido-Maneiro, and P. Poza, "A study of the parameters affecting the particle velocity in cold-spray: Theoretical results and comparison with experimental data," *Addit. Manuf.*, vol. 67, 2023, doi: 10.1016/j.addma.2023.103479.

[45] K. Kowalski, P. Błasiak, and S. Pietrowicz, "A novel cold spray process flow technique - a numerical investigation," *Int. J. Heat Mass Transf.*, vol. 218, 2024, doi: 10.1016/j.ijheatmasstransfer.2023.124817.

[46] W. Wan, W. Li, D. Wu, Z. Zhang, and B. Ning, "3D analysis of gas flow behavior and particle acceleration characteristics in cold spray additive manufacturing based on non-axisymmetric numerical models," *J. Mater. Res. Technol.*, vol. 29, pp. 1335–1349, 2024, doi: 10.1016/j.jmrt.2024.01.204.

[47] W. Y. Li and C. J. Li, "Optimal design of a novel cold spray gun nozzle at a limited space," *J. Therm. Spray Technol.*, vol. 14, no. 3, pp. 391–396, 2005, doi: 10.1361/105996305X59404.

[48] S. Buhl, P. Breuninger, and S. Antonyuk, "Optimization of a laval nozzle for energy-efficient cold spraying of microparticles," *Mater. Manuf. Process.*, vol. 33, no. 2, pp. 115–122, 2018, doi: 10.1080/10426914.2017.1279322.

[49] V. Varadaraajan and P. Mohanty, "Design and optimization of rectangular cold spray nozzle: Radial injection angle, expansion ratio and traverse speed," *Surf. Coatings Technol.*, vol. 316, pp. 246–254, 2017, doi: 10.1016/j.surfcoat.2017.03.005.

[50] C. Cao, W. Li, Z. Zhang, X. Yang, and Y. Xu, "Cold Spray Additive Manufacturing of Ti6Al4V: Special Nozzle Design Using Numerical Simulation and Experimental Validation," *Coatings*, vol. 12, no. 2, 2022, doi: 10.3390/COATINGS12020210.

[51] F. L. Zavalan and A. Rona, "A workflow for designing contoured axisymmetric nozzles for enhancing additively manufactured cold spray deposits," *Addit. Manuf.*,

vol. 62, p. 103379, 2023, doi: 10.1016/j.addma.2022.103379.

[52] A. K. Sharma, A. Vashishtha, D. Callaghan, S. R. Bakshi, M. Kamaraj, and R. Raghavendra, "CFD Investigation of a Co-Flow Nozzle for Cold Spray Additive Manufacturing Applications," *J. Therm. Spray Technol.*, vol. 33, no. 5, pp. 1251–1269, 2024, doi: 10.1007/s11666-024-01764-w.

[53] A. Sova, S. Grigoriev, A. Kochetkova, and I. Smurov, "Influence of powder injection point position on efficiency of powder preheating in cold spray: Numerical study," *Surf. Coatings Technol.*, vol. 242, pp. 226–231, 2014, doi: 10.1016/j.surfcoat.2013.10.078.

[54] W. Wan, W. Li, D. Wu, Z. Qi, and Z. Zhang, "New insights into the effects of powder injector inner diameter and overhang length on particle accelerating behavior in cold spray additive manufacturing by numerical simulation," *Surf. Coatings Technol.*, vol. 444, 2022, doi: 10.1016/j.surfcoat.2022.128670.

[55] M. Khan, M. Zunaid, and Q. Murtaza, "Computational simulation of cold spray coating for optimal injector length," *Case Stud. Therm. Eng.*, vol. 51, no. March, p. 103655, 2023, doi: 10.1016/j.csite.2023.103655.

[56] Y. Xie, M. P. Planche, R. Raoelison, H. Liao, X. Suo, and P. Hervé, "Effect of Substrate Preheating on Adhesive Strength of SS 316L Cold Spray Coatings," *J. Therm. Spray Technol.*, vol. 25, no. 1–2, pp. 123–130, 2016, doi: 10.1007/s11666-015-0312-5.

[57] O. C. Ozdemir *et al.*, "High Rate Deposition in Cold Spray," *J. Therm. Spray Technol.*, vol. 30, no. 1–2, pp. 344–357, 2021, doi: 10.1007/s11666-020-01135-1.

[58] W. Li, N. Xue, L. Shao, Y. Wu, T. Qiu, and L. Zhu, "Effects of spraying parameters and heat treatment temperature on microstructure and properties of single-pass and single-layer cold-sprayed Cu coatings on Al alloy substrate," *Surf. Coatings Technol.*, vol. 490, 2024, doi: 10.1016/j.surfcoat.2024.131184.

[59] J. Pattison, S. Celotto, A. Khan, and W. O'Neill, "Standoff distance and bow shock phenomena in the Cold Spray process," *Surf. Coatings Technol.*, vol. 202, no. 8, pp. 1443–1454, 2008, doi: 10.1016/j.surfcoat.2007.06.065.

[60] W. Y. Li *et al.*, "Effect of standoff distance on coating deposition characteristics in cold spraying," *Mater. Des.*, vol. 29, no. 2, pp. 297–304, 2008, doi: 10.1016/j.matdes.2007.02.005.

[61] B. Moreno-Murguia, A. G. Mora-Garcia, H. Canales-Siller, A. L. Giraldo-Betancur, D. G. Espinosa-Arbelaez, and J. Muñoz-Saldaña, "Influence of stand-off distance and pressure in copper coatings deposition efficiency and particle velocity," *Surf. Coatings Technol.*, vol. 430, 2022, doi: 10.1016/j.surfcoat.2021.127986.

[62] S. Garmeh, M. Jadidi, J. M. Lamarre, and A. Dolatabadi, "Cold Spray Gas Flow Dynamics for On and Off-axis Nozzle/Substrate Hole Geometries," *J. Therm. Spray Technol.*, vol. 32, no. 1, pp. 208–225, 2023, doi: 10.1007/s11666-022-01487-w.

[63] O. Ç. Özdemir, J. M. Conahan, and S. Müftü, "Particle velocimetry, cfd, and the role of particle sphericity in cold spray," *Coatings*, vol. 10, no. 12, pp. 1–26, 2020, doi: 10.3390/coatings10121254.

[64] A. Ardeshiri Lordejani, D. Colzani, M. Guagliano, and S. Bagherifard, "An inclusive numerical framework to assess the role of feedstock features on the quality of cold spray deposits," *Mater. Des.*, vol. 224, 2022, doi: 10.1016/j.matdes.2022.111374.

[65] O. C. Ozdemir and S. Muftu, "Novel Method of Predicting Deposition Efficiency in Cold Spray by Incorporating Sphericity into a 1D Analytical Model," *J. Therm. Spray Technol.*, vol. 32, no. 2–3, pp. 657–672, 2023, doi: 10.1007/s11666-023-01532-2.

[66] Y. Sinnwell, A. Maksakov, S. Palis, and S. Antonyuk, "Influence of the particle morphology on the spray characteristics in low-pressure cold gas process," *Powder Technol.*, vol. 464, 2025, doi: 10.1016/j.powtec.2025.121084.

[67] M. Kamaraj and V. M. Radhakrishnan, "Cold Spray Coating Diagram: Bonding Properties and Construction Methodology," *J. Therm. Spray Technol.*, vol. 28, no. 4, pp. 756–768, 2019, doi: 10.1007/s11666-019-00853-5.

[68] K. Deb, A. Pratap, S. Agarwal, and T. Meyarivan, "A fast and elitist multiobjective genetic algorithm: NSGA-II," *IEEE Trans. Evol. Comput.*, vol. 6, no. 2, pp. 182–197, 2002, doi: 10.1109/4235.996017.

[69] M. H. Shojaeefard and J. Zare, "Modeling and combined application of the modified NSGA-II and TOPSIS to optimize a refrigerant-to-air multi-pass louvered fin-and-flat tube condenser," *Appl. Therm. Eng.*, vol. 103, pp. 212–225, 2016, doi: 10.1016/j.applthermaleng.2016.04.093.

[70] H. Yang, N. Liu, M. Li, M. Gu, and Q. Gao, "Design and optimization of heat pipe-assisted liquid cooling structure for power battery thermal management based on NSGA-II and entropy Weight-TOPSIS method," *Appl. Therm. Eng.*, vol. 272, 2025, doi: 10.1016/j.applthermaleng.2025.126416.

[71] H. Canales, I. G. Cano, and S. Dosta, "Window of deposition description and prediction of deposition efficiency via machine learning techniques in cold spraying," *Surf. Coatings Technol.*, vol. 401, 2020, doi: 10.1016/j.surfcoat.2020.126143.

[72] Z. Wang, S. Cai, W. Chen, R. A. Ali, and K. Jin, "Analysis of Critical Velocity of Cold Spray Based on Machine Learning Method with Feature Selection," *J. Therm. Spray Technol.*, vol. 30, no. 5, pp. 1213–1225, 2021, doi: 10.1007/s11666-021-01198-8.

[73] A. Mohankumar *et al.*, "Optimization of Cold Spray Process Inputs to Minimize Porosity and Maximize Hardness of Metal Matrix Composite Coatings on AZ31B Magnesium Alloy," *J. Nanomater.*, vol. 2022, 2022, doi: 10.1155/2022/7900150.

[74] O. Shorinov, A. Dolmatov, S. Polyviany, and K. Balushok, "Optimization of cold spray process parameters to maximize adhesion and deposition efficiency of Ni+Al2O3 coatings," *Mater. Res. Express*, vol. 10, no. 12, 2023, doi: 10.1088/2053-1591/ad11fd.

[75] M. Ashokkumar, D. Thirumalaikumarasamy, T. Sonar, P. Vignesh, and S. Deepak, "Optimization of cold spray coating parameters using RSM for reducing the porosity level of AA2024/Al2O3 coating on AZ31B magnesium alloy," *Int. J.*

Interact. Des. Manuf., 2023, doi: 10.1007/s12008-023-01597-x.

[76] C. Singhal and Q. Murtaza, "Numerical optimization of cold gas dynamic spray process parameters through response surface methodology," *Adv. Mater. Process. Technol.*, 2024, doi: 10.1080/2374068X.2024.2439710.

[77] T. Kun, H. Wenjie, and W. Yurong, "Optimization of Cold Spray Nozzles Based on the Response Surface Methodology," *J. Eng. Sci.*, vol. 11, no. 1, pp. F1–F11, 2024, doi: 10.21272/jes.2024.11(1).f1.

[78] M. Eberle, S. Pinches, P. Guzman, H. King, H. Zhou, and A. Ang, "Application of machine learning for the prediction of particle velocity distribution and deposition efficiency for cold spraying titanium powder," *Comput. Mater. Sci.*, vol. 244, 2024, doi: 10.1016/j.commatsci.2024.113224.

[79] J. Gutiérrez de Frutos, A. List, S. Nielsen, F. Gärtner, and T. Klassen, "Nozzle Geometry Evaluation for Cold Spray Applications by Using 3D-CFD Calculations," *J. Therm. Spray Technol.*, vol. 34, no. 2, pp. 570–586, 2025, doi: 10.1007/s11666-025-01945-1.

[80] A. Mehmood, M. Zunaid, and A. K. Madan, "A bibliometric analysis of cold spray coating process using VOSviewer," *Mater. Today Proc.*, 2022, doi: 10.1016/j.matpr.2022.12.135.

[81] A. Mehmood, M. Zunaid, and A. K. Madan, "CFD-based multi-objective optimization of cold spray parameters for enhanced coating quality and minimized radial dispersion," *Appl. Therm. Eng.*, p. 129772, 2026, doi: 10.1016/j.applthermaleng.2026.129772.

[82] *ANSYS Inc, Fluent User Guide*. USA, 2021. [Online]. Available: https://www.ansys.com/products/fluids/ansys-fluent

[83] M. Meyer, S. Yin, and R. Lupoi, "Particle in-flight velocity and dispersion measurements at increasing particle feed rates in cold spray," *Proc. Int. Therm. Spray Conf.*, vol. 1, pp. 37–42, 2016, doi: 10.31399/asm.cp.itsc2016p0037.

[84] S. A. Morsi and A. J. Alexander, "An investigation of particle trajectories in two-phase flow systems," *J. Fluid Mech.*, vol. 55, no. 2, pp. 193–208, 1972, doi:

10.1017/S0022112072001806.

[85] A. Haider and O. Levenspiel, “Drag coefficient and terminal velocity of spherical and nonspherical particles,” *Powder Technol.*, vol. 58, no. 1, pp. 63–70, 1989, doi: 10.1016/0032-5910(89)80008-7.

[86] S. Yin, M. Meyer, W. Li, H. Liao, and R. Lupoi, “Gas Flow, Particle Acceleration, and Heat Transfer in Cold Spray: A review,” *J. Therm. Spray Technol.*, vol. 25, no. 5, pp. 874–896, 2016, doi: 10.1007/s11666-016-0406-8.

[87] W.-Y. Li, C.-J. Li, H.-T. Wang, and C.-X. Li, “Measurement and Numerical Simulation of Particle Velocity in Cold Spraying,” *Therm. Spray 2006 Proc. from Int. Therm. Spray Conf.*, vol. 83669, pp. 253–258, 2006, doi: 10.31399/asm.cp.itsc2006p0253.

[88] B. Samareh, O. Stier, V. Lüthen, and A. Dolatabadi, “Assessment of CFD modeling via Flow visualization in cold spray process,” *J. Therm. Spray Technol.*, vol. 18, no. 5–6, pp. 934–943, 2009, doi: 10.1007/s11666-009-9363-9.

[89] J. Fiebig, J. P. Gagnon, G. Mauer, E. Bakan, and R. Vaßen, “In-Flight Measurements of Particle Temperature and Velocity with a High-Speed IR Camera During Cold Gas Spraying of In718 and TiAlCrNb,” *J. Therm. Spray Technol.*, vol. 31, no. 7, pp. 2013–2024, 2022, doi: 10.1007/s11666-022-01426-9.

[90] H. Assadi, F. Gärtner, T. Stoltenhoff, and H. Kreye, “Bonding mechanism in cold gas spraying,” *Acta Mater.*, vol. 51, no. 15, pp. 4379–4394, 2003, doi: 10.1016/S1359-6454(03)00274-X.

[91] A. Mehmood, M. Zunaid, and A. K. Madan, “Multi-objective optimization and performance improvement of CD nozzle design parameters for cold spray coating process using RSM, ANN and GA,” *Mater. Today Commun.*, vol. 40, 2024, doi: 10.1016/j.mtcomm.2024.109446.

[92] S. Dey, N. M. Reang, P. K. Das, and M. Deb, “Comparative study using RSM and ANN modelling for performance-emission prediction of CI engine fuelled with bio-diesohol blends: A fuzzy optimization approach,” *Fuel*, vol. 292, 2021, doi: 10.1016/j.fuel.2021.120356.

[93] T. Goyal, T. S. Sidhu, and R. S. Walia, “Multi-response optimization of process parameters for low-pressure cold spray coating process using taguchi and utility concept,” *J. Therm. Spray Technol.*, vol. 23, no. 1–2, pp. 114–122, 2014, doi: 10.1007/s11666-013-9988-6.

[94] B. Mahato, J. Yoder, G. Simmons, N. Huft, I. Nault, and P. Lucon, “Particle dynamics in low-pressure cold spray additive manufacturing — A numerical and experimental study,” *Addit. Manuf.*, vol. 110, 2025, doi: 10.1016/j.addma.2025.104937.

[95] Z. Ge *et al.*, “Tri-objective optimization and comprehensive performance evaluation of geothermal-driven transcritical organic Rankine cycle,” *Appl. Therm. Eng.*, p. 129221, 2025, doi: 10.1016/j.applthermaleng.2025.129221.

[96] O. Imghoure, N. Belouaggadia, M. Ezzine, R. Lbibb, and Z. Younsi, “Performance evaluation of phase change materials for thermal comfort in a hot climate region,” *Appl. Therm. Eng.*, vol. 186, 2021, doi: 10.1016/j.applthermaleng.2020.116509.

[97] H. Assadi *et al.*, “On parameter selection in cold spraying,” *J. Therm. Spray Technol.*, vol. 20, no. 6, pp. 1161–1176, 2011, doi: 10.1007/s11666-011-9662-9.

[98] V. Luzin, K. Spencer, and M. X. Zhang, “Residual stress and thermo-mechanical properties of cold spray metal coatings,” *Acta Mater.*, vol. 59, no. 3, pp. 1259–1270, 2011, doi: 10.1016/j.actamat.2010.10.058.

[99] M. Terrone, A. Ardeshiri Lordejani, J. Kondas, and S. Bagherifard, “A numerical Approach to design and develop freestanding porous structures through cold spray multi-material deposition,” *Surf. Coatings Technol.*, vol. 421, 2021, doi: 10.1016/j.surfcoat.2021.127423.

[100] P. Cavaliere and A. Silvello, “Processing conditions affecting residual stresses and fatigue properties of cold spray deposits,” *Int. J. Adv. Manuf. Technol.*, vol. 81, no. 9–12, pp. 1857–1862, 2015, doi: 10.1007/s00170-015-7365-y.

[101] H. B. Jung, J. I. Park, S. H. Park, H. J. Kim, C. H. Lee, and J. W. Han, “Effect of the expansion ratio and length ratio on a gas-particle flow in a converging-diverging cold spray nozzle,” *Met. Mater. Int.*, vol. 15, no. 6, pp. 967–970, 2009, doi:

10.1007/s12540-009-0967-x.

[102] P. Liebersbach, A. Foelsche, V. K. Champagne, M. Siopis, A. Nardi, and D. P. Schmidt, "CFD Simulations of Feeder Tube Pressure Oscillations and Prediction of Clogging in Cold Spray Nozzles," *J. Therm. Spray Technol.*, vol. 29, no. 3, pp. 400–412, 2020, doi: 10.1007/s11666-020-00992-0.

[103] L. Alonso, M. A. Garrido, and P. Poza, "An optimisation method for the cold-spray process: On the nozzle geometry," *Mater. Des.*, vol. 214, 2022, doi: 10.1016/j.matdes.2022.110387.

[104] S. Elghobashi, "On predicting particle-laden turbulent flows," *Appl. Sci. Res.*, vol. 52, no. 4, pp. 309–329, 1994, doi: 10.1007/BF00936835.

[105] A. Moridi, S. M. Hassani-Gangaraj, and M. Guagliano, "A hybrid approach to determine critical and erosion velocities in the cold spray process," *Appl. Surf. Sci.*, vol. 273, pp. 617–624, 2013, doi: 10.1016/j.apsusc.2013.02.089.

[106] C. Zhang *et al.*, "Critical velocity and deposition efficiency in cold spray: A reduced-order model and experimental validation," *J. Manuf. Process.*, vol. 134, pp. 547–557, 2025, doi: 10.1016/j.jmapro.2024.12.077.

[107] S. Yin, X. Suo, H. Liao, Z. Guo, and X. Wang, "Significant influence of carrier gas temperature during the cold spray process," *Surf. Eng.*, vol. 30, no. 6, pp. 443–450, 2014, doi: 10.1179/1743294414Y.0000000276.

APPENDIX

Table A1: FCCD design matrix with CFD responses for nozzle geometry optimization

Run No.	Input factors					Response values			
	L_i (mm)	L_d (mm)	D_{id} (mm)	L_i (mm)	D_e (mm)	PV (m/s)	PT (K)	HF (KW/m^2)	SP (MPa)
1	55	185	1	20	7.25	613.8	501.5	10.55	0.441
2	90	70	3	10	8.1	451.7	379.4	4.49	0.405
3	90	70	3	30	8.1	454.5	378.6	4.74	0.405
4	90	70	1	30	6.4	525.4	558.2	10.51	0.586
5	20	300	3	10	6.4	493.7	313.9	4.15	0.455
6	20	300	1	10	6.4	586.5	494.2	10.32	0.443
7	20	300	1	30	6.4	590.3	461.7	10.60	0.447
8	90	70	3	10	6.4	461.7	366.5	4.23	0.597
9	55	185	2	10	7.25	581.1	456.8	8.40	0.443
10	55	185	2	20	7.25	587.2	444.8	8.15	0.444
11	20	70	3	30	6.4	456.9	313.7	4.65	0.581
12	20	70	3	10	6.4	448.9	341.5	4.37	0.558
13	55	185	2	20	6.4	569	438.6	8.17	0.534
14	55	185	2	20	7.25	579.7	439.1	7.96	0.444
15	55	185	2	20	7.25	579.2	442.3	8.20	0.444
16	55	185	2	20	7.25	576.9	440.1	7.96	0.444
17	90	300	3	10	8.1	566.3	341.2	5.70	0.342
18	20	300	1	30	8.1	630	431.6	9.27	0.320
19	90	185	2	20	7.25	586	454.2	8.32	0.447
20	20	70	3	10	8.1	438	341.2	4.04	0.377
21	20	300	1	10	8.1	615.2	481.2	10.56	0.316
22	55	300	2	20	7.25	588.2	429.3	8.24	0.407
23	20	300	3	30	8.1	542.2	303.5	4.05	0.334
24	90	300	1	10	8.1	642.6	524.1	10.63	0.339
25	90	70	3	30	6.4	475.6	371.2	4.68	0.584
26	55	185	2	20	7.25	580.5	427.1	9.13	0.444
27	20	70	1	10	8.1	493.7	463.3	10.04	0.371
28	20	70	3	30	8.1	443.8	318.6	5.07	0.394
29	90	300	3	30	8.1	556.1	339.4	5.05	0.344
30	55	185	2	20	7.25	580.4	426.8	8.17	0.453
31	90	300	1	30	8.1	645.2	506.5	10.69	0.339
32	90	300	3	10	6.4	517.6	342.8	4.82	0.474
33	20	300	3	10	8.1	534.2	309.5	4.00	0.320
34	20	70	1	30	8.1	498	390.2	10.16	0.375

35	55	70	2	20	7.25	493.3	444.7	8.06	0.483
36	90	70	1	10	6.4	523.7	582.3	10.56	0.585
37	90	300	3	30	6.4	516.5	346.7	4.69	0.475
38	20	70	1	30	6.4	515	399.4	10.12	0.555
39	90	300	1	30	6.4	603.7	530.1	10.73	0.463
40	90	70	1	10	8.1	505.7	585.4	10.32	0.399
41	90	300	1	10	6.4	601	538.5	10.22	0.463
42	55	185	2	20	7.25	580.4	427.1	8.17	0.444
43	55	185	2	20	8.1	585.4	430.2	8.10	0.368
44	55	185	2	20	7.25	580.4	426.9	8.17	0.444
45	90	70	1	30	8.1	508.9	561.4	10.21	0.399
46	55	185	3	20	7.25	529.9	348.2	4.73	0.449
47	20	300	3	30	6.4	511.3	307.5	4.59	0.467
48	20	70	1	10	6.4	512.7	467.2	9.94	0.549
49	20	185	2	20	7.25	569.2	378.4	7.83	0.423
50	55	185	2	30	7.25	582.1	422.8	8.25	0.445

Table A2: CFD generated dataset for process parameter optimization

Run No.	Input factors					Response values		
	G_p (MPa)	G_t (K)	D_p (μm)	D_t (mm)	SoD (mm)	PV (m/s)	PT (K)	RD (mm)
1	4	913	5	4	40	921.92	463.9	1.1951
2	3	773	25	3.25	25	618.92	430.5	1.6478
3	3	773	25	3.25	25	619.35	430.5	1.6478
4	3	773	25	3.25	25	619.02	430.5	1.6475
5	3	773	25	4	25	614.51	430.5	0.7184
6	3	633	25	3.25	25	577.86	356.3	1.0057
7	2	913	45	2.5	40	509.41	397.5	1.3814
8	3	773	25	3.25	10	612.17	433.6	1.5902
9	2	913	45	2.5	10	504.82	398.2	1.3477
10	4	633	45	2.5	40	549.28	348.9	1.8729
11	2	633	45	4	40	478.06	355.1	0.9653
12	2	913	45	4	10	511.27	435.8	1.1534
13	4	913	5	2.5	10	920.32	477.3	2.1483
14	4	913	5	2.5	40	932.26	468.3	2.3668
15	3	773	25	3.25	40	626.46	434.2	1.7485
16	4	913	45	2.5	10	597.61	416.1	1.6924
17	2	913	5	2.5	10	854.15	496.5	2.0285
18	2	913	5	4	10	836.85	540.9	1.9585
19	2	633	45	4	10	465.22	356.3	0.9212
20	4	633	45	4	10	533.79	357.8	0.5562

21	2	633	45	2.5	40	467.24	337.2	1.4944
22	3	773	5	3.25	25	840.62	432.2	2.1669
23	4	633	45	2.5	10	539.45	351.3	1.7895
24	2	913	5	4	40	856.59	532.9	2.0550
25	3	773	25	3.25	25	619.86	430.5	1.6478
26	2	633	5	2.5	10	748.49	352.3	2.1256
27	4	773	25	3.25	25	651.40	431.8	1.3986
28	2	633	5	4	40	742.15	370	1.7223
29	2	913	5	2.5	40	855.36	498.3	2.1666
30	4	913	45	4	40	614.35	442.3	0.6670
31	4	633	5	4	40	800.32	310	1.1217
32	2	633	45	2.5	10	463.51	342.5	1.4321
33	4	633	5	4	10	764.96	332.1	0.9916
34	2	633	5	2.5	40	750.28	358.6	2.2864
35	3	773	45	3.25	25	548.27	391.3	1.4679
36	4	913	45	4	10	598.61	442.5	0.5675
37	2	633	5	4	10	736.88	374.3	1.6332
38	4	913	5	4	10	892.48	496.3	1.0444
39	3	913	25	3.25	25	653.86	500	1.7840
40	4	633	5	2.5	10	796.69	340.3	2.2301
41	3	773	25	3.25	25	622.98	430.5	1.6478
42	2	773	25	3.25	25	580.07	422.3	1.4833
43	3	773	25	3.25	25	619.23	430.5	1.6478
44	4	633	45	4	40	550.71	353	0.6343
45	4	913	45	2.5	40	609.27	418.9	1.8067
46	3	773	25	3.25	25	622.97	430.5	1.6478
47	4	633	5	2.5	40	805.64	327	2.4240
48	3	773	25	3.25	25	623.11	430.5	1.6478
49	2	913	45	4	40	527.93	433.5	1.2903
50	3	773	25	2.5	25	622.26	417.3	1.7334

Table A3: Grey relational analysis dataset with GRC, GRG, and grey order

Run No.	Factors				Responses		GRC		GRG	Grey order
	ΔP (MPa)	D_p (μm)	ER	T_c (K)	PV (m/s)	PT (K)	PV (m/s)	PT (K)		
1	0.2	25	8	450	613.02	448	0.4117	0.6604	0.5361	13
2	0.1	5	6	300	804.26	451	0.7433	0.6364	0.6898	7
3	0.3	45	10	600	547.44	453	0.3571	0.6213	0.4892	19
4	0.2	25	6	450	593.23	476	0.3936	0.4884	0.4410	27
5	0.3	5	10	600	858.53	425	0.9635	0.9292	0.9463	2
6	0.3	5	6	600	816.96	476	0.7853	0.4884	0.6368	11
7	0.3	45	6	600	528.49	468	0.3439	0.5276	0.4358	28

8	0.2	25	8	450	613.11	449	0.4118	0.6522	0.5320	15
9	0.3	25	8	450	609.93	448	0.4088	0.6604	0.5346	14
10	**0.2**	**25**	**10**	**450**	**625.09**	**451**	**0.4237**	**0.6364**	**0.5300**	**16**
11	0.2	25	8	450	613.03	451	0.4117	0.6364	0.5241	17
12	0.2	25	8	450	613.31	458	0.4120	0.5866	0.4993	18
13	0.2	25	8	600	620.66	508	0.4192	0.3763	0.3978	31
14	0.3	5	10	300	822.49	396	0.8051	0.8015	0.8033	5
15	0.1	45	6	300	522.63	393	0.3400	0.7664	0.5532	12
16	0.1	45	10	300	542.05	376	0.3533	0.6140	0.4836	20
17	**0.1**	**45**	**6**	**600**	**531.71**	**493**	**0.3461**	**0.4217**	**0.3839**	**32**
18	0.2	25	8	300	603.52	423	0.4028	0.9633	0.6831	8
19	0.2	25	8	450	614.99	464	0.4136	0.5497	0.4817	21
20	0.1	45	10	600	551.08	477	0.3598	0.4839	0.4218	30
21	0.1	25	8	450	618.16	474	0.4167	0.4976	0.4572	26
22	0.1	5	10	600	865.22	434	1.0000	0.8015	0.9008	3
23	0.2	25	8	450	615.09	466	0.4137	0.5385	0.4761	22
24	0.3	5	6	300	783.37	429	0.6832	0.8678	0.7755	6
25	0.2	45	8	450	539.11	424	0.3512	0.9459	0.6486	10
26	0.2	5	8	450	837.51	438	0.8643	0.7554	0.8099	4
27	**0.1**	**5**	**10**	**300**	**844.47**	**421**	**0.8948**	**1.0000**	**0.9474**	**1**
28	0.2	25	8	450	615.28	469	0.4139	0.5224	0.4682	24
29	0.3	45	6	300	512.18	376	0.3333	0.6140	0.4737	23
30	0.1	5	6	600	823.53	476	0.8089	0.4884	0.6487	9
31	0.3	45	10	300	531.86	358	0.3462	0.5072	0.4267	29
32	0.2	25	8	450	615.45	471	0.4141	0.5122	0.4631	25

LIST OF PUBLICATIONS

- **List of papers published in SCIE journals: -**

1. Mehmood, A., Zunaid, M. & Madan, A.K. CFD-based multi-objective optimization of cold spray parameters for enhanced coating quality and minimized radial dispersion. Applied Thermal Engineering (2026).
   DOI: https://doi.org/10.1016/j.applthermaleng.2026.129772
   Elsevier (SCIE-indexed journal, Impact factor 6.9)
2. Mehmood, A., Zunaid, M. & Madan, A.K. Multi-objective optimization and performance improvement of CD nozzle design parameters for cold spray coating process using RSM, ANN and GA. Materials Today Communications (2024).
   DOI: https://doi.org/10.1016/j.mtcomm.2024.109446
   Elsevier (SCIE-indexed journal, Impact factor 4.5)

- **List of papers presented at international conferences: -**

1. CFD Analysis of Particle Sphericity Effects on Velocity and Radial Dispersion in High-Pressure Cold Spray. Ayaz Mehmood, M. Zunaid & A. K Madan **(Conference-ICAMMTS 2026, Noida Institute of Engineering and Technology, Greater Noida, India)**
2. Numerical Investigation of Cold Spray Process Parameters Using Response Surface Methodology and Grey Relational Analysis. Ayaz Mehmood, M. Zunaid & A. K Madan **(Conference-MATHED 2025, National Institute of Technology Hamirpur, India)**
3. A brief review of technical parameter and its application used in cold spray process. Ayaz Mehmood, M. Zunaid & A. K Madan **(Conference-ICAMMT 2022, Maulana Azad National Institute of Technology Bhopal, India)**
   DOI: https://doi.org/10.1007/978-981-99-2921-4_23
4. A bibliometric analysis of cold spray coating process using VOSviewer. Ayaz Mehmood, M. Zunaid & A. K Madan **(Conference-ICAME 2022, National Institute of Technology Delhi, India)**
   DOI: https://doi.org/10.1016/j.matpr.2022.12.135

CURRICULUM VITAE

Ayaz Mehmood

Research Scholar | Mechanical Engineering | Cold Spray Coating | CFD | Thermal Science

Ayaz Mehmood is a research scholar in the Department of Mechanical Engineering at Delhi Technological University (DTU), Delhi. He is currently serving as an Assistant Professor in the Department of Mechanical Engineering at Mewat Engineering College (Waqf), Mewat, Haryana, where he has been working since 2011. Prior to joining Mewat Engineering College, he worked as a Senior Lecturer at the World Institute of Technology, Sohna, Haryana. He also served as Guest Faculty at Zakir Husain College of Engineering and Technology, Aligarh Muslim University, Aligarh, and at University Polytechnic, Aligarh Muslim University. His doctoral research is focused on cold spray coating process, computational fluid dynamics-based analysis, process parameter investigation, and coating performance improvement. His work also involves the study of particle velocity, particle temperature, nozzle flow behavior, gas-particle interaction, and optimization of cold spray operating conditions. He has published research papers in reputed international and national journals and conference proceedings.

Research Interests: Cold Spray Coating, Computational Fluid Dynamics, Heat and Mass Transfer, Thermodynamics, Thermal Science, Particle Dynamics, and Process Optimization.